

**PROCEEDINGS OF
THE 2018
SURF@IFISC
FELLOWSHIPS**



Universitat
de les Illes Balears



CSIC

Proceedings of the 2018 SURF@IFISC Fellowships

The SURF (Summer Undergraduate Research Fellowships) Program is offered by IFISC since 2013 with the goal of attracting excellent undergraduate students with majors compatible with IFISC research lines and offers Summer internships at IFISC, typically during the month of July, advised by members of IFISC Claustro.

SURF attracted for the Summer of 2018 45 candidates from 20 universities and 4 different countries, from which 6 candidates were selected. One (female) candidate turned down the offer and a new candidate was selected.

These are the proceedings:

1. Javier Fernández Sánchez de la Viña and Jose Javier Ramasco, *Big Data: The real estate market*
2. Gabriel Garau Estarellas, Gian Luca Giorgi, Miguel C. Soriano, and Roberta Zambrini, *Application of machine learning to a probing scheme based on quantum synchronization*
3. Álvaro Mas and Rosa López, *Nonlinear thermoelectric transport in a selective spin environment*
4. Álvaro Moreno Abajo, Miguel C. Soriano, and Ingo Fischer, *Autonomous Operation of Optoelectronic Reservoir Computing Systems*
5. David Pérez González, Damià Gomila, and Pere Colet, *Modeling and dynamics of the power grid*
6. Javier Rivera Deán and Claudio R. Mirasso, *Synchronization in a model of coupled neural oscillators*

The following publication has been based on one of the work of one of the SURF Fellows:

Gabriel Garau Estarellas, Gian Luca Giorgi, Miguel C. Soriano, and Roberta Zambrini, *Machine Learning Applied to Quantum Synchronization-Assisted Probing*, *Advanced Quantum Technologies* **2**, 1800085 (2019). DOI: 10.1002/qute.201800085

Big Data: The real state market

Javier Fernández Sánchez de la Viña, José Javier Ramasco,
Riccardo Gallotti, Rafel Crespi and Eduard Alonso
Instituto de Física Interdisciplinar y Sistemas Complejos IFISC (CSIC-UIB)
Campus Universitat de les Illes Balears, E-07122 Palma de Mallorca, Spain

Abstract

Modelling competition between hotel industry, Airbnb housing and long term housing, needs to consider both horizontal (spatial) and vertical (quality) differentiation. We Will try to explain how these markets are connected to each other, specially hotel and Airbnb, which although are not totally substitutable, show a clear competition, which has been labeled by the hotel industry as unfair. Some features about the relationship between short term (Airbnb) and long term housing will be pointed out too. In addition, some ideas of the spatial formation of prices will be discussed from the data.

1 Introduction

Due to the rise of peer-to-peer rental models for vacation housing, especially Airbnb, many criticisms have been received. On one side from the hotel sector, which denounce a supposed unfair competition, and on the other side from the ordinary rental claimants, who accuse Airbnb of causing a rise in rental prices that residents will have to bear. Our purpose will be to analyze, in the island of Mallorca, how competition relationships are established, as well as the general welfare due to the emergence of this business model, also considering positive externalities, such as the benefits of the hotel trade. In addition, given the nature of the sectors, we will take advantage to develop a model of space economy and, ultimately, to aspire to integrate in a single model the space-time competition between the three sectors (including with themselves). From now on, in the theoretical plane (models) we will refer to the vacation and no vacation housing market, but in our case we will identify them with the Airbnb and Idealista platforms, respectively.

The report can be easily divided into two parts. The first one consists in a brief description of the data. The second one is constituted by some approaches to theoretical models.

2 Data analysis

Most of the work has consisted of reading, cleaning and preparing the database, as well as making the plots.

2.1 InsideAirbnb

The first database which we have worked with has been obtained in InsideAirbnb. We should point out that the description is quite poor, given the nature of the data. These consist of the minimum prices offered throughout 2017 for the homes announced on a certain day of 2017.

Although several different kind of housing are considered, we are only interested in the apartments (around 30000), and we work with the variable price/(total number of available places). It is an approximation, while the occupancy ratio varies with the number of available places, but we will omit this fact for convenience, since the bias is committed globally in spatial terms.

Our first goal is trying to understand how Airbnb "competes spatially with itself". Then, we need to look for a proxy in the process of formation of prices. It depends on the unknown tourist demand. What we propose now is a naive model in which demand is approximated by the offer.

We consider that individuals want to go to a certain sector of the city with probability given by the relative supply of the same. Thus, given an individual with a budget B (random and

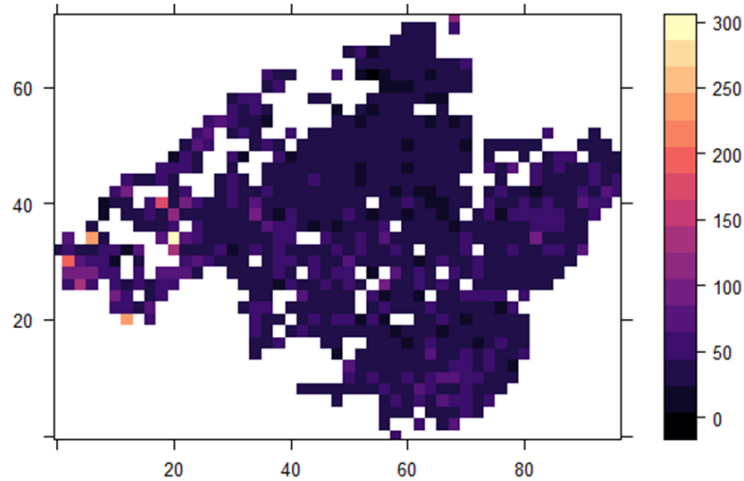


Figure 1: Airbnb average minimum prices (1 pixel=1km·1km). 2017

independent at the time of his stay decision), he may decide whether to rent in his first election, (i, j) , or in a neighboring sector that reports a loss of welfare that will be given by a function f of the distance between sectors, whenever its budget allows it. We define the margin of the budget on the effective price (sum of the price to be paid to the owner plus the cost that the lessee assumes to get away from his first election) as

$$\sigma_{(i,j)}(k, l) = B - (p_{(k,l)} + f_{(i,j)}(k, l)) \quad (1)$$

where (k,l) refers to as many neighbors as be desired.

Thereby, for the simplest case, in which the lessee is only willing to move to an adjoining neighbor: $\sigma_{(i,j)}(i, j) = B - p_{(i,j)}$, $\sigma_{(i,j)}(i + 1, j) = B - (p_{(i+1,j)} + c)$, $\sigma_{(i,j)}(i - 1, j) = B - (p_{(i-1,j)} + c)$, $\sigma_{(i,j)}(i, j + 1) = B - (p_{(i,j+1)} + c)$, $\sigma_{(i,j)}(i, j - 1) = B - (p_{(i,j-1)} + c)$, where c is the first neighbors value of the distance between sectors function, and σ is not defined in any other case. The final decision is made according to:

$$P_{(i,j)}(k, l) = \begin{cases} \frac{\sigma_{(i,j)}(k,l)}{\sum_{(k,l) \in A} \sigma_{(i,j)}(k,l)} & \text{if } \sigma_{(i,j)}(k, l) > 0 \\ 0 & \text{other case} \end{cases}, \quad A := \{(k, l) | \sigma_{(i,j)}(k, l) > 0\} \quad (2)$$

Notice that $P_{(i,j)}(k, l)$ represents the probability of choosing (k,l) when the initial preference of the consumer was (i,j) . The idea of randomizing the decision is to try to leave behind the assumption of perfect rationality. Otherwise, the decision would be deterministic, being the one that maximizes σ . As soon as an agent decides to rent in a sector (k, l) , the rental price in the sector will increase by one unit. Thus, the process will consist of simulating market demand by iterating a large enough number of times until price formation is appreciated.

We have represented (figure[2]) a simulation of this process for Palma de Mallorca with the same data as in figure[1], but with a more refined grid, where the original price for every sector is 1, the simulation has been iterated 1000 times, and only first and second generation (8 in total) neighbors have been considered in the second choice. For each iteration, the price is increased in one unit because of the demand. So, the simulation constructs a price map equal to the offer map. Both variables have been normalized and the function f has been taken as the euclidean distance to the power $n=0.5, 1$ and 2 .

It is easy to perceive in the real data that the supply follows more or less a continuous trend, whereas in the price map any evident standard is observed. As it was expected, we can also see that the smaller the penalty (power) of the function f , the more similar the simulation to the actual offer map. Moreover, the offer map is replicated by the prices, and because of there is no relationship between the real supply and price (as we have said, the reason is the ignorance of the demand), prices are not replicated at all by this silly model.

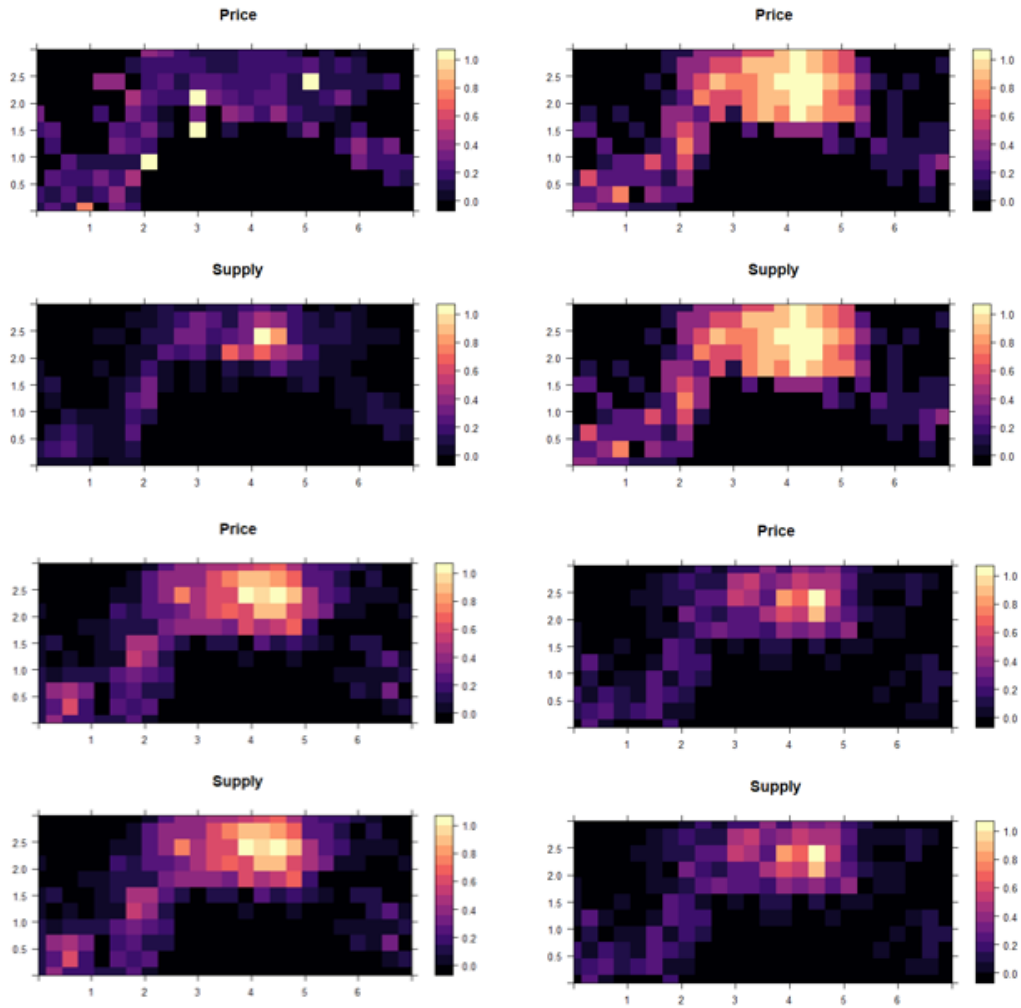


Figure 2: Price and offer space simulation. Top left: real data; top right: $n=2$; bottom left: $n=1$; bottom right: $n=0.5$.

2.2 Idealista

We have also worked with a database of Idealista consisting of the rents made from April to December, in 2017. We have considered a rental has occurred if the same dwelling is not offered on the platform for two consecutive months. In this case there has not been time enough to the interpretation of the data. It may be suitable to measure spatial and/or temporal correlations.

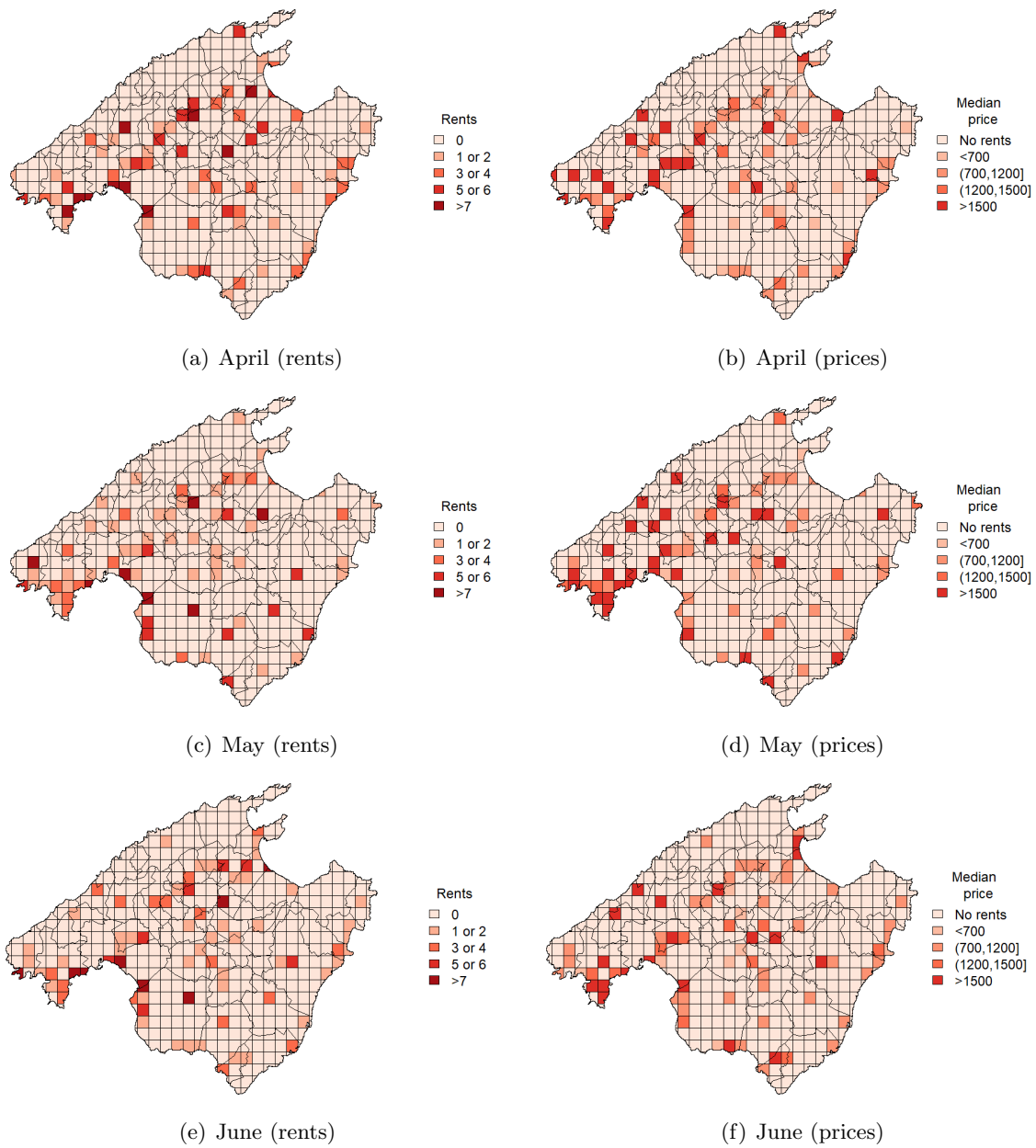


Figure 3: Mallorca. Map of prices and rents. Part I.

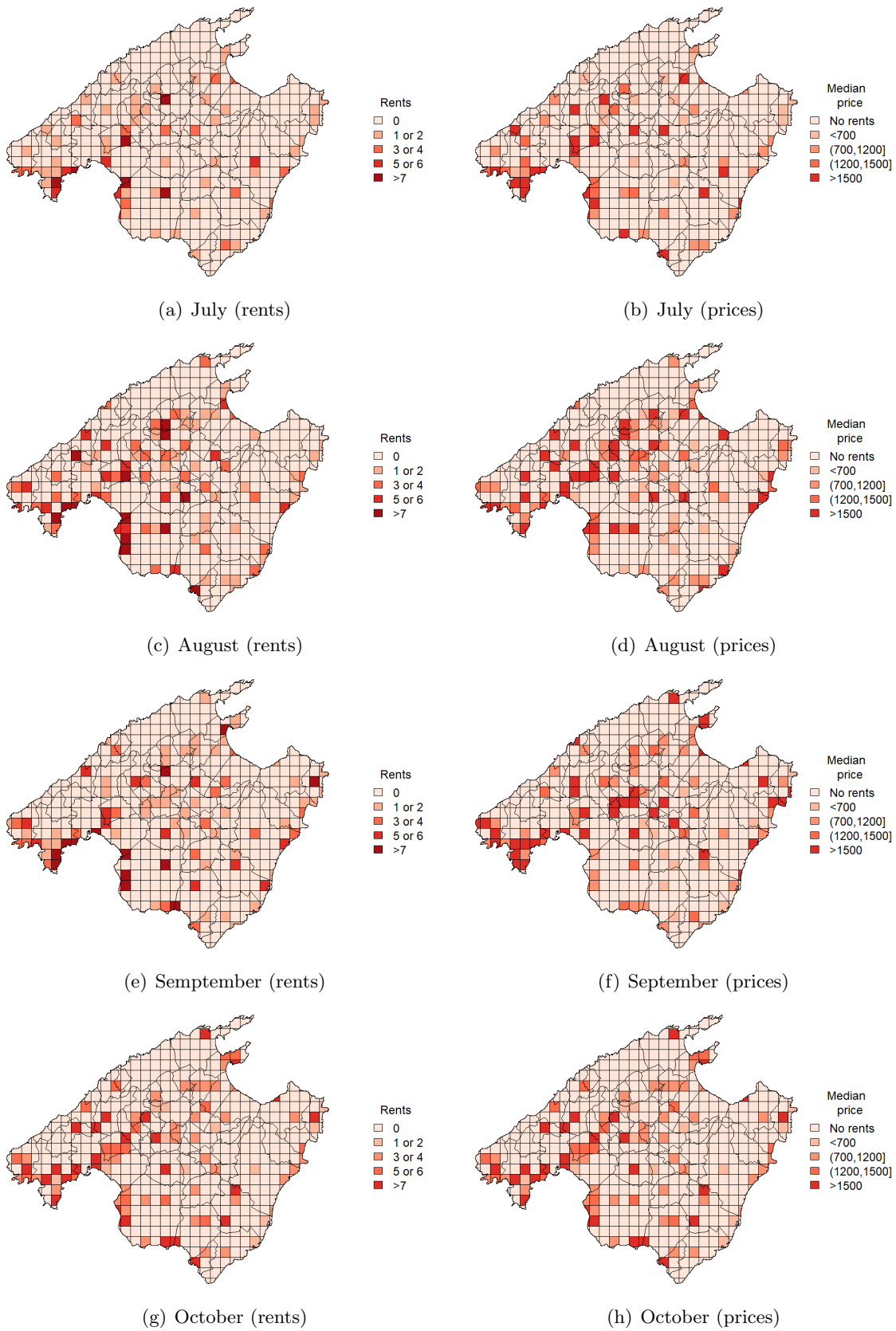


Figure 4: Mallorca. Map of prices and rents. Part II.

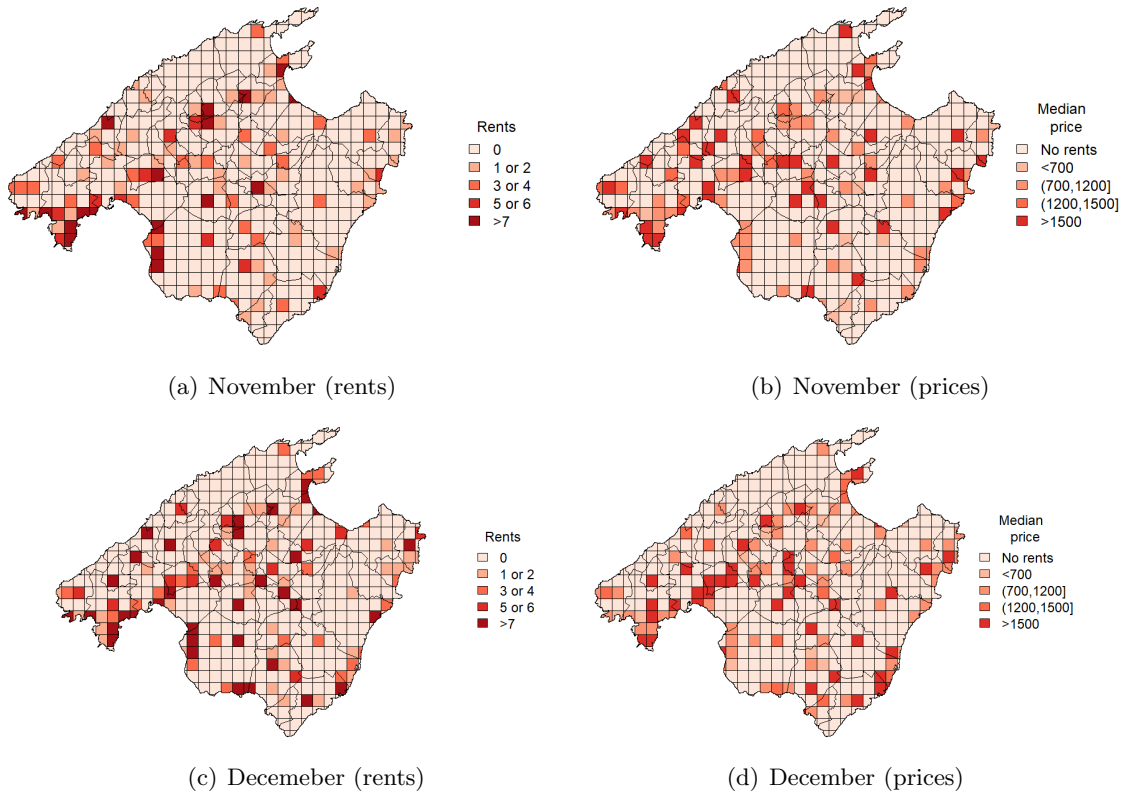


Figure 5: Mallorca. Map of prices and rents. Part III.

We have thought of that an identical representation of Palma and Calvià regions could be interesting. However, in this case we use a more refined grid : 1km per quadrant side instead of 3km per side, as the representations below.

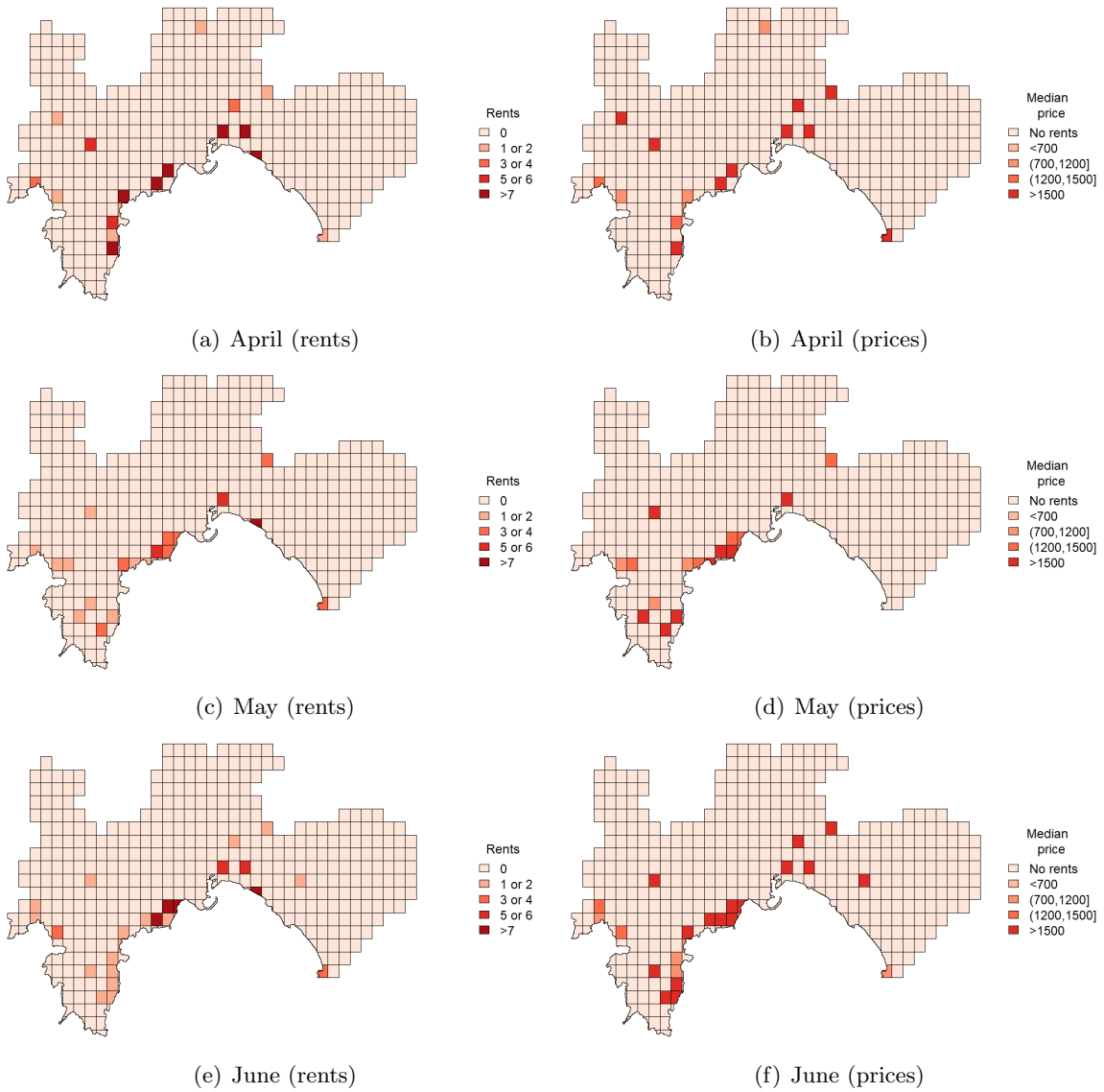


Figure 6: Palma & Calvià. Map of prices and rents. Part I.

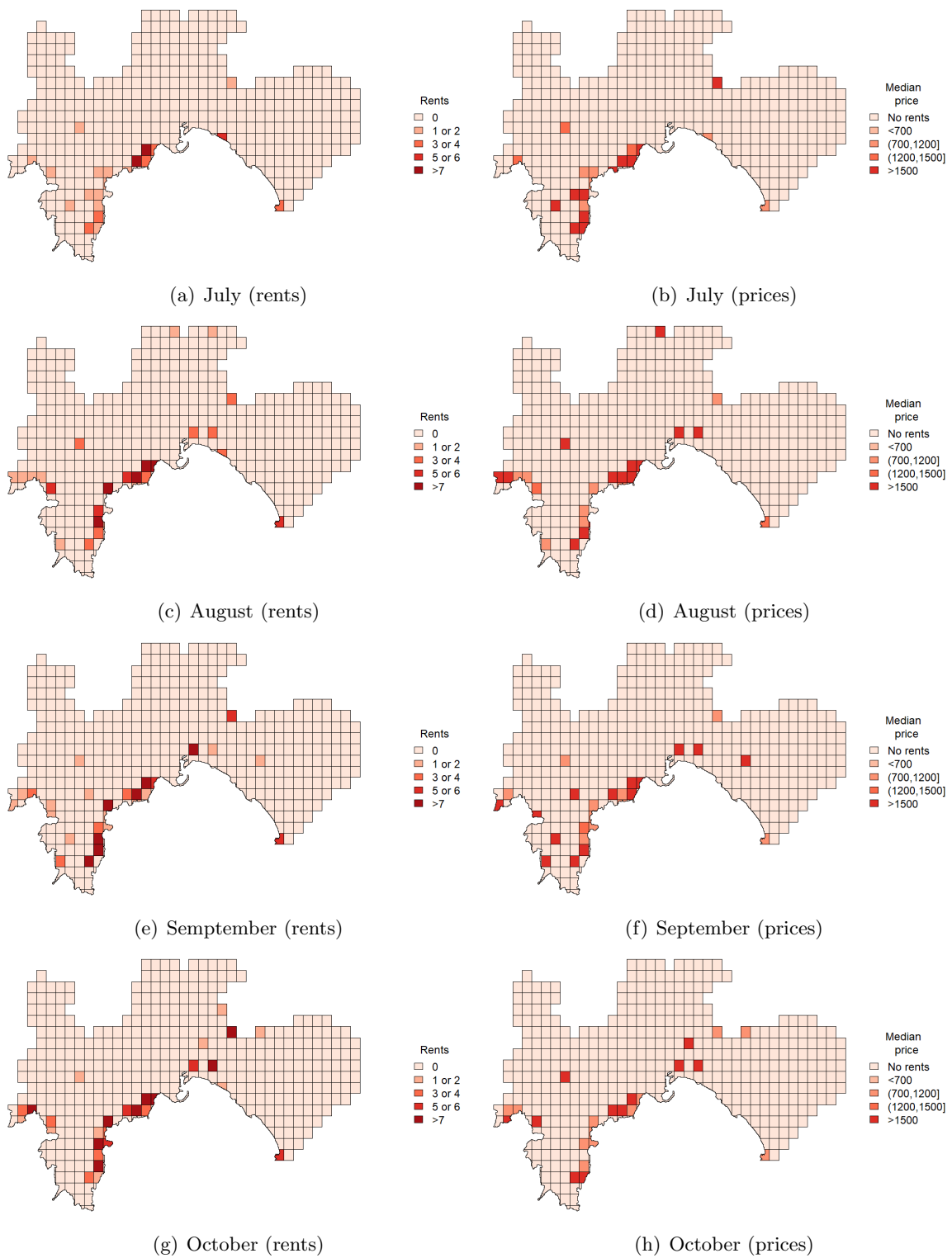


Figure 7: Palma & Calvià. Map of prices and rents. Part II.

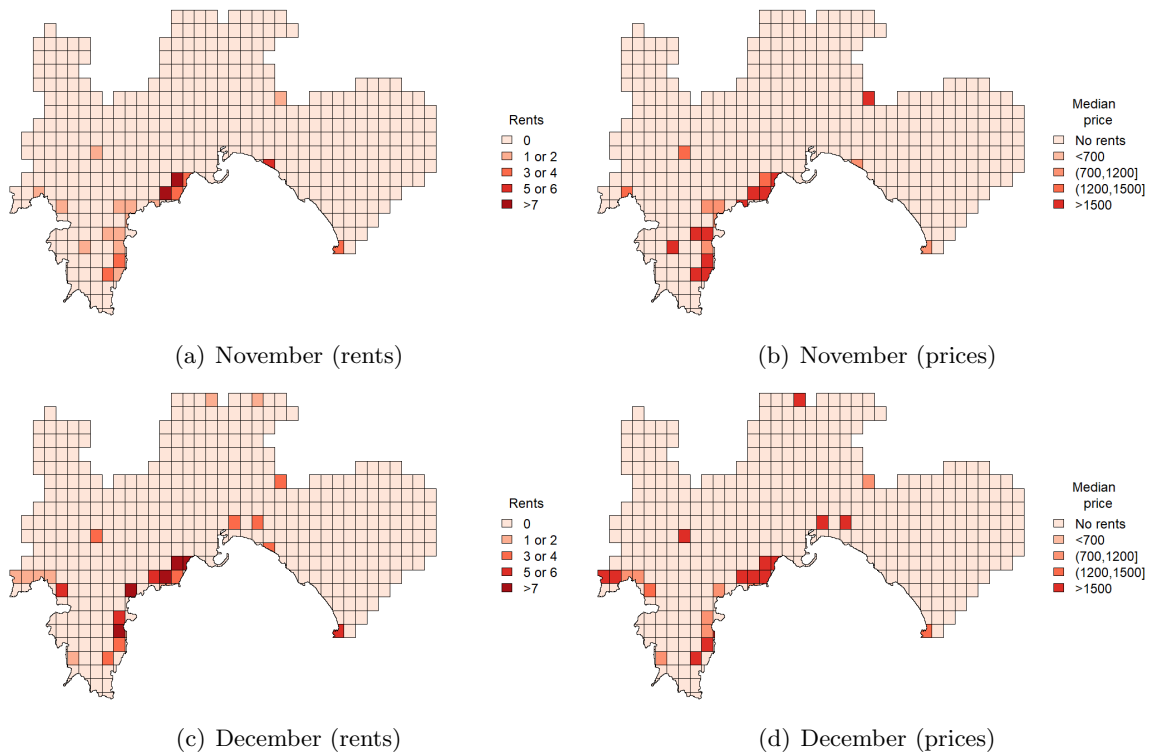


Figure 8: Palma & Calvià. Map of prices and rents. Part III.

3 Theoretical model

In this section, some models for the two competence relationships mentioned will be discussed separately.

3.1 Vacational and no vacational market

At first, we shall think of a simplified framework in which hotel market is not considered. Let suppose that the renters can choose whether they participate in the vacational market or the no vacational (i.e., long term rental) market. Typically, the housing offered in the second market will not be rented all along the year. Thereby, the renter should compare his pay off in both markets: $r \cdot P_V$, P_{NV} , where r is the rate of time in which the dwelling is rented in a year, as long as costs assumed by the owner in both cases are equal (however, it is known that there exist tax benefits which advantage the first choice, but we can also subtract this extra-cost to the renting price in order to do the before comparison).

We start in an equilibrium point where both markets satisfy the demands with prices and quantities $P_0^V, P_0^{NV}, Q_0^V, Q_0^{NV}$, and the owners decide who to rent to according to the previous price pair. Therefore, we say there exists equilibrium if both prices are equal, which is equivalent to say that the owners have not incentives to change to the other market. Then, an increase in the vacational housing demand from D_0^V to D_1^V will cause a excess of demand in the market that would be compensated by an increase in prices from P_0^V to P_0^{V*} . Nevertheless, due to the free choice assumption, together with the pair of prices in both markets, some owners will leave no vacational market in order to face the bigger vacational demand and getting a higher pay off. After that, a movement of both offer curves is observed, and the initial price rise will be reduced until P_1^V (still bigger than P_0^V), while in the other hand prices in no vacational market increase until the equilibrium is restored, in other words: $r \cdot P_1^V = P_1^{NV}$ (see figure[9]). To sum up, every raise in vacational demand will induce an increase in the no vacational housing prices.

We should notice that this analysis is independent of the hotel market as long as the hotel offer is rigid enough to consider that in short-mid term the offer is fixed, while the vacational demand is not. In that case, the inclusion of the hotel market in the framework would involve studying how the vacational housing demand is shared between hotel and private housing demands. Therefore, the

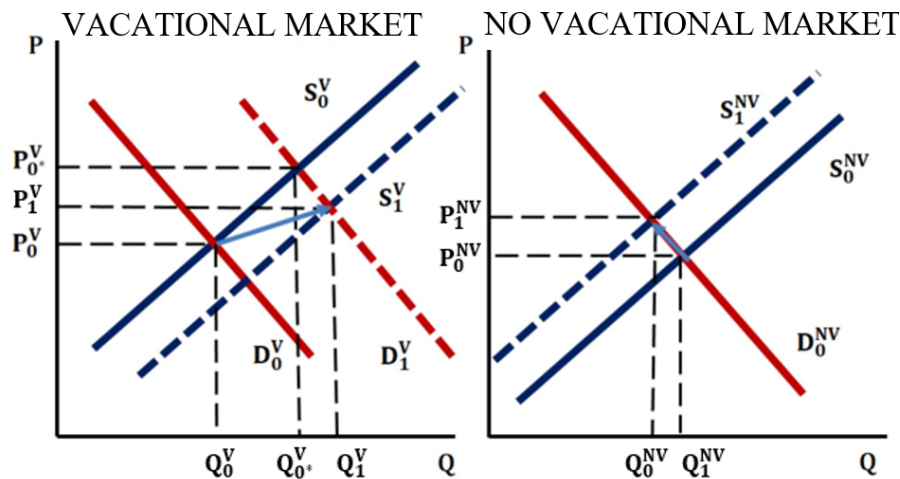


Figure 9: Effect of a rise in the vacational demand on the (no) vacational market.

question as to whether both services are substitutes or have their own public does not, qualitatively affect the discussion. Nevertheless, it is also important to point out that price rises may proceed from the offer side, as via an increase in the IBI (“Impuesto de Bienes Inmuebles”). To contrast this dependence (or fluxes) between both markets, it could be suitable to draw the evolution of the equilibria, which in figure[9] are represented as the small light blue arrows connecting points 0 and 1. Obviously, due to the seasonal behavior in the demand, this contrast should be done in a several years sample, according to the interannual magnitudes.

Another main of the research is the study of the net effect of the vacational renting model based on the peer to peer business model of Airbnb. In accordance with the model proposed, it is obvious the existence of a trade-off involving production surplus of the lessor and the hotelier. As well, two externalities appear, one positive and one negative: on one hand, the raise in the tourism means new opportunities for the industry focused on it (we ought to notice that it is not the case discussed previously, in which the demand was exogeneous instead of induced by the vacational housing offer, and fluxes between hotel and Airbnb do not necessary imply a bigger total vacational demand in the equilibrium); on the other hand, hotel employment jobs are destroyed. However, One might think that tourists replace the hotel with the rent for the sake of the efficiency of the first one (cheaper and more comfortable for the client), and that, via demand, the sector would be forced to be reinvented.

Furthermore, a third externality might be contemplated. In case of an over-specialization of the economy and the offer of holiday homes, other productive activities could be discouraged. In that way, it was paradigmatic what happened in Ibiza some months ago, when due to a lack of doctors, it was necessary to call some doctors outside the island, but with their salaries, they were not able to rent an apartment in the island, and the government had to intervene.

Nowadays, in Mallorca, the answer to this problem has consisted on limiting the number of licenses for vacational renting. This measure grants privileges to the few who had been renting their apartments before the law was decided, so it does nor look like the most accurate decision for the situation. An alternative could be based on agreeing on a number of new licenses every year, which have to be allocated through an auction system. In this way, in addition to seeming to be a more just solution, the Administration will have a higher income.

In short, it is a very difficult conflict to arbitrate for public institutions. In the first place, due to the existence of pressure groups. And secondly (and perhaps the most complicated issue), by the determination of social welfare derived from the different externalities and policies.

3.2 Peer to peer housing and hotel market

Modern theories of product differentiation have been very much influenced by Hotelling (1929) who proposed to use a spatial framework to describe product and price competition in oligopolistic industries. This and following models focus on transportation costs incurred by the consumer

when he has to travel to the product or store. Thereby, in the simplest imaginable framework (a duopolistic industry in a linear city in which consumers are uniformly distributed), the stores choose to locate in the extremes of the city in order not to trigger a low price from the rival, and thus price competition is softened. In other words, both firms decide to take advantage of their local market power due to consumer transportation costs.

Nevertheless, the location space may also be considered as the range of potential variants of a product, where a consumer's location corresponds to his ideal product, and the transportation cost is interpreted as the decrement of utility from not consuming the ideal product.

This kind of differentiation is called horizontal differentiation. More precisely, two products are said to be horizontally differentiated when both products have a positive demand whenever they are offered at the same price. On the other hand, two products are said to be vertically differentiated if one product captures the whole demand when both are supplied at the same price. This second differentiation may be related to a duopolistic industry composed by two firms which offer different quality products, as Gabszewicz and Thisse showed (1979).

We shall leave spatial competition (i.e., horizontal differentiation) aside for a moment in order to focus in the vertical differentiation model proposed by Gabszewicz and Thisse. They considered a market in which consumers had identical tastes but different income levels; and where two brands (A and B) are offered, being relatively close substitutes for each other. Each consumer has to decide whether he buys one unit of the good/service A, of the good/service B, or he prefers to buy nothing. The consumer budget is denoted by R , and utility is represented as a product of utilities $U(x, y) = U_1(x)U_2(y) = U_x \cdot y$, where U_1 measures the utility of the obtainment of the good/service, whereas U_2 measures the utility due to the surplus budget. Let p_A and p_B be A and B prices, as well as $p_0 = 0$ for consistency; $x \in \{A, B, 0\}$, $y \in \{R - p_A, R - p_B, R\}$. So then the decision problem consists of:

$$\text{Arg } \max_{A,B,0} U(X, R - p_X) \quad (3)$$

In some sense, the model proposed by Gabszewicz and Thisse assumes that one brand has more quality than the other (let suppose, w.l.o.g. $U_A > U_B > U_0 > 0$), due to homogeneity in tastes. Moreover, the income distribution is taken as uniform in $[R_0, R_1]$. With these simplifications, maximum price that a consumer located in quantile t is disposed to pay can be calculated since $U(0, R(t)) = U(A|B, R(t) - p_{A|B})$, or $U_0(R_0 + R_1 t) = U_{A|B}(R_0 + R_1 t - p_{A|B})$. Then, we can write the reservation prices:

$$\pi_{A|B}(t) = \frac{U_{A|B} - U_0}{U_{A|B}} \cdot (R_1 + R_2 t) \quad (4)$$

As linear functions of t , it is easy to check the demand of products A and B in the market given prices p_A, p_B , as we show in the figure [10].

The sloping lines represent the magnitudes $\pi_B(t)$ and $(U_A/U_B)\pi_A(t)$. In this example, consumers below t_B do not buy anything; between t_B and t_A , they prefer to buy B than not to buy or buying A; above t_A both products are preferred than not to buy anything, but A is preferred than B if and only if the consumer is above \bar{t} . It is easy to check that $U(A, R(t) - p_A) \geq U(B, R(t) - p_B) \Leftrightarrow U_A p_A - U_B p_B \leq U_A \pi_A(t) - U_B \pi_B(t)$, and that is why the quantity V is indicated in the figure.

Depending on the values of p_A and p_B , three situations were found: the first consists of both sellers A and B are in the market but with potential customers who are not served; in the second case again both sellers A and B are in the market and all customers are served and finally a third region where seller B is out of the market. What Gabszewicz and Thisse were concerned about was to find a price equilibrium, according to different values of U_A, U_B, U_A0, R_0 and R_1 , focusing on which case of the three mentioned corresponds to the equilibrium.

Now, what we are taking apart is the duopolistic market consisting of two relatively substitutable products, in order to study how is the competition between firms offering same products, distributed along a city. Eventually, horizontal differentiation models are based on unidimensional frameworks, in which the firms choose their locations simultaneously and given the locations, they choose prices simultaneously, consisting of a two-stage game. We may ignore the first step, which allow us to solve the model. Indeed, this omission should not worry us, because hotel offer is quite rigid, and Airbnb does not decide where is a new apartment going to be offered, but each potential renter will be who decides whether to rent his immovable apartment or not. Moreover, our model should show competition in a real city, i.e., two dimensions. We shall think off the simplest situa-

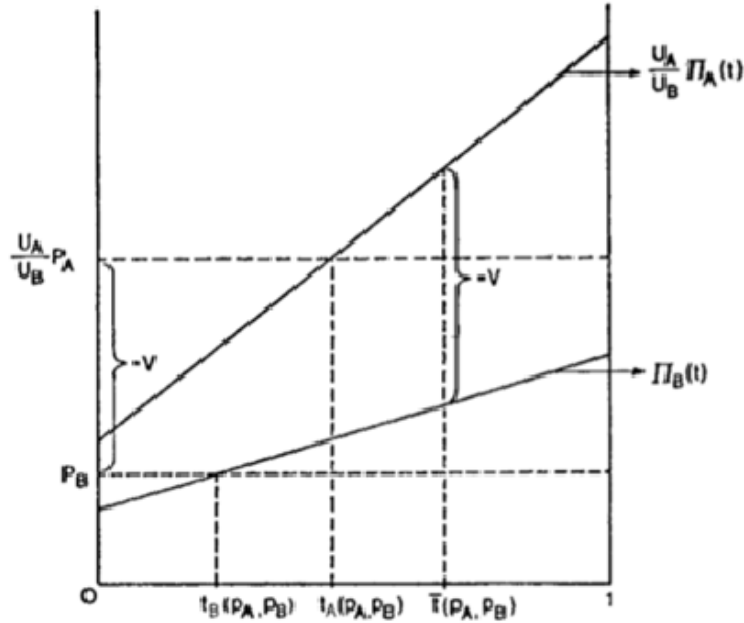


Figure 10: Distribution of the market share according to the budget.

tion: two firms located within the unit sphere. Let f be the density function of consumers in the city, then the demand function in the covered market is deduced:

$$D_{A|B}(p_A, p_B) = \iint_{\Omega} f(x, y) dx dy, \quad \Omega = \{(x, y) | p_{A|B} + d((x, y), A|B) < p_{A|B} + d((x, y), A|B)\} \quad (5)$$

We denote as $d(\cdot)$ the transportation cost for a consumer located in (x, y) purchasing a product from store $A|B$. Typically, this function is postulated as the product of a certain power of the euclidean distance to the store and a constant which is related to the marginal transport cost.

For example, in the figure [11] we consider $d(\cdot)$ as the euclidean distance to the powers $n = 1$ and $n = 1.5$, $p_A = 1.3$ or 1.8 , $p_B = 1$, $f = \frac{1}{\pi}$, and two stores A and B located at $(-0.5, 0)$ and $(0.5, 0)$, respectively. So, lines drawn represent in each case the frontier between the areas of influence of A and B . It is easy to check how the frontier turns perpendicular to the line linking A and B when n goes to 2. We should point out that the density function is irrelevant in the frontier computation, but it might be considered for the frontier in the equilibrium (both firms maximizing profits), in the game in which A and B have to decide their prices. In this example, the area bounded by the frontier is equal to the market share of each producer.

The key is to formulate an appropriate density function, which typically could be built from a few hotspots, as a sum of exponentials, gaussians or other functions which decay from these hotspots. Note that which this function do is to reflect the preferences of the tourists in the city.

Let point to the main problems of these two models. Firstly, horizontal differentiation suppose a complete market, i.e., demand is always satisfied and no limits in the offer are contemplated. As well, these kind of models, which are usually developed from Hotelling's, suppose that consumers necessary purchase to one firm, whereas vertical differentiation model admits the situation in which consumers prefer not to buy anything. This point is really important, because it could distinguish whether Airbnb customers are former hotel customers or Airbnb gains new consumers who would have decided not to trip otherwise. It is also true that some models combining these two kind of differentiation have been developed (see, e.g., [4]) formulating distinct transportation costs in order to represent the quality of the products, but these models focus specially in how much consumers are willing to change their preferences (more or less, the idea is similar to consider together the two interpretations we have mentioned in Hotelling model). Moreover, vertical differentiation could be more complex if we interpret that Airbnb and hotel do not only offer services of different quality,

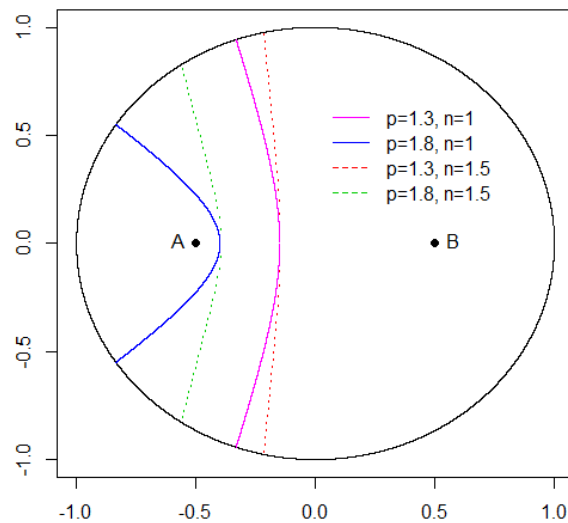


Figure 11: Local market power in a space economy framework.

but they have also their own demand in some cases. For instance, it is known that old people prefer traditional services. It is also common to stay in a hotel for work reasons: price and quality do not explain everything.

What we propose is to consider two business models (hotel and Airbnb), as Gabszewicz and Thisse did, together with several offers distributed throughout a space frame in such a way that an Airbnb offer can compete with a hotel non immediately next (as long as for this particular consumer both services are considered as relatively substitutable). Furthermore, it may be useful to join some close Airbnb as a big producer (a hotel in this case). This method could even be applied to hotels, and then a hotel and an Airbnb offer (with their respective total available rooms) may represent the whole offer for a certain zone. In that case, the work might be simplified, and the problem would be treated in a grid (e.g., one may think of a city broken into identical squared pieces as the represented in descriptive plots [3-8]). As always, the prediction of the model ought to consist on the optimization of Airbnb and hotel profits $p_{A|B} \cdot D_{A|B}$ in a one stage game (choice of price) in the way considered in figure[11], but also regarding at vertical differentiation and a finite number of rooms/products offered.

The combination of these two perspectives could be too hard, and the problem might should be abandoned, looking for some other alternatives, as a Lokta-Volterra Model consisting of two predator species (hotel and Airbnb), with intraspecific and interspecific competition, and a priest, representing customers, related to the load capacity of the system, probably variable because of demand shocks.

4 Conclusions

As we have marked before, this work consists of a first inspection on the problem of the competition between Airbnb, long term housing and hotel industrie. Due to this, this naive study needs a more rigurous and formal extension, but one may think off this work as a set of intuitions which could be taken in consideration in a future research.

Acknowledgments

I would like to acknowledge all the people who i have already included in the beginning of the report, because all of them have helped and directed me to develop my work. I am pretty sure that it would have been quite more difficult if they had not involved as much ash they had. Especially,

I want to thank J.J. Ramasco for all the time and patience he has dedicated me, which has been so much. This work was supported by the SURF@IFISC fellowship.

References

- [1] Jean Tirole. The theory of industrial organization. MIT Press (1994), 277-302.
- [2] Hotelling H. 1929. Stability in Competition. *Economic Journal* 39:41-57.
- [3] Gabszewicz, J. J., & Thisse, J. F. (1979). Price competition, quality and income disparities. *Journal of economic theory*, 20(3), 340-359.
- [4] Tabuchi, T., and J.-F. Thisse (1995). Asymmetric equilibria in spatial competition. *International Journal of Industrial Organization* 13:213-227.
- [5] Ferreira, R. D. S., & Thisse, J. F. (1996). Horizontal and vertical differentiation. *International Journal of Industrial Organization* 14:485-506.
- [6] <https://www.maximelenormand.com/Blog/building-spatial-grid-r>
- [7] <https://www.maximelenormand.com/Blog/cartography-with-r>

Application of machine learning to a probing scheme based on quantum synchronization

Gabriel Garau Estarellas, Gian Luca Giorgi, Miguel C. Soriano, Roberta Zambrini
 Instituto de Física Interdisciplinar y Sistemas Complejos IFISC (CSIC-UIB)
 Campus Universitat de les Illes Balears, E-07122 Palma de Mallorca, Spain

Abstract

We consider an out-of-equilibrium, dissipative qubit interacting with an external bath. Assuming we have no way of measuring the dynamics of the qubit itself, we introduce a probe (an object the dynamics of which we can study) consisting in a second, non-dissipative qubit which is coupled to the first qubit. Exploiting the phenomenon of quantum synchronization emerging between them and reported in Ref [1], we use machine learning techniques to infer the form of the bath by just having access at the evolution of the probe. The machine learning algorithm works better when the frequency of the probe lies in a range within which the synchronization phase depends on the form of the bath. We also verify that the algorithm's precision lowers in the presence of noise in the trajectory of the probe.

1 Introduction

In this report we study an open quantum system formed by a single, out-of-equilibrium spin, which we will refer to as *qubit*, interacting with an environment formed by a (potentially infinite) set of harmonic oscillators, so-called *bath*. Assuming that we have no way to perform direct measurements on the system, we introduce a second qubit, so-called *probe*, which is coupled to the first qubit and the dynamics of which we are able to study. We assume that the probe does not interact with the bath, and thus suffers no decoherence, and that we can control both its natural frequency and the coupling strength between the qubit and the probe. Exploiting the phenomenon of quantum spin synchronization emerging between them, we might be able to infer the shape of the bath spectral density to some extent from only looking at the evolution of the probe over time. Assuming a particular form of the bath, this problem of inference reduces to a parameter estimation problem and under certain assumptions can be solved deterministically. However, the aim of this project is to apply machine learning techniques to obtain a model-independent estimation process. For this reason, let us first give a short introduction to machine learning.

1.1 Machine learning. Supervised and unsupervised learning. QML

Machine learning (ML) is a very broad term, generally referring to the design of algorithms and techniques that are able to extract information from, and make predictions about, certain input data [2] [3]. It is convenient to understand machine learning as the actual cognitive process of an artificial subject; the entity which is fed with the data and is expected to accomplish a certain task or goal (specified by the user) is commonly called *agent* in literature; the system over from which the agent has to infer information is called *environment*.

Traditionally, there are two types of ML: *supervised learning* and *unsupervised learning*.

- **Supervised learning** deals often with classification tasks: that is, given a certain number of data examples, each of them with its corresponding label, and the specified set of possible labels, the agent should be able to correctly classify each of the data points to its correct label. In general, we work with a so-called *training set*, which is a set of labeled points (or *training examples*) $\{(x_i, y_i)\}_{i=1}^N$ where x_i denote the data points and y_i their respective labels. Being provided with these data, the task of the agent is to infer a labeling rule, the so-called *classifier*, i.e. a function that given any new data point (usually called *test example*) x_k correctly maps it to its label y_k . Within this type of learning, there are two common methods: *classification* and *regression*. Classification methods deal with problems in which the labels

are discrete values (or classes) from a finite set of possibilities, and the task of the agent is to assign to any new example the correct label from the same finite set. In regression problems, however, the task of the agent is not to classify the test examples into one of a previously fixed set of classes, but to estimate numerically the value of the label, which is now a continuous variable. Thus, the labels of the training examples are in this case numerical values, and not classes.

- **Unsupervised learning** often deals with data mining problems, in which the data points are not labeled and the main task is to identify certain features of the data set structure. One of the most common examples of unsupervised learning is clustering, in which the task is to gather the data points in different groups in a manner that a certain aim is achieved, commonly minimizing the within-group distance and maximizing the distance between different groups.

1.1.1 Quantum machine learning

Quantum machine learning (QML) can be thought of as the field of interaction between the notions of quantum computing and artificial intelligence [5]. The interest in such discipline has raised in the last decades and we have already experienced significant advances in both directions of influence: on the one hand, quantum-based algorithms have been proved to speed up many machine learning methods and also facilitate interaction between the agent and the user; on the other hand, classical machine learning is already being used in many cutting-edge technologies, including those based on quantum information settings (such as quantum state estimation, see [4]). Any machine learning setting can be classified into one of the four following categories, regarding to whether the agent, the environment, or both are fully quantum systems:

- **CC.** Both the agent and the environment are treated as classical. This may refer to any standard ML problem without a quantum database.
- **QC.** The agent uses quantum-based algorithms to study a classical system. It is the case of quantum annealing approaches.
- **QQ.** Quantum machine learning setting in which environments or databases are quantum-accessible.
- **CQ.** Classical techniques of machine learning are used to study a fully quantum system.

Specifically, this work fits in the last class as we use a specific classical supervised learning method, a feed-forward artificial neural network, in order to infer information from a quantum setting.

1.1.2 Artificial neural networks

Artificial neural networks (ANNs) or simply neural networks (NNs) are structures used to tackle machine learning problems. Their basic components are the so-called *artificial neurons* (ANs), which are real-valued functions $AN : \mathbb{R}^k \rightarrow \mathbb{R}$ parametrized by a vector of real weights $\vec{w} = (w_i)_i$ which determine the connection strength between neurons and an activation function $\varphi : \mathbb{R} \rightarrow \mathbb{R}$ and defined as following [5]:

$$AN(\vec{x}) = \varphi \left(\sum_i x_i w_i \right) \quad (1)$$

where $\vec{x} = (x_i)_i \in \mathbb{R}^k$ is the vector of input data which the neuron receives from other neurons or directly from the training set. The task of the training is to optimize the weights \vec{w} and, possibly, the parameters that determine the activation function φ of each neuron, as to minimize the error in the classification of the training set.

By combining different ANs we get a neural network. In this work we will use a specific kind of ANN, the so-called *multilayer perceptron* (MLP), which is formed by an input layer, one or more hidden layers (here we will focus on the use of a single hidden layer) and an output layer. The most common activation functions used in this kind of network are the sigmoid functions, such as the *logistic function* which we will use: $\varphi(x) = \frac{1}{1+\exp(-x)}$. The weights of the neurons in the hidden layer can be understood as the strength of the connection with each of the nodes in the input layer. These weights are then trained, for example using a so-called *gradient descent* iterative

method, in order to find a local minimum of the total error produced in the entire output, introducing corrections for each new training example. For further details on how this method works, see [6].

The computational capabilities of this kind of network is determined only by the number of neurons in its hidden layer. It can be shown that if sufficiently many neurons are available, a three-layer network can be trained to learn any dataset [7]; however, increasing the number of neurons has a cost in terms of computational time. All of this will be studied in section 3.

2 Theoretical model

2.1 General description

We consider a qubit q dissipating into an environment modeled by independent harmonic oscillators. The evolution of the system is governed by the following Hamiltonian:

$$H_0 = \frac{\omega_q}{2} \sigma_q^z + \sum_k \Omega_k a_k^\dagger a_k + \sum_k g_k (a_k^\dagger + a_k) \sigma_q^x \quad (2)$$

where the first summand represents the energy of the qubit, the second represents the energy of the bath and the last one represents the interaction between the qubit and the bath, being σ_q^i Pauli matrices for $i \in \{x, y, z\}$. For each of the energies Ω_k of the bath (we set $\hbar = 1$ throughout this work), a_k^\dagger and a_k represent the correspondent creation and annihilation operators and the coefficient g_k determines the strength of the coupling between the qubit and this mode. The function mapping each frequency $\omega > 0$ to this coupling strength across the bath's full frequency spectrum is the so-called *spectral density* of the bath, which enters in the description of the reduced dynamics of the system and is given in this case by $J(\omega) = \sum_k g_k^2 \delta(\omega - \Omega_k)$. Throughout this work we will assume a spectral density of the form $J(\omega) = \gamma_0 \omega^s$, where γ_0 is a scaling factor representing the coupling strength between the qubit and the bath and the parameter s characterizes the form of the bath's spectrum. We also assume that the system qubit interacts with an accessible probe through an Ising-like coupling, thus the Hamiltonian of the total system (qubit, probe and bath) is

$$H_{total} = H_0 + \frac{\omega_p}{2} \sigma_p^z + \lambda \sigma_q^x \sigma_p^x \quad (3)$$

where ω_p is the frequency of the probe and λ represents the coupling strength between the qubit and the probe; we assume that we can control both of these quantities. Considering the Hamiltonian of the system formed by the qubit and the probe, given by $H_{qp} = \frac{\omega_q}{2} \sigma_q^z + \frac{\omega_p}{2} \sigma_p^z + \lambda \sigma_q^x \sigma_p^x$, we can find its eigenvalues, which are related with the frequencies of each qubit and the coupling constant λ . The coupled system (qubit and probe) has two normal modes or frequencies of oscillation, which are associated to the energies E_1 and E_2 given by the equations:

$$\begin{aligned} 2E_1 &= \sqrt{4\lambda^2 + \omega_+^2} + \sqrt{4\lambda^2 + \omega_-^2} \\ 2E_2 &= \sqrt{4\lambda^2 + \omega_+^2} - \sqrt{4\lambda^2 + \omega_-^2} \end{aligned} \quad (4)$$

where $\omega_\pm = \omega_q \pm \omega_p$. The eigenvalues of H_{qp} are given by $\{\pm \frac{E_1 + E_2}{2}, \pm \frac{E_1 - E_2}{2}\}$, and the corresponding eigenvectors constitute the so-called *non-local basis*. Our aim now is to calculate the density operator matrix of the system formed by the qubit and the probe, $\hat{\rho} = [\rho_{ab}]_{ab}$. To do so, the usual procedure is to perform a partial trace over the total density matrix in order to eliminate the degrees of freedom of the bath [8]. Considering the Born-Markov regime and under other theoretical assumptions such as the weak coupling between the qubit and the bath ($\gamma_0 \ll 1$), we get to the following master equation for the elements of $\hat{\rho}$:

$$\dot{\rho}_{ab} = -i\omega_{ab}\rho_{ab} - \sum_{m,n} R_{abmn}\rho_{mn} \quad (5)$$

where $\omega_{ab} = E_a - E_b$ are the differences between the eigenvalues of H_{qp} and R_{abmn} the elements of the Redfield tensor, which are given by

$$R_{abmn} = \delta_{bn} \sum_r S_{ar} S_{rm} \Gamma^+(\omega_{rm}) - S_{am} S_{nb} \Gamma^+(\omega_{am}) + \delta_{am} \sum_r S_{nr} S_{rb} \Gamma^-(\omega_{nr}) - S_{am} S_{nb} \Gamma^-(\omega_{nb}) \quad (6)$$

being $S_{ij}^q = \langle i | \sigma_q^x | j \rangle$ the coefficients of the Pauli-X matrix associated to the qubit written in the non-local basis, and $\Gamma^\pm(x) = \frac{\pi}{8} [J(x) - J(-x)] \left[\coth\left(\frac{\beta x}{2}\right) \mp 1 \right]$, where $\beta = 1/k_B T$ is the inverse of the temperature of the bath, and it will be set to $T = 0$ throughout this work.

Once found the density operator matrix $\hat{\rho}(t)$, one can calculate the expected value of the local variables by tracing $\langle \sigma_x^k(t) \rangle = \text{Tr}(\hat{\rho}(t) \hat{S}_k)$ for $k \in \{q, p\}$, where \hat{S}_k is the Pauli-X matrix associated to the qubit or the probe, written in the non-local basis.

2.2 Evolution of the system

As discussed in Ref. [1], the system described above can either end up in a synchronized state, in which both the qubit and the probe oscillate at a common single frequency in a long time limit, or in a non-synchronized state, in which both of the normal modes of oscillation survive and thus the evolutions of the qubit and the probe appear irregular and different between them. In the case of synchronization, we can either find that the two qubits oscillate in phase, what we will refer to as *in phase synchronization*, or in antiphase, what we will refer to as *antiphase synchronization*¹.

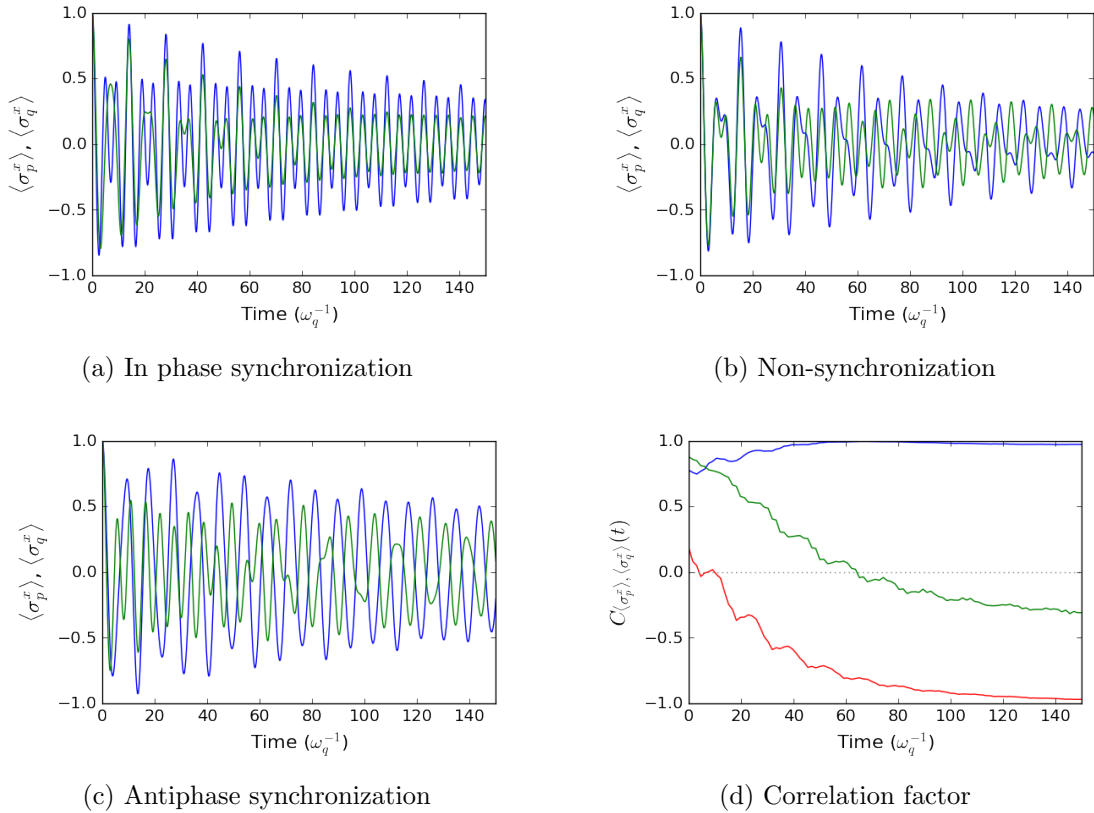


Figure 1: (a), (b) and (c) show the evolutions of three systems exhibiting in phase synchronization, non-synchronization and antiphase synchronization, respectively; the blue line represents $\langle \sigma_p^x \rangle$ and the green line represents $\langle \sigma_q^x \rangle$ in all cases. In 1a, we have used $\omega_p = 1.25$ and $s = 0.5$. In 1b, $\omega_p = 1$ and $s = 1$. In 1c, $\omega_p = 0.75$ and $s = 2$. All cases are calculated using the parameters $\gamma_0 = 0.01$ and $\lambda = 0.2\omega_q$, and the initial state is $|\psi(0)\rangle = (|0\rangle + |1\rangle)(|0\rangle + |1\rangle)/2$ written in the local basis. (d) shows the Pearson correlation coefficient as a function of time (setting $\Delta t = 50\omega_q^{-1}$) for the three trajectories: the blue line corresponds to 1a, the green line to 1b and the red line to 1c.

One of the main results in Ref. [1] states that the condition for the absence of synchronization is satisfied along a line in the diagram $\omega_p - s$, which corresponds to the yellow stripe in figure 3, top. We will refer to this line as the *transition region* (or transition line) as it separates the regions of the diagram which correspond to in phase and antiphase synchronization. One can quantify the

¹If not specified, the units of ω_p must be read as multiples of ω_q and the units of time as multiples of ω_q^{-1} throughout this work.

synchronization between the two qubits with the so-called *Pearson correlation coefficient* function, defined by the following expression [9]:

$$C_{f,g}(t, \Delta t) = \frac{\overline{\delta f \delta g}}{\sqrt{\overline{\delta f^2} \overline{\delta g^2}}} \quad (7)$$

where the upper bar stands for the mean in the time interval $[t, t + \Delta t]$, that is:

$$\overline{f} = \frac{1}{\Delta t} \int_t^{t+\Delta t} f(u) du \quad (8)$$

and $\delta f = f - \overline{f}$. With this definition, using $\langle \sigma_p^x \rangle$ and $\langle \sigma_q^x \rangle$ as the functions f and g , and choosing convenient values of t (over the relevant transient before synchronization takes place) and Δt (it must average over several oscillations), this correlation factor serves as a measure of the synchronization between the two qubits. If $C \simeq 1$ (or -1) there is in phase (or antiphase) synchronization, while $C \simeq 0$ denotes lack of synchronization.

In figure 1 we can see examples of in phase and antiphase synchronization, and non-synchronization. We can see that in Fig 1a, both qubits ($\langle \sigma_p^x \rangle, \langle \sigma_q^x \rangle$) evolve into in phase synchronization within a few oscillations, while in Fig 1c they end up oscillating in antiphase although the transient time is longer; Fig 1b represents the behavior of a non-synchronized system. Finally, Fig 1d shows the evolution of the correlation coefficient for each of the trajectories: the blue line shows a rapid evolution towards $C = 1$ (in phase synchronization), the red line evolves slowly towards $C = -1$ (antiphase) and the green line stabilizes to an intermediate value, denoting lack of synchronization.

For further details on the model and results see [1].

3 Results and discussion

Assuming a bath spectrum with a power form $J(\omega) = \gamma_0 \omega^s$ for $\omega > 0$, our aim now is to estimate the parameter s by just looking at the probe evolution, $\langle \sigma_x^p(t) \rangle$. For this, we prepare a training set consisting of a set of N trajectories with their respective known labels, and use a multilayer perceptron with a single hidden layer (namely, the model *MLPClassifier* of the module *sklearn.neural_network* in Python programming language), we build a classifier which should be able to correctly map any new given trajectory to its class of bath spectrum, characterized by the parameter s . In particular, we want our agent to be able to differentiate among the cases $s = 0.5$, $s = 1$ and $s = 2$; that is, sub-Ohmic, Ohmic and super-Ohmic spectra of dissipation. Thus, we prepare a sample of N trajectories for each value of s and we allow the probe frequency ω_p to run over different values, ranging from a certain value ω_{min} to ω_{max} and uniformly distributed, while fixing $\omega_q = 1$. The input features to our machine learning model are the M points of the Fourier transform $\hat{f}(\omega)$ of the evolution of $\langle \sigma_x^p(t) \rangle$ in the interval $\{0, t_{max}\}$ (we will use $t_{max} = 100\omega_q^{-1}$ throughout this work). In figure 2 we can see how the information the agent "receives" looks like. In this case the sample was distributed in the interval $\omega_p \in [0.9, 1.15]$, so we choose the minimum number of points such that both "peaks" (which are the normal modes E_1 and E_2 from equations 4) are well represented. As the discretization in the frequency ω is fixed by the inverse of the time window length, in this case $t_{max} = 100\omega_q^{-1}$, the plot has a limited resolution $\Delta\omega = 1/t_{max} = 0.01\omega_q$. Thus, the differences among the Fourier transforms for each value of s are mainly determined by the slight difference in the height of the peaks $\hat{f}(E_1)$ and $\hat{f}(E_2)$, as we can see in the figure.

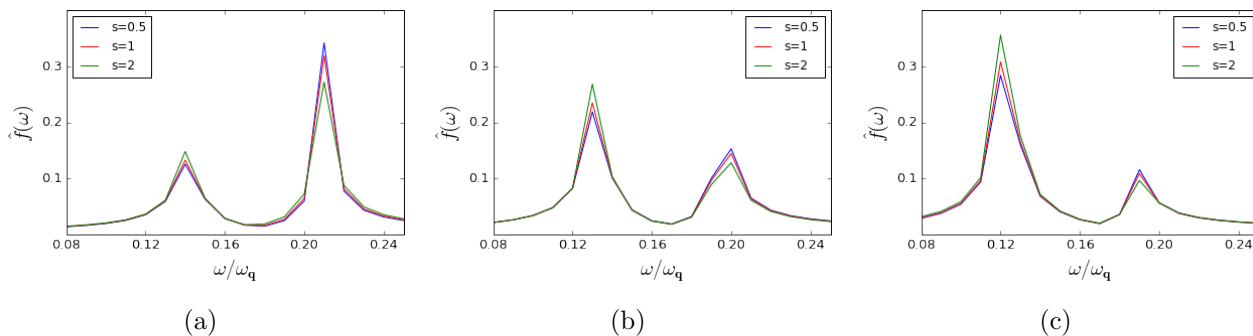


Figure 2: Fourier transform in the interval $[0, 100\omega_q^{-1}]$ for each value of s , for (a) $\omega_p = 1.15\omega_q$, (b) $\omega_p = \omega_q$ and (c) $\omega_p = 0.9\omega_q$. The resolution in the frequency scale is given by $\Delta\omega = 1/t_{max} = 0.01\omega_q$, and the set of points which characterize the Fourier transform has been chosen as to represent both "peaks" (the normal modes E_1 and E_2 in equations 4) with the minimum possible number of points, considering that the sample used for the learning is distributed in the interval $\omega_p \in [0.9\omega_q, 1.15\omega_q]$ and $\lambda = 0.2\omega_q$. The qubit-bath coupling coefficient is $\gamma_0 = 0.03$ in this case, in order to better visualize the differences between the trajectories for each value of s .

We can distinguish the two normal mode peaks in all of the spectra show in figure 2. However, in Fig 2a the higher energy peak dominates over the other, meaning that for $\omega_p = 1.15$ the system ends up in a synchronization in phase for the three values of s . In contrast, in Fig 2c it is the low energy peak which is higher, meaning that the system ends up in antiphase synchronization. Finally, in Fig 2b both peaks are of a similar height, and the one that dominates depends on the value of s : if we were representing the Fourier transform for a longer time, we would see that for $s = 0.5$ only the high energy peak would survive, while for $s = 2$ it would be the low energy peak and for $s = 1$ both peaks would survive, as it corresponds to a non-synchronized dynamics. Also, one can see that, within each figure, the trajectory for $s = 2$ exhibits a higher peak for E_1 and the trajectory for $s = 0.5$ has a higher peak for E_2 . After preparing all the sample trajectories, we randomly choose a given fraction P of the sample to be the training set and use the $1 - P$ left as the test input. As we have generated the whole sample controlling the parameters, we know the correct labels of the test examples, so after the agent performs its prediction on this set we can compare this to the correct test classification and thus quantify its efficiency using the percentage of error.

3.1 Error as a function of the detuning: influence of the phase-antiphase transition

Our main aim here is to determine whether the machine learning classification efficiency is enhanced by the sharp transition between phase and antiphase synchronization (corresponding to the yellow stripe in figure 3, top), which is one of the main results in [1]. That is, we want to study if the agent performs better if trained (and tested) with the values of ω_p for which different values of s determine whether the higher energy mode E_1 or the lower E_2 dominates over time (yielding in phase or antiphase synchronization, respectively). For this reason, we generate 7 different sample sets, each of them consisting of $N = 301$ trajectories corresponding to values of ω_p uniformly distributed in the interval $I_k = [0.5 + 0.15 \cdot (k - 1), 0.5 + 0.15 \cdot k]$ for $k \in \{1, \dots, 7\}$, the central interval of which roughly corresponds with the transition region, and calculate the error in the agent classification (see figure 3, bottom).

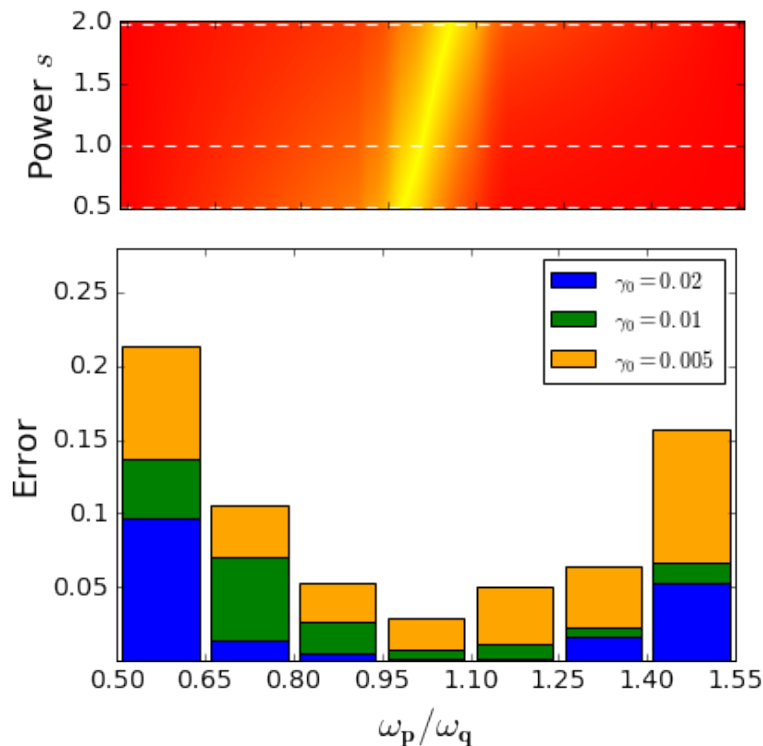


Figure 3: At the top, the absolute value of the correlation factor C , fixing $t = 80\omega_q^{-1}$ and $\Delta t = 20\omega_q^{-1}$. The yellow band corresponds to lack of synchronization ($C \simeq 0$), while the region at the left of the band corresponds to in phase synchronization ($C > 0$) and the left region corresponds to antiphase ($C < 0$). At the bottom, the histogram of the fraction of error (number of errors in classification divided by number of test examples) produced by the agent in the classification between $s = 0.5$, $s = 1$ and $s = 2$, for different intervals of ω_p and for different values of the coupling γ_0 . We have used (approximately) 3 (values of s) $\cdot 301$ (values of ω_p) $\cdot 0.8$ (fraction of training) $\simeq 720$ training examples and $3 \cdot 301 \cdot 0.2 \simeq 180$ test examples and a single hidden layer of 200 neurons with the logistic activation function. The upper limits of the blue, green and orange bars correspond to the fraction of error with $\gamma_0 = 0.02$, $\gamma_0 = 0.01$ and $\gamma_0 = 0.005$, respectively.

One can see from the figure that in the region of the sharp discontinuity between phase and antiphase synchronization (yellow stripe) the agent performs better in the classification, independently from the value of γ_0 used, while the error grows as we get to values of ω_p far away from the discontinuity region. In addition, for a fixed interval the error lowers as the value of γ_0 grows. This result is due to the fact that the scale of time within which the system falls into synchronization is inversely proportional to the damping rate (quantified by the coefficient γ_0); equivalently, as the damping grows, the Fourier transforms for different values of s and the same time window are more differentiated, because the fading peak loses height at a higher velocity. The asymmetry in the histogram can be due to the influence of the initial conditions on the enhancement of one of the normal modes; however, it can also be a statistical inexactitude or just the result of an asymmetric binning along the synchronization region. It would be possible to establish how the details of the histogram in Fig 3 change when assessing these factors.

3.1.1 Performance as a function of the number of training examples and the number of neurons.

Our goal in this section is to study how the efficiency of the agent depends on the parameters of the machine learning setting. Namely, we want to see how does the error in classification change as we vary the number of training examples used and the number of neurons in the hidden layer of our multilayer perceptron. Intuitively, as both of these magnitudes grow, the error will lower, but also the time and complexity of computation will grow considerably as the agent needs to process more information. That is why it may be interesting to study these variations, to determine up to which point it is worthy to raise the complexity of the setting, given a certain goal (for example, a

desired maximum of the error rate). In figure 4, a 3D bar plot of the already mentioned function is displayed.

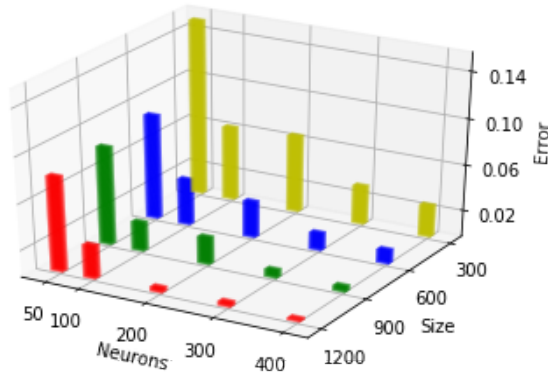


Figure 4: Fraction of error in the classification among $s = 0.5$, $s = 1$ and $s = 2$ as a function of the number of training examples, or training size ('Size' axis) and the number of neurons employed in the hidden layer of our MLP ('Neurons' axis). We have taken as sample the trajectories for 501 uniformly distributed values of $\omega_p \in [0.9, 1.15]$ and each of the three values of s , choosing randomly a certain percentage of the trajectories to be training examples and using the rest for test.

We can see that, as expected, increasing both the number of neurons and the size of the training set leads to a reduction of the error produced in the classification. However, if sufficiently many examples are used, one can see that increasing the number of neurons has a limited impact, as little precision is gained in expense of a notable rise of the computational cost. For instance, we can see from the figure that when using a training set of 1200 examples, already less than 1% of error is produced using only 200 neurons. Doubling the number of neurons leads to a barely smaller error while almost leading to a threefold increase in the computational time.

3.2 Classification with noise

A step forward one can take in order to prove the efficiency of machine learning is to include noise in the trajectories of $\langle \sigma_p^x \rangle$, setting a general and more realistic case; this is also needed thinking in experimental data. This noise is considered to be white, independent and gaussian, with a mean value of 0 and a standard deviation that can be expressed as a percentage of the total amplitude of the function over which it is applied. Therefore, we have added random noises to our trajectories and studied how the error in the classification varies as a function of the amplitude of noise applied. In Fig 5 we can see the results.

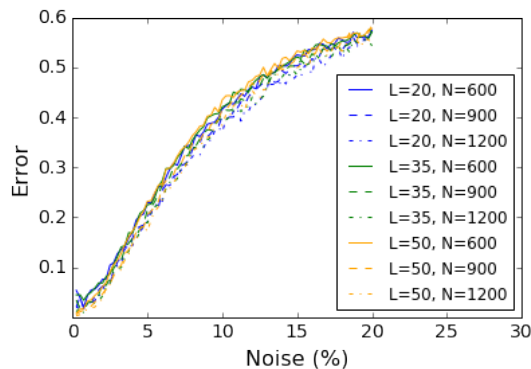


Figure 5: Mean error in the classification between $s = 0.5$, $s = 1$ and $s = 2$ as a function of the percentage of noise. In the legend, L denotes the number of neurons used and N the size of the training. The values of ω_p used to calculate the sample trajectories are uniformly distributed in the interval $[0.9, 1.15]$. The percentage of noise represents the relation between its amplitude (understood as the standard deviation) and the total amplitude of the function $\langle \sigma_p^x(t) \rangle$.

One can observe that the differences in the error among the different values of L and N are negligible in comparison to the dependence on the noise. The error tends to grow linearly or even superlinearly for low values of the noise, but eventually it saturates because in any case it should not surpass the error for a random classification, which would be of 66.7% (two thirds).

3.3 Regression as a function of the noise

In this section, we present the results of the performance of the agent in the regression of the parameter s . Thus, as explained in section 1.1, the task of the agent is no longer to classify the trajectories into three groups according to their value of s , but to estimate the value of s . For this reason, we calculate the trajectories of $\langle \sigma_p^x \rangle$ over time for different values of s and ω_p , and prepare the sample trajectories consisting of the Fourier transform in a certain interval, just as before, with the sole difference that we don't use just three values of s but we calculate trajectories for all values of $s \in \{0.5 + 0.01 \cdot i\}_{i=0}^{51}$, so as to have better precision in regression, and label each training example with the exact value of s used. In this case we use the model *MLPRegressor* of the module *sklearn.neural_network* in Python to perform the regression task. We quantify the average error by calculating the mean distance (module of the difference) between the value of s predicted by the agent and the actual value of s for each of the test examples. Figure 6 shows the results of the mean error produced by the agent for different numbers of training examples.

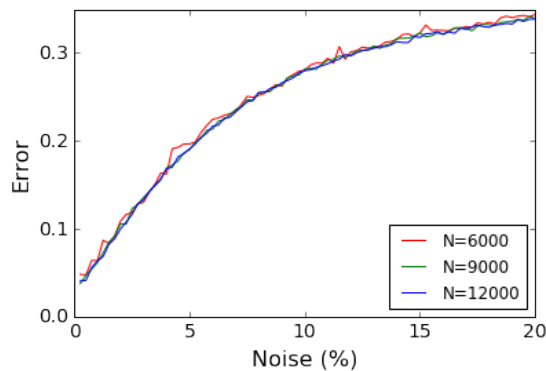


Figure 6: Mean error produced in regression as a function of the percentage of noise added to the trajectories. We have used in all cases 50 neurons and calculated the trajectories for all values of $\omega_p \in \{0.9 + 0.005 \cdot i\}_{i=0}^5$. The percentage of noise represents the relation between its amplitude (understood as the standard deviation) and the total amplitude of the function $\langle \sigma_p^x(t) \rangle$.

One can see that the general trend is that the error grows with the amount of noise independently of the number of examples, as expected; in fact, the number of examples has a negligible effect on the error in comparison to the effect of the noise above a sufficiently large number of examples. However, such as happened in the case of classification, the error saturates for high values of noise; in this case, however, there is no natural limit to explain the saturation of the error, because the regression task could yield, in principle, any real value of s . Nonetheless, supposing that the regression values must be contained in the interval $[0.5, 2]$, as it is logical to think, the error produced by the agent must not surpass the error committed in randomly choosing a value in this interval, which corresponds to an average distance of 0.5; that is, a third of the interval.

4 Conclusions

In this work we have studied the implementation of a machine learning method to predict a certain feature of a specific quantum system, namely the power of the spectral density of the bath. We have seen how, using a three-layered perceptron model, the agent is able to distinguish the different values of the parameter s , performing especially well in the region of transition, the interval in ω_p where different values of s yield either in phase or antiphase synchronization. At the same time, we have seen that higher values of γ_0 yield better results in classification, as the system comes into synchronization within a scale of time which is inversely proportional to the damping. We have also verified the fact that the agent's performance improves as we increase the complexity of the algorithm (i.e: the number of neurons and the number of training examples). Finally, we have

seen how performance worsens when adding noise to the trajectories, both in classification and in regression tasks.

This work can be extended in several directions: for example, one could study how performance varies when changing certain parameters of the system (such as introducing a cut-off frequency ω_c in the spectral density) or of the data (such as enlarging or displacing the time window over which we calculate the Fourier transform). Even more, one can switch the task and try to estimate γ_0 ; in fact, we have already performed discrete classification for different values of this parameter and got results of a similar order of error as in the classification of s . Also, we could try to estimate at the same time various parameters, such as γ_0 and s and, ultimately, use a similar procedure to infer a general polynomial-type spectrum; for example, fixing the degree n of the polynomial, the problem would reduce to estimating the $n + 1$ real parameters that define the polynomial. Finally, one could consider the effect of changing the structure of the neural network itself, either by changing the number of hidden layers used in the MLP, the number of neurons in each layer, or the activation function of each neuron, among other variables. In short, this is only a simple and prototypical model of a full-scale scenario of possibilities.

5 Acknowledgments

This work was supported by the SURF@IFISC fellowship.

References

- [1] G.L. Giorgi, F. Galve and R. Zambrini. *Probing the spectral density of a dissipative qubit via quantum synchronization*. arXiv:1607.02912. Phys. Rev. A **94**, 052121 (2016)
- [2] Dana Angluin. *Queries and concept learning*. *Machine learning* 2(4):319–342. (1988)
- [3] L. Devroye, L. Györfi, and G. Lugosi. *A Probabilistic Theory of Pattern Recognition*. Springer (1996)
- [4] F. Albarrán-Arriagada, J.C. Retamal, E. Solano, L. Lamata. *Measurement-based adaptation protocol with quantum reinforcement learning*. arXiv:803.05340. (March 2018)
- [5] Vedran Dunjko and Hans J Briegel, Rep. Prog. Phys. 81 074001 (2018)
- [6] Simon S. Haykin *Neural networks: a comprehensive foundation*. (1999)
- [7] Kurt Hornik. *Approximation capabilities of multilayer feedforward networks*. *Neural Networks*, 4(2):251–257 [https://doi.org/10.1016/0893-6080\(91\)90009-t](https://doi.org/10.1016/0893-6080(91)90009-t). (January 1991)
- [8] H.-P. Breuer and F. Petruccione. *The Theory of Open Quantum Systems*. Oxford University Press, New York. (2002)
- [9] F. Galve, G. L. Giorgi, & R. Zambrini, *Quantum correlations and synchronization measures* in Lectures on General Quantum Correlations and their Applications, Edited by F. Fernandes Fanchini, D. de Oliveira Soares Pinto, G. Adesso, pp. 393 – 420 (Springer, 2017)

Nonlinear thermoelectric transport in a selective spin environment.

Álvaro Mas, Rosa López

Instituto de Física Interdisciplinar y Sistemas Complejos IFISC (CSIC-UIB)
 Campus Universitat de les Illes Balears, E-07122 Palma de Mallorca, Spain

Abstract

We studied the main properties of quantum transport in a quantum Hall bar connected to two reservoirs and a quantum dot with different voltages. This system allows us, under some conditions, to transport electrons against the bias without violating the second law of thermodynamics by introducing a demon which works due to the chirality of the edge modes. We described the system with some electrostatic approximations to end up with a more complete picture of the problem, analyzing the range of voltages and the asymmetries necessary to establish an electric and thermal current. We found that high voltages and quantum asymmetries in the barriers of the nanostructure are necessary but no electrostatic asymmetries are needed if we stay at low enough voltages.

1 Introduction

Quantum transport in nanostructures is crucial to new developments in technology so it has become overwhelmingly important to study simple systems which could act as a simple machine but requiring much less external work. The description of the problem could be rather complicated and we need to study simplified systems to understand the main properties of the process. Thus, our objective is to study a simple system which could be modified to become more complete but gives an overall idea of the transport.

However, quantum transport theory in our system is almost closed so we need to find some theoretical applications that may be implemented in the future. We aim to construct a thermal machine by running an external agent in a nanostructure that does not require a lot of external work. This external agent is sometimes called the demon, as a reference to the Maxwell's Demon Paradox [1]. Maxwell proposed a system which consisted of an ideal gas and a demon who is able to discern and separate those particles which move faster and those which move slower. Then, in one side there would be cold particles and in the other side there would be hot particles. Thus, the entropy decreases in the system and the second law of thermodynamics is supposedly violated. The paradox may be solved considering that there exists another physical magnitude, the information, which generates entropy and must be taken into account in the balance. This demon could be carried out in different systems, acting on different ways but with the same basic idea; it decreases the local entropy by acquiring information from it. In summary, our aim is to implement a demon similar to the above-mentioned in our problem [2].

2 Theoretical model

We start the description of a quantum Hall bar with a quantum dot inserted. This dot allows the implementation of an external agent capable of driving a current against the bias or cooling a cold reservoir with very little external work, absent if it is ideal, as a result of taking information from the quantum dot. The interest of the studied system is that it could work as an efficient thermal machine in some specific conditions. The existence of asymmetries in the system will be necessary for the agent to work correctly.

We impose the particularity of having a one-level energy quantum dot for simplification [3]. The bar is connected to two reservoirs of electrons, each one at a different potential, so the system is moved out of equilibrium. Thus, the quantum dot can be described by two capacitances and two tunneling constants, depending on the features of the potential barriers which define the dot [3]. When a magnetic field is applied in a certain direction, electrons inside the bar will move in a circle with a cyclotron frequency which characterizes the motion. However, near the edges new

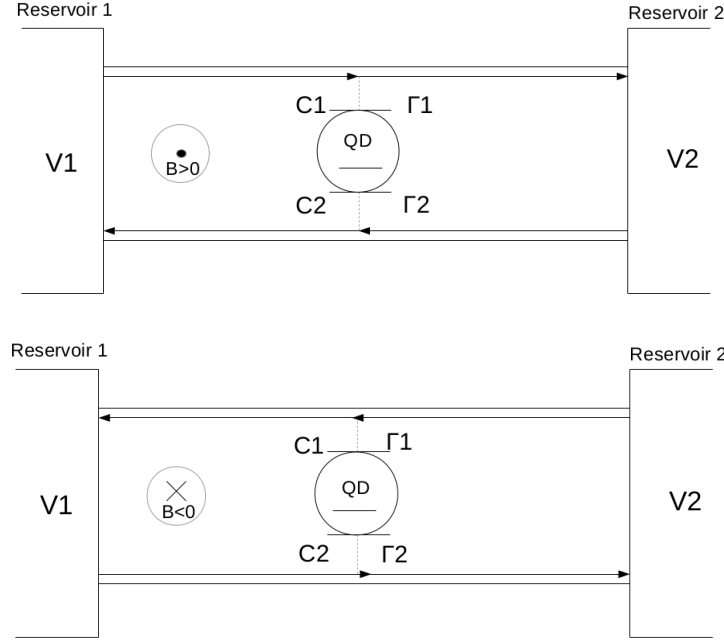


Figure 1: Picture of the problem system. A quantum dot is connected to two reservoirs with different potentials. It is characterized by two capacitances and two tunneling constants in the simple electrostatic model.

modes appear as a consequence of the finite volume. These modes help electrons move through the material as it is described in figure 1 [2, 3].

The key element of the project is the fact that these chiral modes are not invariant under the inversion of the magnetic field. When the latter occurs, the edge modes change their polarity, and electrons move just to the opposite directions, coupling with the quantum dot on a different way. This leads to a change of the dot energy level, which provides a fundamental tool to implement the demon. From now to section 3.2 we are just reproducing the results obtained by G. Roselló [2] with little changes in the values of the parameters.

2.1 Rate equations

Once determined the energies inside the dot, which will be found later, it is convenient to find some expressions for the currents. First, we need to calculate the probabilities of finding an electron inside the dot or not. Thus, we use the Master equation formalism that gives an interpretation of the time evolution of these probabilities. In order to obtain the equations, it is only necessary to express a balance of probabilities. The result is the following:

$$\dot{p}_0 = (W_{1 \rightarrow 0}^L + W_{1 \rightarrow 0}^R)p_1 - (W_{0 \rightarrow 1}^L + W_{0 \rightarrow 1}^R)p_0 \quad (1)$$

$$\dot{p}_1 = (W_{0 \rightarrow 1}^L + W_{0 \rightarrow 1}^R)p_0 - (W_{1 \rightarrow 0}^L + W_{1 \rightarrow 0}^R)p_1 \quad (2)$$

Here $W_{j \rightarrow i}^{L/R}$ are the transition rates. This can also be represented in matrix form:

$$\begin{pmatrix} \dot{p}_0 \\ \dot{p}_1 \end{pmatrix} = \begin{pmatrix} -W_{\uparrow} & W_{\downarrow} \\ W_{\uparrow} & -W_{\downarrow} \end{pmatrix} \begin{pmatrix} p_0 \\ p_1 \end{pmatrix} \quad (3)$$

To simplify we make use of the fact that we are in a stationary state. It can be proved that this final state always exists as long as the parameters and coefficients that relate the thermodynamic forces are constants. A stationary state implies:

$$\begin{pmatrix} -W_{\uparrow} & W_{\downarrow} \\ W_{\uparrow} & -W_{\downarrow} \end{pmatrix} \begin{pmatrix} p_0 \\ p_1 \end{pmatrix} = \begin{pmatrix} 0 \\ 0 \end{pmatrix} \quad (4)$$

Resulting in the following values for the probabilities:

$$p_1 = \frac{W_{0 \rightarrow 1}^L + W_{0 \rightarrow 1}^R}{W_{0 \rightarrow 1}^L + W_{0 \rightarrow 1}^R + W_{1 \rightarrow 0}^L + W_{1 \rightarrow 0}^R} \quad (5)$$

$$p_0 = 1 - p_1 = \frac{W_{1 \rightarrow 0}^L + W_{1 \rightarrow 0}^R}{W_{0 \rightarrow 1}^L + W_{0 \rightarrow 1}^R + W_{1 \rightarrow 0}^L + W_{1 \rightarrow 0}^R} \quad (6)$$

Transition rates are calculated taking into consideration the Fermi's golden rule, and using the density of states, in this case the Fermi's distribution, resulting in:

$$W_{1 \rightarrow 0}^i = \Gamma_{0i} f(\mu_{1i}) \quad (7)$$

$$W_{0 \rightarrow 1}^i = \Gamma_{1i} (1 - f(\mu_{2i})) \quad (8)$$

In these relations, i represents the barrier associated, either left (L) or right (R). The use of 1,2 in the chemical potential are determined by the sign of the applied field, according to the protocol that will be explained in the next section. To obtain Eq.(8), we have considered the holes distribution in the reservoirs since we need a hole to be filled by the electron. Besides, f is the well-known Fermi's distribution:

$$f(x) = \frac{1}{1 + e^{\beta x}} \quad (9)$$

Furthermore we need the dependence of the tunneling constants with the energy, since that is a needed condition to succeed in our theory. Their analytic expression comes from the WKB approximation:

$$\Gamma_{0i} = \Gamma_i e^{k_i(\mu_1 - E_i)} \quad (10)$$

$$\Gamma_{1i} = \Gamma_i e^{k_i(\mu_2 - E_i)} \quad (11)$$

Γ_i are positive parameters of the potentials, E_i are their top energy and k_i is a free parameter.

2.2 Implementing the demon

We are now in good conditions to implement the demon in our system taking advantage of the chirality of the edge modes. We establish the next protocol, bearing in mind all the before-mentioned description.

1. A magnetic field is turned on in the positive axis direction. This means that the edges are the same as the ones in figure 1. Electrons moves, a priori, in the direction of the bias. There is, nonetheless, a probability that one particle enters the dot.
2. When this occurs, the demon notices that the dot is filled, and changes the orientation of the magnetic field, leading to a change of the dot energy level from μ_1 to μ_2 . This is the most important step and the one that allows the demon to work adequately. Moreover, this is the reason why assuming an electrostatic asymmetry is crucial.
3. The edge modes have changed their orientation, and there is now a higher probability for the electron to leave the dot towards the left reservoir instead of the right one, where it comes from. This is actually true due to the increase of energy inside the quantum dot. When it leaves, it can be said that the electron has been transported from right, where the electrostatic potential is lower, to left, where the potential is higher.
4. Once the dot is empty, the demon changes again the orientation of the magnetic field, so that energy is dropped and the system returns to the initial conditions again.

By repeating this protocol, we should be able to measure an electrical current going from right to left, based on microscopic quantum effects. The implementation of the demon is not trivial since we need a device which detects when the dot is filled, and changes the magnetic field instantly. Indeed, this instantaneous change in the magnetic field was supposed in the section 4 when it was assumed that $-W_{\uparrow}$ is associated with the chemical potential μ_1 and $-W_{\downarrow}$ with μ_2 . The only question left is whether this process violates the second law of thermodynamics, ultimately the same problem that appeared when the Maxwell Demon Paradox was formulated. Apparently, it does, but we will work deeper in the following section to demonstrate that, actually, no violation exists if we introduce the information in the entropy balance.

2.3 Currents and information flow

The total current through the system is simply obtained from considering a balance equation. For the rest of the section we are taking as positive all the currents and fluxes which enter the dot, and negative the ones entering the reservoirs or leaving the dot. The current to the right may be expressed:

$$I_R = p_0 W_{0 \rightarrow 1}^R - p_1 W_{1 \rightarrow 0}^R \quad (12)$$

Substituting the expression 3.5 it results:

$$I_R = \frac{W_{1 \rightarrow 0}^L W_{0 \rightarrow 1}^R - W_{0 \rightarrow 1}^L W_{1 \rightarrow 0}^R}{W_{1 \rightarrow 0}^L + W_{1 \rightarrow 0}^R + W_{0 \rightarrow 1}^L + W_{0 \rightarrow 1}^R} \quad (13)$$

Our aim is to establish a current against the voltage gradient, what means that $I_R > 0$. This happens when $W_{1 \rightarrow 0}^L W_{0 \rightarrow 1}^R - W_{0 \rightarrow 1}^L W_{1 \rightarrow 0}^R > 0$. If we take $\Gamma_i = \Gamma \forall i$ we get to the condition that $k_L > k_R$. Since, evidently, charge must be conserved in the system, we may express the current to the left in terms of the previous current:

$$I_L = -I_R \quad (14)$$

Now we proceed with the analysis of the heat currents, and afterwards, the entropy of the system. We take the ideas used by M. Esposito [6]. The heat current to the left and to the right are calculated considering the balance of energy transported by electrons. The expression is therefore similar to the one written above but in terms of energy instead of probabilities:

$$I_{heatR} = p_0 W_{0 \rightarrow 1}^R \mu_{1R} - p_1 W_{1 \rightarrow 0}^R \mu_{2R} \quad (15)$$

$$I_{heatL} = p_0 W_{0 \rightarrow 1}^L \mu_{1L} - p_1 W_{1 \rightarrow 0}^L \mu_{2L} \quad (16)$$

If we sum both currents we obtain:

$$I_{heatR} + I_{heatL} = I_R(V_1 - V_2) + \mu_1 p_0 (W_{0 \rightarrow 1}^L + W_{0 \rightarrow 1}^R) - \mu_2 p_1 (W_{1 \rightarrow 0}^L + W_{1 \rightarrow 0}^R) \quad (17)$$

The first term in the last expression is a dissipating current because of the Joule heat generated by the electric current. In fact, the sign is negative, what indicates that the heat energy is going outside the quantum dot. The current through the demon is also necessary to study the whole problem. This energy current generates entropy irrespective of the heat currents. It can be expressed in terms of a balance equation as well. The result, using the same agreement of signs as before, is the following:

$$J_{energy} = (\mu_1 - \mu_2) \frac{(W_{0 \rightarrow 1}^L + W_{0 \rightarrow 1}^R)(W_{1 \rightarrow 0}^L + W_{1 \rightarrow 0}^R)}{W_{1 \rightarrow 0}^L + W_{1 \rightarrow 0}^R + W_{0 \rightarrow 1}^L + W_{0 \rightarrow 1}^R} \quad (18)$$

The entropy produced by the heat currents and the energy current in the demon is:

$$S_n = \frac{J_{energy} + J_{heatL} + J_{heatR}}{T} \quad (19)$$

Some easy computing shows that the entropy created by these phenomena decreases in time, something that violates the second law of thermodynamics. This is controversial as this would mean that either the second law is not universally closed or some assumption in our description is erroneous. Nonetheless, we can use other means to calculate the entropy flow in the system which will show that everything is correct and compatible with the theory of thermodynamics. This new mean is using the Shannon formula [8] to calculate the entropy flow in the system [6, 7]. We only need to know the currents and the rate equations to determine this quantity.

$$\dot{S}_e = I_R \ln \frac{W_{0 \rightarrow 1}^L W_{1 \rightarrow 0}^R}{W_{1 \rightarrow 0}^L W_{0 \rightarrow 1}^R} \quad (20)$$

It is important to highlight that using the entropy balance we find a simple expression for the entropy production S_i :

$$S_i = -\dot{S}_e \quad (21)$$

Again, it is quite evident that this quantity differs from the previous one. This means that the act of the demon is reflected on a mean flux of entropy. To account for this fact we assume that the demon requires information of the system to run. That is to say, the extraction of information generates a current that provides additional entropy so that the whole entropy production is positive. Thus, the information current can be expressed as:

$$I_F = \dot{S}_e - S_n \quad (22)$$

3 Electrostatic descriptions and results

3.1 Electrostatic model with two capacitances

We first describe the system as it is shown in figure 1. One important remark is that we are implementing proper conditions that prevent the device from accommodating more than one electron in the same level. Therefore, electrostatic repulsion between electrons is large enough compared with the chemical potential of the reservoirs. We can prepare the system on that way with a voltage gate that allows us to control the energy level in the quantum dot. Consequently, the following condition must be necessarily satisfied [3]:

$$K_B T \ll \frac{e^2}{C} \quad (23)$$

Where C is the sum of the capacitances. This means that we can consider only one-electron processes through the quantum dot as long as temperature is low enough so that electrons coming from the reservoirs cannot overpass the electrostatic repulsion energy. Another possibility that will be utilized later is that the capacitance C is almost zero. When an external magnetic field is applied we distinguish two cases:

- $B > 0$. Electrons moves in the direction of the modes and V_i and C_i are coupled for $i = 1, 2$. Thus, the chemical potential μ_1 changes.
- $B < 0$. Edge modes change their direction and C_i is coupled with V_j , for $i, j = 1, 2$ and $i \neq j$. Here, the edge mode raises the potential μ_2 .

It is always convenient to define a new dimensionless parameter which gives an easy physical interpretation of the asymmetry between capacitances:

$$\eta = \frac{C_1 - C_2}{C_1 + C_2} \quad (24)$$

Depending on the direction of the magnetic field we find two different energy levels in the quantum dot:

$$\mu_1 = \epsilon_0 + \frac{(C_1 V_1 + C_2 V_2)}{(C_1 + C_2)} \quad (25)$$

$$\mu_2 = \epsilon_0 + \frac{(C_1 V_2 + C_2 V_1)}{(C_1 + C_2)} \quad (26)$$

This expressions may also be rewritten in terms of the parameter η :

- For $B > 0$:

$$\mu_{1L} = \mu_1 - V_1 = \epsilon_0 + \frac{1 - \eta}{2} \Delta V \quad (27)$$

$$\mu_{1R} = \mu_1 - V_2 = \epsilon_0 - \frac{1 + \eta}{2} \Delta V \quad (28)$$

- For $B < 0$:

$$\mu_{2L} = \mu_2 - V_1 = \epsilon_0 + \frac{1 + \eta}{2} \Delta V \quad (29)$$

$$\mu_{2R} = \mu_2 - V_2 = \epsilon_0 - \frac{1 - \eta}{2} \Delta V \quad (30)$$

To obtain these results we have used basic electromagnetism relations, considering charge is conserved. We have neglected the quadratic term in charge (basically, the energy necessary to put another electron in the dot) as we have used the condition (23). Furthermore, the difference between both energy levels gives a degree of efficiency, as the demon works better when energy levels are more separated. It can be proved that this depends exclusively on the potentials and η :

$$\mu_2 - \mu_1 = \eta \Delta V \quad (31)$$

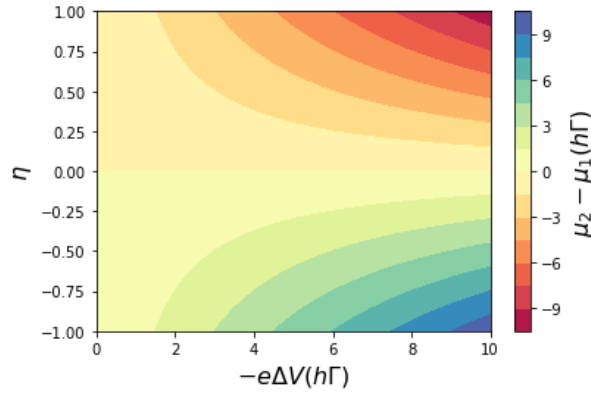


Figure 2: Potential difference for $\epsilon_0 = 0$. For $\eta < 0$ it is positive and for $\eta > 0$ it is negative.

If we represent the current for different values of the parameters that quantify the electrostatic asymmetries in the system we can analyze how important they are to drive the current against the spontaneity. This is shown in Fig.3. For Fig.3a it was assumed $k_L = k_R$, meaning no difference between barriers are taken into consideration. The first evidence is that no positive current appears independent of the conditions of our system. This means that electrons goes in the direction of decreasing voltage and the demon is clearly not driving the current against the bias. Thus, potential barriers in the dot must be undoubtedly different, that is, there must be a quantum asymmetry apart from the electrostatic one. In the second case, we assume $k_L = 3k_R$, and we conclude that for certain values of the parameters there is a positive current and the demon works correctly. Indeed, this occurs for high voltage differences in the contacts and high differences between capacitances. Finally, we studied the case $k_L = k_R/3$, in which no positive current exists so we can conclude that $k_L > k_R$ to make the demon work well as we deduced in section 2.

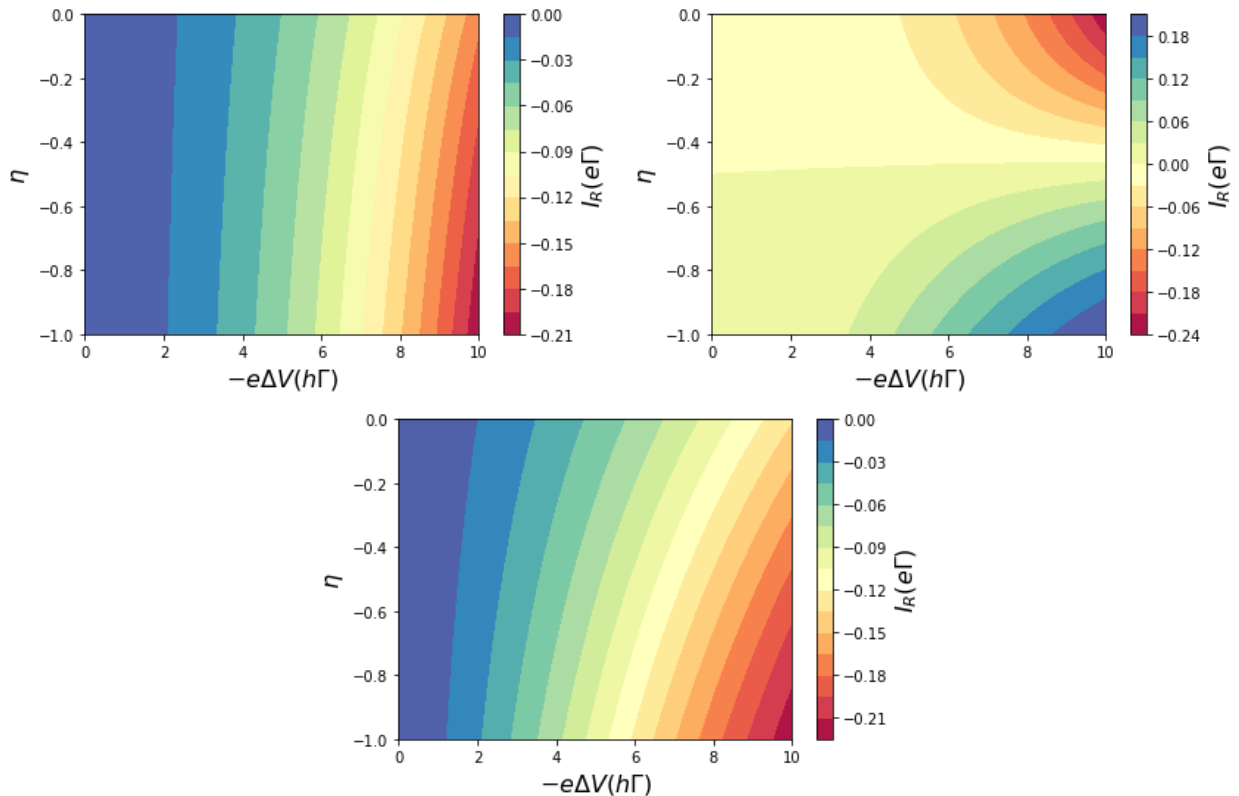


Figure 3: a)Representation of the current for $k_L = k_R$. b)Representation of the current for $k_L = 3k_R$ c)Representation of the current for $k_L = k_R/3$. For all of them it has been considered that $k_R = 0.1$ and $T = 10h\Gamma$. The barriers dependence is $\Gamma_i = 1$ and $E_{L/R} = 10h\Gamma$.

The information current has also been represented in Fig.4. for all the cases studied before. We prove that there exists a very little information current when $k_L = k_R$. In the case $k_L < k_R$ the

information current is found when voltage is high enough and the asymmetry in capacitances is quite big, which corresponds to the region where there is an electric current in the direction of the voltage gradient. However, the information current is generally low. The interest comes when we analyze the case in which $k_L > k_R$. There, in the region where we could find a current against the bias we find a high information current as well. Indeed, that information current is negative, what means that the demon is extracting information from the system to make electrons moves against the expected. The existence of such an information current makes our physical interpretation quite plausible and the theory seems correct. However, we need to investigate whether this simple view is enough to describe the behaviour of our system or making it more complete eliminates some requirements for the demon to work.

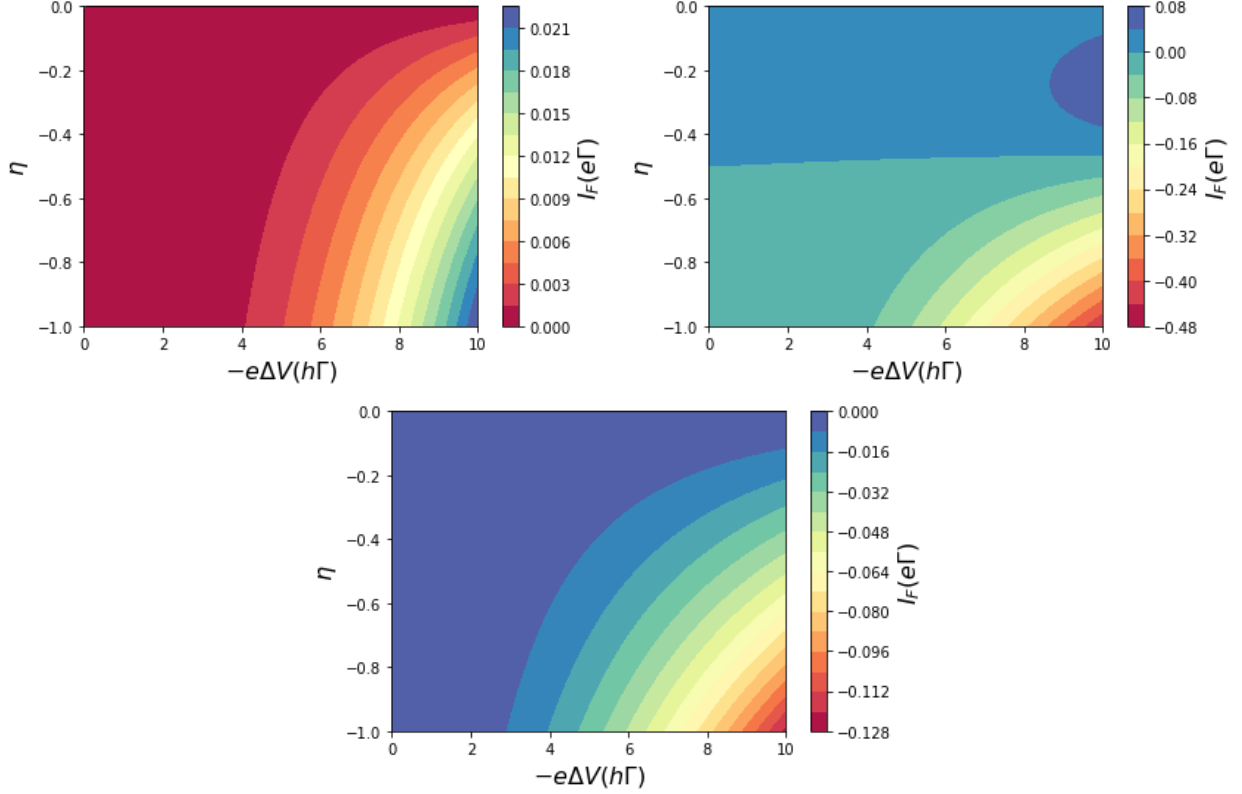


Figure 4: a)Representation of the information current for $k_L = k_R$. b)Representation of the information current for $k_L = 3k_R$ c)Representation of the information current for $k_L = k_R/3$. For all of them it has been considered that $k_R = 0.1$ and $T = 10h\Gamma$. The barriers dependence is $\Gamma_i = 1$ and $E_i = 10h\Gamma$. The ground state is $E_0 = 0$.

3.2 Discretized electrostatic model in linear approximation

In the above sections we have studied the system considering the simple electrostatic model described at the beginning; only two different capacitances account for the interaction between the dot and both edge modes. Our objective now is to use all the formalism in the same way but with a more exhaustive description of the electrostatic interaction between modes and dot. The description is the one explained in references [9, 10]. On the other hand, we suppose that energy interactions could be expressed, when the potential difference is not quite apart from equilibrium, as:

$$U(\vec{r}) = U_{eq} + \sum_k u_k V_k + \mathcal{O}(V_k^2) \quad (32)$$

Where U_{eq} is the equilibrium energy and $u_k = \frac{\partial U}{\partial V_k}$ are the characteristic potentials. For the rest of the project we are supposing that chemical potential in equilibrium is arbitrarily zero.

Hence, we will adopt another viewpoint of the system, dividing it in five regions, in each one the energy U is different as a result of interacting distinctively with the quantum dot. The division is shown in Fig.5, same used in [9, 10]. We have supposed five regions but the division could be

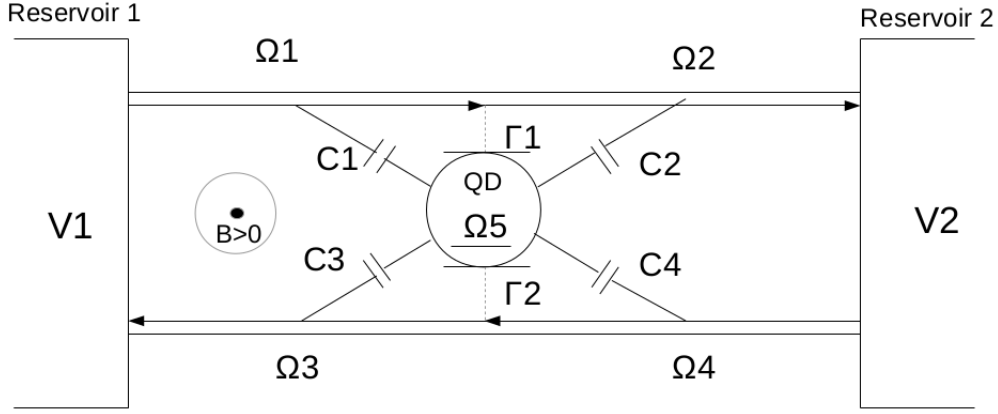


Figure 5: Picture of the system divided into the five regions. In each one, the internal potential is different as well as the coupling with the quantum dot

as complicated as we wished; five is enough for a more complete description with no complicated equations that may distance us from the important physical deductions.

We use now the injectivities, defined as a charge density of states. These terms allows us to establish a direct relation between charge and potential.

$$q_j = e^2 \sum_k D_{ik}(V_k - U_i) \quad (33)$$

The physical meaning of the injectivity is the following: it indicates the density of states existing in one defined region as a consequence of the electrons coming from the i -th lead. The calculation of these quantities is simple taking advantage of its simple physical interpretation. Hence, if the electron coming from one lead has to be transmitted through the barrier to arrive to region i , we have to weight the value of the i -injectivity by the transmission constant T^Q . If it must be reflected to end up in the region we will use the weight $R^Q = 1 - T^Q$. If the electron cannot appear in one region coming from that lead, then the associated injectivity will be zero [9, 5]. Thus, we obtain eight of our injectivities for our problem:

$$D_{11} = D_1 \quad (34) \quad D_{12} = 0 \quad (38)$$

$$D_{21} = D_2 R^Q \quad (35) \quad D_{22} = D_2 T^Q \quad (39)$$

$$D_{31} = D_3 T^Q \quad (36) \quad D_{32} = D_3 R^Q \quad (40)$$

$$D_{41} = 0 \quad (37) \quad D_{42} = D_4 \quad (41)$$

Besides, for simplification it will be supposed that $D_1 = D_2 = D_3 = D_4 = D$. The transmission and reflection coefficients can be deduced taking into consideration that the quantum dot can be viewed as a double potential barrier,

$$T^Q = \frac{\Gamma_{1R}\Gamma_{1L}}{\epsilon_0^2 + \frac{\Gamma^2}{4}} \quad (42)$$

The transmission rates $\Gamma_{1/0(L/R)}$ are different for each barrier and for low voltages we can express:

$$\Gamma_{1/0L} = \Gamma_L e^{k_L(\mu_{2/1} - E_L)} = \Gamma_L(1 + \mathcal{O}(\Delta V)) \quad (43)$$

$$\Gamma_{1/0R} = \Gamma_R e^{k_R(\mu_{2/1} - E_R)} = \Gamma_R(1 + \mathcal{O}(\Delta V)) \quad (44)$$

Thus, we maintain the quantum asymmetry. When the magnetic field is inverted the transmission rates at first order remain constant as well. Then we can simplify notation assuming that we use simply the first term in the series to calculate the internal potential in the dot $\Gamma_{1/0(L/R)} \approx \Gamma_{L/R}$. The reason why we can express the tunneling constant as the above expression is because the exponential term of the tunneling constants depends on the voltage which is being considered very low. In addition, it has also been defined $\Gamma = \Gamma_L + \Gamma_R$.

For $D_{51/2}$ we need to suppose that the electron only overpass one of the barrier but not the other, so it end up in the region 5. Utilizing this argument we determine the two remaining injectivities,

$$D_{51} = \frac{T^Q}{2\pi\Gamma_R} \quad (45) \quad D_{51} = \frac{T^Q}{2\pi\Gamma_L} \quad (46)$$

In order to calculate the internal potentials we need another equation for the charge. We can recover now the process followed in section 3.1 and define again the capacitances. As Coulomb interaction is now different from one region to another, we find not only two capacitances but a complete 5x5 geometrical matrix of capacitances:

$$q_j = \sum_j C_{ij} U_j \quad (47)$$

Assuming that our system has been prepared as it is indicated in figure 5 when $B > 0$, capacitances between regions are zero except the ones coupling with the dot. Here, we introduce something new that differs radically from the first picture of the problem. We will consider that all capacitances are equal, therefore, no asymmetry between capacitances exists and we will carry out all the theory to account for the fact that possibly that asymmetry may not be required for the demon to work.

Equaling both equations for the charge we find a linear system that can be solved analytically,

$$\begin{pmatrix} U_1 \\ U_2 \\ U_3 \\ U_4 \\ U_5 \end{pmatrix} = \begin{pmatrix} C+D & 0 & 0 & 0 & -C \\ 0 & C+D & 0 & 0 & -C \\ 0 & 0 & C+D & 0 & -C \\ 0 & 0 & 0 & C+D & -C \\ -C & -C & -C & -C & 4C+A \end{pmatrix}^{-1} \begin{pmatrix} D & 0 \\ DR^Q & T^Q D \\ T^Q D & DR^Q \\ 0 & D \\ D_{51} & D_{52} \end{pmatrix} \begin{pmatrix} V_1 \\ V_2 \end{pmatrix} \quad (48)$$

Where A is defined as:

$$A = D_{51} + D_{52} = \frac{T^Q \Gamma}{2\pi\Gamma_R \Gamma_L} \quad (49)$$

The internal potential in which we should focus for implementing the demon is the one inside the quantum dot. Its formal expression is [10]:

$$U_5^+ = \frac{V_1(4\pi D C \Gamma_R \Gamma_L + T^Q \Gamma_L (C + D)) + V_2(4\pi D \Gamma_L \Gamma_R C + T^Q \Gamma_R (C + D))}{8\pi C D \Gamma_R \Gamma_L + T^Q \Gamma (C + D)} \quad (50)$$

The reason why we focus on this potential is that we need a variation of the energy when the magnetic field is in the opposite direction, that is, we need energies to be different when edge modes change their polarity. This argument was used in the first section too when we defined the two chemical potentials μ_1 and μ_2 , one for each polarization of the magnetic field. Therefore, $\epsilon_0 + U_5$ will play the same role as those quantities. By analogy we define,

$$\mu'_1 = \epsilon_0 + U_5^+ \quad (51)$$

Where the + indicates that the magnetic field is positive and the prime indicates that this term differs from the one calculated in section 3.1.

Once we have determined the energy level due to Coulomb interactions for a positive magnetic field, we continue with the description of the same interaction for a negative magnetic field. Again, the change of the system when the sign of the field is changed will be the key fact for the implementation of the demon's protocol. The capacitances are the same as they depend only on the geometrical distribution of the regions but the injectivities are modified since edge modes make electrons move in the opposite direction. Hence, we find the following ten injectivities:

$$D_{11} = D_1 T^Q \quad (52) \quad D_{12} = D_1 R^Q \quad (57)$$

$$D_{21} = 0 \quad (53) \quad D_{22} = D_2 \quad (58)$$

$$D_{31} = D_3 \quad (54) \quad D_{32} = 0 \quad (59)$$

$$D_{41} = D_4 R^Q \quad (55) \quad D_{42} = D_4 T^Q \quad (60)$$

$$D_{51} = \frac{T^Q}{2\pi\Gamma_L} \quad (56) \quad D_{52} = \frac{T^Q}{2\pi\Gamma_R} \quad (61)$$

Again we assume $D_1 = D_2 = D_3 = D_4 = D$. Using Eqs.(33),(47) we get to the formal result:

$$\begin{pmatrix} U_1 \\ U_2 \\ U_3 \\ U_4 \\ U_5 \end{pmatrix} = \begin{pmatrix} C+D & 0 & 0 & 0 & -C \\ 0 & C+D & 0 & 0 & -C \\ 0 & 0 & C+D & 0 & -C \\ 0 & 0 & 0 & C+D & -C \\ -C & -C & -C & -C & 4C+A \end{pmatrix}^{-1} \begin{pmatrix} T^Q D & DR^Q \\ 0 & D \\ D & 0 \\ DR^Q & T^Q D \\ D_{51} & D_{52} \end{pmatrix} \begin{pmatrix} V_1 \\ V_2 \end{pmatrix} \quad (62)$$

The explicit expression for the internal energy in the quantum dot is [10]:

$$U_5^- = \frac{V_2(4\pi D C \Gamma_R \Gamma_L + T^Q \Gamma_L (C+D)) + V_1(4\pi D \Gamma_L \Gamma_R C + T^Q \Gamma_R (C+D))}{8\pi C D \Gamma_R \Gamma_L + T^Q \Gamma (C+D)} \quad (63)$$

And by analogy we define the new chemical potential for negative magnetic field applied:

$$\mu'_2 = \epsilon_0 + U_5^- \quad (64)$$

The energy splitting is shown in Fig.6 for different values of the capacitance and ζ . We have defined ζ as a parameter which measure the asymmetry of the barriers,

$$\zeta = \frac{\Gamma_L}{\Gamma_R} \quad (65)$$

It is clear that when both barriers are equivalent we find no splitting as a consequence of eliminating the asymmetry. When $\Gamma_L < \Gamma_R$ we find that $\mu'_1 < \mu'_2$ so the positive current should be found for values of $\zeta < 1$. This does not mean that the right barrier needs to be higher than the left one; it only needs to happen for low voltages when we approximate the exponential as a constant. For high voltages the right barrier has to be lower than the left one as we proved in the previous section. The contrary happens when $\Gamma_L > \Gamma_R$. This is quite coherent since, at first, this should be an intuitive symmetry of the system. Besides, we prove that energies increase their difference when the voltage is higher as we expected.

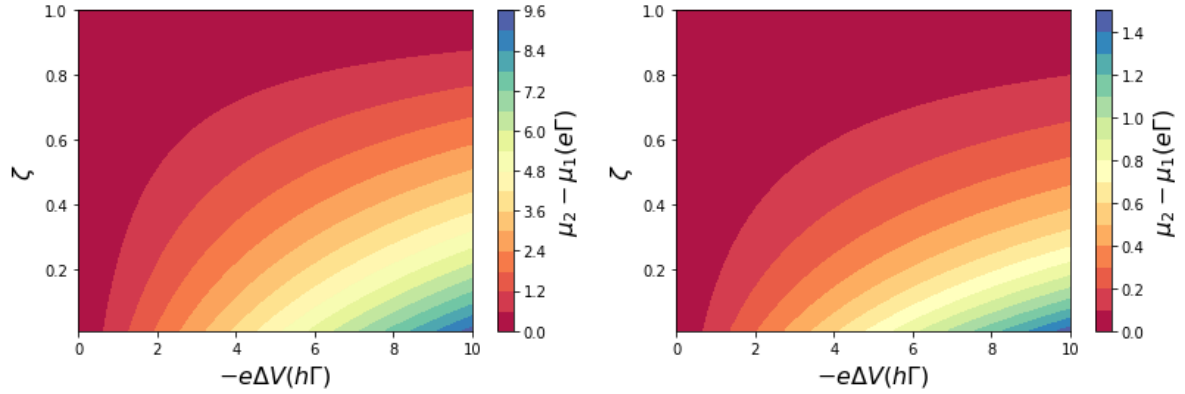


Figure 6: On the left, representation of the splitting $\mu_2 - \mu_1$ for $C = 0.01$. On the right, representation of the splitting $\mu_2 - \mu_1$ for $C = 1$. In both cases we have taken $D = 10$ and $E_0 = 1h\Gamma$

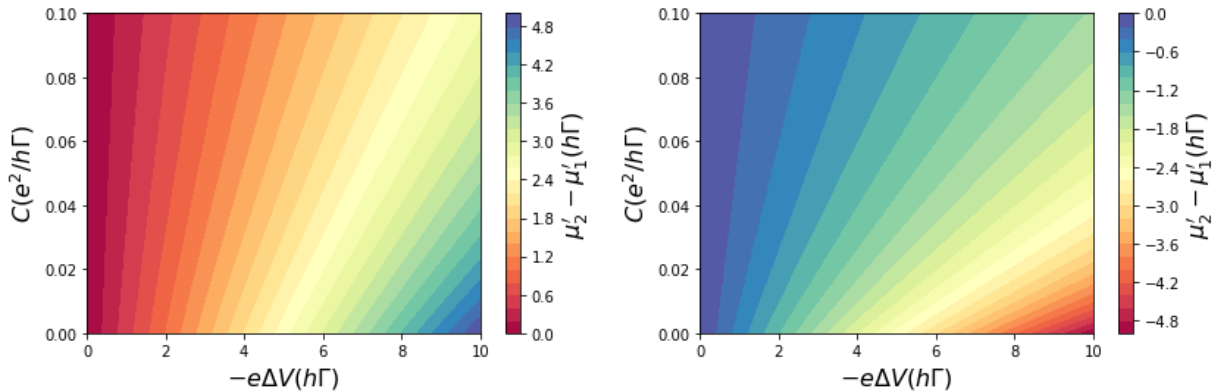


Figure 7: On the left, representation of the splitting $\mu_2 - \mu_1$ for $\zeta = 1/3$. On the right, representation of the splitting $\mu_2 - \mu_1$ for $\zeta = 3$. In both cases we have taken $D = 10$ and $E_0 = 1h\Gamma$

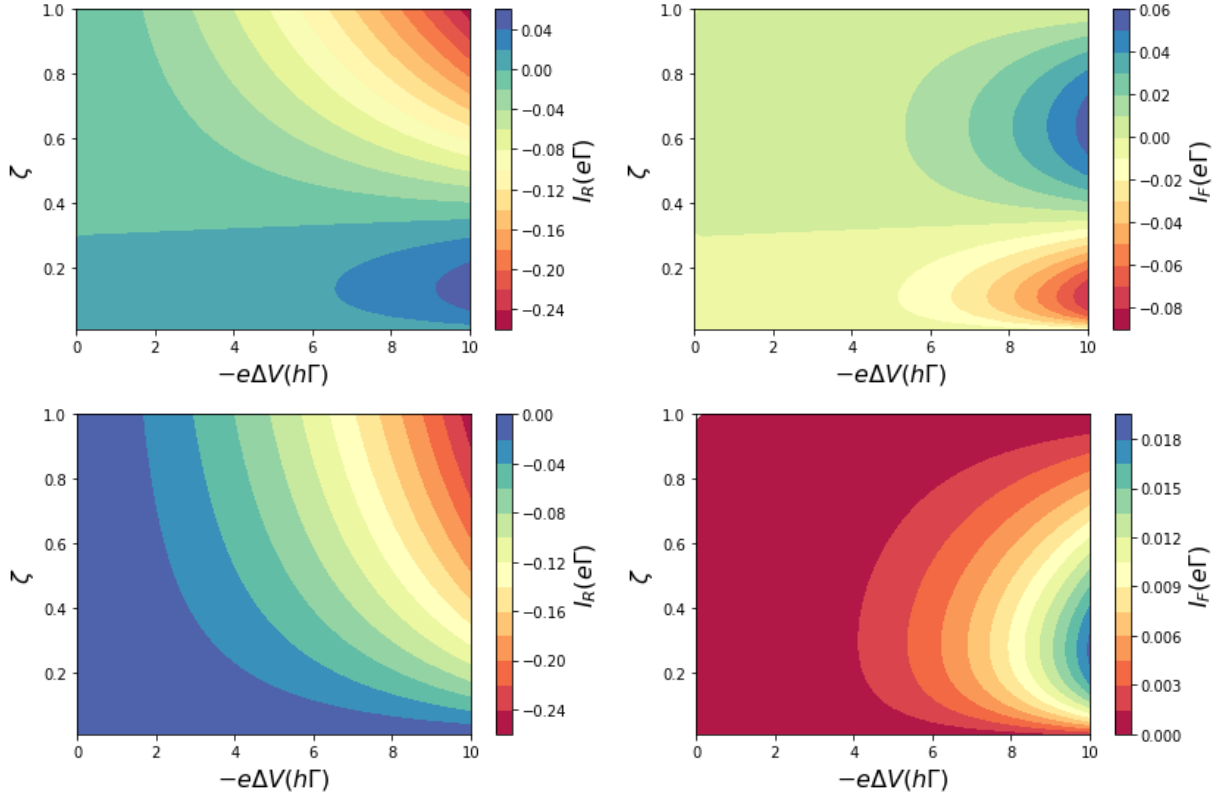


Figure 8: Above, representation of the currents for $C = 0.01$. Below, representation of the currents for $C = 1$. The rest of parameters are the same of the previous plots. To calculate the current it was been taken $k_L = 0.3$ and $k_R = 0.1$

If we apply all the mechanism described in the first part we can compute the currents driven in the system. Now we have to take into account that the barrier tunneling constants depend on the energy, so instead of working with the constant term in the series, it is convenient to use its whole contribution for the compute of the master equations:

$$\Gamma_{1/0L} = \Gamma_L e^{k_L(\mu_{2/1} - E_L)} \quad (66)$$

$$\Gamma_{1/0R} = \Gamma_R e^{k_R(\mu_{2/1} - E_R)} \quad (67)$$

Indeed, the electric and information currents are depicted in Fig.8, again for different values of the capacitance C .

We obtain that there exists a region where the current is positive. This region is found for high voltages within the linear regime, $\zeta \sim 0.2$ and low capacitances. In fact, if we put a higher capacitance no positive current is found and it becomes more negative as we increase the voltage. This means that we need a high interaction between electrons in the dot to make the transport effective. This high interaction needed will be used in the next section so it should be a remarkable result. The value of ζ gives and idea of the features of the barriers that we need to impose to transport the electrons against the voltage gradient. Since $\zeta < 1$ we can conclude that the left barrier must be weaker than the right one in first approximation. Then as we consider than $k_L > k_R$, out of the constant approximation the left barrier should be stronger, as it happens in the first formalism described in this work. Lastly, we should highlight that we have used an approximation for low voltages in $\Gamma_{L/R}$. This makes our implementation difficult because the region where positive currents appear are high voltages in the range of work, so the approximations (43) and (44) introduce more errors in the results.

We can also compare the efficiency of the current due to the change of parameters. Clearly, the absolute value of the current is lower in this case than it was when we considered only two different capacitances. Thus, the electrostatic asymmetry in the capacitances is not a necessary condition, but if that difference existed we should be able to improve the work of the demon.

As we expected, the information current is more important when the current is going against the bias, what means that the demon is extracting information from the system; the extraction is reflected in the negative sign of the information current. Out of that zone, the information current

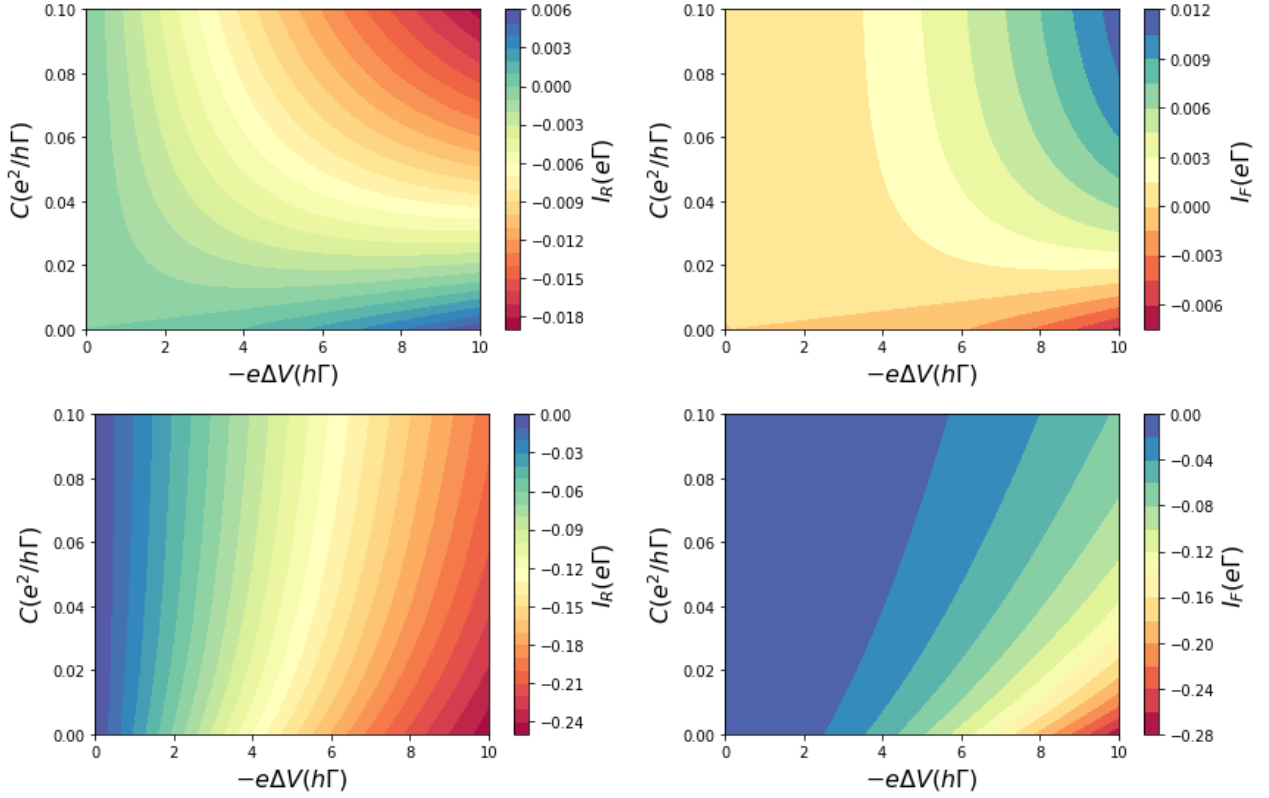


Figure 9: Above, representation of the currents for $\zeta = 1/3$. Below, representation of the currents for $\zeta = 3$. The rest of values are the same as the ones used before

is negligible, therefore the demon is not working. We may also plot the currents as functions of C for different values of ζ (Fig.9).

On the other hand, it is convenient to analyze if the efficiency of our system may be improved by changing the value of some capacitances. We now suppose that $C_1 = C_2 = (1 + \eta)/2$ and $C_3 = C_4 = (1 - \eta)/2$. If we do so, we easily get to an analytic expression for $U_5^{+/-}$.

$$U_5^+ = u_1 V_1 + u_2 V_2 \quad (68)$$

$$u_1^+ = \frac{\Gamma_L(4C^2 D \Gamma_R (1 - \eta^2) + 8CD^2 \Gamma_R \pi (1 + R^Q \eta) + C^2 T^Q (1 - \eta^2) + 4D^2 T^Q + 4CDT^Q)}{8C^2 D \Gamma_L \Gamma_R \pi (1 - \eta^2) + C^2 T^Q \Gamma (1 - \eta^2) + 4CDT^Q \Gamma + 4D^2 T^Q \Gamma + 16\Gamma_R \Gamma_L \pi CD^2} \quad (69)$$

$$u_2^+ = \frac{\Gamma_R(4C^2 D \Gamma_L (1 - \eta^2) + 8CD^2 \Gamma_L \pi (1 - R^Q \eta) + C^2 T^Q (1 - \eta^2) + 4D^2 T^Q + 4CDT^Q)}{8C^2 D \Gamma_L \Gamma_R \pi (1 - \eta^2) + C^2 T^Q \Gamma (1 - \eta^2) + 4CDT^Q \Gamma + 4D^2 T^Q \Gamma + 16\Gamma_R \Gamma_L \pi CD^2} \quad (70)$$

$$U_5^- = u_1^- V_1 + u_2^- V_2 \quad (71)$$

$$u_1^- = \frac{\Gamma_R(4C^2 D \Gamma_L (1 - \eta^2) + 8CD^2 \Gamma_L \pi (1 - R^Q \eta) + C^2 T^Q (1 - \eta^2) + 4D^2 T^Q + 4CDT^Q)}{8C^2 D \Gamma_L \Gamma_R \pi (1 - \eta^2) + C^2 T^Q \Gamma (1 - \eta^2) + 4CDT^Q \Gamma + 4D^2 T^Q \Gamma + 16\Gamma_R \Gamma_L \pi CD^2} \quad (72)$$

$$u_2^- = \frac{\Gamma_L(4C^2 D \Gamma_R (1 - \eta^2) + 8CD^2 \Gamma_R \pi (1 + R^Q \eta) + C^2 T^Q (1 - \eta^2) + 4D^2 T^Q + 4CDT^Q)}{8C^2 D \Gamma_L \Gamma_R \pi (1 - \eta^2) + C^2 T^Q \Gamma (1 - \eta^2) + 4CDT^Q \Gamma + 4D^2 T^Q \Gamma + 16\Gamma_R \Gamma_L \pi CD^2} \quad (73)$$

We should focus on the case in which no barrier asymmetry is present so $\Gamma_R = \Gamma_L = \Gamma/2$ [10].

$$u_1^+ = \frac{2C^2 D \Gamma \pi (1 - \eta^2) + 4CD^2 \Gamma \pi (1 + R^Q \eta) + C^2 T^Q (1 - \eta^2) + 4CDT^Q + 4T^Q D^2}{4C^2 D \Gamma \pi (1 - \eta^2) + 2C^2 T^Q (1 - \eta^2) + 8CDT^Q + 8D^2 T^Q + 8CD^2 \Gamma \pi} \quad (74)$$

$$u_2^+ = \frac{2C^2 D \Gamma \pi (1 - \eta^2) + 4CD^2 \Gamma \pi (1 - R^Q \eta) + C^2 T^Q (1 - \eta^2) + 4CDT^Q + 4T^Q D^2}{4C^2 D \Gamma \pi (1 - \eta^2) + 2C^2 T^Q (1 - \eta^2) + 8CDT^Q + 8D^2 T^Q + 8CD^2 \Gamma \pi} \quad (75)$$

$$u_1^- = \frac{2C^2 D \Gamma \pi (1 - \eta^2) + 4CD^2 \Gamma \pi (1 - R^Q \eta) + C^2 T^Q (1 - \eta^2) + 4CDT^Q + 4T^Q D^2}{4C^2 D \Gamma \pi (1 - \eta^2) + 2C^2 T^Q (1 - \eta^2) + 8CDT^Q + 8D^2 T^Q + 8CD^2 \Gamma \pi} \quad (76)$$

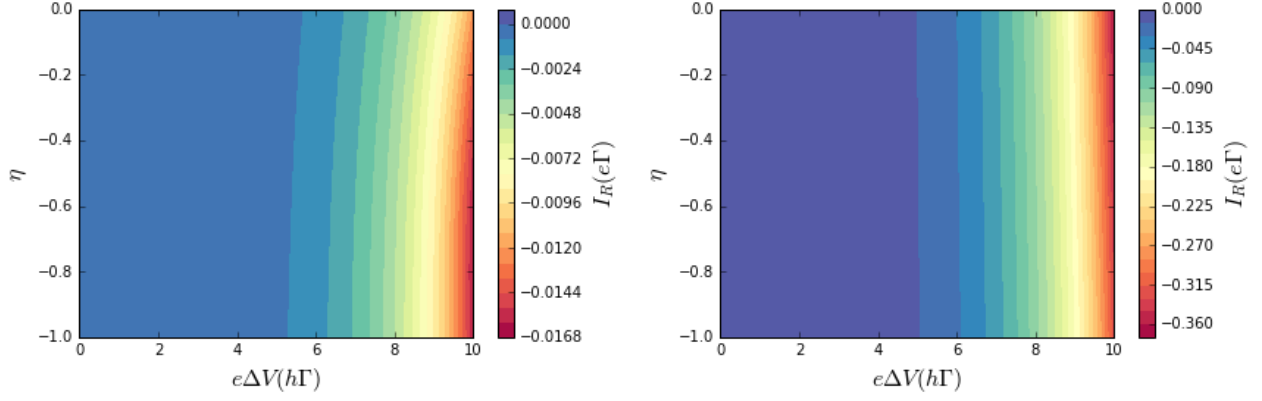


Figure 10: a) Representation of the current for $\Gamma_{1(L/R)}/\Gamma_{0(L/R)} = 0.1$. b) Representation of the current for $\Gamma_{1(L/R)}/\Gamma_{0(L/R)} = 1$

$$u_2^- = \frac{2C^2 D \Gamma \pi (1 - \eta^2) + 4C D^2 \Gamma \pi (1 + R^Q \eta) + C^2 T^Q (1 - \eta^2) + 4C D T^Q + 4T^Q D^2}{4C^2 D \Gamma \pi (1 - \eta^2) + 2C^2 T^Q (1 - \eta^2) + 8C D T^Q + 8D^2 T^Q + 8C D^2 \Gamma \pi} \quad (77)$$

No positive current appears as we can see in Fig.10. This is a remarkable result, since we can conclude that the quantum asymmetry is necessary to accomplish our objective. It is to say, we need both barriers to be different and energy-dependent to implement the demon. Nonetheless, the electrostatic asymmetry introduced in the first part of the project is not absolutely necessary, even though it could, perhaps, favour the efficiency of the demon. However, we have not studied the case with both asymmetries with this model in this project.

3.3 Non-linear electrostatic model

Our objective now is to give a more accurate description of the potential in the dot than the ones used before to close the overall view of the electrostatic system. Firstly, we need to propose a model that may quantify adequately the coulomb interaction. Basically, we are doing the same analysis but the charge now will be described considering non-linear terms in voltage, and not only the approximated injectivities. The concrete motivation and the deep formalism are explained in the references [5]. Here, we are reproducing the results shown there for the internal potential so that we can apply them to the implementation of the demon. Hence, to calculate the internal potential in the quantum dot we utilize the following charge equation:

$$\sum_j C_{kj} U_j = \delta q = q_{tot} - q_{eq} \quad (78)$$

$$q_{tot} = \frac{e}{\pi} \int d\epsilon \frac{\Gamma_L f_{1L} + \Gamma_R f_{1R}}{(\epsilon - \epsilon_0 - eU^+)^2 + \Gamma^2} \quad (79)$$

Where the second part comes from a more exhaustive calculation, using Green's functions formalism, that, for simplicity, we will omit in this work [11, 5]. Besides, it might be assumed that $C_{kj} = 0 \forall k, j$, what means that interaction is very high. This is coherent since we are considering that the repulsion between electrons is really strong and thus, it is impossible to have two electrons inside the dot. The equilibrium charge is the one that can be measured if there is not a voltage difference between the reservoirs. It can be calculated taking into account that Fermi's distribution is ultimately the same in both leads if the system is in equilibrium, and using the equation 85 we can express:

$$q_{eq} = \frac{e}{\pi} \int d\epsilon \frac{\Gamma f}{(\epsilon - \epsilon_0)^2 + \Gamma^2} \quad (80)$$

We suppose again that $\mu_F = 0$. Our purpose is to obtain the value of U^+ that verifies $\delta q = 0$. To do so, we calculate the analytic expression for the integrals [12],

$$q_{tot} = \frac{e}{2} - \frac{e}{\pi} \mathcal{I} \left(\frac{\zeta}{1 + \zeta} \Psi \left(\frac{1}{2} + \frac{i(\epsilon_0 + U - V1)}{2\pi T} + \frac{\Gamma}{2\pi T} \right) + \frac{1}{1 + \zeta} \Psi \left(\frac{1}{2} + \frac{i(\epsilon_0 + U - V2)}{2\pi T} + \frac{\Gamma}{2\pi T} \right) \right) \quad (81)$$

$$q_{eq} = \frac{e}{2} - \frac{e}{\pi} \mathcal{I} \left(\Psi \left(\frac{1}{2} + \frac{i\epsilon_0}{2\pi T} + \frac{\Gamma}{2\pi T} \right) \right) \quad (82)$$

If we represent the equilibrium charge and the excess charge for different temperatures we can get an idea of how important the dependencies with it and with E_0 are. Indeed, for the rest of the problem we will consider a lower temperature than the one used previously to account for this fact.

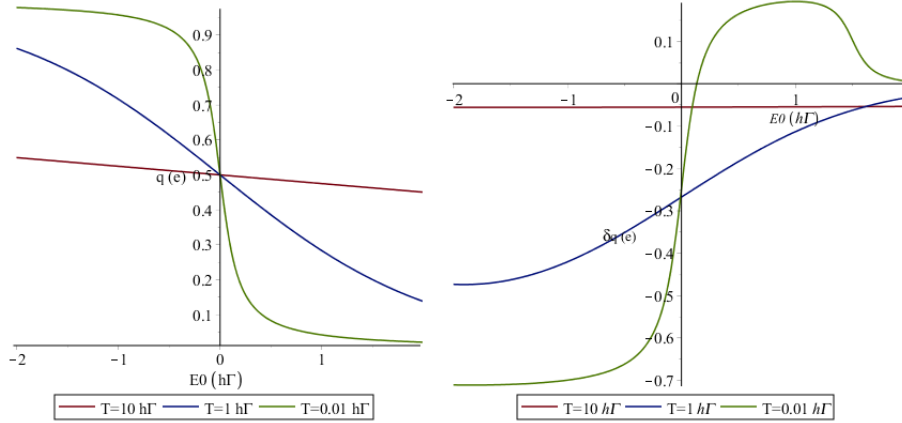


Figure 11: Equilibrium charge and excess charge for different temperatures, taken $eV = 5h\Gamma$, $\zeta = 1/3$ and $U = 1h\Gamma$.

The equilibrium charge is modified with the Fermi's distribution so when temperature is high it is almost linear, but when temperature is increased, the behaviour of the curve differs from linear. Moreover, the equilibrium charge tend to zero when the ground state is higher, and to one when is lower. That means that only one electron should be able to enter the dot and the mean charge depends on how high the state in the nanostructure is. The excess charge has a more complicated behaviour but we can see that for low temperatures it changes completely from linear to non-linear. Besides, in Fig.12 we can observe that there is always a value of U that makes zero the excess charge, what means that a physical solution for our problem always exists.

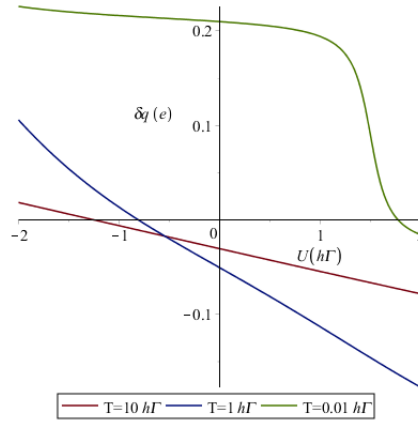


Figure 12: Excess charge as a function of U for $E_0 = 1h\Gamma$

Since this last equation is non-linear, the solution needs to be computed numerically. Once we know the value of U , which corresponds to the one inside the dot, we need to repeat all this formalism but describing the system for negative magnetic fields. The coupling between the dot and the reservoirs is modified due to the change of the edge modes polarity. Therefore, the total charge in the system may be expressed on a similar, but changing the Fermi's distributions that appears with the tunneling constants:

$$q_{tot} = \frac{e}{\pi} \int d\epsilon \frac{\Gamma_L f_{2R} + \Gamma_R f_{2L}}{(\epsilon - \epsilon_0 - eU)^2 + \Gamma^2} \quad (83)$$

The bare charge or equilibrium charge is, evidently, invariant under inversion of the magnetic field. Then the results are the same but digamma functions are multiplied by different weights:

$$q_{tot} = \frac{e}{2} - \frac{e}{\pi} \mathcal{S} \left(\frac{1}{1+\zeta} \Psi \left(\frac{1}{2} + \frac{i(\epsilon_0 + U - V1)}{2\pi T} + \frac{\Gamma}{2\pi T} \right) + \frac{\zeta}{1+\zeta} \Psi \left(\frac{1}{2} + \frac{i(\epsilon_0 + U - V2)}{2\pi T} + \frac{\Gamma}{2\pi T} \right) \right) \quad (84)$$

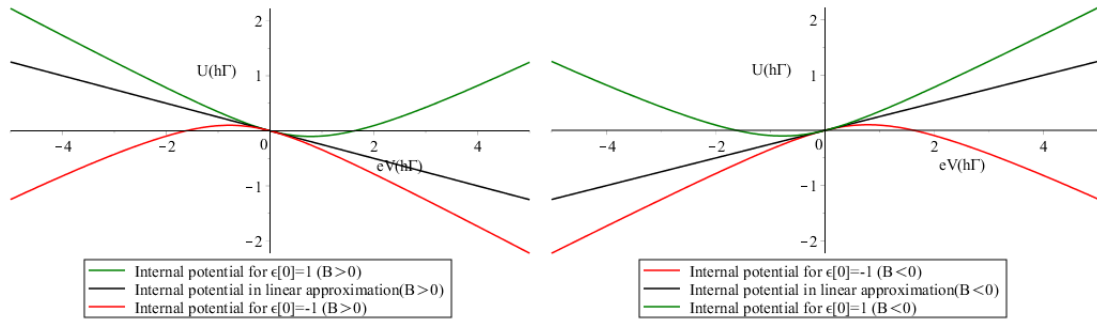


Figure 13: Internal potential in the dot for positive magnetic field on the left and negative magnetic field on the right as functions of the potential. It has been taken $T = 1$, $\Gamma_R = 0.1$ and $\zeta = 0.3$

The solution of Eq.(78) for different values of E_0 are depicted in Fig.13 for a concrete range of voltages.

In the same figure the linear approximation is depicted using the formalism described in the previous section, imposing $C = 0$ to the equations 50 and 63. The results are similar to the one obtained in [5]. The analytic expression for the linear behaviour is simple,

$$U_5^\pm = \pm \frac{1 - \zeta}{2(1 + \zeta)} \Delta V + \mathcal{O}(V_k^2) \quad (85)$$

As we can easily see, the linear approximation is independent of the value of E_0 since all the curves coincide near the zero voltage. Indeed, it depends only on the asymmetry between barriers [5]. Besides, for higher voltages the curves differ radically one from the other. As we need high voltages to implement a demon correctly, we should take into account this non linear terms if we want to give a more accurate description. When the magnetic field is reversed, the chiral modes couple differently with the quantum dot, but there exists a clear symmetry as it can be seen in the same figure. The internal potential is an odd function of B and V , fact that can be deduced from the schematic figures of the system shown in the first section.

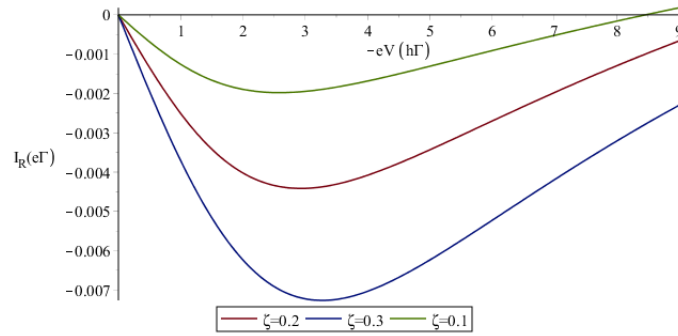


Figure 14: Current to the right in the system. It has been taken $T = 1$, $\Gamma_R = 0.1$ and different values of ζ

The current calculated using the master equations, as a result of using this method to obtain the internal potentials, should be positive to accomplish our objective. Actually, there exists a region where the current appears positive as it is shown in Fig.14. In fact, we can compare this result to the one obtained using the linear approximation with $C = 0$.

As we expected, the curves in linear and non linear approximation coincide at low voltages (Fig.15). However, for large voltages their difference is quite relevant even although their qualitative behaviour is also similar. For both cases we find a positive current but with the non-linear terms it is needed a lower voltage so the model is actually more efficient.

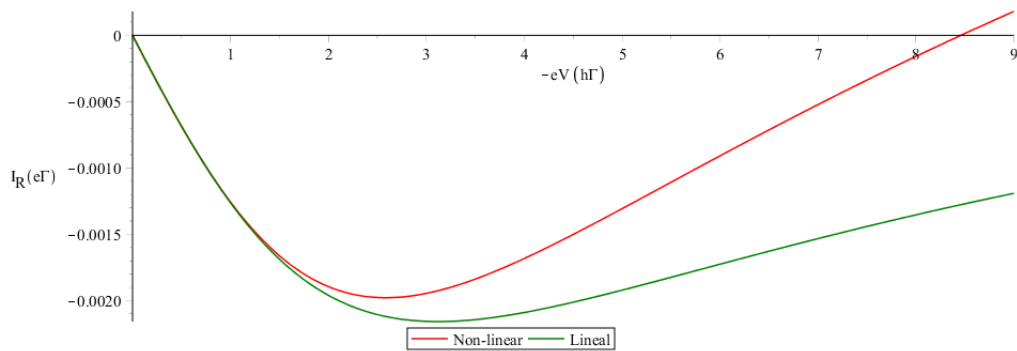


Figure 15: Current to the right in the system for $\zeta = 0.1, T = 1$ and $\Gamma_R = 0.1$ in linear approximation for $C = 0$ and non-linear model.

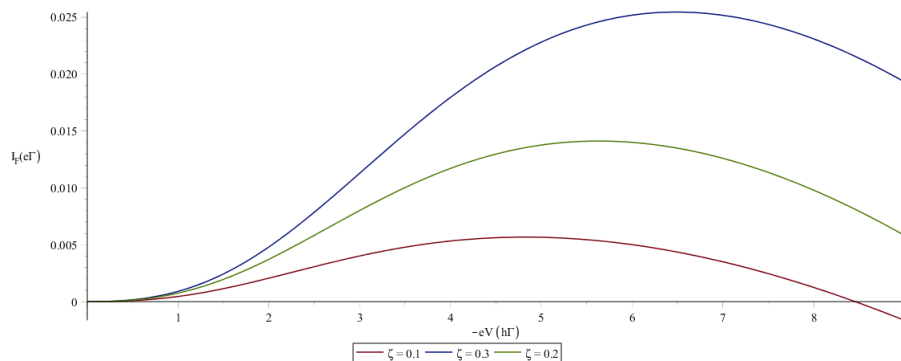


Figure 16: Current of information in the system. It has been taken $T = 1, \Gamma_R = 0.1$ and different values of ζ

In terms of information, the demon extracts it when the current is against the bias, same argument found before. In Fig.16 the information current is shown for different values of ζ . Consequently, we have obtained very similar results using this auto-consistent method for different parameters of the system considering the limit $C = 0$. Nonetheless, the extraction of information happens at $-eV > 8h\Gamma$, voltages that are too high to satisfy perfectly the conditions of the previous approximations.

4 Conclusions

The work developed in this project is undoubtedly fruitful since it allowed us to establish some conditions that are absolutely necessary in the preparation of our system to accomplish the implementation of the demon. Thus, quantum asymmetry is necessary but electrostatic asymmetry may not be necessary if we stick to a more exhaustive model even considering non-linear terms. However, it is important to be cautious because we have assumed that only low voltages are applied to make some approximations, but we have concluded that the demon only works at appreciable voltages. Perhaps, studying the range in which our approximation for $\Gamma_{L/R}$ are valid (Eqs.(43),(44)), which is the main mathematical tool used to obtain the results, may be fundamental in following works to verify our theory. Therefore, these results are important for the advance of the theory of the quantum transport as well as future implementation of new nanostructures, as we believe that these ideas could lead to implementations in real devices.

In terms of academic learning, this project was absolutely helpful to understand not only the physical view of quantum transport in nano-scale but also to work with different software. Although one month is a short period of time to develop a solid project, it is important to say that this work was a first approximation to the theoretical work so the fellowship was useful to realize how this kind of work is.

5 Acknowledgments

First, I would like to thank the SURF@IFISC fellowship commission for giving me the opportunity of working a whole month in this project and introducing me in the world of researching. I also

appreciate the effort of the researchers and administrative who helped me during my stay in the IFISC. Especially, I would like to thank Dr. Rosa López, co-author of this project, for looking after my work during my stay in the IFISC and being crucial to the success of my work. I would also remark the help that Guillem Roselló gave me when I was still reproducing his results and for the interest during the rest of the work. Moreover, I appreciate the help that Dr. David Sánchez offered me in order to explain some of the formalism that was still not clear and helped me to obtain the fundamental results, and the two lectures which I attended to about quantum transport given by him. Finally, I would like to thank M.A. Matías, coordinator of the fellowship for the attention given to me during the month of working.

This work was supported by the SURF@IFISC fellowship.

References

- [1] Harvey Leff, Andrew F. Rex *Maxwell's Demon 2: Entropy, Classical and Quantum Information, Computing* December, 13 2002
- [2] Guillem Roselló *Doctoral Thesis* Personal Communications
- [3] D.Sánchez *Phys. Rev. B* 79,045305 (2009)
- [4] D.Sánchez and M.Büttiker, *Phys. Rev. B* 72,201308(R) (2005)
- [5] D.Sánchez and R.López *Phys. Rev. Lett.* 110, 026804 (2013)
- [6] M. Esposito and G. Schaller *EPL* 99, 30003 (2012)
- [7] Massimiliano Esposito and Christian Van den Broeck *Phys. Rev. E* 82, 011143 (2010)
- [8] Michael A.Nielsen and Isaac L.Chuang *Quantum information and quantum Information* (2000)
- [9] D.Sánchez and M.Büttiker, *Phys. Rev. Lett.* 93,106802 (2004)
- [10] S.Y.Hwang, D.Sánchez, M.Lee and R.López *New J. Phys.* 15 105012 (2013)
- [11] H.Haug and A.-P.Jauho. *Quantum Kinetics in Transport and Optics of Semiconductors* (1996)
- [12] Jong Soo Lim *Mesoscopic Coulomb Drag: Taking into Account Cotunneling Processes*. School of Physics, Korea Institute for Advanced Study, Seoul 130-722, Korea. April 4, 2016

Autonomous Operation of Optoelectronic Reservoir Computing Systems

Álvaro Moreno Abajo, Miguel C. Soriano, Ingo Fischer
 Instituto de Física Interdisciplinar y Sistemas Complejos IFISC (CSIC-UIB)
 Campus Universitat de les Illes Balears, E-07122 Palma de Mallorca, Spain

Abstract

In this report a mixed approach combining aspects of reservoir computing and extreme learning machines is used to perform machine learning in a minimal set-up using a Field Programmable Gate Array (FPGA). Based on previous efforts by Quim Llorens[1], M. Häussler[4] and J. Striebel[5], we have focused on the characterization of some recent experimental findings by studying the FPGA and the Analog to Digital/Digital to Analog converter (ADA) in a more systematic way. This also will serve for preparing the complete RC experiment, as the FPGA programming is prepared to carry all the experiment stages in the same way. We finally prove that it is possible to predict the short-term evolution of a temporal series using only an ADA attached to a FPGA and connecting the analog output directly to the analog input, due to the ADA non-linear behaviour.

1 Introduction

Despite the term Machine Learning (ML) was born in the middle of 20th century, nowadays ML is becoming a near-ubiquitous field in our society with a full range of practical applications. Inspired in how the brain works, a recent and very powerful approach to ML are Neural Networks¹. In this framework, we will focus in two of the most popular so-called random-projection techniques[2]: Reservoir Computing (RC) and Extreme Learning Machines (ELM). Both share their basic components, with a similar three layers structure: an input layer, a hidden layer (the reservoir), and an output layer. We here introduce the notion of layers and its components, the neurons or nodes, as we will call them, since it is the terminology commonly used for neural networks.

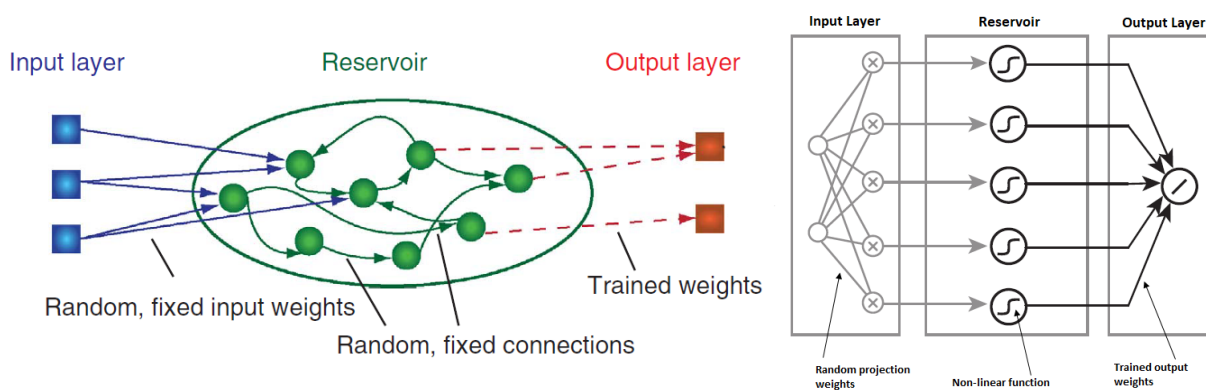


Figure 1: Schematic representations of RC (on the left) and ELM (on the right). Figures adapted from [3], [2] respectively.

Despite important differences between the connectivity within the hidden layer, RC and ELM have in common a general scheme which can be seen in figure 1. Firstly, the input layer feeds the reservoir by mapping the incoming or input signal through random weight connections. The reservoir is the hidden layer of the system, usually consisting on a large number of non-linear nodes,

¹For learning more about ML and Neural Networks I strongly recommend to visit <https://ml.berkeley.edu/blog/tutorials/>.

that is the reservoir nodes performs a non-linear transformation. Here comes the difference: while in ELM there is no connectivity among the hidden nodes, in RC the reservoir nodes are randomly interconnected creating a recurrent fixed network, with internal feedback loops. This difference is also illustrated in figure 1. Then, the states (values) of the nodes are read and the result is given through the output layer, performing a weighted sum.

These methods can solve complex problems such as time series prediction and classification tasks²[3], in an efficient and widely adaptable process. Its flexibility lies on the fact that only the output weights must be adjusted, so that the computed output weighted sum approximates a target value. This keeps the reservoir dynamical properties unaltered since its internal connexions remain fixed, being the same system applicable to several problems. Output weights are computed (process called *training*) by minimizing the squared error between real target and predicted output values. In our case, this corresponds to a simple linear regression.

These machine learning approaches face such complex tasks efficiently due to the non-linear transformation performed by the nodes. The reservoir non-linearly transforms the input signal, mapping it into a high-dimensional space in which the signal becomes linearly separable. This rather abstract concept is illustrated in figure 2: in a low-dimensional space we can not separate with a linear function red from yellow balls, that is we can not classify them. When we apply the non-linear transformation the response of each kind of ball is different, which adds an extra information state. When representing this non-linear mapping another dimension corresponding to this new value is added, obtaining a higher-dimension space in which the balls will be linearly separable.

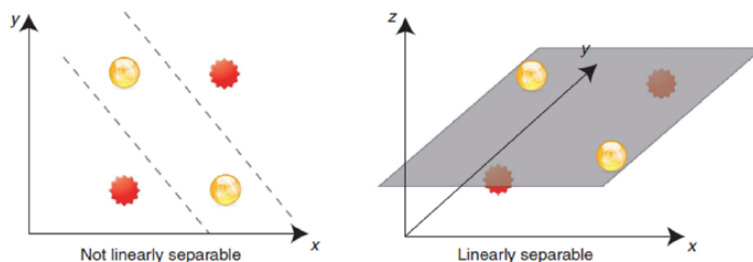


Figure 2: *Representation of linear separation when mapping into a higher dimensional space. Figure adapted from [3].*

All these characteristics can be summarized in three requirements that the reservoir must fulfill in order to be fully efficient[3]:

- The system must be able to map the signal into a high-dimensional space by non-linear transformation.
- The non-linear function must be robust against noise. If it is too sensitive, similar inputs could yield noticeably different values, leading to wrong classifications (it would be like separating two slightly different yellow balls).
- In the particular case of RC, the recurrent network should show fading memory (short-term memory). The reservoir states are influenced by recent previous inputs, but not by those from the far past.

Regarding this report, the approach we present is a simplification of these models that lies in between of RC and ELM. Instead of having physical nodes, we employ time-multiplexing for defining virtual nodes[2]. The input data is multiplied by a random vector (the mask) of length N , where N is the number of nodes we want to define. This way we are doing a random weighted mapping over a chosen number of nodes, as it can be seen in figure 3. In fact, this procedure is equivalent to that of a standard reservoir. In our case, data will be only sent and received, with no explicit non-linear transformation in the process (we will prove that there is actually an effective non-linear transformation). Our objective then is to predict a time-dependent signal, particularly a \sin^2 , using this minimal approach.

²In fact, the ELM are suitable for prediction and classification problems and the RC works really well with time-dependent data[2].

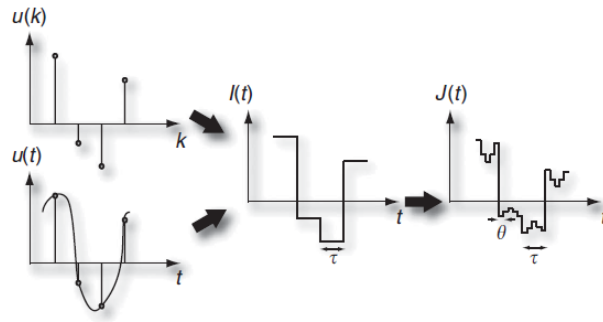


Figure 3: *Mask multiplication*. τ is the time separation between signal points, and θ the time length of a node; then it is fulfilled that $\theta = \tau/N$. Figure adapted from [3].

2 Experimental set-up and Methodology

The set-up for this experiment consists of two elements: the FPGA (Field Programmable Gate Array) and the ADA (Analog to Digital/Digital to Analog converter) daughter card attached to the FPGA. By connecting one analog output of the ADA directly to one of its analog inputs, we have a self-enclosed experimental set-up. Although the complete RC experiment described in [1] uses the optoelectronic circuit too, we chose to simplify it since previous attempts of closing the loop using the optoelectronic system were not fully successful [1]. This simplified approach allows us to carry out a more systematic study, just focusing on the FPGA and the ADA. More information about these elements can be found in [1, 4]. In addition, figure 4 shows a picture with the main parts of the set-up indicated.

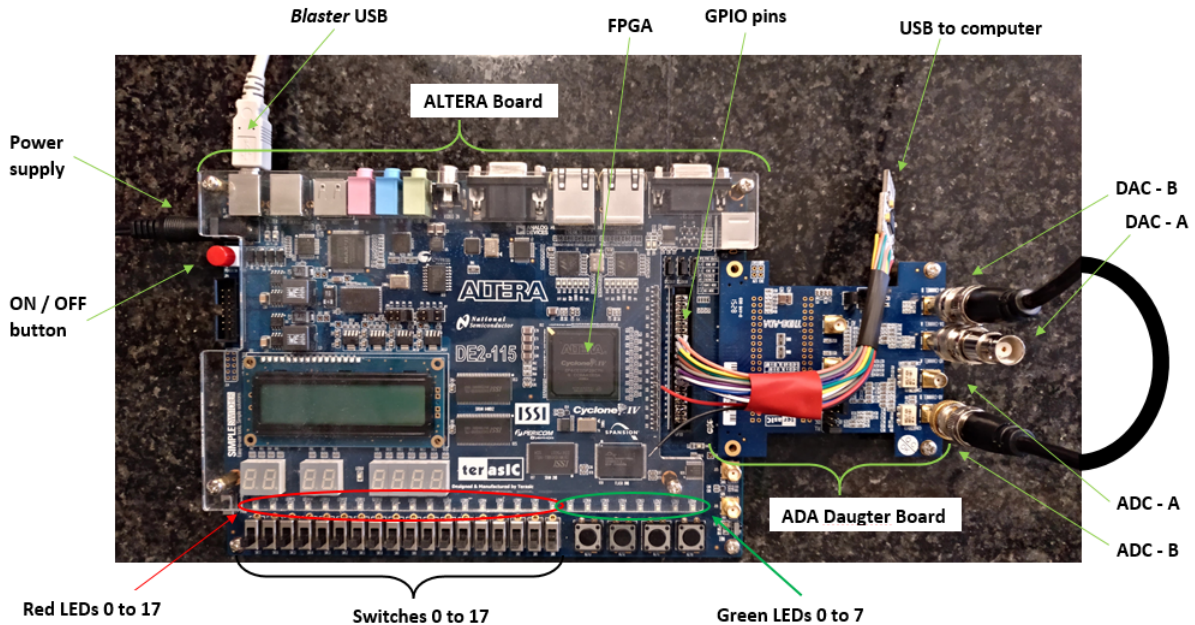


Figure 4: *Experimental set-up*.

A key point of the experiment was how to properly program the FPGA, which was done using Quartus II. The Quartus II projects are written in *Verilog* programming language, which is a HDL (Hardware Description Language); in [4] are some tutorials for learning *Verilog*. It is worth to mention that the FPGA has an internal clock that can be modified, and it executes the corresponding code at every time the clock signal changes, according to the specified frequency. That leads us to check carefully the timing of the experiment, the most challenging part of this project. Before getting into detail of each part of the procedure, we will explain the general steps for running the FPGA:

1. Once opened the Quartus II project we want to work with, the FPGA is programmed through

the *Blaster*. Make sure the second switch, SW[2]³, is down. This switch controls when the program is running, and every time it is switched down the variables are reinitialized, so you can run the FPGA multiple times without reprogram it every time.

2. Open *SignalTap* in case you want to visualize the state of the variables during the running. This can be found in the *Tools* menu in Quartus II window. *SignalTap* is a tool that shows the value of the selected variables, outputs or inputs set in your code at every clock of the FPGA. It is really useful for both the collection of the results and the visualization of the performance (and find out where the potential glitches occur). Run *SignalTap*, it will be waiting for a trigger of SW[2].
3. Switch SW[2] on. Now the code starts to run. The FPGA LEDs are used as “control prints” of the program: when some important steps are done one of the LEDs turns on, so that we can easily visualize if there has been any problem during the experiment (for instance if not all the expected LEDs are on, or they have done so in the wrong order). It is important to bear in mind that *SignalTap* will receive data till its reserved memory space fills up, being this one quite limited. So one needs to verify if all the process data is registered.
4. When all the LED lights are on the program has finished (usually takes less than a second), then switch SW[2] off. The *SignalTap* window will now display the acquired data. If necessary, the data can be exported to an EXCEL file.

Regarding the experiment, there are two main differences with the previous implementations in [1, 4]. On the one hand, as we have mentioned earlier we did not use the optoelectronic devices, connecting the DAC-B (Digital to Analog Channel B) directly to the ADC-B as it can be seen in figure 4. Importantly, in this set-up there is no limitation of the number of nodes as it was before matched to the optic fibre length [1]. Here we have chosen to use 500 nodes, but keeping the 11 last nodes set to 0 for taking care of the delay between outputting and receiving the values introduced by the ADA. We will discuss later the choice of 500 nodes in more detail. We also kept the time length of each node, $\theta = 50ns$, matching the frequency of the FPGA’s clock, $20MHz$.

On the other hand, and the most important difference with the previous designs, we are not using the AWG (Autonomous Wave Generator) for introducing the signal data into the system. In our implementation, the \sin^2 points, mask multiplied, are sent by the FPGA through the DAC-B port in every step of the experiment. In this manner, it is possible to proceed with each step more systematically as well as having higher control of the timing and, in particular, when the system changes from the forced mode to the autonomous mode.

The experimental protocol has three stages, or levels of complexity:

Training of the output weights

First of all we must generate the files with the \sin^2 data points and the 500 nodes input mask. For the data, 20 points per \sin^2 period were selected and a total of 4000 points were generated using *data_mif_gen_500.py* python code. These had to be divided into 20 files with 200 points each due to FPGA’s memory limitation⁴. In this code you may notice that the \sin^2 data is rescaled and then multiplied by two factors of 8192 and 1024. This adjustment, or “normalization”, was done since the data must fit the 14-bits resolution of ADA converter and the FPGA works with integer values. Also a factor was introduced as the voltage range of the AWG did not match the real ADA voltage range (these points are widely discussed in Quim’s report [1]). Nevertheless, we did not require this factor because we introduce the data points directly using the FPGA.

The 500 nodes mask is generated using codes *mask_gen_500.py* and *mask_mif_gen_500.py*, which generates a random mask with 6 possible values: $-1, -0.6, -0.2, 0.2, 0.6, 1$. The last 11 nodes of the mask are set to 0 in order to keep those nodes to 0. All data files used by the FPGA must be in the same format, a MIF file⁵, with extension *.mif*. Also they must be written in a binary base that preserves sign (signed binary) which is called *two’s-complement*. This is due to the fact that

³Previous versions of the programs used SW[1] or SW[0] instead, but we realized that they were not working correctly due to the excess of use.

⁴We must consider that the resulting file containing the received values will have $200 \times 500 = 100000$ numbers. That is what actually limits the space in memory.

⁵Quartus II note: Files used by the functions of the *Verilog* code in Quartus can be selected using *MegaWizard* tool, as well as changing the clocks frequency.

the FPGA works with *two's-complement* integer values (more about this numerical system in [1, 4]).

Once the data and the mask are generated, the Quartus II project for this part is *reservoir_data_to_usb*, in *reservoir_data_to_usb_copy* folder. The FPGA will send every $50ns$ a \sin^2 point multiplied by one value of the mask. When the 500 values (500 nodes) are sent, the process starts again with the following data point. When the green LEDs 6 and 7, and the red LED 1 are on, the program has finished. The code was originally designed to send the received data through a USB port attached to GPIO-pins, yet we decided not to use it since the connection often failed. Instead we register the incoming data with *SignalTap*. The delay between outputting and receiving can be easily seen here: with this set-up there is a 10 clocks delay, about $500ns$.

Repeating the process for each data file, we get the training data. Using *sine2_nodes_data_ev_500_crossval_shuffle.py* we obtain the trained weights. This Python code organizes the data into a matrix of 500 columns, each one of them corresponding to one node, and cuts off the last 11 nodes (they are set to 0). An extra column filled with 1 is added corresponding to the offset node: the predicted value will be the sum of the nodes states times the weights plus the offset. Finally, this code performs a linear regression with the next point of the original time series as target for each row, so that given the state of the nodes we can calculate the next point of the time series. The resulting *.mif* file contains the weight matrix.

Not all of the input data is used by the linear regression; an 80% is dedicated to training, whereas the other 20% is kept for an error testing calculating the NMSE (Normalized Mean Square Error) after applying these weights. Additionally, the script contains a cross-validation routine to shuffle the data points used for training or testing, in order to make the methodology more consistent [1, 5]. Several weights matrices are calculated each time therefore. I introduced a modification such that the least NMSE weights were chosen, so as to have the best ones.

Afterwards, we also took advantage of this modification in the code for studying the relation between the precision achieved and the number of nodes in *training_vs_number_nodes.py*. This program repeats the process of shuffling and calculating the weights so that an statistical study of the mean NMSE as a function of the number of nodes can be done. It also provides a better result for the weights leading to a lower NMSE value.

Real time prediction

This second step is not actually part of our main experimental objectives, so we will not present results about it, but it is really useful for both understanding how the FPGA is working in order to prepare the code for the next step, and check if the previous one has been successful. The Quartus II project is *weight_multiplication* in *Weight_multiplication* folder. In the same way as before, mask multiplied data points are sent every $50ns$ through the DAC-B. When a sent value is received through ADC-B, this is multiplied with the corresponding weight and added to a variable called *sum*, with the offset previously added. When all 489 (500 – 11 final nodes set to 0) node states of a \sin^2 point have been read, multiplied and added to *sum*, this variable will have the same value (or at least should be similar to) as the following point of the time series (according to how we have trained the weights).

After each cycle, the variable is reinitialized so that it can be done again with the following data point. When green LEDs 6 and 7, and red LEDs 0 and 1 are on, the program has finished. Using *SignalTap* it is possible to record the values of *sum* before being set to 0, which should match the input data. Plotting them with the real time series provides a simple and fast way to check if the code is doing what it is supposed to and if the weights were properly calculated. This procedure also allows to visualize the calculated weights accuracy.

It is important to notice that these calculations are done on-the-run, meaning that no extra time is required to perform the multiplication or the sum. At every clock the next node state is received, multiplied and added, so when the last value comes in the variable *sum* has the value of the next predicted time series point.

Autonomous generation

The third one is the our actual experimental target, the autonomous generation of the time series by the FPGA. As before, the Quartus II project is *weight_multiplication* in *HAL_9000* folder. In this part the operation of the FPGA is equal to the previous step, yet with one difference that leads us to divide the process into two parts: the *forced mode* and the *autonomous mode*. In *forced mode* the FPGA sends data of the original time series, as done so far. After 40 points (two periods of the \sin^2), it changes to *autonomous mode*. Now the time series point used to send the next mask multiplied data it is not the real one but the calculated using the trained weights, stored in *sum*. Consequently, there is no more need of the original data as the FPGA will generate it autonomously. The LED colour codes to check the operation of this program is the same as the previous one.

For the autonomous generation setting the last 11 nodes to 0 becomes mandatory. We have said that there is a delay of about $500ns$ (10 nodes) between outputting the signal and receiving it, introduced mainly by the ADA converter. In *autonomous mode* when the last node of a certain time series point is sent, the first one of the following point must be ready for being outputted. However, this point is calculated using all the node states once received, being the last one received $500ns$ after it was sent. In order to account for this latency gap, we kept those nodes to 0 using the mask, as Quim did in [1]. In this manner, these node states are not needed to calculate the next point of the time series, and the value is ready for being outputted on time.

The correct timing if this part together with the proper coordination of the transition from forced to autonomous mode are quite challenging and two of the most delicate steps of this experiment. That is why these points must be carried out accurately, determining the delay for each particular case. The code works with using a delay that was measured experimentally using *SignalTap*, so this empirical delay must be changed if the set-up is modified.

3 Results

In this experiment we are using a \sin^2 function as the time series we want to generate autonomously. The point of using it rather than a more complex one is to study the FPGA and ADA behaviour with this simple set-up. Originally, we did not expect the system to be able to carry out an autonomous generation, since only by connecting the ADA board to itself we are not providing the system with a recurrent connection to previous input steps. Hence there is no memory and, moreover, any kind of non-linearity that could decrease the NMSE of the prediction. Despite of it, we saw that achieving some autonomous generation is possible using only these two elements.

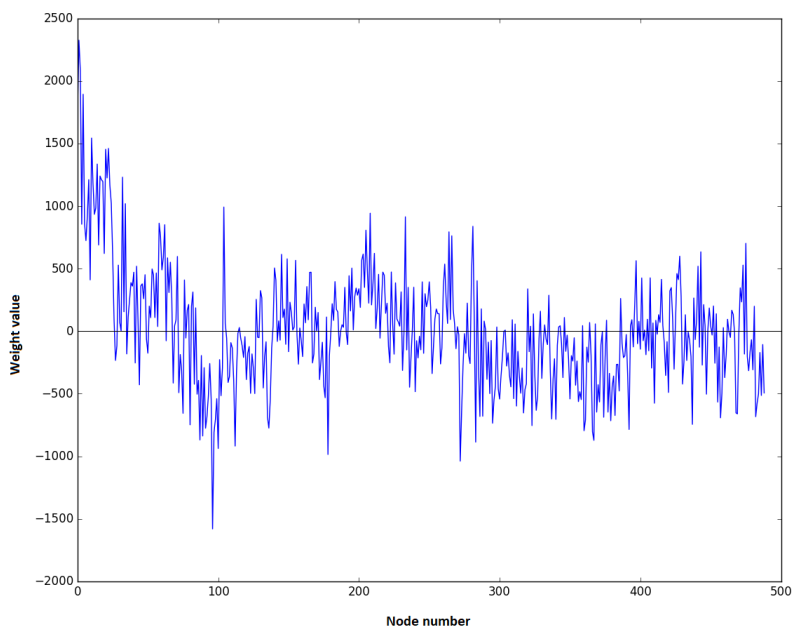


Figure 5: *Weights values corresponding to each of the 489 non-zero nodes.*

First result comes out when plotting the weights values, which can see in figure 5. This figure illustrates that the weights present some structure. This particular one shows the weights for 500 nodes, but this pattern remains independently of the number of nodes. When performing the linear regression, more relevance is given to, approximately, the first half of the nodes than to the second one. So there is more information in those initial nodes rather than in the last ones. It is interesting finding out this structure, because it is a sign of the system not processing all nodes equally, which should be the case according to the symmetry of the system.

Previous experiments were limited to use a maximum of 96 virtual nodes, which were defined by the length of the optical fibre in the optical part of the set-up and the clock of the ADA [1]. Since we notice that the prediction performance could be hindered by the use of such few number of nodes, we decided then to increase this number to 500, as there is no physical limitation to restrict the length of the input mask in our case. We could verify that the lowest instance of the prediction error in the cross-validation procedure decreased. Actually, for a larger number of nodes and the best set of output weights, when plotting the real time calculated points with the real time series, they matched considerably better. Nevertheless, we show in Figure 6 that the mean NMSE does not decrease with the number of nodes, only decreases the prediction for the best set of weights. In fact the mean NMSE is the largest for 500 nodes.

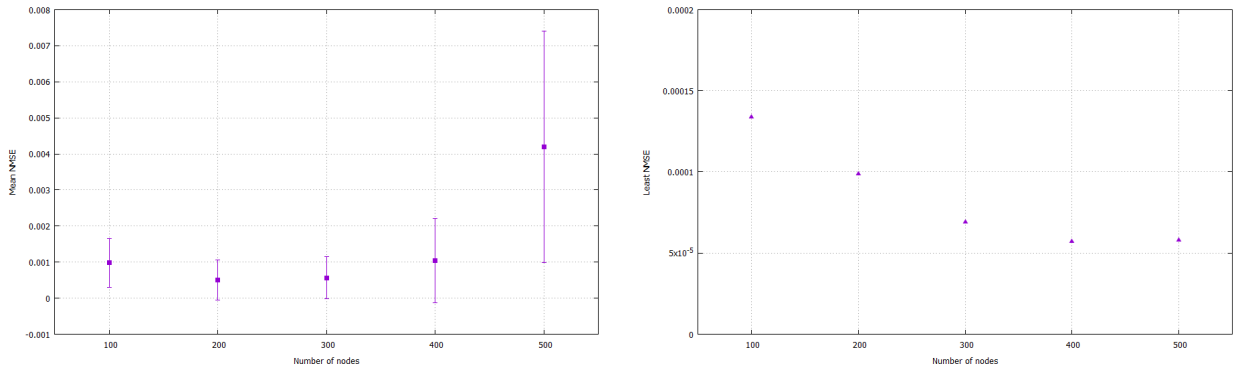


Figure 6: *On the left side, mean NMSE against the number of nodes. On the right side, the least NMSE achieved in the cross-validation process against the number of nodes.*

In contrast to the mean NMSE, the least NMSE does decrease with the number of nodes. Since we can choose to perform the testing with the best set of output weights obtained from the different instances of the cross-validation procedure, we continue working with 500 nodes for the autonomous operation. About these results, two things can be pointed out. First, we could expect that the more nodes we use the better the prediction will be, which is what the right handed graph in figure 6 is showing. That means increasing the nodes can actually result in a smaller error for some realizations. What is happening for the mean NMSE is that the linear regression performed by the program is solving a linear system of equations minimizing the NMSE. Increasing the variables⁶ of course gives better chances of approximating the target data, but it is also a source of error as we are making the numerical problem bigger and more complex. Hence the solutions given by the regression will be more scattered when the number of nodes gets higher, as the standard deviation indicates. Other regression methods may alleviate this problem.

In addition, notice that while the minimum NMSE reduces, we can not expect it to be reducing continuously with the number of nodes. It can be observed in figure 6 that from 300 nodes forward the values only change slightly. That means there is a precision limit which we can not overcome. Taking into account that it is supposed to be a linear system, and that the electronic circuit itself will always introduce some noise, it is reasonable to assume that such an error minimum exists. We could use more nodes, yet we will not be able to reduce it. A more involved experimental configuration would be necessary in order to do so. That is also a reason for not having more than 500 nodes in this report.

It is interesting to point out that this discussion can be included in a more general problem

⁶Keeping in mind that more variables will need more conditions for the method to converge, that is more training data.

involving RC or ELM, which is finding out the optimal number of nodes for an specific system. This is not a solved issue, and I will not discuss about it, but it gives a glance of how wide this problem can be.

Coming back to the experiment itself, we have mentioned that the system is supposed to be linear, as it only involves the FPGA and the ADA. However when the second stage, real time prediction, was carried out, we found out that it was able to predict the next point. According to requirements of an operative reservoir mentioned in the first section, this should not be able to happen since we are not having a non-linear transformation or memory. For understanding these results better, consider two points of the same \sin^2 period, both with same value but different history, as marked by the horizontal line in figure 7. As they have the same value, if just a linear transformation were involved the prediction would not distinguish when the function is growing or decreasing, i.e. the next point is higher or lower. Training would only reflect that half time is one case and half time is the other, and in fact we would fail systematically in the prediction for this kind of points.

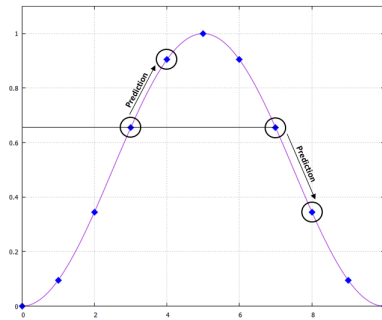


Figure 7: *Example of next \sin^2 point prediction.*

This made us suspect the ADA was not entirely linear and/or that we had some sort of implicit memory. We decided to plot the received data against the sent one. Choosing some nodes randomly, we have depicted their read states along the time-series points in function of their input original value. The result can be seen in figure 8. The enlargements show in detail how the points are scattered and they separate from linearity, represented by the dashed line. For instance, the green dots are a good representation of the observed phenomena. For each input value two groups can be seen, above and below the line, distinguishing the two types of points of the sinusoidal discussed above. This shows that there is a non-linearity in the ADA and/or that we had some sort of implicit memory.

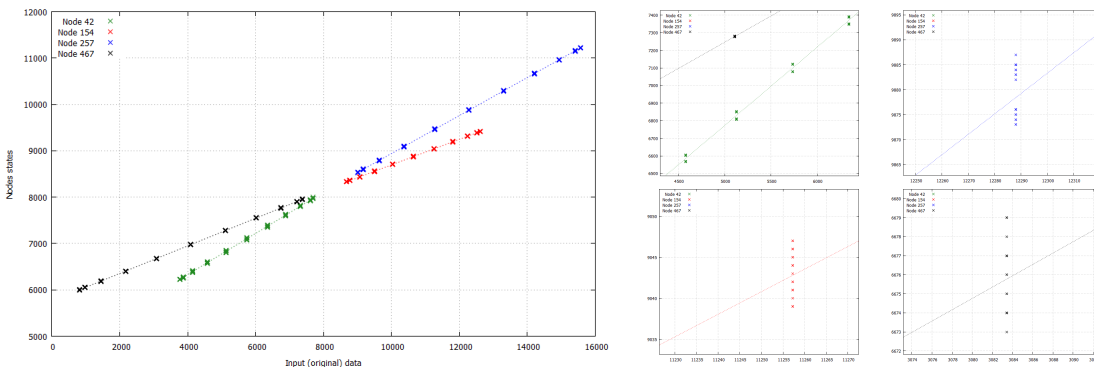


Figure 8: *Read nodes states vs. input data (\sin^2 points times the mask). For each instance of the data there are 200 points. The enlargements show the detail of some points in a closer range.*

The small fluctuations introduced by the ADA when converting from digital to analog an vice-versa are introducing some error in the prediction calculus, but it is at the same time the reason why we can predict. Those slight variations, fruit of a combination of noise and the analog transformation, carry the information the weights need to distinguish which point is coming in, and therefore which one must be the following one. If the distribution of the read nodes states were

100% random, there would be no way to know where inside the periodic signal the point is located in. This tiny deviation from linearity of the ADA converter is reflected into those fluctuations, being enough for training the weights, and therefore for calculating the next point.

The hypothesis of this non-linearity origin, moreover of ADA's own non-linearity associated to its not-perfect electronic components, is more related with a kind of fading memory, which remember is the other important condition for RC. We were able to appreciate in the oscilloscope that the signal was not going to 0 immediately when the outputted values did for the last 11 nodes, but it took some time the signal to decrease. That means the response time of the ADA could be greater than the nodes length (50ns); therefore the state of a node might be influenced by previous nodes' states, which is a memory indeed. Furthermore, we have to bear in mind that the ADC does not read strictly a DC constant voltage value, it detects signal in a sense of voltage variation. So in the measure the previous node state is somehow involved, another reason for having this fading memory. All this could explain why we observe the deviation from linearity in a supposedly linear system.

Finally, an autonomous generation of the signal was tested and characterized. The output weights used had a NMSE of $5.797 \cdot 10^{-05}$ in the testing part of the training Python program. It is the best error obtained in training stage. As it is presented in figure 9, an autonomous generation of the signal could be achieved. From the point 40 where the system changes to autonomous mode, two complete periods are successfully predicted with low error. From then on the predicted signal amplitude decreases progressively, keeping the same frequency and sinusoidal behaviour throughout the process. It is not till the last 200 points that the phase of the autonomous signal changes and signals start to desynchronise.

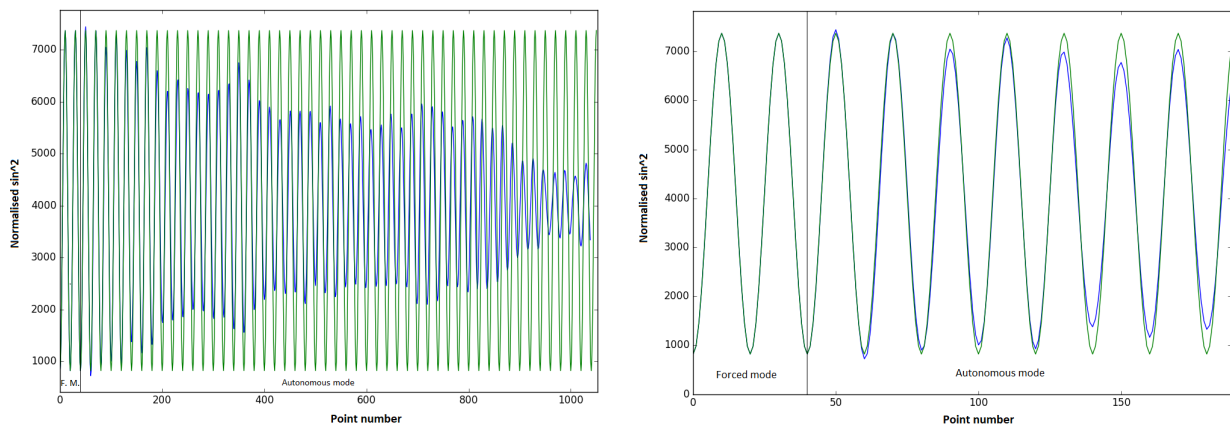


Figure 9: *Autonomous generation of a \sin^2 signal, and an enlargement of the first 200 points. In green the original signal, in blue the generated one. The black line delimits where the transition from forced mode to autonomous mode takes place.*

4 Discussion and Outlook

The system used to run the experiment has proven to be able of dealing with an autonomous generation. There are, however, some aspects of the FPGA and the ADA that can make working with them trickier than it seems. Some of their corresponding strengths and weaknesses are listed below, with particular emphasis on those which in my opinion are important for future development of this experiment.

Advantages:

A key factor here is the digital-analog conversion, that connects with the analog part of the experiment. The ADA board attached to the FPGA gives us good control on sending and receiving data from the analog system, which has to go through this conversion. In our case, the “analog system” is just a wire, but focusing on RC using optoelectronic systems with delay, knowing how this conversion is done is crucial. Also the FPGA has a fast processing due to its design for doing processes in parallel. This is quite useful as you can program it for conducting different computations at the

same time. The most important feature though is its clock; the internal clock reaches frequencies of MHz, executing the given code at every cycle. By looking at the different variables in *SignalTap* we can control pretty well the timing of the experiment, what sends, receives and calculates step by step.

Disadvantages:

Even if we have such a control of timing, that does not mean it is easy to program. Quartus II uses *Verilog* as a programming language, which is not a commonly known one. Learning how it works is not as fast as someone would like, specially not having a background in similar languages (like C or others HDLs). It also takes its time to get familiarised with the FPGA. The ADA turns things trickier on top of that⁷, as it has a 14-bits resolution, added to the two's complement binary used by the FPGA, forces you to pay real attention to how the data is being handled. Last but not least, the FPGA has a finite internal memory, which is a strong limitation in the data amount you can manage at once. For example, I had to divide into 20 files the data for training, repeating the same process for each file. It affects *SignalTap* too, so it is definitely an issue to bear in mind when programming the FPGA.

Turning the attention back to the future development, I believe that some improvements and extensions can be done since I am positive that better results are achievable. The main objective of the whole complete project is connecting and running the optoelectronic system with delay for testing the RC. Before taking this step though, some halfway experiments could be run in order to advance keeping a systematic study.

Something we tried to test was introducing explicit memory to the system. That is giving a multiple input: instead of calculating the next point using the nodes states of the previous point, train it for doing so with the last two or tree last points (mask-multiplied) of the time series. That should bring more information when training the weights so as to have a lower prediction error. However, the training did not get better results than only using one point, so we focused on other parts as few days remained. I had no time for revising and finishing the code for this test, so perhaps it can still work if someone picks it up again.

The other point that might be interesting to study is adding to the FPGA+ADA system a proper non-linearity that we can control. If possible, it could be a useful intermediate step connecting the ADA to a non-linear node (like the Mach-Zehnder-Modulator[1] but without the delay loop), just to carry out the non-linear transformation of the data. This should reduce significantly the prediction error, as it makes the nodes more distinguishable for the training. Furthermore, this may help characterising the intermediate optoelectronic elements without the added difficulties of a system with delay, which is in my opinion a necessary step.

Before concluding this report, I would like to set out a couple of questions regarding the first phase of this experiment, the training, for which I was not able to give conclusive answers. First one has already been discussed, it is why fitting the weights works numerically worse with high number of nodes when clearly the minimum NMSE instance of the cross-validation procedure gets smaller. It is remarkable too that results vary with the number of files used, that means with amount of data for training. Obviously the method needs a minimum amount of examples to find a solution, yet I checked that providing it with too many also has a negative impact (in fact, from 20 files I used about half of them in training). While the training stage works correctly, paying attention to these numerical issues may improve the results.

Secondly, we have explained that the received data by the ADA is read by *SignalTap*, then used for training. It reads the values as binary numbers, and the training will only work if those values are converted from normal binary, not two's complement. This shocked me because the FPGA performs all calculations and sends signed binary in two's complement, while it seems that it is reading the incoming signal as just unsigned binary. Even if the current procedure works, I did not fully understand how the FPGA is processing the ADA's income, which depending on future applications may be interesting to find out.

⁷While is not so relevant for our case of study, it is worth to mention that the ADA also imposes a high-pass frequency filter[4], which might be relevant in future applications.

5 Conclusions

We have demonstrated that it is possible to get autonomous generation of a signal using only a FPGA and an ADA, showing the power of machine learning methods with random projections like RC and ELM, that can work efficiently even in their simplest form. This definitely paves the way for a future expansion to RC using the optoelectronic system with delay. If the set-up is extended progressively with systematic testing, the new approach that does not make use of the AWG can solve the problems that came up in previous versions. The Quartus II projects should be ready for working in these new experiments, with few adjustments but preserving their structure.

In my opinion the most challenging part of this work is dealing with the *Verilog* programming of the FPGA, as well as getting used to previous people's work and code. In this way and following Quim's premise[1], I have tried to leave everything as organized and commented as possible, so that next students spend the least possible time in organization. I hope this work may help to whoever comes next to continue and luckily finish this project.

Acknowledgments

The author would like to thank Miguel C. Soriano and Ingo Fischer for their support and full confidence. Also, the author would like to give thanks to Pau Massuti-Ballester, for being available for helpful discussions and advice about how to deal with Quartus II and *SignalTap*. This work was supported by the SURF@IFISC fellowship.

References

- [1] Quim Llorens, Miguel C. Soriano, Ingo Fischer, Apostolos Argyris, *Optoelectronic Reservoir Computing: closing the loop for an autonomous signal generator*, SURF@IFISC fellowship report, IFISC (2017).
- [2] S. Ortín, M. C. Soriano, L. Pesquera, D. Brunner, D. San-Martín, I. Fischer, C. R. Mirasso & J. M. Gutiérrez, *A Unified Framework for Reservoir Computing and Extreme Learning Machines based on a Single Time-delayed Neuron*, Sci. Rep. 5, 14945; doi: 10.1038 / srep14945 (2015).
- [3] L. Appeltant, M.C. Soriano, G. Van der Sande, J. Danckaert, S. Massar, J. Dambre, B. Schrauwen, C.R. Mirasso & I. Fischer, *Information processing using a single dynamical node as complex system*, Nat. Commun. 2:468 doi: 10.1038 / ncomms1476 (2011).
- [4] M. Häussler and I. Fischer, *Realisation of an analog real-time predicting system using a reservoir computer and an FPGA*, Erasmus+ Internship Report, IFISC (2017).
- [5] J. Striebel and I. Fischer, *Emulating Chaotic Systems with an Optoelectronic Reservoir Computer*, Erasmus+ Internship Report, IFISC (2017).

Modeling and dynamics of the power grid

David PÉREZ GONZÁLEZ, Dr. Damià GOMILA VILLALONGA, Dr. Pere COLET
 Instituto de Física Interdisciplinar y Sistemas Complejos IFISC (CSIC-UIB)
 Campus Universitat de les Illes Balears, E-07122 Palma de Mallorca, Spain

Abstract

The power grid is a socio-technical system where users and machines interact on a network supervised by the system operator. Traditionally, the control is applied at the supply side, such that power plants adapt continuously their power to deliver all the energy demanded by the users. This model is however very expensive, as it requires fast response idle power plants to ensure the supply at demand peaks consuming very expensive fuels. The increase of the demand and the integration of renewable energy sources are also increasing the fluctuations of the system due to fast demand-supply unbalances, challenging the traditional system operation. Control systems applied to the demand side, such that users adapt their energy consumption to energy availability, have been proposed. In this project, we will explore the dynamics of the power grid under demand side control methods introducing a daily variation. We find that a fluctuation in the switching on probability rate affects the number of pending tasks. We also conclude that a proportional variation in the ϵ_1 value is not a good solution for decreasing the number of pending tasks.

1 Introduction

Power grid frequency control is a very important and expensive issue nowadays due to the increase of electric demand and the renewable sources dependence. This controlling can cause expenses to the power plants. For that reason, several approaches have been attempted in order to reduce the fluctuations in the frequency in a way that the power grid does not need to have too extra energy in case a peak of demanding is generated. Several approaches have been attempted, such as sending a real time price signal from your consumption to figure out if you may switch on or off some devices depending on the frequency. On one hand, if the frequency decreases, the price rises, inducing customers to switch off them. On the other hand, if the frequency rises, the price decreases. Our method, that is explained in this report, is taking into account directly the frequency instead of the price. [1, 2]

In the following, we are describing how to model a power grid and then, how to implement a controlling system in the demand side in such a way that certain appliances modify their operation to adapt to the power availability studying, for instance, its effect on the frequency. This method is called dynamic demand control (DDC), where smart devices are able to delay when they are switching on or off depending on the frequency of the system. The power plant equations and one stochastic model for the demand are introduced in this model. [1, 2]

Nevertheless, one of the problem that can arise from this method is the synchronisation of all the appliances to switch on (off) once the frequency is above (below) a threshold we have introduced. This condition can lead to a peak in the demand provoking an oscillatory instability in the frequency. To address this issue, randomisation of the switching rate of each smart appliance is also included. [1]

All these effects can be studied with the model studied here. Nevertheless, this work has been done by Eder Batista et al in [1]. There, the probability of switching on or off of an appliance is the same ($p = q$, with p the switching on rate and q the switching off rate). Thus, fluctuations along the day cannot be studied. Our work is implementing a generic algorithm of DDC in Python to study if the constraints need to be adapted to the daily demand variations or not.

First of all, we must check our model to figure out if the program itself is running well or not. For that, we are comparing some examples with the same parameters as the ones done by Eder Batista et al in [1] to see if the results obtained are the same. It turns out that our algorithm is able to reproduce them with a quite similar equivalence.

This report is organised as follows. In Sect. 2, we describe the standard power plant model, the stochastic model for demand and the model for dynamic demand control. In Sect. 3, we show

the results obtained in the comparison with the examples already studied ([1]) to figure out the validity of our algorithm and we also introduce the effects of the variance of p and q on frequency fluctuations taking into account the daily demand variations. Finally, in Sect 4, we indicate the implications of our results and some possible extensions of this method.

2 Theoretical model

This model is formed by a generator and a governor, where the generator is producing the electricity from some energy resource such as solar panels, fuel or gas, and the governor is the specific control method for adapting the energy generation depending on the demand.

By applying the Newton law on the turbine, the well-known swing equation describing the dynamics of the generator can be derived [1]:

$$\frac{d\omega}{dt} = \frac{\omega}{2HP_G}(P_m - P_e) \quad (1)$$

where P_G and H are the nominal capacity and the inertia constant of the generator, P_m is the mechanical power generated by the turbine (or other means), and P_e is the total power of the electric current that the demand needs.

The total electric load P_e can be divided into two parts: a non frequency-sensitive load and frequency-sensitive load, such that:

$$P_e(\omega, t) = (1 + D \frac{\omega - \omega_R}{\omega_R}) \quad (2)$$

where ω_R is the grid reference frequency, D is proportional to the fraction of the load which is frequency sensitive and $P(t)$ is the load at $\omega = \omega_R$.

With both equations (1) and (2), we can observe that since the electrical power increases because of the demand and, in consequence, is larger than the mechanical power, the frequency of the system comes down. Conversely, if the governor is telling the generator to produce more mechanical power than system demands, the frequency rises. That is why the governor must restore the frequency to its reference value (ω_R), and it does so in two steps. First, it tends to stop the fluctuation in the frequency by increasing (or decreasing) the mechanical power. This process takes around ten seconds. After that, a second step is taken. Extra energy to the generation from a spinning reserve is incorporated in order to reestablish the frequency to its reference value ω_R . These primary and secondary regulations are taken into account with the following differential equations:

$$\frac{dP_m}{dt} = \frac{1}{\tau_g} [P_s - P_m - \frac{P_G}{R\omega_R}(\omega - \omega_R)] \quad (3)$$

$$\frac{dP_s}{dt} = -\frac{K}{\omega_R}(\omega - \omega_R) \quad (4)$$

where R is the governor speed regulation, P_s is the spinning reserve power used at a given time, K is the gain of the secondary controller and τ_G is the time constant of the turbine.

Once our model for the power plant is explained, now we can introduce the stochastic demand model to reproduce the main statistical properties of real demand fluctuations. For that, we consider N appliances where each of them can be either in the on state (with a rated power P_0) or in the off state with no consumption. We assume that a device running would switch off with probability rate q . This probability rate is such that qdt is the probability itself that the on state appliance is turned off in the time interval dt . Conversely, a device in the off state would switch on with probability rate p . For the sake of simplicity, $p = q$ is taken, but in our work these two rates are modified in different ways to consider daily demand patterns and to be able to obtain new data about the optimal values of the constraints we present in the next pages. Thus, the time dependent load of appliances i , is given by:

$$P_i(t) = \begin{cases} P_0, & \text{on state at time } t \\ 0, & \text{off state at time } t \end{cases} \quad (5)$$

The total load of the system is given by the addition of the load of the N devices:

$$P(t) = \sum_{i=1}^N P_i(t) \quad (6)$$

This stochastic model comes from a Markov process[3] for a system composed of N particles each one making transitions between two states (on, off) with rates p and q . When there are not interactions between the appliances and both probabilities rates are the same, then, we can confirm the average power demand is $\langle P \rangle = NP_0/2$. Once the stationary regime is reached, the fluctuations are proportional to \sqrt{N} . The variance at all times is:

$$\sigma_P^2(t) = NP_0^2[\mu(t) - \mu^2(t)] \quad (7)$$

where the probability $\mu(t)$ of finding a device on is given by:

$$\mu(t) = \frac{1}{2}(1 - e^{-2pt}) + \mu(0)e^{-2pt} \quad (8)$$

Once this model is implemented in Python and we have checked the well-working with the parameters used by [1], we need to implement the Dynamic Demand Control (DDC).

With this controlling system, we are delaying the device switching on or off depending on where the frequency is. If a device is supposed to be switched on randomly, first the frequency is checked. Thus, now we are working with smart devices. When the frequency is within a suitable range, then, the appliance turns on. Nevertheless, if the frequency is below a threshold ($\omega < \omega_R - \epsilon$), this action is prevented. Conversely, a smart device in the on state that randomly would switch off effectively do so only if the frequency is not above a threshold ($\omega > \omega_R + \epsilon$).

Otherwise, all these actions prevented are taken into account as pending task in order to be recovered later in periods of favorable frequency conditions. We define the pending tasks Q_j of smart device i as the absolute value of the energy that this device has consumed in excess or in shortage with respect to the reference case of no applying any DDC. Total pending tasks on the whole grid are given by:

$$Q = \sum_j Q_j \quad (9)$$

Those energy-consuming pending tasks can only be recovered if the frequency is above a second threshold ($\omega > \omega_R + \epsilon_1$), while energy-saving pending tasks can only be recovered when the frequency is below another threshold ($\omega < \omega_R - \epsilon_1$). Smart devices with pending tasks monitor the frequency continuously for that, but actually they do so with probability γ in order to avoid simultaneous switching-on (off) of several appliances.

To prove how good the control is, we can calculate the complementary cumulative distribution $R(\Delta\omega)$, which corresponds to the probability of having a frequency fluctuation with absolute value larger than $\Delta\omega$. We get a set of value $\Delta\omega_k$ at discrete times $t_k, k = 1, \dots, M$ from numerical simulations. Then, this set is reordered from the smallest to the largest value $\Delta\omega_i$, so that i is the rank of $\Delta\omega_i, i = 1, \dots, M$. The mathematical expression is presented as:

$$R(\Delta\omega_i) = 1 - \frac{i-1}{M-1} \quad (10)$$

3 Results and discussion

Throughout our work, we are taking the same values in the differential equations presented in the Sect. 2 ((1), (3) and (4)) for the constants. These values are the ones used in [1], that is, $P_G = 37320 \text{ MW}$ and $H = 4 \text{ s}$, $\omega_R = 50 \text{ Hz}$ and $D = 0.026$, $K = 6600 \text{ MW/s}$ and $\tau_G = 0.78 \text{ s}$. For the stochastic model, we are taking $p = 6.55 \cdot 10^{-4} \text{ s}^{-1}$ first to check its validity. After that, we are changing its value periodically to check how the fluctuations are affected.

For the number of devices, we are selecting $N = 1000$. With that, the proper values obtained by [1] to achieve efficient DDC operation are $\epsilon = 0.05$, $\epsilon_1 = 0.06$ and $\gamma = 1, 2 \cdot 10^{-3}$.

First of all, we are calculating the response of the system after a sudden load increase that takes place at time $t = 1$ minute, as we can see in the figure 1. Once we introduce this change in the system, the frequency decreases suddenly. Then, the primary regulation is activated and within ten seconds approximately, the frequency stops decreasing. After that, it is stabilised at a value below ω_R ($\omega = 49.937 \text{ Hz}$). Once this is happening, the secondary regulation starts to work recovering the frequency to its reference value $\omega = 50 \text{ Hz}$ within about 12 minutes, which corresponds to the response found in [1].

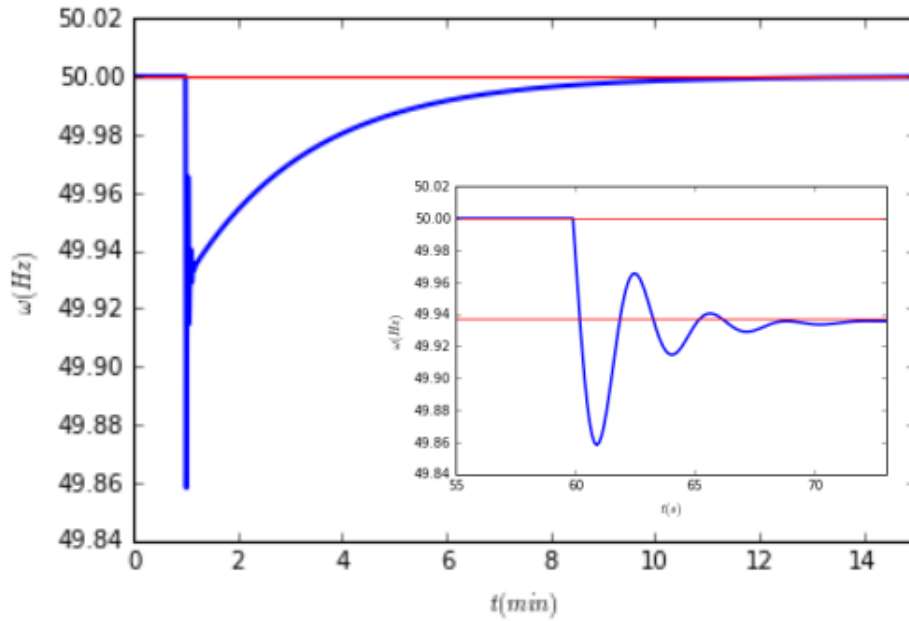


Figure 1: Frequency Response after a sudden increase of the demand.

Once we have checked that our model for the power plant is working well, we need to figure out if the stochastic model implemented in Python is doing so as well. For that, we focus on the fluctuations in the total load.

Nevertheless, we need to take care of the time scale. On one hand, if we go to short time scales, the picture obtained is essentially a random walk with the exception that the number of appliances is finite, so, in consequence, the random walk is bounded and fluctuations can not grow indefinitely. This can be observed in the Fig. 2. On the other hand, at large time scales, the fluctuations look more like white Gaussian noise, as we can see in the Fig. 3.

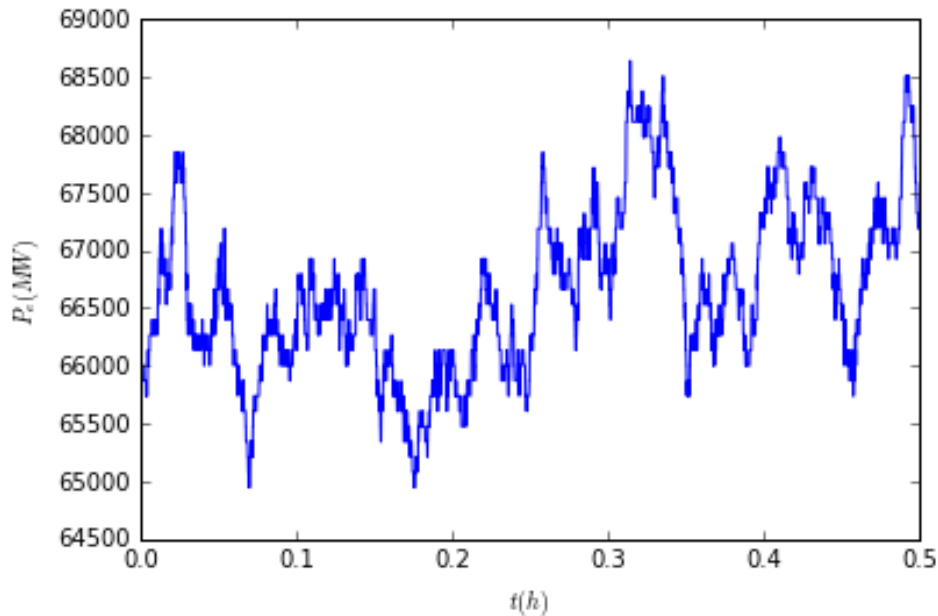


Figure 2: Demand fluctuations at short time scales for $N = 1000$ devices of power $P = 132\text{MW}$. The switching probability is $p = 6,55 \cdot 10^{-4}\text{s}^{-1}$

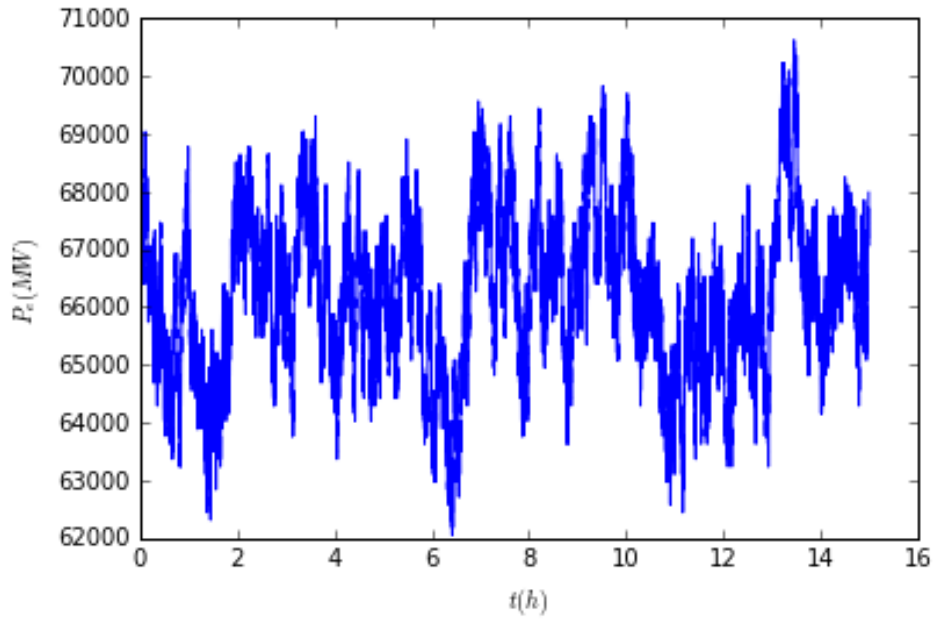


Figure 3: *Demand fluctuations at large time scales for $N = 1000$ devices of power $P = 132\text{MW}$. The switching probability is $p = 6,55 \cdot 10^{-4}\text{s}^{-1}$*

Now we are testing the well-working mode of our DDC implemented in Python.

For that, we are taking a large trajectory in the first case (120 hours). In the Fig. 4, we are showing the well performance of our DDC model. Our model is keeping the fluctuations of the frequency within a range chosen with the parameters ϵ and ϵ_1 . Both threshold are overtaken only in some periods. This is, actually, what we are looking for because those fluctuations give the chance to recover pending tasks.

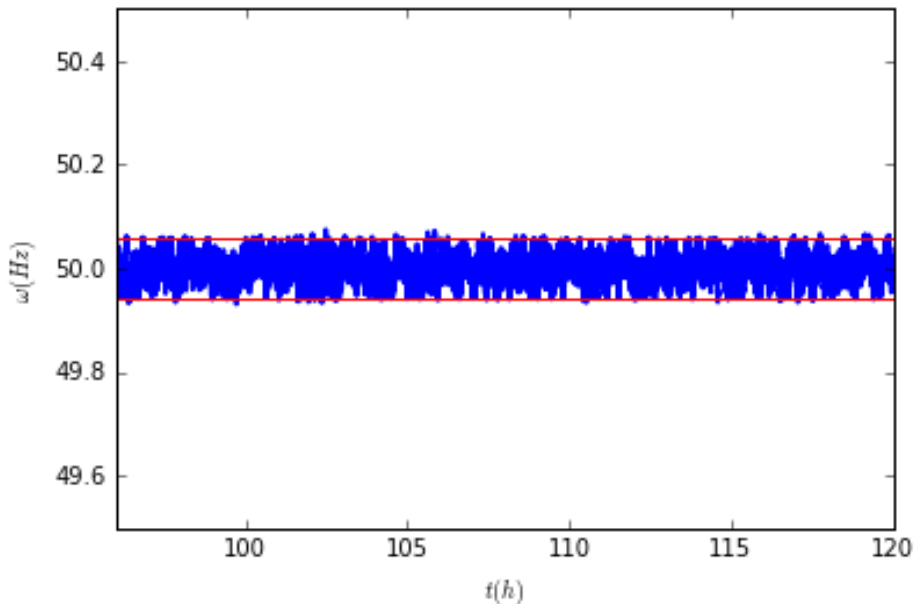


Figure 4: *Time series of the frequency for a fixed value of p .*

The pending tasks in last part of the trajectory (last 15 hours) are shown in the Fig. 5. This range was chosen to be compared with [1] because it represents a stationary state. Effectively, the pending tasks are fluctuating within a range up to 20 MWh. This result converges with the one obtained in [1].

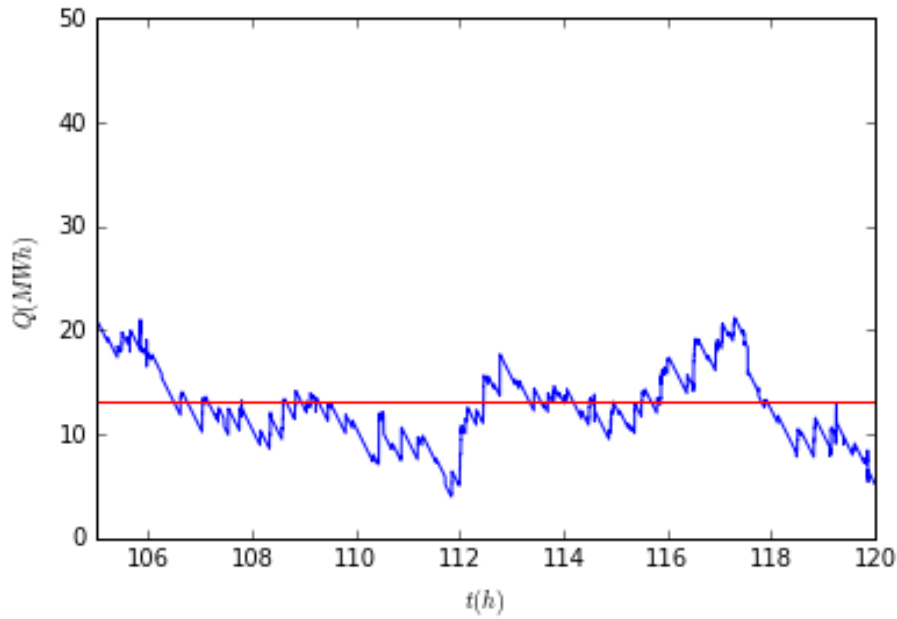


Figure 5: Time series of the pending tasks for a fixed value of p .

Furthermore, the frequency variance is also shown in the Fig. 6. In this figure, we can observe the coincidence of the increasing of pending tasks with low values of frequency variance and, conversely, how the number of pending tasks decreases when high values of frequency variance are approached.

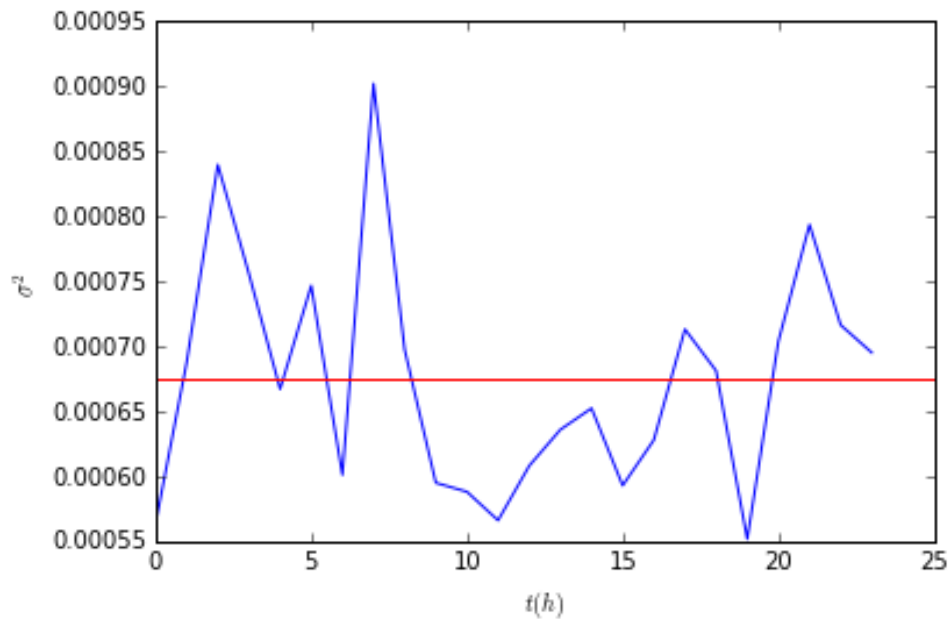


Figure 6: Time series of the frequency variance for a fixed value of p .

Since the time-consuming of this trajectory was quite high, we have considered to study our model in short scales. Thus, for this second case, we are taking a shorter trajectory (50 hours). Nevertheless, to get good enough values, we notice we need to go through the last hours of this trajectory. Specifically, the last 24 hours are studied.

As we can observe in the Fig. 7, the statistical properties are almost equal to the ones obtained before and in this case the run-time is less than before. So, more attempts can be approached.

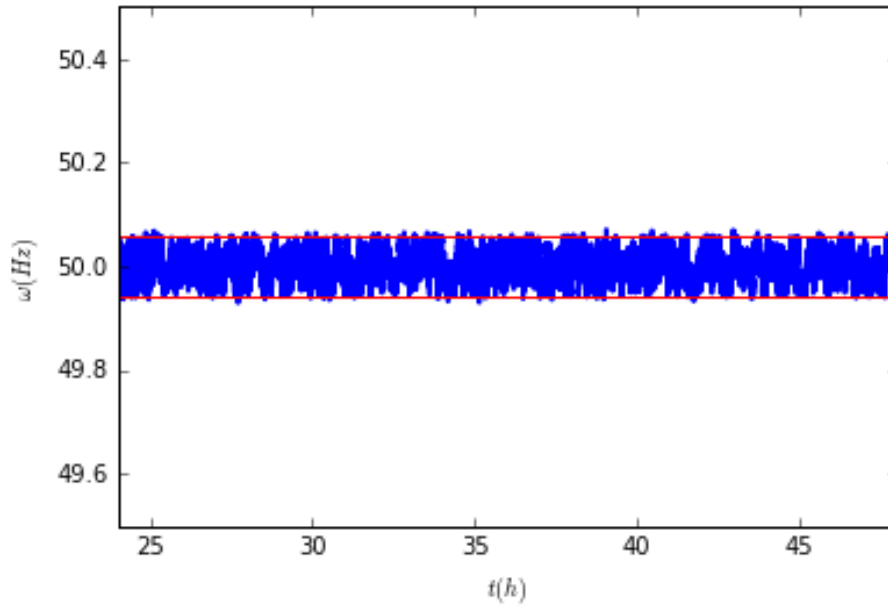


Figure 7: Time series of the frequency for a fixed value of p .

Also, as we can see in the Fig. 8, the number of pending tasks keeps within a range that can be accepted, even though, it turns out we have more fluctuations. Since we are not in a perfect stationary stage, this fact is normal.

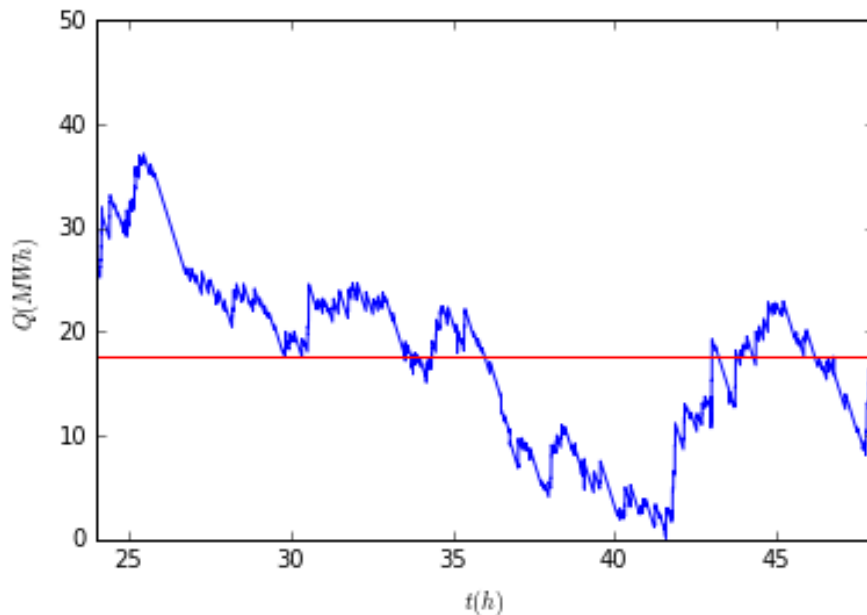


Figure 8: Time series of the pending tasks for a fixed value of p .

Again, the frequency variance is keeping a proportional behaviour with the changes in the number of pending tasks as we can see in the Fig. 9.

Furthermore, this choice is helping us afterwards to compare this result with the ones obtained when we are changing the p value.

We are taking the values of the frequency variance from three attempts and we are representing it in the Fig. 10, but, as we can check, they are not enough for representing a smooth behaviour. For instance, we have discard to try that because of the time-consuming.

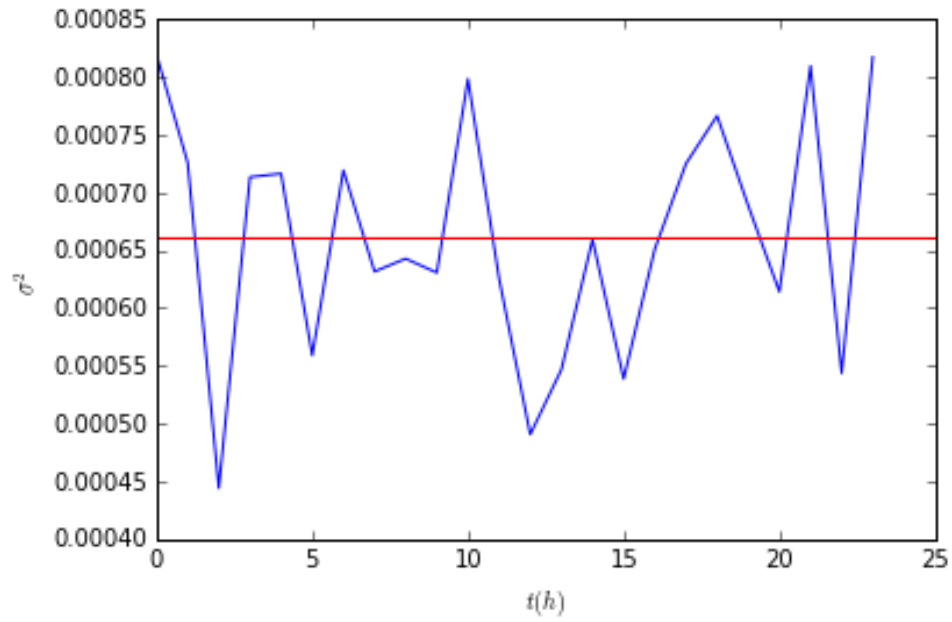


Figure 9: Time series of the frequency variance for a fixed value of p .

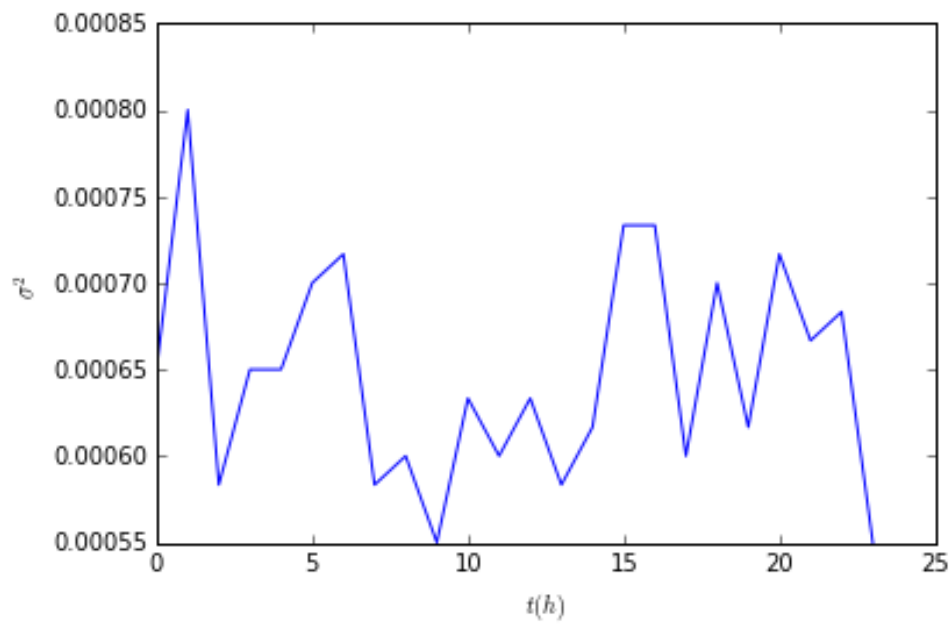


Figure 10: Time series of the average of three different frequency variance for a fixed value of p .

Now, once we have already checked our model is working well and we have the same statistical properties that the ones obtained in [1], we are allowed to include a daily pattern in the value of p .

This pattern is introduced as a cosines function to represent the daily fluctuations found in [4]. The function is restricted to have a period equal to 24 hours and a maximum fluctuation (amplitude) of the 30 per cent of its optimal value. The fluctuations in the frequency are shown in the Fig. 11.

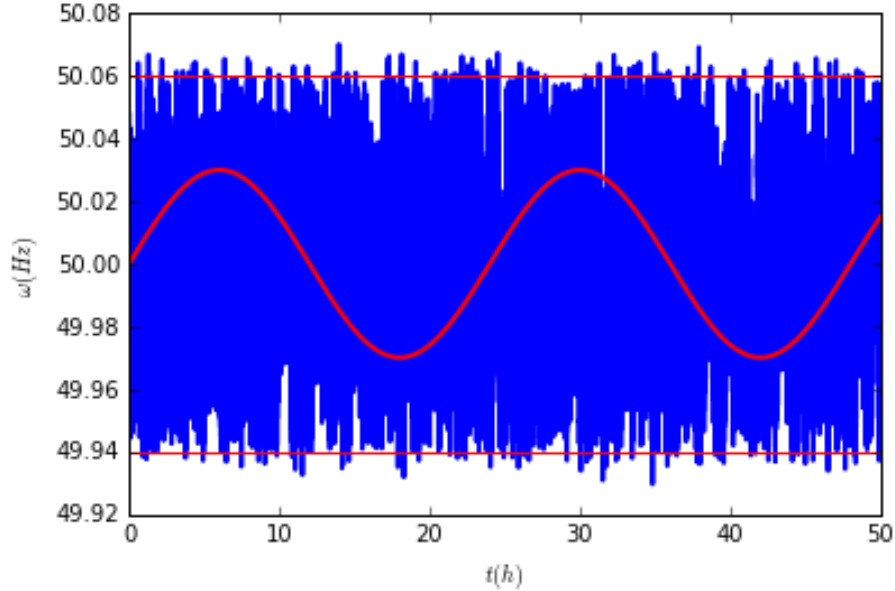


Figure 11: Time series of the frequency for a value of p following a restricted cosines function. A cosines function is represented (red thick line) to observe how the pattern affects the frequency.

We can observe that the pattern is affecting the fluctuations, but keeping a logical behaviour. Nevertheless, as we said before, our study is focus on the laste 24 hours shown in the Fig. 12.

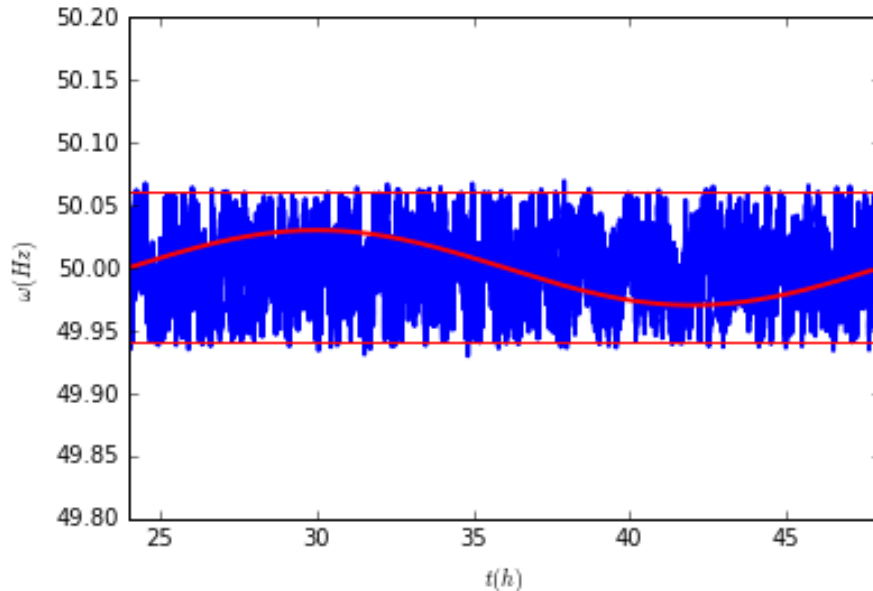


Figure 12: Time series of the frequency for a value of p following a restricted cosines function. A cosines function is represented (red thick line) to observe how the pattern affects the frequency.

We find that the pattern included in the p value is producing more peaks that cross the threshold in certain times. When the p value is stabilised, the largest peaks appear. For instance, the number of pending tasks decreases. This can be checked in the Fig. 13.

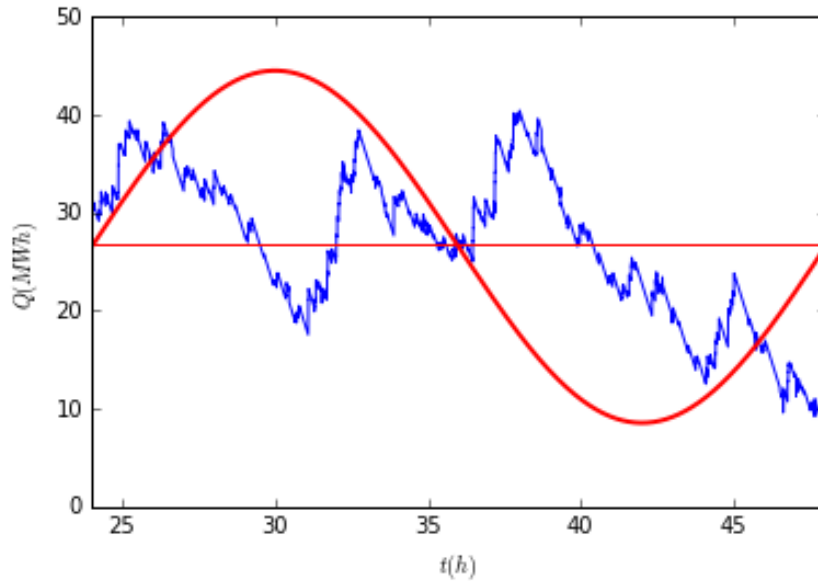


Figure 13: Time series of the pending tasks for a value of p following a restricted cosines function. A cosines function is represented (red thick line) to observe how the pattern affects the number of pending tasks.

Also, the frequency variance is behaving according to this analysis. A peak in the frequency variance produces that the pending tasks decreases because it is representing the fluctuations of the frequency in time windows of one hour. The last 24 hours of the frequency variance are represented in the Fig. 14.

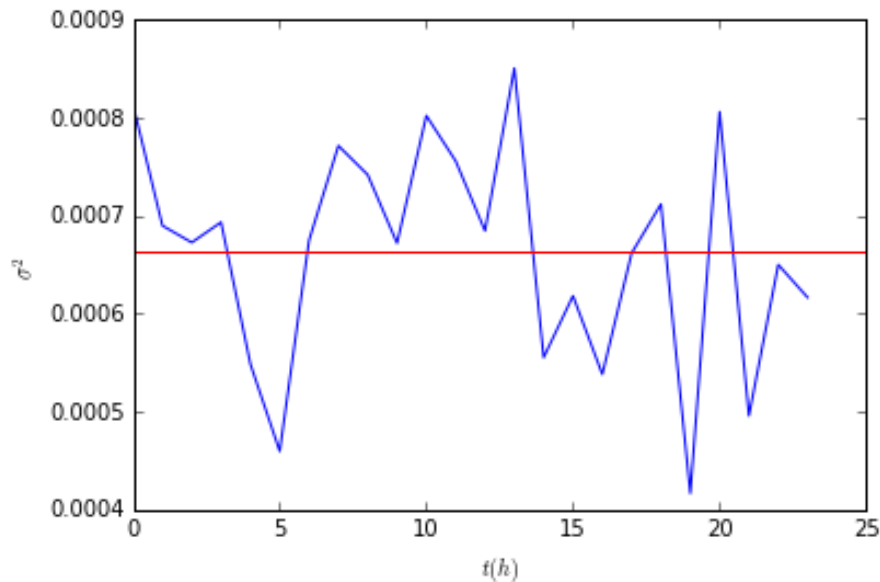


Figure 14: Time series of the frequency variance for a value of p following a restricted cosines function. The average value (red line) is plotted.

Furthermore, the number of appliances that are switched on are shown in the Fig. 15. We can see that the pattern chosen is perfectly recognised.

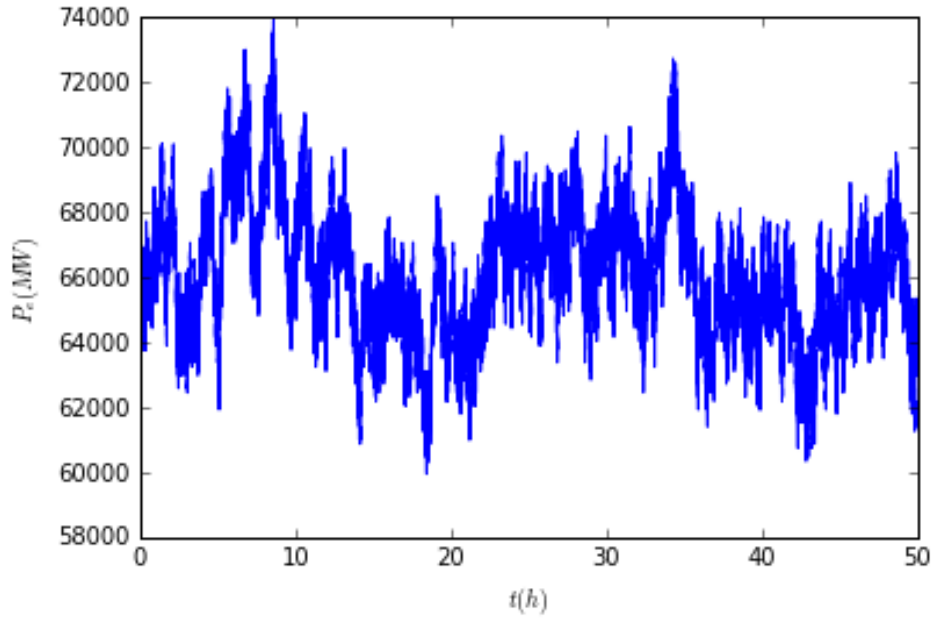


Figure 15: Time series of the number of switched on appliances for a value of p following a restricted cosines function.

The next step would be to adapt the value of the thresholds to this pattern. In our case, we have included an attempt where the ϵ_1 value is following the same pattern that the p value.

The result is shown in the Fig. 16. It can be checked that an unreal behaviour in the frequency can be introduced. This is leading us to confirm that this trial is not a realistic one.

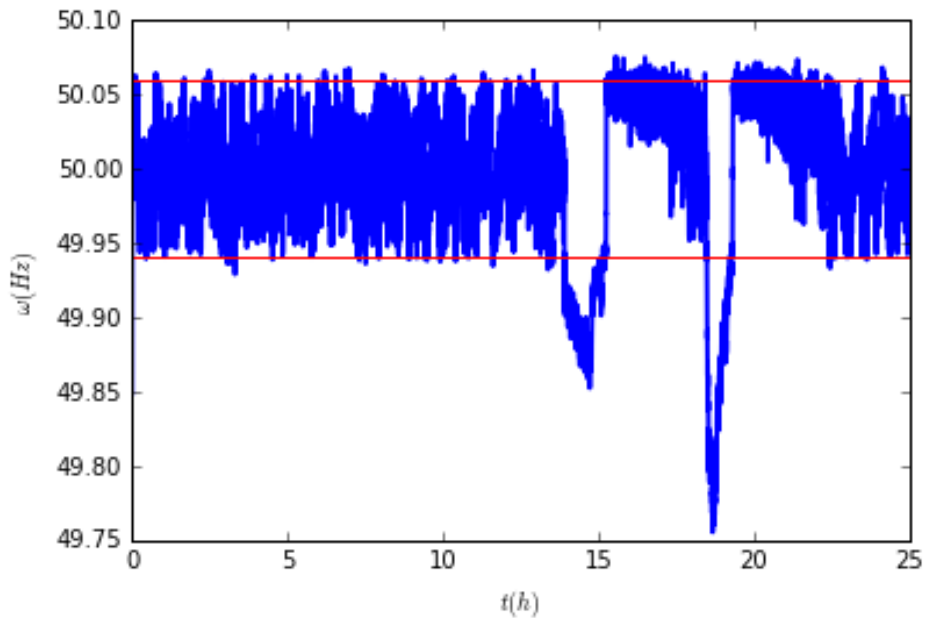


Figure 16: Time series of the frequency for a daily pattern included in the p and ϵ_1 values.

Furthermore, the number of pending tasks is also shown (in the Fig. 17 in this case to see how a chaotic behaviour in the frequency can affect to this number).

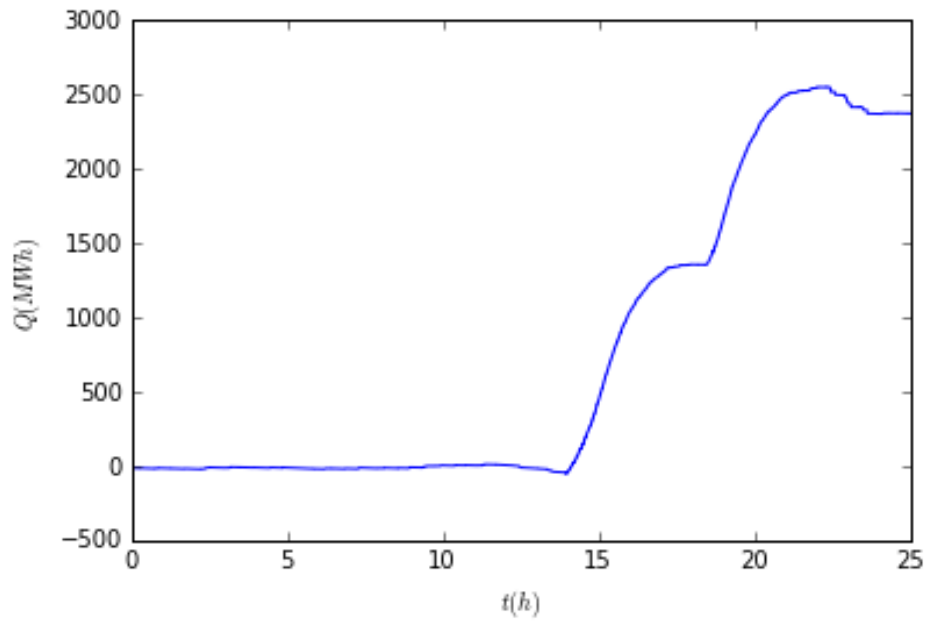


Figure 17: Time series of the pending tasks for a daily pattern included in the p and ϵ_1 values.

The frequency variance is also shown in the Fig. 18.

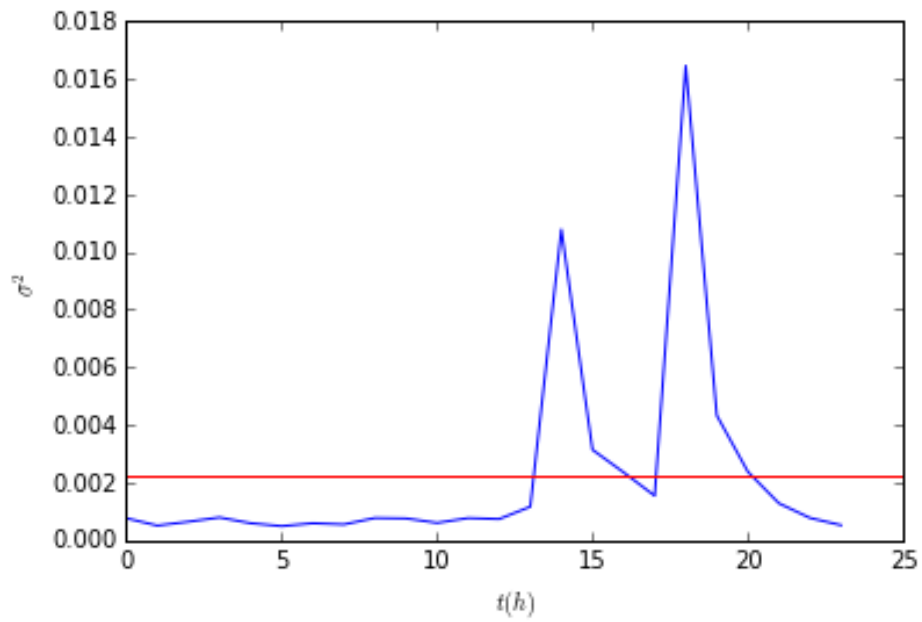


Figure 18: Time series of the frequency variance for a daily pattern included in the p and ϵ_1 values. The average value (red line) is plotted.

Finally, the number of switched on appliances is also represented in the Fig. 19.

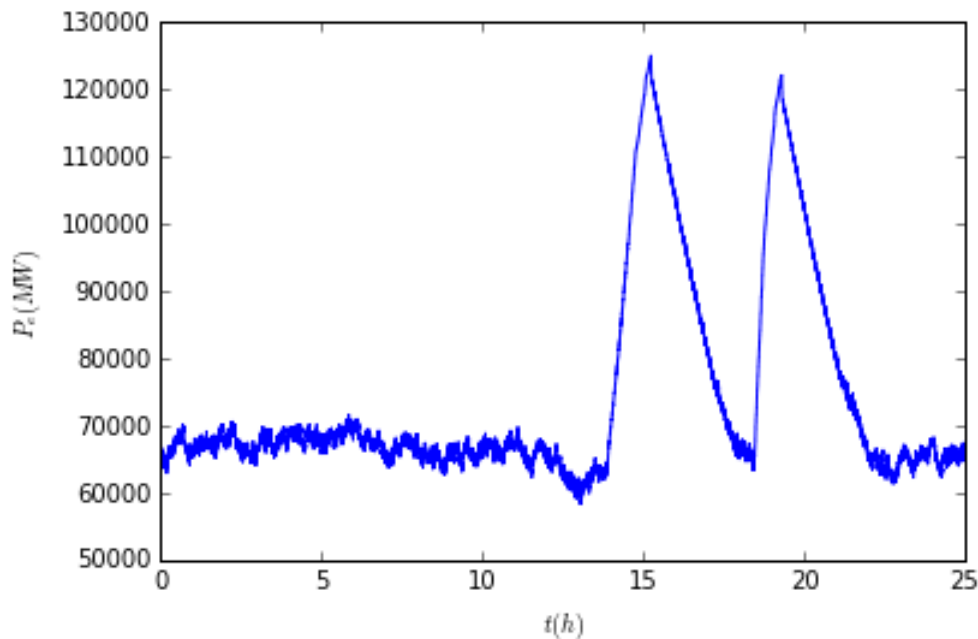


Figure 19: Time series of the number of switched on appliances for a daily pattern included in the p and ϵ_1 values.

4 Conclusions

We have implemented a simple model to study the effects of dynamic demand control on the frequency of the power grid in Python successfully. This model has proved the well performance of the differential equations for a power plant with primary and secondary regulation. Apart from that, a stochastic model for the power demand has been achieved. It has been confirmed that our model is able to reproduce the statistical properties of real measurements of the frequency fluctuations adjusting a single parameter, namely the switching probability of the devices.

We have shown that the implementation of a daily pattern in this parameter can affect the optimal results and, in consequence, the optimal constraints found by [1]. With that, we have observed the realistic response given by the model to this perturbation. Once the switching on probability of the appliances (p) increases, the power plants are not able to supply enough energy. Then, the pending tasks rise up as well. Nevertheless, these pending tasks are recovered later when the slope of the p is not that large.

For studying the new optimal values for those parameters, we tried to include the pattern perturbation in the ϵ_1 value (the threshold for recovering pending tasks). Nevertheless, the result obtained was not the expected. The frequency starts to behave in a chaotic way at some point, so it is unrealistic.

For instance, another good approach can be to modify the value of both thresholds or including some parameter to take into account the value of the frequency variance.

5 Appendix

5.1 Power Plant Equations as SDEs

With the help of [3], a study of Stochastic Differential Equations was approached. For instance, we tried to introduce the noise produced by our stochastic demand model in the equations taking into account the working mode of these theory.

A way to study this approach is to use a very simple white noise. The result is shown in the Fig. 20.

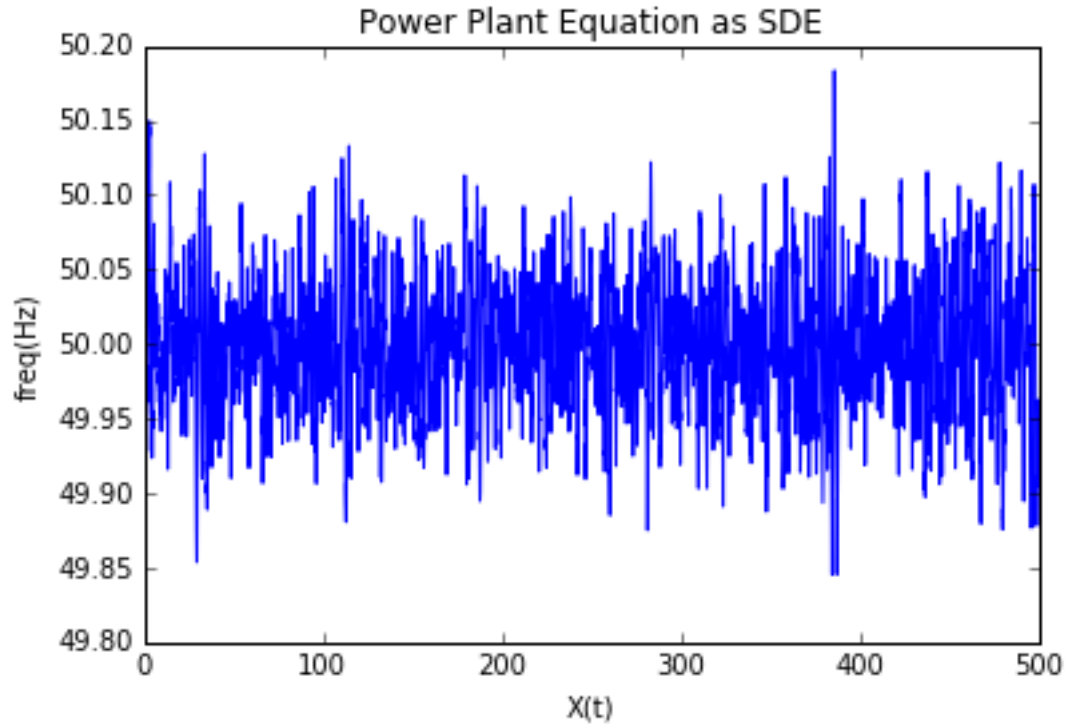


Figure 20: Time series of the frequency introducing white noise in the Power Plant Equations.

As we can observe, the pattern in the frequency is quite similar to the one achieved with our stochastic demand model. For instance, this result is leading us to think that, if it is possible to define the noise produce by our stochastic demand model, we can introduce it directly to the equations. However, this approach is beyond the scope of this work and will be considered elsewhere.

Acknowledgments

Acknowledge support and useful discussions with all the fellows from SURF and my both supervisors Damià Gomila and Pere Colet.

This work was supported by the SURF@IFISC fellowship.

References

- [1] E.B. Tchawou Tchuisseu, D. Gomila, D.Brunner and P.Colet, *Effects of dynamic-demand-control appliances on the power grid frequency* Phys. Rev. E 96, 022302 (2017).
- [2] E.B. Tchawou Tchuisseu, D. Gomila and P.Colet, *Reduction of power grid fluctuations by communication between smart devices* (2018).
- [3] R.Toral and P.Colet, *Stochastic Numerical Methods: An Introduction for Students and Scientists* (2014). DOI: 10.1002/9783527683147
- [4] <https://demanda.ree.es/visiona/peninsula/demanda/total>, 27/07/2018

Synchronization in a model of coupled neural oscillators

Javier Rivera Deán, Claudio R. Mirasso

Instituto de Física Interdisciplinar y Sistemas Complejos IFISC (CSIC-UIB)
 Campus Universitat de les Illes Balears, E-07122 Palma de Mallorca, Spain

Abstract

The emergence of synchronization in brain networks is a fundamental issue in neuroscience. For instance, when two or more neurons or neuronal populations are unidirectionally coupled, delayed synchronization is expected. In this case, the sender predicts the dynamics of the receiver. However, depending on the oscillation frequency between the nodes or the type of coupling, other types of synchronization can be observed (zero-lag, anticipated, etc.). In this work it is proposed to study the dynamics of a chain of coupled oscillators to better understand the mechanism that yield the different kind of synchronization depending on the circuit structure. The results will be contrasted against numerical simulations of a chain of coupled neurons.

1 Introduction

According to [5], it is said that two periodic pulses are synchronous when they occur at the same time or with a constant phase shift. Synchronization phenomena in neurons have very important consequences in the whole brain's workout, as locomotion processes, but also can lead to pathological types of activities as epilepsy. Therefore, in this case, we will study systems constituted up to two oscillators, employing Kuramoto model which emulates the behaviour of neurons and see, depending on the kind of coupling (excitatory or inhibitory) and how it is (class 1 or class 2), under which situations synchronization processes take place.

With this purpose, we will start by analysing the behaviour of an individual oscillator when we apply a certain pulse over it at a given time t_0 and, after that, we will introduce a sinusoidal modulation. The purpose of introducing this functions is to emulate the coupling of this oscillator to another ones without dealing with them, something that will be done in the subsequent sections.

As it was commented above, we will only study systems up to two oscillators and, as well, two different configurations will be considered: the master-slave configuration which is an unidirectionally coupling, and a two mutually coupled system, employing for so different kind of couplings.

In all those cases we will restrict ourselves to the stable solutions as we want to obtain synchronized results and, once discussed all those cases, we will modulate them by a sine function and see if there are any circumstance that permits them to be stable.

2 Theoretical model

It is known that neurons are a certain kind of cells that constitute the fundamental bricks which allows the transmission of information in most of the living beings, and this circulation is due to electric pulses that are transmitted through them. Hence, consider a certain neuron like the one depicted in appendix A. If nothing is done to it, its membrane has a certain electric potential called *stationary membrane potential* and, under this conditions, an electrical current, and therefore information, cannot pass through it, that is, this neuron is located at its stationary state. This membrane potential exists thanks to the fact that a given concentration of different ions are located inside and outside the membrane.

Under this equilibrium situation, suppose that we manage to alter that membrane potential in such a way that we depolarize the neuron's membrane. If a certain limit is reached, called *excitation threshold*, the Na^+ channels open suddenly allowing sodium getting to the interneuronal space, and changing therefore the neuron's potential. However, this situation does not hold for long, as the K^+ channels also open allowing potassium to exit the neuron, obtaining again the stationary membrane potential.

Nevertheless, this process do not take place all along the axon, that is, it only affects the local part of the neuron that has been excited and perturb its surroundings in such a way that the excitation is transmitted all along the axon, giving rise to the known as *electrical pulse*.

In general, that excitation is caused by other neurons and, as it happens in many other fields in Physics, the response of the other neurons is not just given by summing up all individual behaviours: is a collective response. Indeed, that kind of answers are also obtained in very simple systems made only by two coupled neurons, leading to synchronization phenomenons. In this case we are going to use a very simple model in which the role of a neuron is played by an oscillator, representing their phase the transmitted information.

2.1 Kuramoto model

The Kuramoto model ([1]), proposed by Yoshiki Kuramoto in 1975, describes the behaviour of a large set of coupled oscillators and, for so, is widely used to study the conduct of neurons. It is described by

$$\dot{\theta}_i = \omega_i + \sum_{j=1}^N \kappa_{ij} \sin(\theta_j - \theta_i - \delta_{ij}), \quad i = 1, \dots, N \quad (2.1)$$

where ω_i is the natural frequency of each oscillator which is biased away because of its interaction with the surroundings, represented by the second term, where κ_{ij} is the coupling constant and δ_{ij} is a phase. As this set-up will represent a set of neurons, then κ_{ij} can be either positive or negative depending on the kind of synaptic coupling: excitatory or inhibitory, respectively. Also, δ_{ij} represents the delay of the information transmission between neurons and will be inside the interval $[-\pi, \pi]$. As this quantity represents a time delay, it may seem appropriate to work with positive values, but the results that we shall obtain along this dissertation can be discussed in a more clearly way if we restrict ourselves to that range.

2.2 Excitatory and inhibitory couplings

The connection that a neuron establish with the others is called synapse and takes place in the known as synaptic space, filled by extra-celular liquid that splits the presynaptic neuron's membrane from the postsynaptic one.

In these connections, a certain kind of substances known as neurotransmitters are interchanged and, depending on its composition and concentration, we can talk about different kind of synaptic couplings.

- **Excitatory.** The neurotransmitters open Na^+ and K^+ channels which induces de depolarization of the postsynaptic membrane.
- **Inhibitory.** The neurotransmitters open K^+ and Cl^- channels that hyperpolarize the postsynaptic membrane.

2.3 Class 1 and class 2 couplings

According to [6], in 1948, Alan Hodgkin injected steps of current of various amplitudes into excitable membranes and looked at the resulting spiking behaviour. Depending on the average frequency of such firing, Hodgkin identified two major classes of excitability:

- **Class 1 neuronal excitability.** Action potentials can be generated with arbitrarily low frequency, depending on the strength of the applied current. Class 1 neurons fire with low frequencies, covering a range of about 2 and 100 Hz.
- **Class 2 neuronal excitability.** Action potentials are generated in a certain frequency band that is relatively insensitive to changes in the strength of applied current. The frequency of class 2 neurons is quite limited, generally between 150 and 200 Hz but it can vary from neuron to neuron.

3 Individual oscillator

Consider only one oscillator. Therefore, the system of equations shown in eq. (2.1) is reduced to

$$\dot{\theta}_1 = \omega_1. \quad (3.1)$$

Assume now that a modulation of that oscillation is performed by a certain function $f(t)$. In that case eq. (3.1) is given by

$$\dot{\theta}_1 = \omega_1 + f(t). \quad (3.2)$$

In this section we are going to study what happens if we apply a certain pulse A during an interval Δt in such a way that $f(t)$ is represented by

$$f(t) = \begin{cases} A, & \text{if } t < t_0, t > t_1, \Delta t = t_1 - t_0 \\ 0, & \text{otherwise} \end{cases}, \quad (3.3)$$

and what happens if that signal is modulated by an oscillating function as, for instance, a sine wave

$$f(t) = A \sin(\omega_e t) \quad (3.4)$$

where ω_e is the frequency of the oscillation introduced.

3.1 Modulation by a squared pulse

In order to study the modulation of our signal by a squared pulse, a relevant quantity for us is the known as *Phase Response Curve* (PRC) which, according to [2] is characterized by

$$\text{PRC} = \theta_0 - \theta_{\text{mod}} \quad (3.5)$$

where θ_0 is the phase without any modulation and θ_{mod} is the modulated one. However, in the graphics shown in this section, we will call PRC to the quantity PRC/π .

The reason why the PRC is an important tool lies beneath the fact that these perturbations can produce a delayed or an anticipated signal with respect to the one without any external input. Therefore, depending on the sign of this magnitude, we can differ between a delay or an advance of that signal.

3.1.1 Very low pulses ($A \ll \omega_1$)

All the numerical operations that appear in this section have been done employing Simpson's rule and, concretely for this part, we have considered a pulse of amplitude $A = 0.1 \text{ rad}\cdot\text{s}^{-1}$, being the natural frequency of the oscillator $\omega = \pi \text{ rad}\cdot\text{s}^{-1}$ so the period of the original signal will be $T = 2.0$ s. In the pictures shown in figure 1, the results corresponding to different durations for the pulses are presented, where it can be seen that, while the perturbation is switched on, the affected signal overtake the one which is unperturbed and, as the excitation is constant, it rises linearly with time. The same behaviour as the one obtained for low pulses will be expected if we apply higher values of that quantity, being the magnitude of the separation between signals the main difference.

3.1.2 Medium pulses ($A \simeq \omega$)

By medium pulses, it is understood that the amplitude is quite similar to the natural frequency of the oscillator. Nevertheless, for the representation shown in figure 2, we will work with $A = \pi = \omega$. As it was commented before, in those figures it can be seen that delays of a bigger magnitude than the ones for low pulses are obtained. However, as we are working with $A = \pi \text{ rad}\cdot\text{s}^{-1}$, if we stand for time intervals $\Delta t = n \cdot T$ with $n \in \mathbb{Z}$, then, once the pulse is over, the phase of the perturbed signal gets again in consonance with the unperturbed oscillation. In other cases in which $A \neq \omega$ the same relationship is satisfied but then n is not necessarily always an integer number.

3.1.3 High pulses ($A \gg \omega$)

Finally, in this case, a pulse $A = 15 \text{ rad}\cdot\text{s}^{-1}$ is applied being the results obtained shown in figure 3. As it can be seen there, they verify what has been commented above. However, a little difference appears here and is that while the pulse is switched on, sometimes the highest value of the peak does not reach the phase $\theta = 2\pi$ and it decays at lower values. This fact is caused by the method employed to perform the representations because we are obligating the phase to turn 0 when it reaches a value higher than 2π and, for high pulses, this is obtained in a quicker way. This *problem* can be solved if we decrease the interval between two consecutive times, but that implies an increase in the computation time which, unfortunately, does not behave linearly.

If instead of applying an isolated pulse, a periodic pulse is applied, the same results as the ones shown in these representations are expected. Nevertheless, the main difference will be in the repetition of that perturbation along time. If we work with $\Delta t = n \cdot T$, $n \in \mathbb{R}$, while the pulse is not applied, the modified pulse will coincide with the unperturbed one as it happened before.

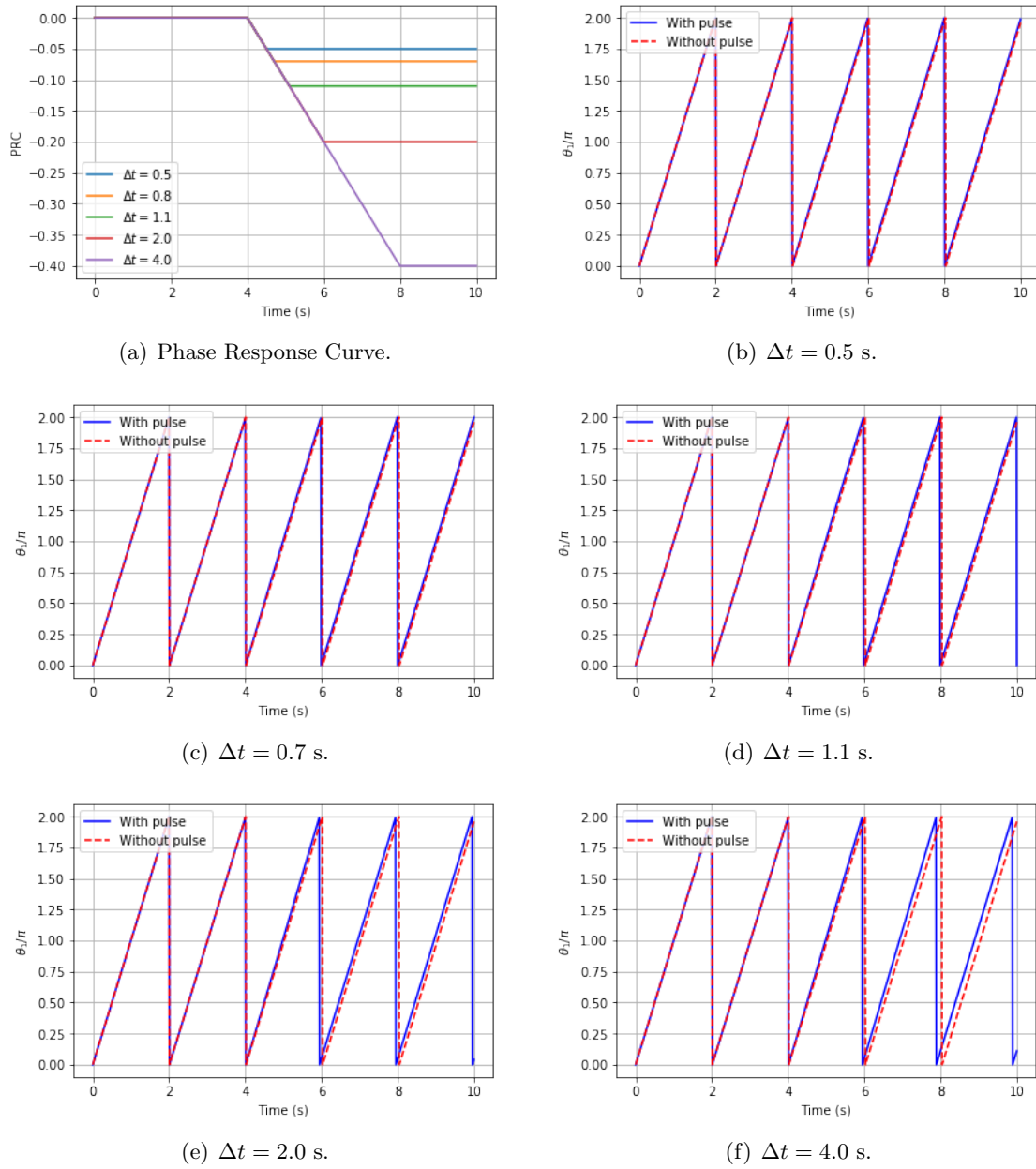


Figure 1: Phase Response Curve and phase curve for each of the cases studied applying very low pulses.

3.2 Modulation by a sine function

According to expressions eq. (3.2) and eq. (3.4), the evolution of the phase of our oscillator is governed by

$$\dot{\theta}_1 = \omega_1 + A \sin(\omega_e t). \quad (3.6)$$

Considering the initial phase of our oscillator to be zero ($\theta(0) = 0$), something that can be done either by waiting a suitable interval of time or by redefining the angles of the oscillation, the time dependence of the phase of our oscillator is characterized by

$$\theta_1(t) = \omega t + \frac{A}{\omega_e} \left[1 - \cos(\omega_e t) \right] \quad (3.7)$$

In this section, we will study the behaviour of that oscillation when we vary adequately the frequency and the modulation's amplitude.

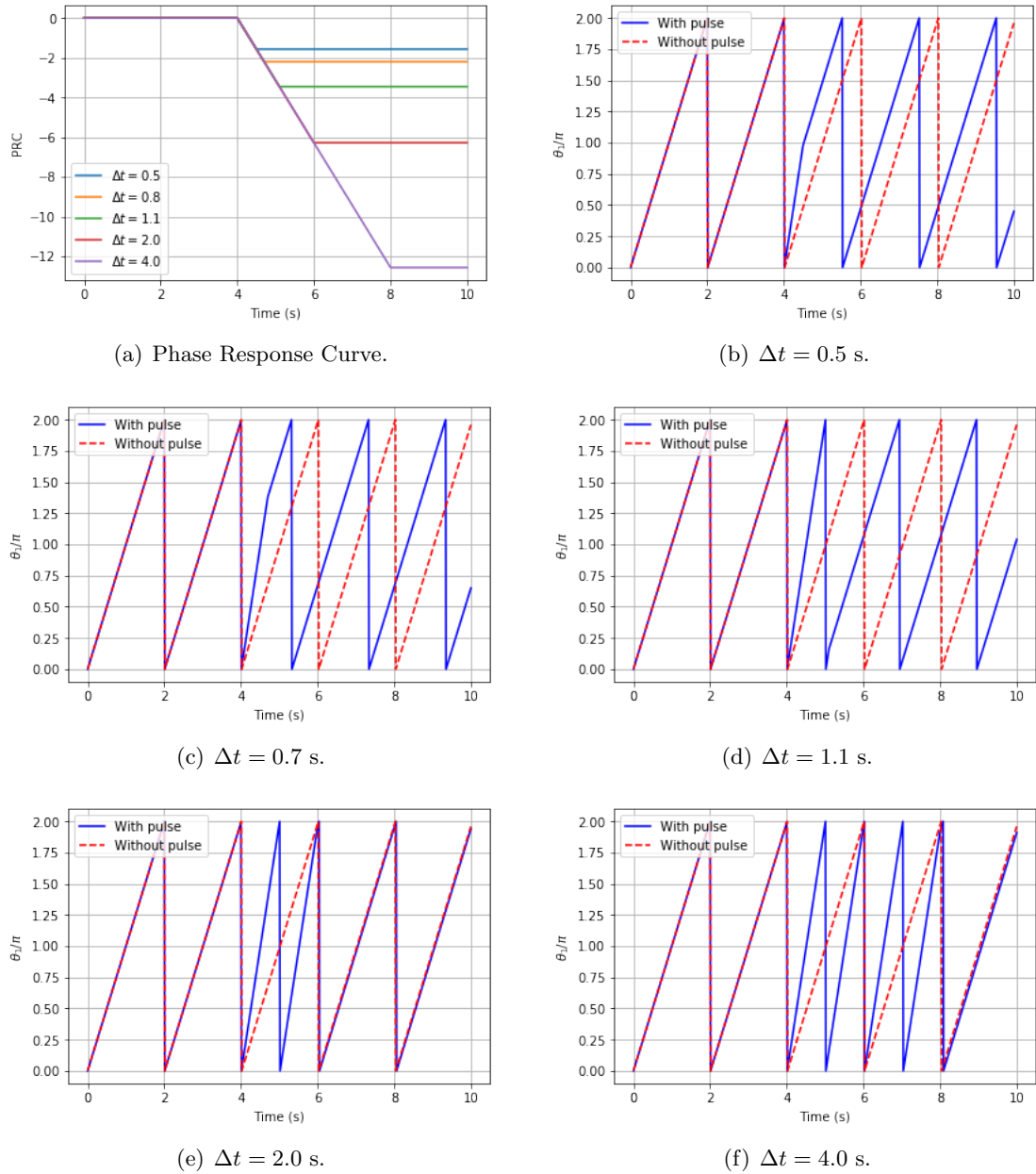


Figure 2: Phase Response Curve and phase curve for each of the cases studied applying medium pulses ($A = \pi = \omega$).

3.2.1 Very low modulated frequency ($\omega \gg \omega_e$)

To study this limit, the Taylor expansion of the cosine will be considered, neglecting second and higher order terms in our expressions. Therefore, eq (3.7) is given by

$$\theta_1(t) \approx \omega t + \mathcal{O}(\omega^2), \quad (3.8)$$

where we see that the natural oscillation remains practically unperturbed or, in this way, we have to wait a long enough time to see appreciable changes. A similar result is obtained if we are working with very low amplitudes but in this case, even if we wait a long enough time, changes will not be observed.

3.2.2 Medium modulated frequency ($\omega \simeq \omega_e$)

In this case, the frequencies that will be used are $\omega_e = 1.0, 2.0 \text{ rad}\cdot\text{s}^{-1}$ with amplitudes $A = 5.0, 10.0 \text{ rad}\cdot\text{s}^{-1}$, being the results obtained presented on figure 4. In this image, we see how the perturbation introduced modules the natural frequency of the oscillator: when the frequency increases, the number of peaks which reaches the value $\theta_1/\pi = 2.0$ is lower due to the fact that a less number of natural oscillations are contained inside one modulated peak. Likewise, for higher values of the

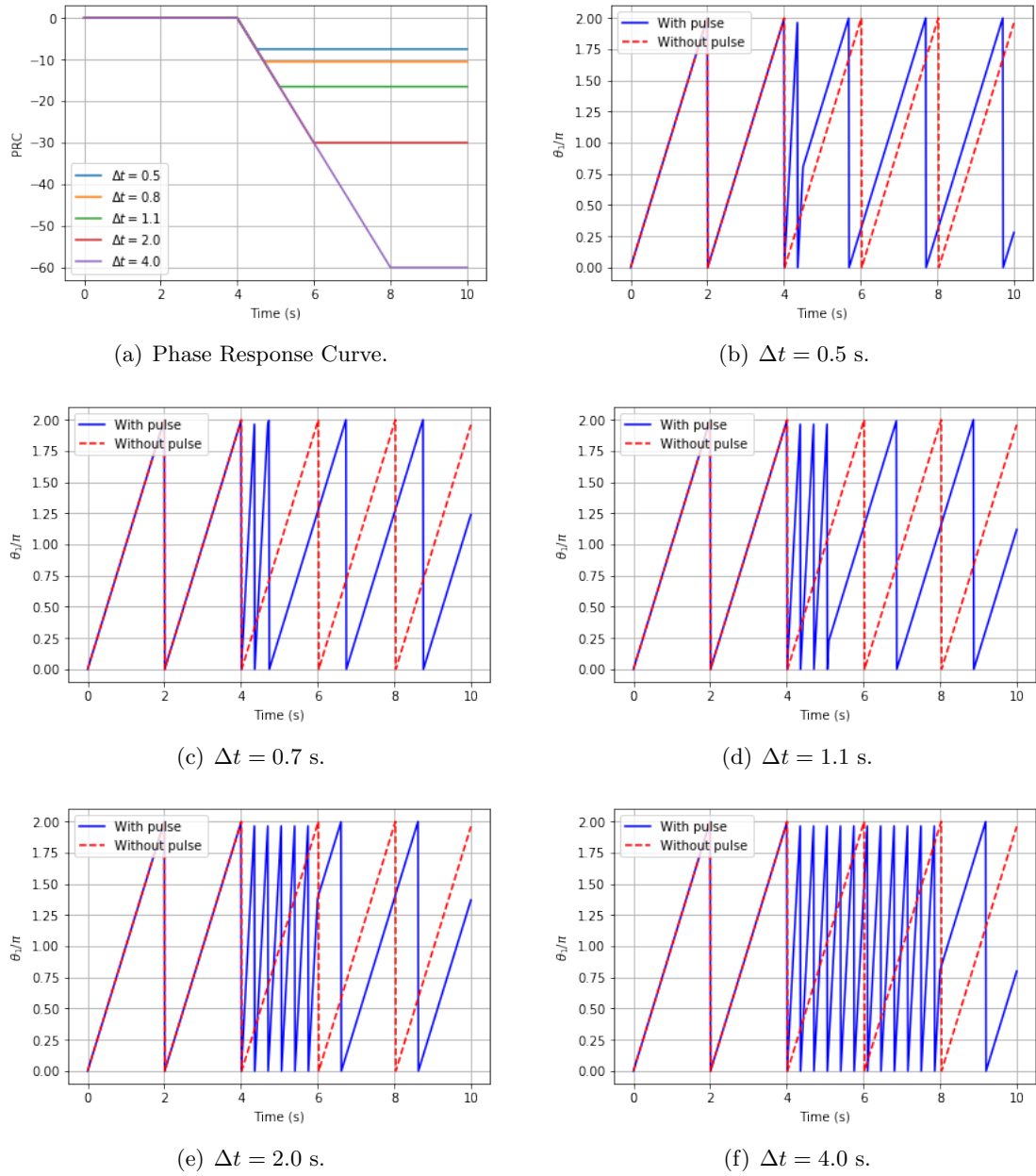


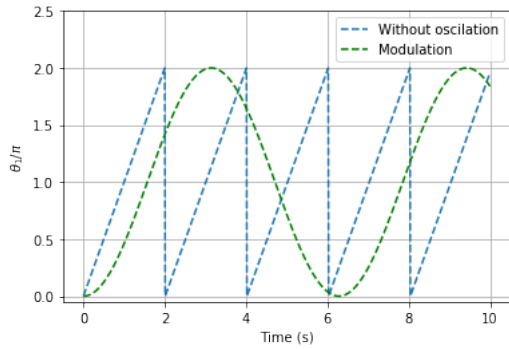
Figure 3: Phase Response Curve and phase curve for each of the cases studied applying high pulses.

amplitude, the number of peaks also increase but also its amplitude because the change is more sharply.

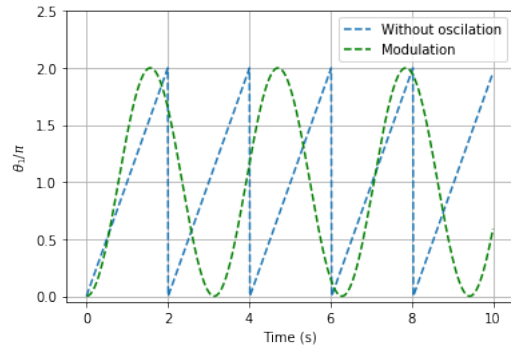
3.2.3 High modulated frequency ($\omega \gg \omega_e$)

In this last case, the amplitudes used are exactly the same as the ones used before but, now, the frequency is $\omega = 15.0 \text{ rad}\cdot\text{s}^{-1}$. As the modulated oscillations occur very fast, during a *natural period*¹, peaks all along the natural oscillation will be obtained, as it can be seen in figure 5, and the change that the amplitude introduces only affects the size of those peaks.

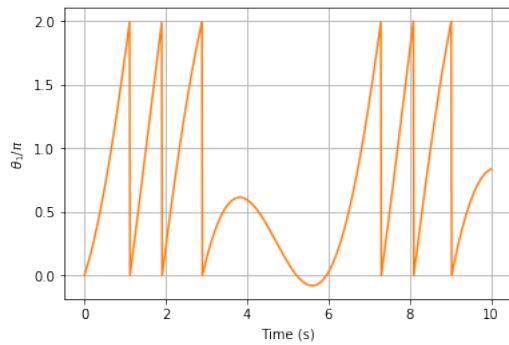
¹The natural oscillation's period.



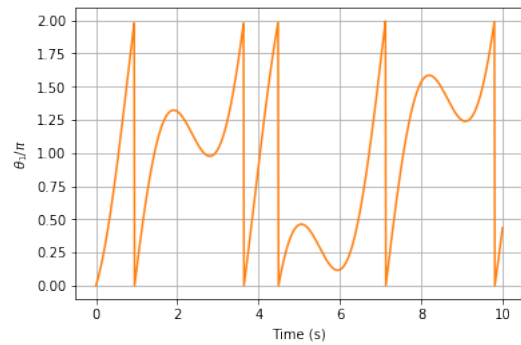
(a) Signal without modulation (in colour blue) and the perturbation (in colour green and not scaled) for $\omega_e = 1.0 \text{ rad} \cdot \text{s}^{-1}$.



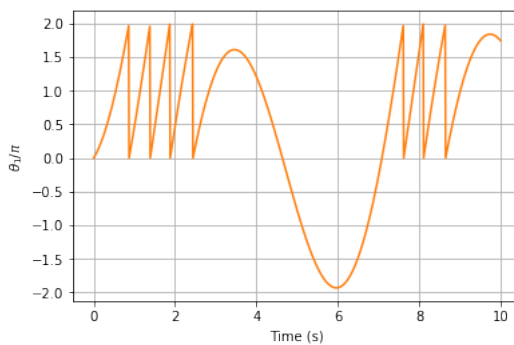
(b) Signal without modulation (in colour blue) and the perturbation (in colour green and not scaled) for $\omega_e = 2.0 \text{ rad} \cdot \text{s}^{-1}$.



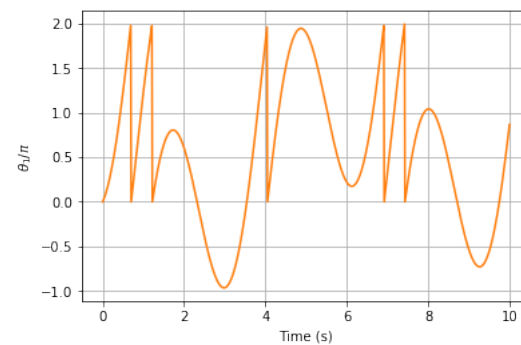
(c) $A = 5.0 \text{ rad} \cdot \text{s}^{-1}$, $\omega_e = 1.0 \text{ rad} \cdot \text{s}^{-1}$.



(d) $A = 5.0 \text{ rad} \cdot \text{s}^{-1}$, $\omega_e = 2.0 \text{ rad} \cdot \text{s}^{-1}$.

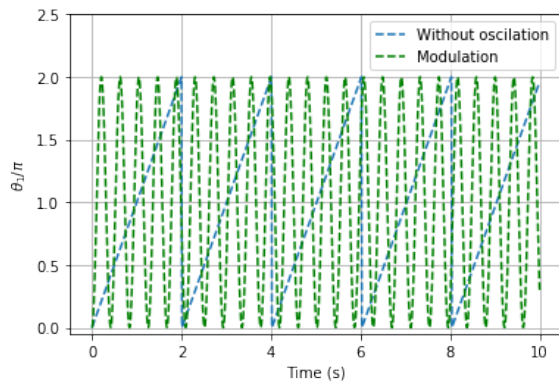


(e) $A = 10.0 \text{ rad} \cdot \text{s}^{-1}$, $\omega_e = 1.0 \text{ rad} \cdot \text{s}^{-1}$.

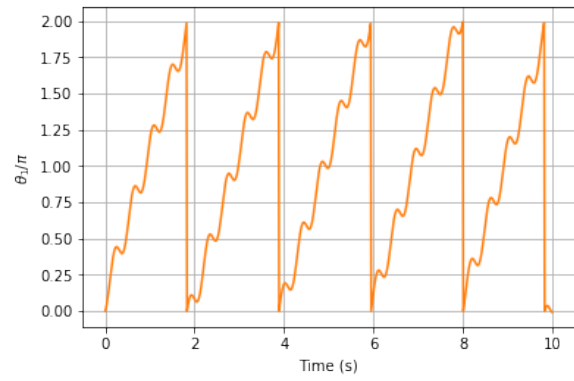


(f) $A = 10.0 \text{ rad} \cdot \text{s}^{-1}$, $\omega_e = 2.0 \text{ rad} \cdot \text{s}^{-1}$.

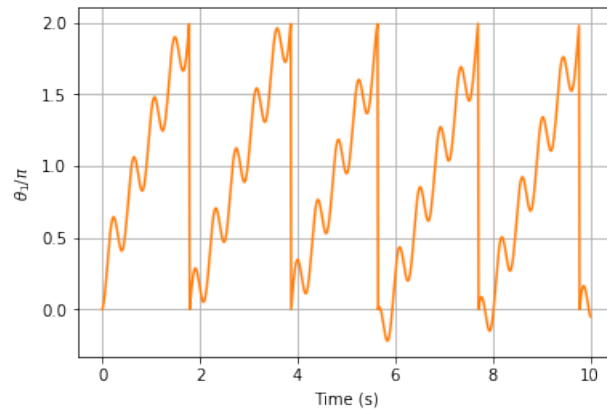
Figure 4: Results obtained for medium modulated frequency.



(a) Signal without modulation (in colour blue) and the perturbation (in colour green and not scaled) for $\omega_e = 15.0 \text{ rad} \cdot \text{s}^{-1}$.



(b) $A = 5.0 \text{ rad}\cdot\text{s}^{-1}$, $\omega_e = 15.0 \text{ rad}\cdot\text{s}^{-1}$.



(c) $A = 10.0 \text{ rad}\cdot\text{s}^{-1}$, $\omega_e = 15.0 \text{ rad}\cdot\text{s}^{-1}$.

Figure 5: Results obtained for high modulated frequency.

4 Master-slave configuration with a class 2 coupling

In this section, a specific kind of coupling between two oscillators is studied: the master-slave configuration. As we see in figure 6, the two oscillators are coupled unidirectionally being the one located at the right, also known as *slave*, perturbed in an excitatory way by the oscillator located at the left, also known as *master* ([7]).

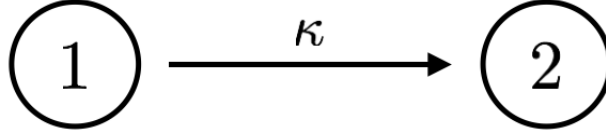


Figure 6: Master-slave configuration for a set of two oscillators.

For this set, according to eq. (2.1), the equations which describe the motion of the phase are

$$\begin{aligned}\dot{\theta}_1 &= \omega_1 \\ \dot{\theta}_2 &= \omega_2 + \kappa \sin(\theta_1 - \theta_2 - \delta)\end{aligned}\quad (4.1)$$

Different configurations for this system will be studied according to the possible different values of the parameters we have. We will start by considering the case in which $\omega_1 = \omega_2 = \omega$ in two possible situations: allowing phase locking ($\dot{\theta}_{12} = 0$) and not allowing phase locking. Later, the same study will be done for the case in which $\omega_1 \neq \omega_2$ and finally we will add a certain sine modulation to the master oscillator and see how the slave is affected because of it.

4.1 Equal natural frequencies ($\omega_1 = \omega_2 = \omega$)

Under this assumption, eq. (4.1) takes the form

$$\begin{aligned}\dot{\theta}_1 &= \omega \\ \dot{\theta}_2 &= \omega + \kappa \sin(\theta_1 - \theta_2 - \delta)\end{aligned}\quad (4.2)$$

and the evolution of the phase difference is characterized then by

$$\dot{\theta}_{12} = -\kappa \sin(\theta_1 - \theta_2 - \delta). \quad (4.3)$$

4.1.1 Phase locking

The reason why we are interested in the solutions for whom the phases are locked, lies on the fact that, if a way in which the phase difference $\theta_{12} = \theta_1 - \theta_2 < 0$ is found, that is, the phase of the slave is ahead of master's phase, anticipated synchronization takes place. Thereby, if this is a stable solution, all initial phases located at the surroundings of that point will decay to it. In the case we are analysing, it follows immediately from eq. (4.3) that

$$\theta_{12}^* = \delta \quad (4.4)$$

where θ_{12}^* denotes the phase difference under phase locking condition. Here we see that it remains constant and indeed is equal to the delay δ . However, depending on the sign of the delay δ , anticipated synchronization takes place or not. Concretely, if $\delta < 0$ this phenomenon occurs and, otherwise, it will not.

4.1.2 Not imposing phase locking condition

By solving eq. (4.3), the behaviour of θ_{12} is obtained in the case we are not imposing phase locking condition and is given by

$$\theta_{12} = \delta - 2 \arctan [A \exp(-\kappa t)]. \quad (4.5)$$

As it can be seen here, when t is long enough the phase difference remains constant, recovering then the result for phase locking. Thereby, we have a certain time interval in which the slave oscillator manages to follow the movement of the master oscillator and, by increasing the coupling constant κ , we achieve the phase-locking regime where, if $\delta < 0$ the slave anticipates the master and

if $\delta > 0$, the other possible case is obtained. In figure 7 we show numerical simulations of eq. (4.2) for different values of κ and δ but employing the same initial conditions for both oscillators which are $\theta_1(0) = 0$ and $\theta_2(0) = \pi$. Also, in figure 8, the slave oscillator's *adaptation* regime is shown more explicitly, where we have only changed the initial conditions, having now $\theta_2(0) = \pi/2$.

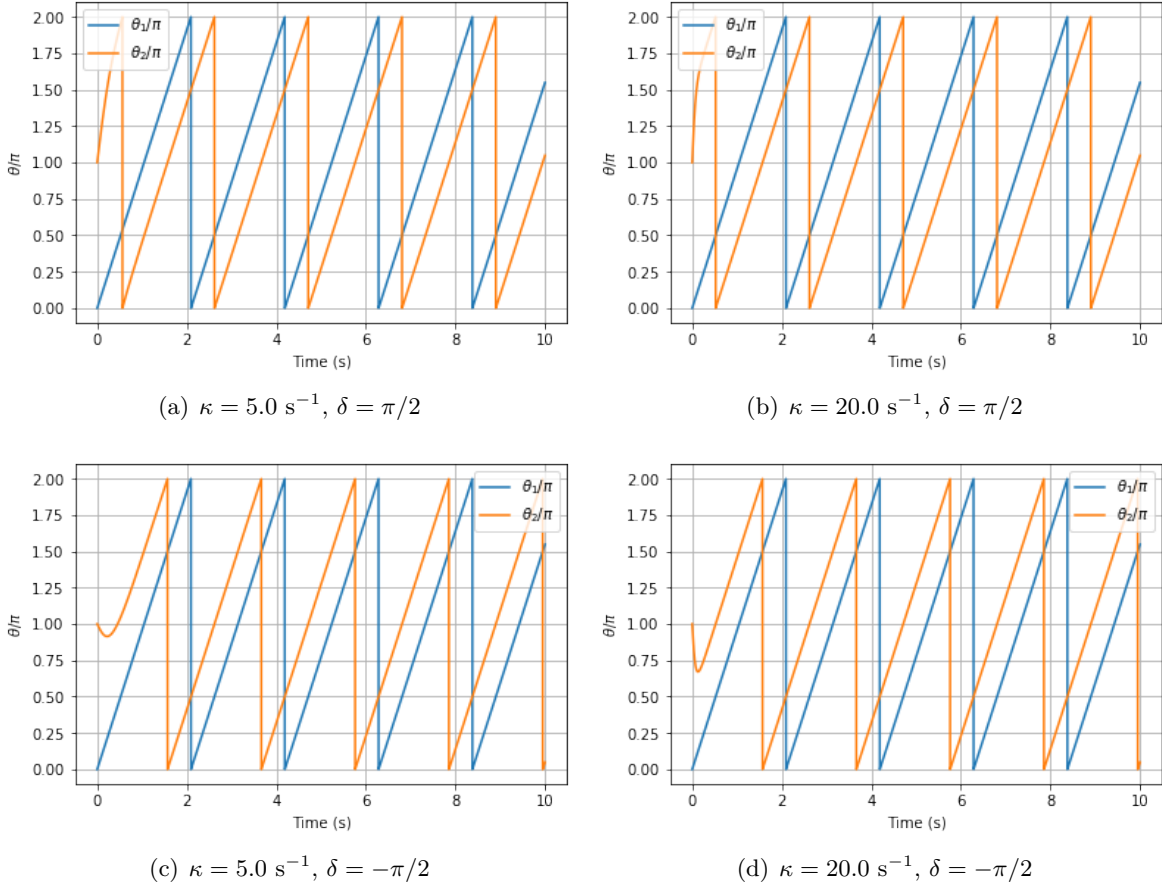


Figure 7: Numerical simulations of eq. (4.2) for different values of κ and δ . The initial conditions for both oscillators are $\theta_1(0) = 0$ and $\theta_2(0) = \pi$.

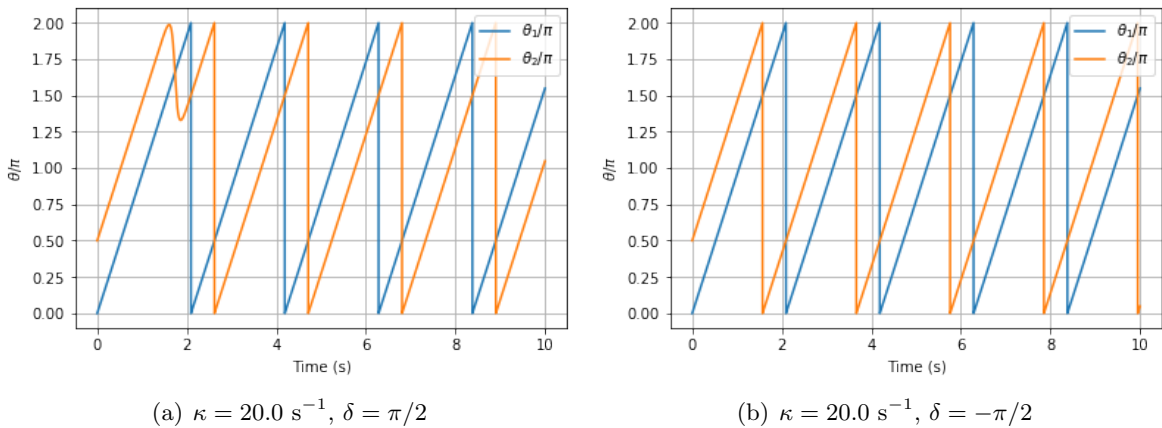


Figure 8: Numerical simulations of eq. (4.2) for different values of δ . The initial conditions for both oscillators are $\theta_1(0) = 0$ and $\theta_2(0) = \pi/2$.

4.2 Different natural oscillations ($\omega_1 \neq \omega_2$)

Unlike the case shown before, now both oscillators do not have the same natural frequency. Therefore, we will expect a dependence with these quantities in the study of anticipation phenomena,

being the procedure in which this is analysed the same as the case for same frequencies.

4.2.1 Phase locking

The time evolution of the phase difference between the oscillators, according to eq. (4.2) which represents this general case, is characterized by

$$\dot{\theta}_{12} = \Delta\omega - \kappa \sin(\theta_{12} - \delta) \quad (4.6)$$

where $\Delta\omega = \omega_1 - \omega_2$. Under phase locking condition, that phase difference is given by

$$\theta_{12}^* = \delta + \arcsin\left(\frac{\Delta\omega}{\kappa}\right), \quad (4.7)$$

being the condition for this to be valid $|\Delta\omega| \leq |\kappa|$. Here we see that the final value of the phase difference depends on the natural frequencies of the oscillators, as it was commented above, and if we want to obtain an anticipated synchronization by fixing the values of κ and δ in such a way that $\kappa > 0$ and $0 < \delta < \pi$, then the following condition must be satisfied

$$\Delta\omega < -\kappa \sin \delta, \quad (4.8)$$

that is, anticipated synchronization will only occur if $\omega_2 > \omega_1 + \kappa \sin \delta$ as it can be shown on figure 9 where we took $\kappa = 5.0 \text{ s}^{-1}$, $\omega_1 = 3.0 \text{ rad} \cdot \text{s}^{-1}$ and $\delta = \pi/2$.

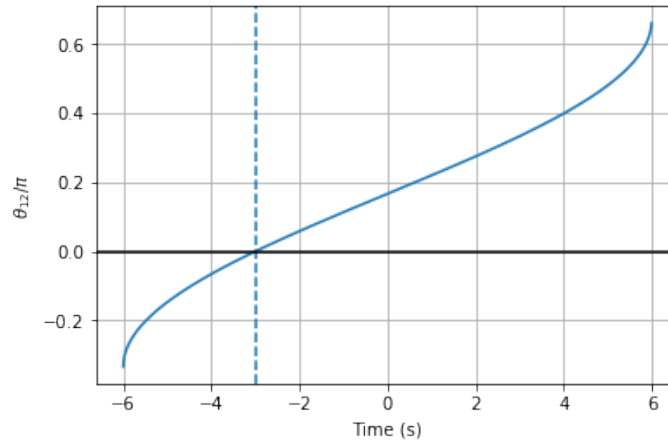


Figure 9: Representation of the phase difference considering phase locking condition for different values of $\Delta\omega$. The horizontal dashed line corresponds to $\Delta\omega = -\kappa \sin \delta$.

4.2.2 Not imposing phase locking condition

If we are not considering the phase locking condition, then it is necessary to solve eq. (4.3) which leads to the following expression

$$\int \frac{d\theta_{12}}{\Delta\omega/\kappa - \sin(\theta_{12} - \delta)} = \kappa t + A. \quad (4.9)$$

We are interested in solving the first part of the equality but it depends on the possible cases we shall study. In this section, we will assume that $\kappa > 0$ and $\Delta\omega$ can take either positive or negative values. To evaluate this integral, we will focus on the case in which $\Delta\omega < 0$ and the results obtained will be applied to the another possibility ($\Delta\omega > 0$). Also, to simplify later expressions, we will denote c to the quantity $\Delta\omega/\kappa^2$ and $x = \theta_{12} - \delta$, in such a way that the integral that shall be evaluated is

$$I = - \int \frac{dx}{c + \sin x}. \quad (4.10)$$

By performing the change $z = \tan(x/2)$, eq. (4.10) takes the form

$$I = -2 \int \frac{dz}{cz^2 + 2z + c} = -2 \int \frac{dz}{(\sqrt{c}z + 1/\sqrt{c})^2 + (c^2 - 1)/c}. \quad (4.11)$$

Reached this point, we have to distinguish between three different cases: $c = 1$, $c > 1$ and $c < 1$.

²Later in this text, we will change that definition conveniently.

Case c = 1 In this case, we are under the situation in which $\Delta\omega = \kappa$ so the integral shown in eq. (4.11) turns into

$$I = -2 \int \frac{dz}{(z+1)^2} = \frac{2}{\tan(x/2) + 1}, \quad (4.12)$$

which substituted into eq. (4.9) leads to

$$\frac{2}{\tan(x/2) + 1} = \kappa t + A \rightarrow x = 2 \arctan\left(\frac{2}{\kappa t + A} - 1\right) \quad (4.13)$$

and with the definition previously given for x ,

$$\theta_{12} = \delta + 2 \arctan\left(\frac{2}{\kappa t + A} - 1\right). \quad (4.14)$$

Therefore, we see that by waiting long enough times, the phase difference between both oscillators tends to $\theta_{12} = \delta - \pi/2$ so if we consider this system to be a set of two neurons in such way that δ represents the time delay of the signal which travels one neuron to the other, we can obtain anticipated, delayed or in-phase signals between them, as it is shown in figure 10.

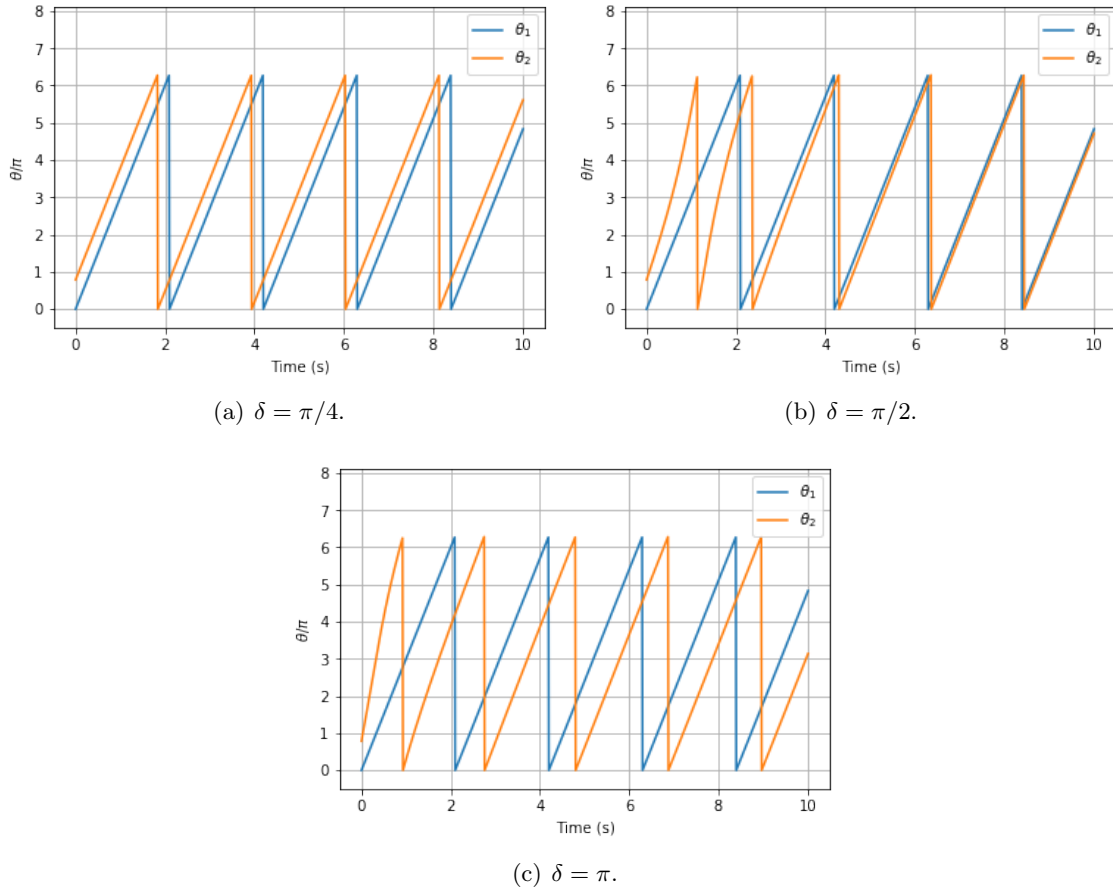


Figure 10: Anticipated, in-phase and delayed signals in the second oscillator respectively, obtained employing numerical methods. The calculus has been done with $\kappa = 2.0 \text{ s}^{-1}$, $\omega_1 = 3.0 \text{ rad}\cdot\text{s}^{-1}$ and $\omega_2 = 5.0 \text{ rad}\cdot\text{s}^{-1}$.

It can be proved easily from the expressions obtained before that, working with $\Delta\omega > 0$ and $\kappa > 0$, leads at long times to $\theta_{12} = \delta + \pi/2$.

Case c < 1 In this case we are in the situation in which $\Delta\omega < \kappa$ so the integral shown in eq. (4.10) turns into

$$\begin{aligned} I &= -\frac{2c}{1-c^2} \int \frac{dz}{[(cz+1)/\sqrt{1-c^2}]^2 - 1} = \\ &= \frac{1}{\sqrt{1-c^2}} \ln \left| \frac{cz+1+\sqrt{1-c^2}}{cz+1-\sqrt{1-c^2}} \right|, \end{aligned} \quad (4.15)$$

which substituted into eq. (4.9) leads to

$$\frac{1}{\sqrt{1-c^2}} \ln \left| \frac{cz+1+\sqrt{1-c^2}}{cz+1-\sqrt{1-c^2}} \right| = \kappa t + A. \quad (4.16)$$

From here, we can see that the phase difference is given by

$$\theta_{12} = \delta + 2 \arctan \left(\frac{(1-\sqrt{1-c^2}) \exp((\kappa t + A)\sqrt{1-c^2}) - 1 - \sqrt{1-c^2}}{c(1 - \exp((\kappa t + A)\sqrt{1-c^2}))} \right). \quad (4.17)$$

Considering very long times, eq. (4.17) can be written as follows

$$\theta_{12} = \delta - 2 \arctan \left(\frac{1 - \sqrt{1-c^2}}{c} \right). \quad (4.18)$$

If $c \rightarrow 1$, the result studied in the case before is obtained. However, if we consider c to be a very small quantity, then the phase difference is $\theta_{12} = \delta$, recovering the result obtained for $\omega_1 = \omega_2 = \omega$ but in this case, those two frequencies do not have to be equal one to the other if the coupling constant κ is long enough. Thereby, if $\delta > 0$, the master is ahead the slave and if $\delta < 0$, the other way round takes place, as we can see on figure 11 where the numerical simulations have been done with the values $\omega_1 = 3.0 \text{ rad}\cdot\text{s}^{-1}$, $\omega_2 = 7.0 \text{ rad}\cdot\text{s}^{-1}$ and $\kappa = 100.0 \text{ rad}\cdot\text{s}^{-1}$.

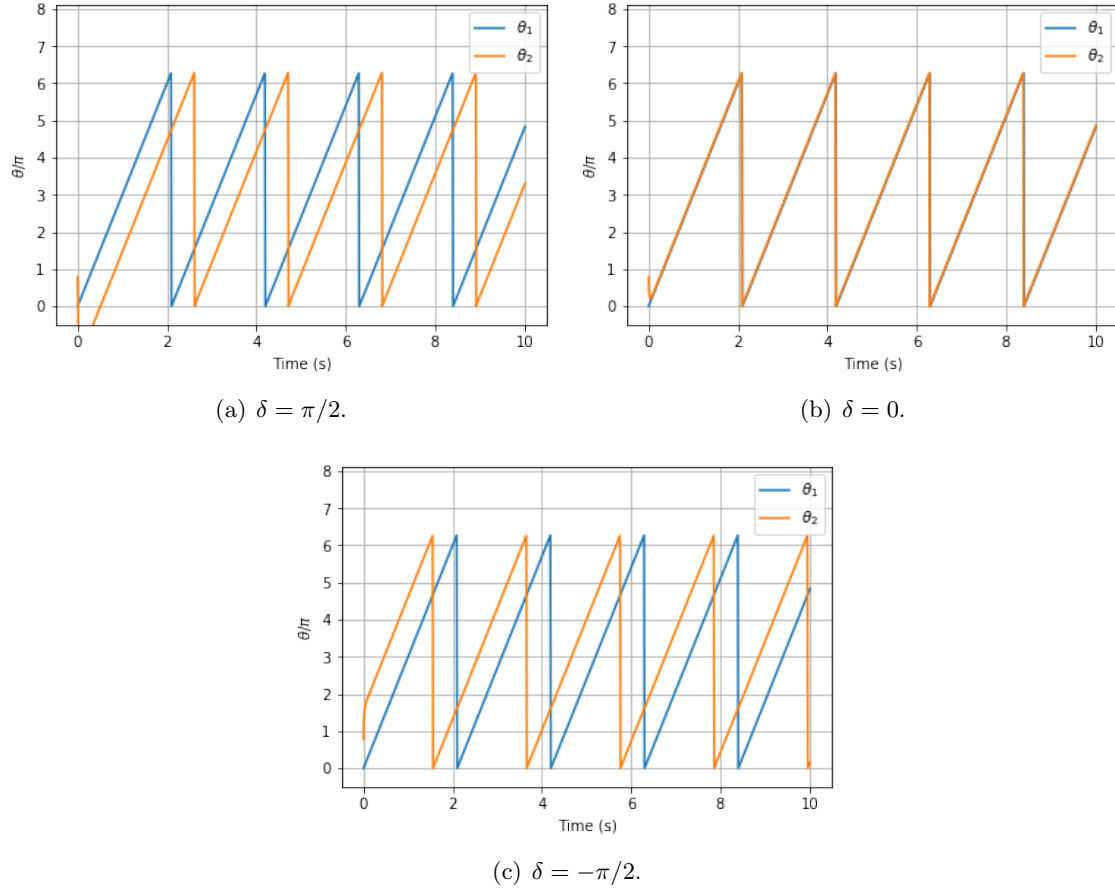


Figure 11: Delayed, in-phase and anticipated signals in the second oscillator respectively, obtained employing numerical methods. The calculus has been done with $\kappa = 100.0 \text{ rad}\cdot\text{s}^{-1}$, $\omega_1 = 3.0 \text{ rad}\cdot\text{s}^{-1}$ and $\omega_2 = 7.0 \text{ rad}\cdot\text{s}^{-1}$.

Case $c > 1$ In this case we are in the situation in which $\Delta\omega > \kappa$ so the integral shown in eq. (4.10) turns into

$$\begin{aligned} I &= -\frac{2c}{c^2-1} \int \frac{dz}{1 + [(cz+1)/\sqrt{c^2-1}]^2} = \\ &= -\frac{2}{\sqrt{c^2-1}} \arctan \left(\frac{cz+1}{\sqrt{c^2-1}} \right), \end{aligned} \quad (4.19)$$

which substituted into eq. (4.9) leads to

$$-\frac{2}{\sqrt{c^2-1}} \arctan\left(\frac{cz+1}{\sqrt{c^2-1}}\right) = \kappa t + A. \quad (4.20)$$

From here, it can be seen that the phase difference between the oscillators is given by

$$\theta_{12} = \delta - 2 \arctan\left(\frac{1 + \sqrt{c^2-1} \tan[\sqrt{c^2-1}(\kappa t + A)/2]}{c}\right), \quad (4.21)$$

and, as expected, when $c \rightarrow 1$ then $\theta_{12} = \delta - \pi/2$. On the other hand, as the time dependence is inside a $\tan(x)$ function, it will be oscillating continuously in the interval $(-\infty, \infty)$ and, for so, the phase difference will be changing throughout the system's evolution, as it can be seen on figure 12.

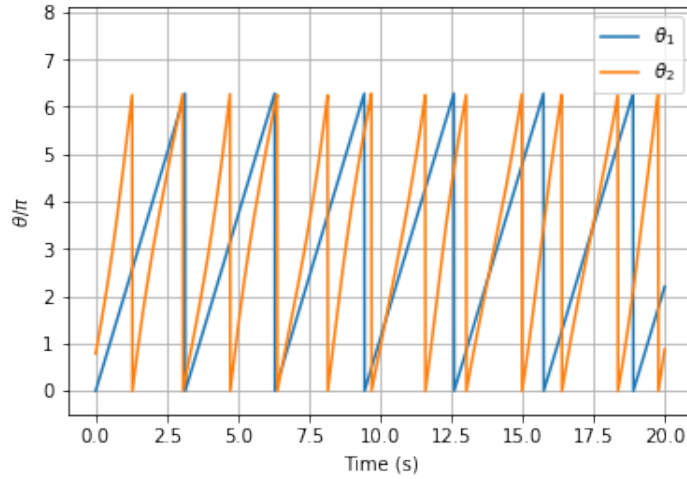


Figure 12: Representation of the case in which $c > 1$. The numerical simulation has been done with $\omega_1 = 2.0 \text{ rad}\cdot\text{s}^{-1}$, $\omega_2 = 4.0 \text{ rad}\cdot\text{s}^{-1}$ and $\kappa = 1.0 \text{ rad}\cdot\text{s}^{-1}$.

5 Two mutually coupled oscillators with a class 2 coupling

In this section, a configuration of two mutually coupled oscillators will be studied, that is, a system as the one shown in figure 13. We shall consider different cases depending on the kind of coupling we have: excitatory ($\kappa > 0$) or inhibitory ($\kappa < 0$).

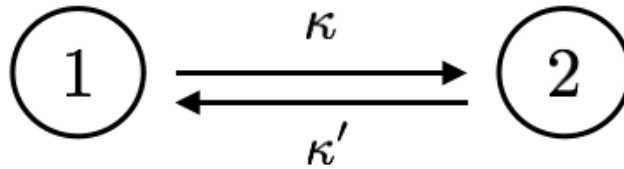


Figure 13: Mutually general coupled oscillator scheme.

The system of equations that govern this configuration is given by

$$\begin{aligned} \dot{\theta}_1 &= \omega_1 + \kappa' \sin(\theta_2 - \theta_1 - \delta) \\ \dot{\theta}_2 &= \omega_2 + \kappa \sin(\theta_1 - \theta_2 - \delta) \end{aligned} \quad (5.1)$$

Different cases will be studied now depending on the oscillator's natural frequencies and the coupling constants between the oscillators.

5.1 Excitatory junction with same coupling constants and same natural frequencies

Under this situation in which $\kappa = \kappa'$ and $\omega_1 = \omega_2 = \omega$, eq. (5.1) takes the following form

$$\begin{cases} \dot{\theta}_1 = \omega - \kappa \sin(\theta_{12} + \delta) \\ \dot{\theta}_2 = \omega + \kappa \sin(\theta_{12} - \delta) \end{cases} \quad (5.2)$$

From here, it can be seen easily that the phase difference between oscillators is characterized by

$$\dot{\theta}_{12} = -2\kappa \cos \delta \sin \theta_{12}, \quad (5.3)$$

which can also be written as follows

$$\int \frac{d\theta_{12}}{\sin \theta_{12}} = -2\kappa t \cos \delta + A. \quad (5.4)$$

The integral that appears in the first term of the equation can be solved performing the change of variable $z = \tan \theta_{12}/2$, obtaining for the resultant differential equation

$$\ln [\tan(\theta_{12}/2)] = -2\kappa t \cos \delta + A \Rightarrow \theta_{12} = 2 \arctan(\exp\{-2\kappa t \cos \delta + A\}). \quad (5.5)$$

Reached this point, we will analyse what happens at long enough times but, for so, we have to distinguish between different situations.

$\boxed{\cos \delta > 0}$ In this case, the exponential is negative so at very long times it tends to zero, having then $\theta_{12} = 0$. As initially both oscillators has the same natural frequency and the phase is locked, at $t \rightarrow \infty$ that magnitude will be

$$\dot{\theta}_1 = \dot{\theta}_2 = \omega - \kappa \sin \delta. \quad (5.6)$$

The cosine function will be positive if $-\pi/2 < \delta < \pi/2$ but depending on which interval is located, the oscillator's frequencies will be higher or lower than its initial value. Concretely, it will be satisfied that

- if $0 < \delta < \pi/2$ then $\dot{\theta}_1 = \dot{\theta}_2 < \omega$;
- if $-\pi/2 < \delta < 0$ then $\dot{\theta}_1 = \dot{\theta}_2 > \omega$,

as it is stated by the numerical simulations, whose results are shown in figure 14.

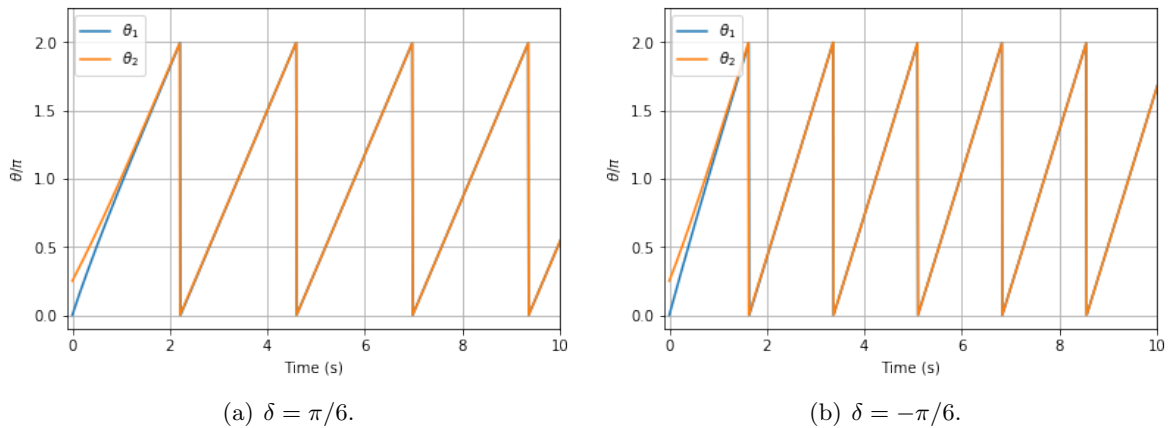


Figure 14: Results obtained with the numerical simulations for values of δ located at the interval $[-\pi/2, \pi/2]$.

$\boxed{\cos \delta < 0}$ In this case, the exponential is positive so at very long times it tends to infinite, having then $\theta_{12} = \pi$ ³. Also, the oscillators frequencies at this regime are equal one to the other taking the following value

$$\dot{\theta}_1 = \dot{\theta}_2 = \omega + \kappa \sin \delta. \quad (5.7)$$

The cosine function will be negative if $\pi/2 < 0 < -\pi/2$ but depending on which concrete interval, the oscillators frequencies will be higher or lower than its initial value. Actually

³Note that the negative value is not allowed because the x of the $\arctan x$ function is positive.

- if $\pi/2 < \delta < \pi$ then $\dot{\theta}_1 = \dot{\theta}_2 > \omega$;
- if $\pi < \delta < -\pi/2$ then $\dot{\theta}_1 = \dot{\theta}_2 < \omega$,

as stated in the numerical simulations shown in figure 15.

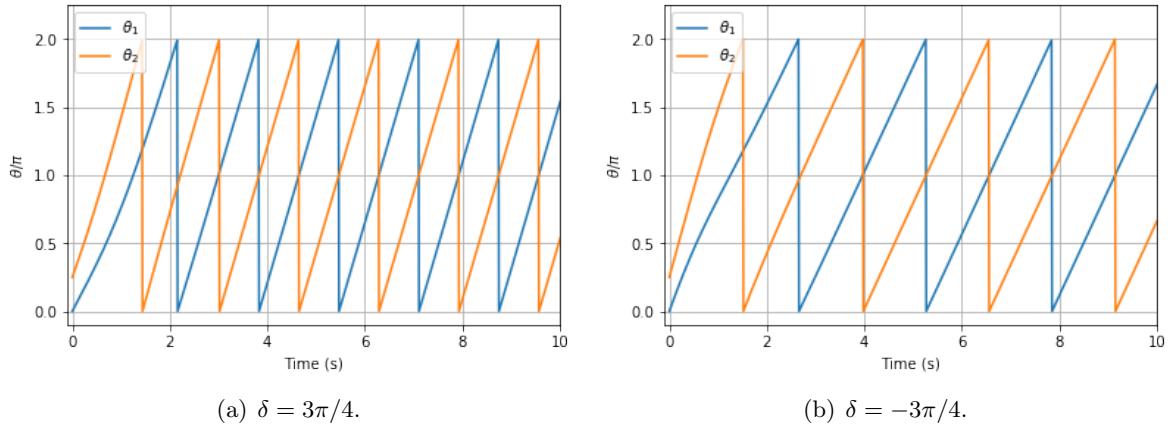


Figure 15: Results obtained with the numerical simulations for values of δ located at the interval $[\pi/2, -\pi/2]$.

Notice that the case in which $\cos \delta = 0$ is not interesting at all because, from eq. (6.3) we see that $\dot{\theta}_{12} = 0$, being the phase difference between the oscillators given by the problem's initial conditions.

5.2 Inhibitory junction with same coupling constants and same natural frequencies

This case is quite similar to the one studied before where the main difference lies in the fact that $\kappa = \kappa' < 0$. Thereby, eq. (5.1) takes the following form

$$\begin{aligned} \dot{\theta}_1 &= \omega + \kappa \sin(\theta_{12} + \delta) \\ \dot{\theta}_2 &= \omega - \kappa \sin(\theta_{12} - \delta) \end{aligned} \quad (5.8)$$

From here it can be seen easily that the phase difference between oscillators is characterized by

$$\dot{\theta}_{12} = 2\kappa \cos \delta \sin \theta_{12}, \quad (5.9)$$

which can also be written as follows

$$\int \frac{d\theta_{12}}{\sin \theta_{12}} = 2\kappa t \cos \delta + A, \quad (5.10)$$

and according to what we have commented before, that differential equation leads to the following relationship for θ_{12}

$$\theta_{12} = 2 \arctan(\exp\{2\kappa t \cos \delta + A\}). \quad (5.11)$$

Again, to analyse what happens at long enough times, we need to distinguish between different situations.

$\cos \delta > 0$ In this case, the exponential is positive so at very long times it tends to infinite, having then $\theta_{12} = \pi$. Thereby, the oscillator's frequencies are characterized by eq. (5.6) and as the cosine function will be positive if $-\pi/2 < \delta < \pi/2$, therefore we will have different values depending on the interval we are working with. Actually

- if $0 < \delta < \pi/2$ then $\dot{\theta}_1 = \dot{\theta}_2 < \omega$;
- if $-\pi/2 < \delta < 0$ then $\dot{\theta}_1 = \dot{\theta}_2 > \omega$,

as stated by the numerical simulations, whose results are shown in figure 16.

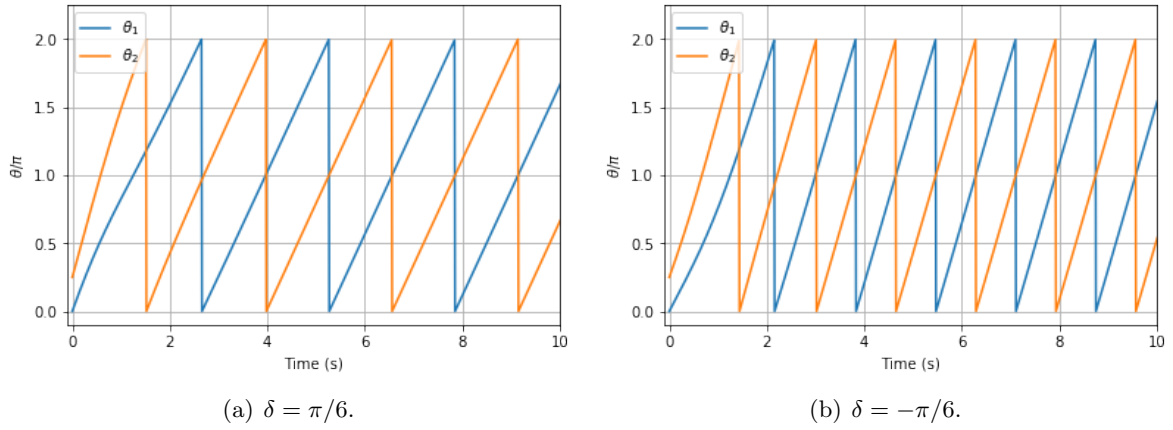


Figure 16: Results obtained with the numerical simulations for values of δ located at the interval $[-\pi/2, \pi/2]$.

$\cos \delta < 0$ In this case, the exponential is negative so at very long times it tends to zero, having then $\theta_{12} = 0$. Thereby, the oscillator's frequencies are characterized by eq. (5.7) and as the cosine function will be negative if $\pi/2 < \delta < \pi/2$, therefore we will have different values depending on the interval we are working with. Concretely

- if $\pi/2 < \delta < \pi$ then $\dot{\theta}_1 = \dot{\theta}_2 > \omega$;
- if $\pi < \delta < -\pi/2$ then $\dot{\theta}_1 = \dot{\theta}_2 < \omega$,

as stated in the numerical simulations whose results are shown in figure 17.

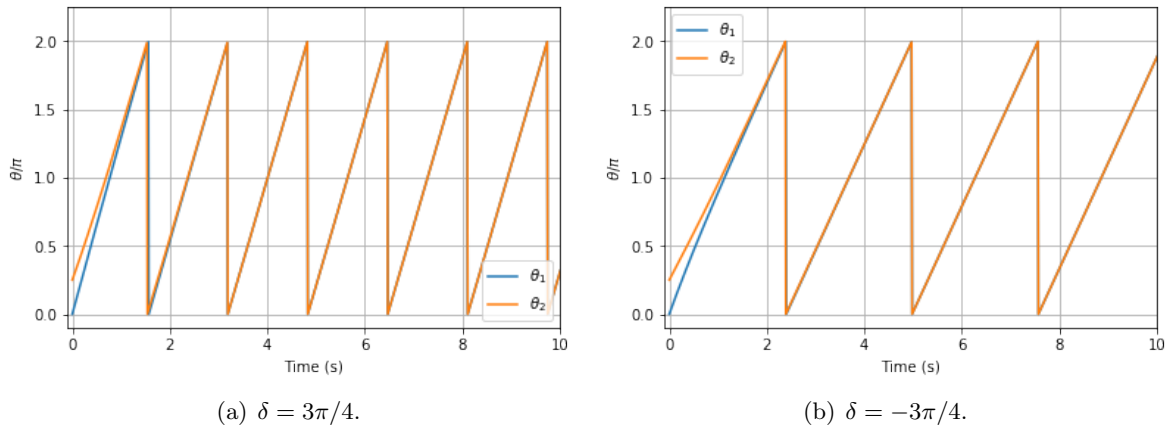


Figure 17: Results obtained with the numerical simulations for values of δ located at the interval $[\pi/2, -\pi/2]$.

Discussion From these cases we have just analysed, it can be seen that the delay δ still plays a fundamental role as it is the parameter that lets having the possible different kind of signals: in-phase or anticipated.

5.3 Excitatory junction with same coupling constants but different natural frequencies

Under this assumption in which $\kappa = \kappa' > 0$ and $\omega_1 \neq \omega_2$, eq. (5.1) can be written as follows

$$\begin{aligned} \dot{\theta}_1 &= \omega_1 - \kappa \sin(\theta_{12} + \delta) \\ \dot{\theta}_2 &= \omega_2 + \kappa \sin(\theta_{12} - \delta) \end{aligned} \quad (5.12)$$

Therefore, the phase difference between oscillators is characterized by

$$\dot{\theta}_{12} = \Delta\omega - 2\kappa \cos \delta \sin \theta_{12}, \quad (5.13)$$

with $\Delta\omega = \omega_1 - \omega_2$. This expression can also be written as

$$\int \frac{d\theta_{12}}{c - \sin\theta_{12}} = 2\kappa t \cos\delta + A \quad (5.14)$$

where $c = \Delta\omega/2\kappa \cos\delta$. We are interested in the case $\Delta\omega < 0$ so we have to talk again two possible situations: $\cos\delta > 0$ and $\cos\delta < 0$.

5.3.1 Delay signal contained in $[-\pi/2, \pi/2]$

This assumptions implies that the constant c defined above is negative so eq. (5.14) can be also written as

$$- \int \frac{d\theta_{12}}{c + \sin\theta_{12}} = 2\kappa t \cos\delta + A. \quad (5.15)$$

Nevertheless, the integral that appears in this last equation is quiet similar to the one shown in eq. (4.10) so the different cases we must study now are exactly the same ones that appear there.

Case $c = 1$

In this case, the phase difference between oscillators is characterized by

$$\theta_{12} = 2 \arctan\left(\frac{2}{2\kappa t \cos\delta + A} - 1\right), \quad (5.16)$$

and at very long times we find that $\theta_{12} = -\pi/2$, that is, a phase locked situation is reached. Therefore, in spite of the fact that the initial oscillator's natural frequencies are different, at long enough times they reach equal values, having then

$$\begin{aligned} \dot{\theta}_1 &= \omega_1 + \kappa \cos\delta \\ \dot{\theta}_2 &= \omega_2 - \kappa \cos\delta \end{aligned} \quad (5.17)$$

In the simulation shown in figure 18, we have chosen the values $\omega_1 = 3.0 \text{ rad}\cdot\text{s}^{-1}$, $\omega_2 = 5.0 \text{ rad}\cdot\text{s}^{-1}$, $\delta = \pi/3$, $\kappa = 2.0 \text{ rad}\cdot\text{s}^{-1}$. Thereby, $\dot{\theta}_1 = \dot{\theta}_2 = 4.0 \text{ rad}\cdot\text{s}^{-1}$.

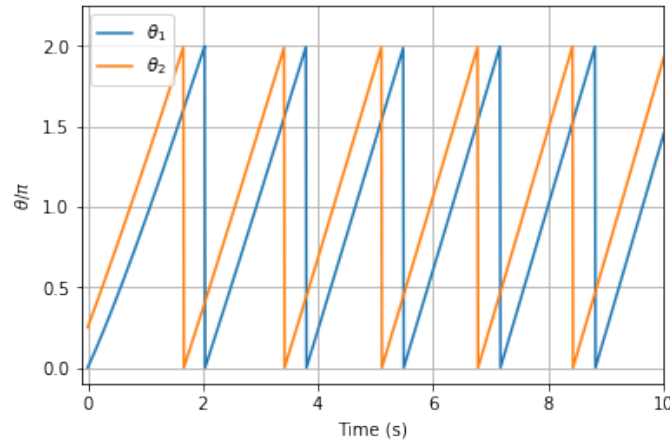


Figure 18: Results obtained with the numerical simulations for the case in which $\cos\delta > 0$ and with $\omega_1 = 3.0 \text{ rad}\cdot\text{s}^{-1}$, $\omega_2 = 5.0 \text{ rad}\cdot\text{s}^{-1}$, $\delta = \pi/3$, $\kappa = 2.0 \text{ rad}\cdot\text{s}^{-1}$.

Case $c < 1$

In this case, the phase difference between oscillators is characterized by

$$\theta_{12} = 2 \arctan\left(\frac{(1 - \sqrt{1 - c^2}) \exp[\sqrt{1 - c^2}(2\kappa t \cos\delta + A)] - 1 - \sqrt{1 - c^2}}{c(1 - \exp[\sqrt{1 - c^2}(2\kappa t \cos\delta + A)])}\right) \quad (5.18)$$

and for long enough times

$$\theta_{12} = -2 \arctan\left(\frac{1 - \sqrt{1 - c^2}}{c}\right). \quad (5.19)$$

Notice that if $c \rightarrow 1$, then $\theta_{12} \rightarrow -\pi/2$ which is the result obtained for the case $c = 1$, as expected. Note also that we will always obtain in this case a delayed signal because both, numerator and denominator of the fraction, are positive quantities, i.e., the phases associated will be located at the fourth quadrant. As an example, in figure 19, numerical simulations have been done for $\omega_1 = 3.0 \text{ rad}\cdot\text{s}^{-1}$, $\omega_2 = 4.0 \text{ rad}\cdot\text{s}^{-1}$, $\kappa = 2.0 \text{ rad}\cdot\text{s}^{-1}$ and for $\delta = \pi/3, \pi/6$.

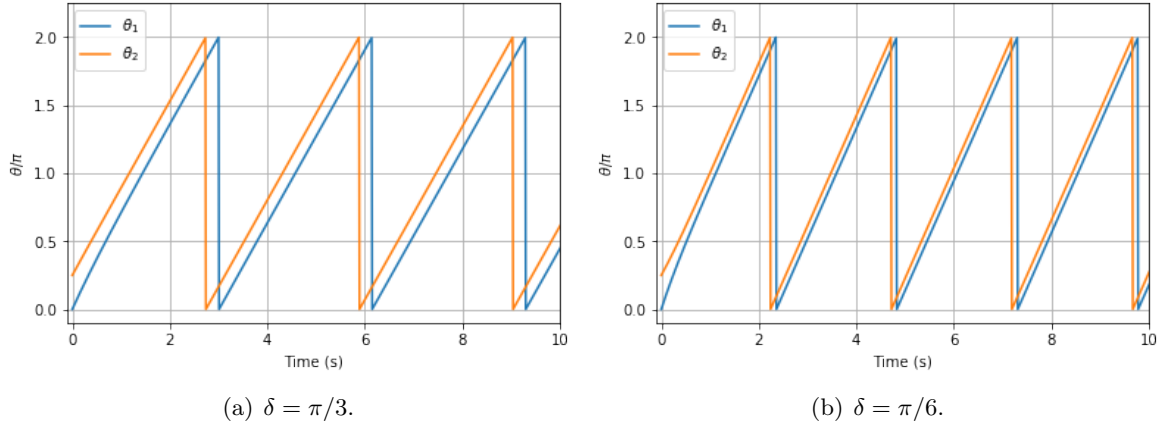


Figure 19: Numerical simulation for the case in which $c < 1$. Notice that, as commented, the phase difference is always negative having then a phase delay.

Case $c > 1$ In this case, the phase difference between oscillators is characterized by

$$\theta_{12} = -2 \arctan \left(\frac{1 + \sqrt{c^2 - 1} \tan(\sqrt{c^2 - 1}(\kappa t \cos \delta + A))}{c} \right). \quad (5.20)$$

Here we see that the time dependence inside the tangent function is linear which implies that the argument of the arctan x will be always oscillating between positive and negative values. Therefore, the phase difference will be continuously fluctuating.

5.3.2 Delay signal contained in $[\pi/2, -\pi/2]$

Here, the constant c is positive because $\cos \delta < 0$. Thereby, eq. (5.14) can be also written as

$$\int \frac{d\theta_{12}}{c - \sin \theta_{12}} = -2\kappa t \cos \delta + A. \quad (5.21)$$

Notice that the negative sign of $\cos \delta$ has been taken out explicitly. Also, the integral that appears is quite similar to the one analysed before and, again, we have to distinguish between all the different possible cases.

Case $c = 1$ In this case, the phase difference is given by

$$\theta_{12} = 2 \arctan \left(1 + \frac{2}{2\kappa t \cos \delta + A} \right), \quad (5.22)$$

and at very long times we find that θ_{12} , i.e., a phase locked situation in which the second oscillator is delayed with respect to the first one. Hence, the frequencies for both of them are characterized by eq. (5.17) and are shown in figure 20 where the same constants have been used but with $\delta = 2\pi/3$.

Case $c < 1$ In this case, the phase difference between oscillators is given by

$$\theta_{12} = 2 \arctan \left(\frac{(1 + \sqrt{1 - c^2}) \exp[\sqrt{1 - c^2}(2\kappa t \cos \delta + A)] - 1 + \sqrt{1 - c^2}}{c(\exp[\sqrt{1 - c^2}(2\kappa t \cos \delta + A)] - 1)} \right), \quad (5.23)$$

and for long enough times

$$\theta_{12} = 2 \arctan \left(\frac{1 + \sqrt{1 - c^2}}{c} \right). \quad (5.24)$$

Taking the limit in which $c \rightarrow 1$, we recover the value obtained in the case $c = 1$, i.e., $\theta_{12} \rightarrow \pi/2$. Notice also that, in opposition to the case studied before, we always obtain an anticipated signal as the phase obtained is located always at the first quadrant. As an example, in figure 21, numerical simulations have been done for $\omega_1 = 3.0 \text{ rad}\cdot\text{s}^{-1}$, $\omega_2 = 4.0 \text{ rad}\cdot\text{s}^{-1}$, $\kappa = 2.0 \text{ rad}\cdot\text{s}^{-1}$ and for $\delta = 4\pi/5, 3\pi/5$.

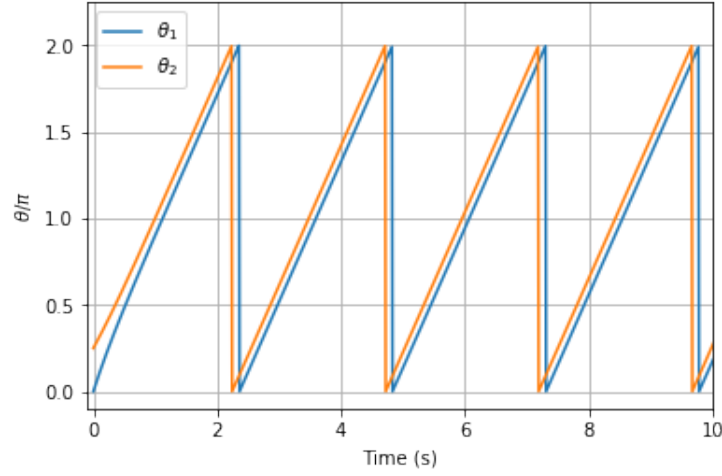


Figure 20: Results obtained with the numerical simulations for the case in which $\cos \delta > 0$ and with $\omega_1 = 3.0 \text{ rad}\cdot\text{s}^{-1}$, $\omega_2 = 5.0 \text{ rad}\cdot\text{s}^{-1}$, $\delta = 2\pi/3$, $\kappa = 2.0 \text{ rad}\cdot\text{s}^{-1}$.

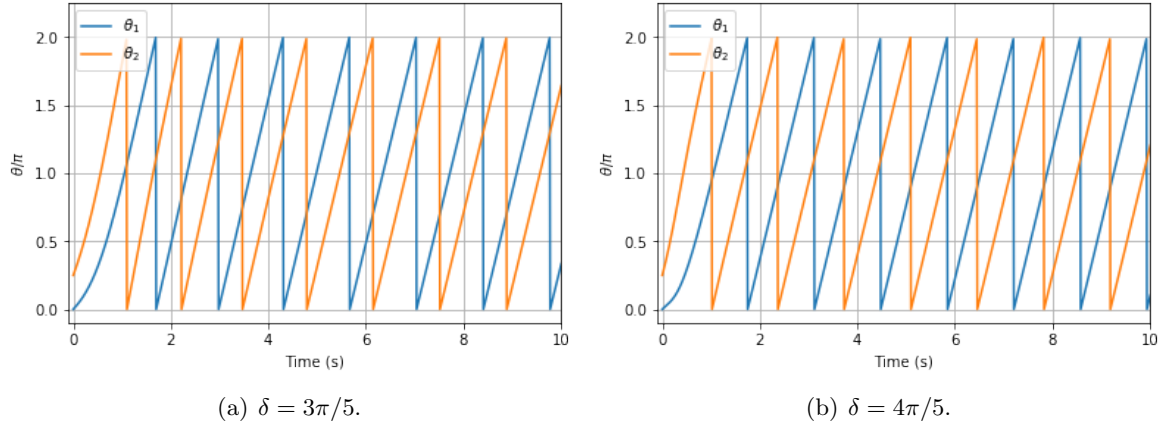


Figure 21: Numerical simulation for the case in which $c < 1$. Notice that, as commented, the phase difference is always negative having then a phase delay.

Case $c > 1$

In this case, the phase difference between oscillators is given by

$$\theta_{12} = -2 \arctan \left(\frac{1 + \sqrt{c^2 - 1} \tan(\sqrt{c^2 - 1}(-\kappa t \cos \delta + A))}{c} \right), \quad (5.25)$$

where we can see that the phase will be continuously oscillating.

Discussion

In all the cases we have studied along this section, delayed or anticipated signals have been obtained, but a situation in which both oscillators are in phase does not appear. The main reason for that lies on the eq. (5.13), which shall be interpreted as the equation for an oscillator whose natural frequency is $\Delta\omega$ and which is perturbed by a modulated function with coupling constant $2\kappa \cos \delta$ that depends, somehow, in the own oscillation of the system. As this perturbation is sinusoidal, it will never cancel the natural oscillation so $\theta_{12} \neq 0$. Nevertheless, if this perturbation was a $\cos x$ function, then we should obtain a situation in which $\theta_{12} = 0$, concretely when the corresponding definition of the constant c takes the value 1.

5.4 Excitatory and inhibitory junctions with same coupling constants and same natural frequencies

Under this situation in which $\kappa > 0$, $\kappa' < 0$, $\kappa = -\kappa'$ and $\omega_1 = \omega_2 = \omega$, eq. (5.1) takes the form

$$\begin{aligned} \dot{\theta}_1 &= \omega + \kappa \sin(\theta_{12} + \delta) \\ \dot{\theta}_2 &= \omega + \kappa \sin(\theta_{12} - \delta) \end{aligned} \quad (5.26)$$

From here, it can be seen easily that the phase difference between oscillators is characterized by

$$\dot{\theta}_{12} = 2\kappa \sin \delta \cos \theta_{12}, \quad (5.27)$$

by applying trigonometric relationships. Therefore, once solved this differential equation, it can be seen that the following expression is obtained

$$\frac{\sin \theta_{12} + 1}{\cos \theta_{12}} = \exp(2\kappa t \sin \delta + A). \quad (5.28)$$

Reached this point, we can differ between two situations: $0 < \delta < \pi$ or $-\pi < \delta < 0$. For the first one, the exponential will be positive so for long enough times we obtain $\theta_{12} \rightarrow \pi/2$, that is, the slave is delayed with respect to the master. Nevertheless, for the second situation we will have a negative exponential which leads to $\theta_{12} \rightarrow -\pi/2$ being the slave ahead of the master.

Indeed, these results obtained analytically coincide with the numerical simulations (figure 22) where we have chosen $\omega_1 = \omega_2 = \pi \text{ rad}\cdot\text{s}^{-1}$ and $\kappa = -\kappa' = 1.0 \text{ rad}\cdot\text{s}^{-1}$.

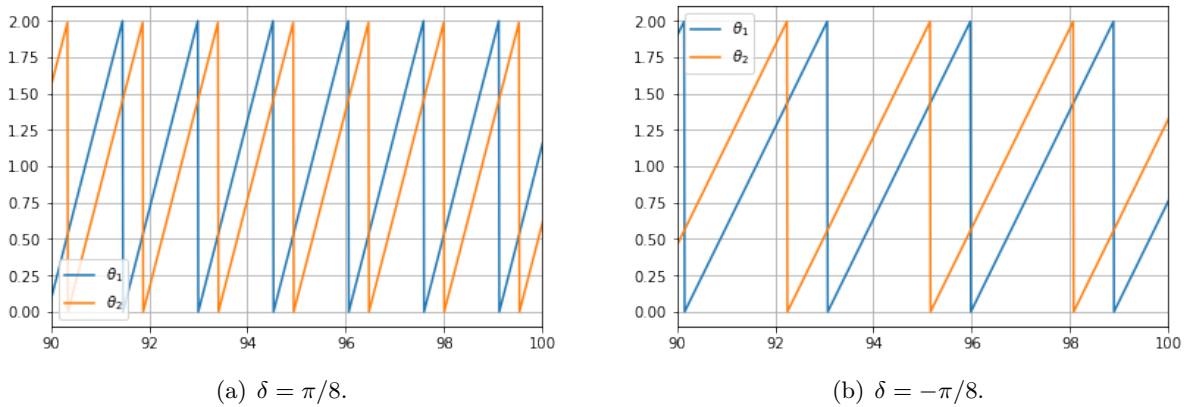


Figure 22: Numerical simulations for mutually coupled oscillators under the conditions $\omega_1 = \omega_2$ and $\kappa = -\kappa'$. This results correspond to the time interval [90, 100] s.

5.5 Excitatory and inhibitory junctions with same coupling constants and different natural frequencies

In the analysis that will be performed in this subsection, $\Delta\omega$ will always be negative. However, it is necessary to distinguish between the situations in which $0 < \delta < \pi$ and $-\pi < \delta < 0$.

5.5.1 Positive delay of the signal

Now, the only difference with respect to eq. (5.26) is that $\omega_1 \neq \omega_2$ so the phase difference is given by

$$\dot{\theta}_{12} = -\Delta\omega + 2\kappa \sin \delta \cos \theta_{12}, \quad (5.29)$$

and this differential equation shall be written as

$$\int \frac{d\theta_{12}}{c - \cos \theta_{12}} = -2t\kappa \sin \delta + A, \quad (5.30)$$

where we have defined $c = \Delta\omega/2\kappa \sin \delta$. As it happens on the cases shown before, depending on the value of that constant, we can distinguish between different possibilities: $c = 1$, $c < 1$ and $c > 1$. However, for all of them, the same change of variable is performed in the integral located at the first term of eq. (5.30), $z = \tan(\theta_{12}/2)$, having then

$$I = 2 \int \frac{dz}{(c+1)z^2 + (c-1)}. \quad (5.31)$$

Case $c = 1$ In this case, the integral that appears in eq. (5.31) reduces to

$$I = \int \frac{dz}{z^2} = -\frac{1}{z}. \quad (5.32)$$

Therefore, the phase difference is given by

$$\theta_{12} = 2 \arctan\left(\frac{1}{2t\kappa \sin \delta + A}\right), \quad (5.33)$$

and by waiting a long enough time, taking into account that the dividend is always positive, the phase difference θ_{12} tends to 0, as it is shown in figure 23 where we have taken $\omega_1 = 2.0 \text{ rad}\cdot\text{s}^{-1}$, $\omega_2 = 4.0 \text{ rad}\cdot\text{s}^{-1}$, $\kappa = -\kappa' = 1.0 \text{ rad}\cdot\text{s}^{-1}$ and $\delta = \pi/2$.

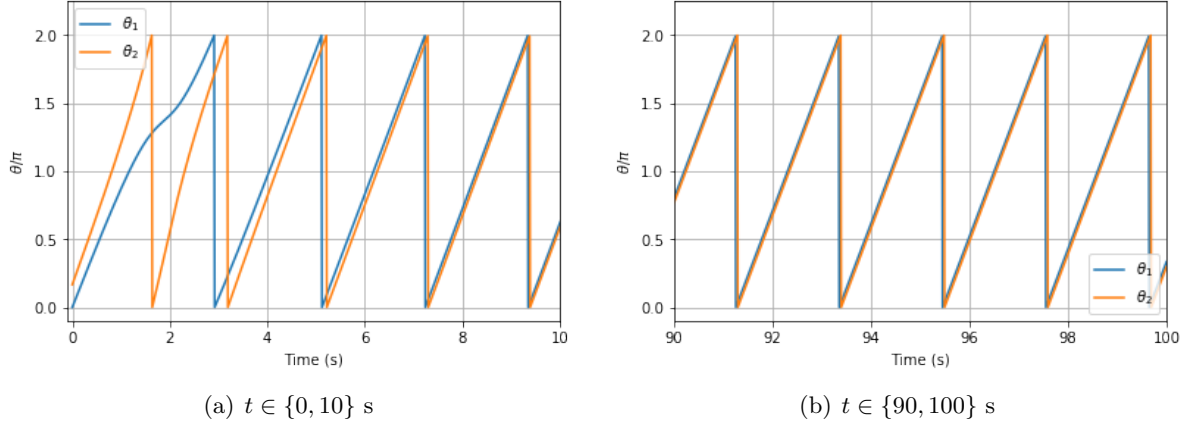


Figure 23: Representation for the case $c = 1$ where we see that, when t is very high the phase difference between the oscillators is null. At the beginning of the dynamics, the first oscillator adapts its movement with the main objective to reach the situation shown at the right.

Case $c < 1$ In this case, the integral that appears in eq. (5.31) takes the form

$$I = \frac{-1}{1-c} \left[\int \frac{dz}{\sqrt{(c+1)/(1-c)z+1}} - \int \frac{dz}{\sqrt{(c+1)/(1-c)z-1}} \right] \quad (5.34)$$

and, introducing it in eq. (5.30), we obtain that the phase difference is

$$\theta_{12} = 2 \arctan\left(\sqrt{\frac{1-c}{c+1}} \cdot \frac{\exp\{\sqrt{1-c^2}(2t\kappa \sin \delta + A)\} + 1}{\exp\{\sqrt{1-c^2}(2t\kappa \sin \delta + A)\} - 1}\right). \quad (5.35)$$

Nevertheless, for long enough times, this last relationship turns into

$$\theta_{12} = 2 \arctan\left(\sqrt{\frac{1-c}{c+1}}\right). \quad (5.36)$$

Choosing $\delta = \pi/2$, $\Delta\omega = 2.0 \text{ rad}\cdot\text{s}^{-1}$ and $\kappa = -\kappa' = 2.0 \text{ rad}\cdot\text{s}^{-1}$, then, theoretically, $\theta_{12} = \pi/3$, which coincide with the numerical value shown in figure 24.

Case $c > 1$ Finally, in this case we find that the integral of eq. (5.31) can be written as follows

$$I = \frac{2}{c-1} \int \frac{dz}{[\sqrt{(c+1)/(c-1)z}]^2 + 1} = \frac{2}{\sqrt{c^2-1}} \arctan\left(\sqrt{\frac{c+1}{c-1}}z\right) \quad (5.37)$$

so the phase difference will be given by

$$\theta_{12} = 2 \arctan\left(\sqrt{\frac{c-1}{c+1}} \tan\left(\sqrt{c^2-1}[\kappa t \sin \delta + A]\right)\right). \quad (5.38)$$

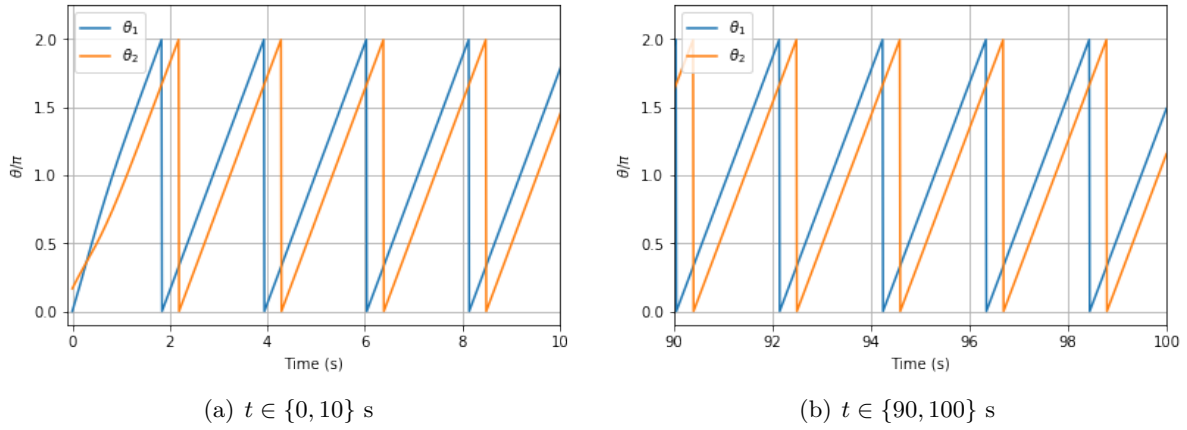


Figure 24: Representation for the case $c < 1$ where we see that, when t is very high and for certain values of $\Delta\omega$, δ and κ , the phase difference between the oscillators is $\pi/3$.

Under this conditions, something very interesting happens because, as t is continuously varying, taking positive and negative values, the phase difference will be changing all along the time evolution of the system but periodically since $\tan x$ is a periodic function. In fact, by choosing the parameters $\Delta\omega = 4.0 \text{ rad}\cdot\text{s}^{-1}$, $\kappa = -\kappa' = 1.0 \text{ rad}\cdot\text{s}^{-1}$ and $\delta = \pi/2$, the situation described above is obtained by the numerical simulations (see figure 25).

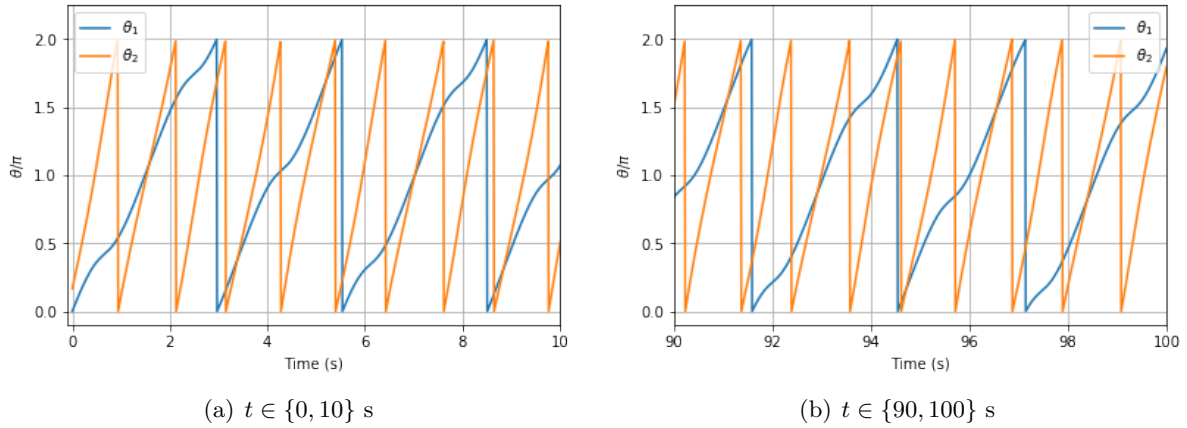


Figure 25: Representation for the case $c > 1$ where we see that, the phase difference between both oscillators is continuously varying periodically.

Discussion

The common factor of all the cases we have studied in this subsection, is that the signal of the second oscillator is either in phase (first case) or delayed (second case). The last case can be considered as the *chaotic* one as the phase difference is continuously changing but periodically.

However, in order to give an interpretation to this results, let us focus on eq. (5.5), which tells us that our system can be understood as a single oscillator whose natural frequency is $\Delta\omega$ and that is perturbed by an external signal of amplitude $2\kappa\sin\delta$ which, somehow, is coupled to the oscillator's oscillation. Then, when we are in the case in which $c = 1$, this signal has the same amplitude as the natural oscillation, but the main difference is that one is positive and the other one is negative, which cancels out giving a zero different phase. In the following case, $c < 1$, the external oscillation is bigger than the natural frequency so it can null it completely but when that oscillation is zero, the frequency rises quickly because of the natural oscillation, leading to a certain phase difference. Finally, in the case $c > 1$, the natural frequency is bigger than the amplitude so this last one cannot cancel it at all, having then different phases differences at different times. However, as the perturbation is a periodic function, then the changes on the phase will also be periodic.

5.5.2 Negative delay of the signal

In this other case, the phase difference takes the following form

$$\dot{\theta}_{12} = -\Delta\omega - 2\kappa \sin \delta \cos \theta_{12}, \quad (5.39)$$

which can be written as follows

$$\int \frac{d\theta_{12}}{c + \cos \theta_{12}} = -2t\kappa \sin \delta + A. \quad (5.40)$$

Reached this point we are on disposal of analysing the different situations shown on the previous subsection. For so, the change of variable that we will perform over the integral located at the first member is $z = \tan(\theta_{12}/2)$, having in this case

$$I = 2 \int \frac{dz}{(c-1)z^2 + (c+1)}. \quad (5.41)$$

Case $c = 1$

The integral that appears in eq. (5.41) takes in this case the following form

$$I = 2 \int \frac{dz}{c+1} = \frac{2z}{c+1}, \quad (5.42)$$

being the phase difference then

$$\theta_{12} = 2 \arctan((c+1)[- \kappa t \sin \delta + A]). \quad (5.43)$$

From here, we see that, for long enough times, $\theta_{12} \rightarrow -\pi$, and unlike the case studied above, the phase of the oscillations are in anti-phase. Indeed, this can be seen in figure 26 where $\omega_1 = 2.0 \text{ rad}\cdot\text{s}^{-1}$, $\omega_2 = 4.0 \text{ rad}\cdot\text{s}^{-1}$, $\kappa = -\kappa = 1.0 \text{ rad}\cdot\text{s}^{-1}$ and $\delta = -\pi/2$.

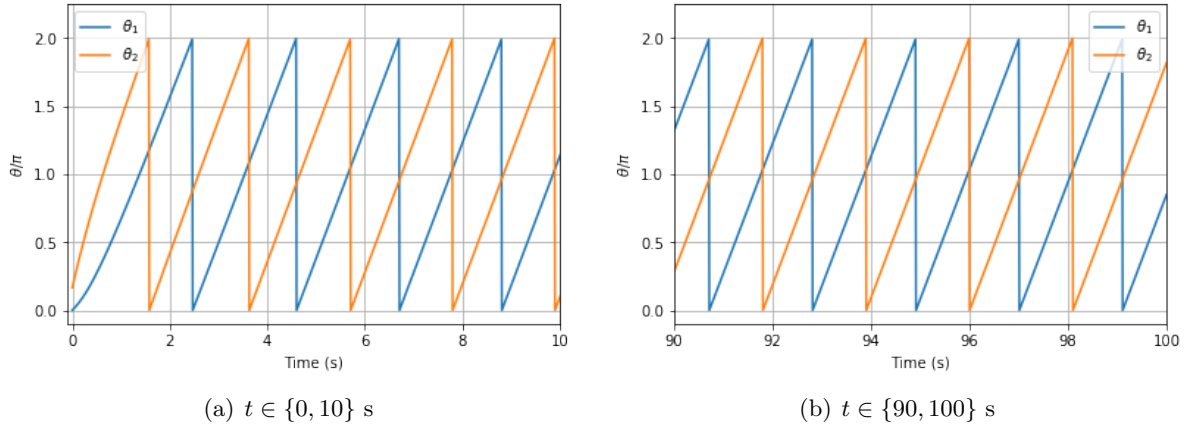


Figure 26: Representation for the case $c = 1$ where we see that, when t is very high, the phase difference between the oscillators is π .

Case $c < 1$

In this case, the integral shown in eq. (5.41) can be written as

$$\begin{aligned} I &= -\frac{2}{c+1} \int \frac{dz}{[\sqrt{(1-c)/(c+1)}z]^2 - 1} = \\ &= \frac{1}{c+1} \ln \left| \frac{\sqrt{1-cz} + \sqrt{c+1}}{\sqrt{1-cz} - \sqrt{c+1}} \right| \end{aligned} \quad (5.44)$$

which leads to the following phase difference

$$\theta_{12} = 2 \arctan \left(\sqrt{\frac{c+1}{c-1}} \frac{\exp[(c+1)(-\kappa t \sin \delta + A)] - 1}{\exp[(c+1)(-\kappa t \sin \delta + A)] + 1} \right). \quad (5.45)$$

For long enough times, this last equation leads to the following relationship, which is quite similar to eq. (5.36),

$$\theta_{12} = 2 \arctan\left(\sqrt{\frac{c+1}{1-c}}\right) \quad (5.46)$$

and employing the same parameters used in that case, we obtain that the phase difference between those two oscillators tend to $-2\pi/3$, result which coincides with the numerical simulations shown in figure 27.

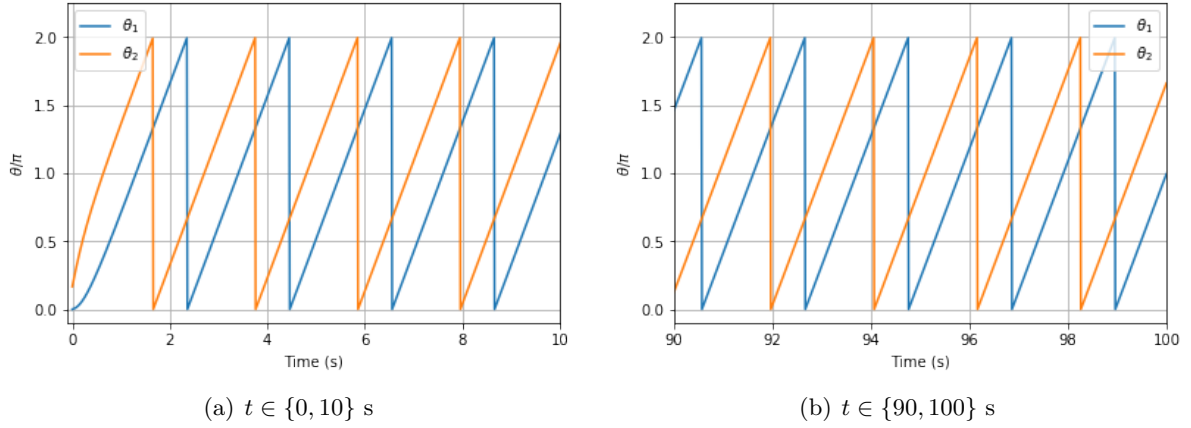


Figure 27: Representation for the case $c < 1$ where we see that, when t is very high and for certain values of $\Delta\omega$, δ and κ , the phase difference between the oscillators is $-2\pi/3$.

Case $c > 1$ Finally, in this last case, we find that eq. (5.41) can be written as

$$I = \frac{2}{c+1} \int \frac{dz}{([\sqrt{(c-1)/(c+1)}z]^2 + 1)} = \frac{2}{c+1} \arctan\left(\sqrt{\frac{c-1}{c+1}}z\right), \quad (5.47)$$

being the phase difference

$$\theta_{12} = 2 \arctan\left(\sqrt{\frac{c+1}{c-1}} \tan [(c+1)(-\kappa t \sin \delta + A)]\right). \quad (5.48)$$

As it happens in the correspondent case for positive values of δ , it is obtained that the phase difference will be continuously and periodically varying as it is shown in figure 28.

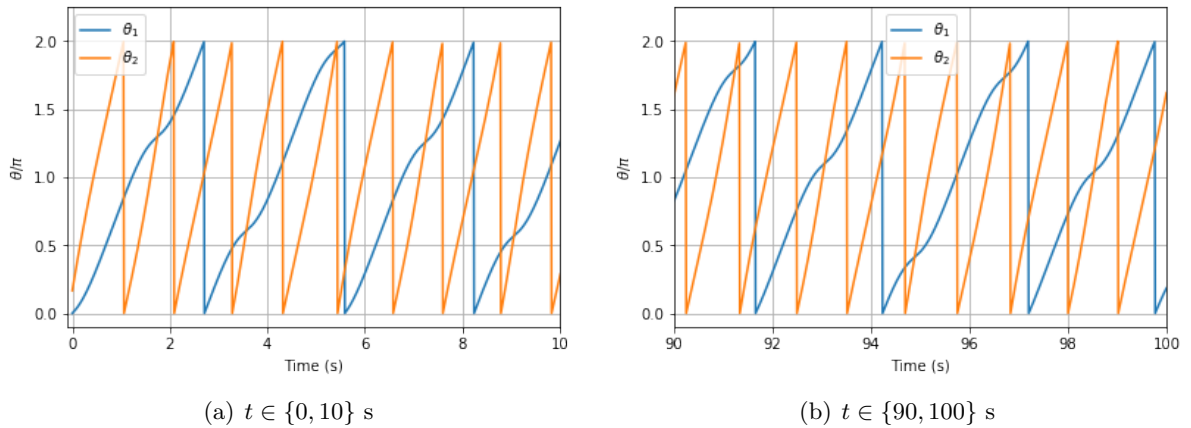


Figure 28: Representation for the case $c > 1$ where we see that, the phase difference between both oscillators is continuously varying periodically.

Discussion Similarly to the case studied for positive values of the delay, the common factor of all the cases studied is that the signal of the second oscillator is always ahead to the first oscillator's signal (except in the last case studied) and, indeed, the equation can be also considered to be an isolated oscillator with a certain phase.

5.6 Excitatory and inhibitory junctions with different coupling constants and natural frequencies

This is one of the most general cases we can consider and, indeed, it is not going to be solved exactly as we have been doing until now. In fact, we will try to show that this system can be reduced to the ones analysed before by studying a given simple example.

According to the situation which we are working with, eq. (5.1) shall be rewritten as

$$\begin{aligned}\dot{\theta}_1 &= \omega_1 + \kappa' \sin(\theta_{12} + \delta) \\ \dot{\theta}_2 &= \omega_2 + \kappa \sin(\theta_{12} - \delta)\end{aligned}, \quad (5.49)$$

and the phase difference between oscillators will be characterized by

$$\dot{\theta}_{12} = \Delta\omega + \kappa' \sin(\theta_{12} + \delta) - \kappa \sin(\theta_{12} - \delta). \quad (5.50)$$

However, if we want to predict the behaviour of this system under certain considerations, it seems convenient to write this last expression in another way. Indeed, by using trigonometric relationships, it can be demonstrated that

$$\dot{\theta}_{12} = -\Delta\omega + \kappa_1 \sin \theta_{12} + \kappa_2 \cos \theta_{12}, \quad (5.51)$$

where $\kappa_1 = (\kappa' - \kappa) \cos \delta$, $\kappa_2 = (\kappa' + \kappa) \sin \delta$ and we have assumed that $\omega_2 > \omega_1$. This result tells us that our oscillator, whose natural frequency is $\Delta\omega$, is perturbed by two kinds of couplings, one which goes with the sine of θ_{12} and the other one goes with the cosine of that quantity. But in the analysis performed all along this section, we have been dealing with this kind of disturbances and from the corresponding results, we can induce the system's behaviour.

For instance, suppose that $\kappa_2 = \Delta\omega$ and $\sin \delta > 0$. According to what we have commented before (section 5.5.1), under these circumstances the term $-\Delta\omega + \kappa_2 \cos \theta_{12}$ is null. Thereby, eq. (5.51) will lead to

$$\dot{\theta}_{12} = \kappa_1 \sin \theta_{12}, \quad (5.52)$$

and by choosing $|\kappa'| < |\kappa|$, in accordance to the results shown in figure 17, the phase difference should be zero.

If we now take $\omega_1 = 1.0 \text{ rad}\cdot\text{s}^{-1}$, $\omega_2 = 4.0 \text{ rad}\cdot\text{s}^{-1}$, $\kappa_1 = -2.0 \text{ rad}\cdot\text{s}^{-1}$, $\kappa_2 = 4.0 \text{ rad}\cdot\text{s}^{-1}$ and $\delta = \pi/2$, employing numerical simulations, we obtain a result which is in concordance with what we have predicted.

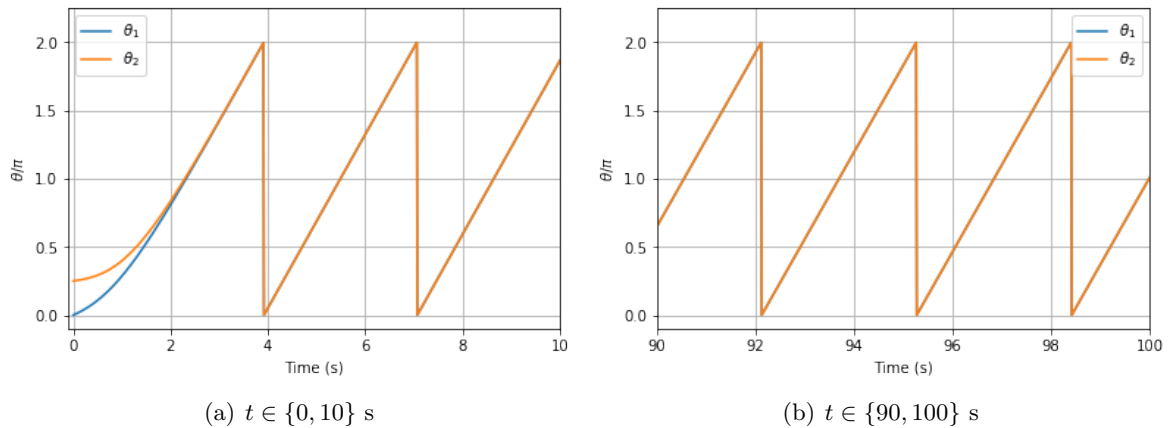


Figure 29: Representation for the case in which $\Delta\omega = \kappa_1$ whose behaviour was predicted previously. The parameters employed for this purpose are $\omega_1 = 1.0 \text{ rad}\cdot\text{s}^{-1}$, $\omega_2 = 4.0 \text{ rad}\cdot\text{s}^{-1}$, $\kappa_1 = -2.0 \text{ rad}\cdot\text{s}^{-1}$, $\kappa_2 = 4.0 \text{ rad}\cdot\text{s}^{-1}$ and $\delta = \pi/2$.

Discussion With this simple example what we are trying to show is that one of the most general cases for this set of oscillators can be reduced to the analysis of a unique oscillator. Also, the effect of those perturbations over that oscillator correspond to analytically solvable cases that have been studied all along this last section.

6 Master-slave configuration with a class 1 coupling

Until now, we have been working with the Kuramoto model employing a coupling characterized by a sine function which has a 2π period and that takes either positive and negative values. Now, we want to work with another kind of coupling which has the same period but that takes only positive values, and for so, a good choice seems the function $\sin^2(x/2)$. Thereby, the equations that characterize the master-slave configuration (eq. 4.1) will be rewritten as

$$\begin{aligned}\dot{\theta}_1 &= \omega_1 \\ \dot{\theta}_2 &= \omega_2 + \frac{\kappa}{2} \left[1 - \cos(\theta_1 - \theta_2 - \delta) \right] \end{aligned} \quad , \quad (6.1)$$

where we have taken into account that

$$\sin^2(x) = \frac{1 - \cos(2x)}{2}. \quad (6.2)$$

The procedure that we are going to follow in order to study this system with the new coupling is exactly the same we have done previously with the class 2 coupling.

6.1 Equal natural frequencies ($\omega_1 = \omega_2 = \omega$)

In this first case we are going to study, eq. (6.1) takes the form

$$\begin{aligned}\dot{\theta}_1 &= \omega \\ \dot{\theta}_2 &= \omega + \frac{\kappa}{2} \left[1 - \cos(\theta_{12} - \delta) \right] \end{aligned} \quad , \quad (6.3)$$

being the phase difference between both oscillators

$$\dot{\theta}_{12} = -\frac{\kappa}{2} \left[1 - \cos(\theta_{12} - \delta) \right]. \quad (6.4)$$

From this last relationship and assuming that we are under phase locking conditions, it can be seen easily that $\theta_{12}^* = \delta$. On the other hand, if we are considering the general case, then the differential equation presented above has to be solved. This one can be written as

$$\int \frac{d\theta_{12}}{1 - \cos(\theta_{12} - \delta)} = -\frac{2}{\kappa} t + A, \quad (6.5)$$

and solving the integral that appears in the first term, we get that the dependence of the phase difference with the time variable is given by

$$\theta_{12} = \delta + 2 \arctan\left(\frac{1}{t/\kappa + A}\right). \quad (6.6)$$

From here we see that for long enough times, θ_{12} tends to δ , as it predicts the phase locking solution. Hence, independently on the initial conditions of the problem, that is, the initial phase difference between oscillators, at the end of the day we will obtain $\theta_{12} = \delta$, which means that the phase locked solution is stable. This analytical result has been checked with the numerical simulations satisfactorily (see figure 30) where we have taken $\omega = \pi \text{ rad}\cdot\text{s}^{-1}$, $\kappa = 1.0 \text{ rad}\cdot\text{s}^{-1}$ and different values for δ . If this last quantity is positive, negative or zero, then anticipated, delayed and in-phase synchronization will be obtained, respectively.

6.2 Different natural oscillations ($\omega_1 \neq \omega_2$)

If the natural frequencies for both oscillators are different, then from eq. (6.1) we get that the phase difference between them is given by

$$\dot{\theta}_{12} = \Delta\omega - \frac{\kappa}{2} \left[1 - \cos(\theta_{12} - \delta) \right]. \quad (6.7)$$

In this case, it seems relevant to distinguish between the phase locked solutions and those ones in which this condition is not applied, as we will have to distinguish what happens for different values of a certain constant $c = 2\Delta\omega/\kappa$.

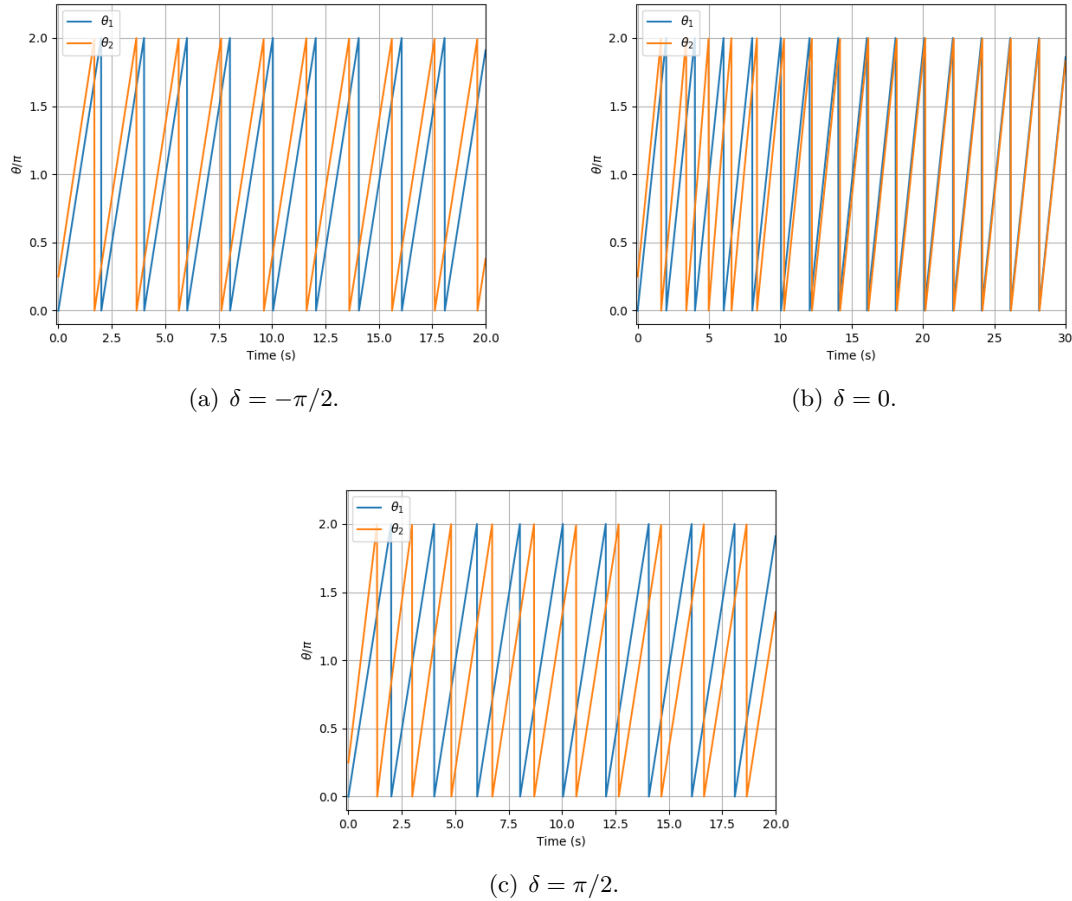


Figure 30: Numerical simulations for different values of δ and $\omega = \pi \text{ rad}\cdot\text{s}^{-1}$, $\kappa = 1.0 \text{ rad}\cdot\text{s}^{-1}$. Anticipated, in-phase and delayed signals are obtained, respectively.

6.2.1 Phase locking

Imposing phase locking condition to eq. (6.7), we obtain

$$\theta_{12}^* = \delta + \arccos(1 - c) \quad (6.8)$$

where we have defined $c = 2\Delta\omega/\kappa$. From this result we see that there are certain values of $\Delta\omega$ which are not allowed. Indeed the condition that c must satisfy is

$$|1 - c| \leq 1 \quad (6.9)$$

being one of its implications that c cannot take negative values, that is, $\omega_2 \not\prec \omega_1$. Another one, is that $c \not\prec 2$, but this one shall be analysed later.

The reason why negatives values of c are not possible here while with the other coupling they can be appear without any problem, lies on the fact that now the coupling only takes positive values while in the other case negative values were also allowed. When the slave oscillator has a bigger frequency than the master one, information in principle has to flow from the former to the latter but the unidirectionality of the coupling do not allow this. In the first case analysed (section 4.1.2), the negative values of the sine were able to change the arrow's sense (see figure 6) but now, we only have positive values which does not allow information's transmission from slave to master, having then in those cases unstable solutions and, thus, no possibility of having synchronization phenomenons.

6.2.2 Not imposing phase locking condition

According to what we have seen in the study of phase locking, only certain values of c will give us phase locked solutions and they involve the case in which $\omega_1 > \omega_2$ but satisfying always the

condition $c < 2$. We are going now to analyse deeply this situation and, for so, we must solve the differential equation

$$\int \frac{d\theta_{12}}{(c-1) + \cos(\theta_{12} - \delta)} = \frac{2}{\kappa}t + A, \quad (6.10)$$

so, in short, we have to examine the following integral

$$I = \int \frac{dx}{(c-1) + \cos x} \quad (6.11)$$

under different situations.

Case $c = 1$ In this case, the integral shown in eq. (6.11) gets reduced to

$$I = \int \frac{dx}{\cos x}, \quad (6.12)$$

and it is solved by performing the change $z = \tan(x/2)$, having then

$$I = \ln \left| \frac{z+1}{z-1} \right| \quad (6.13)$$

which substituted in eq. (6.10) leads to

$$\theta_{12} = \delta + 2 \arctan \left(\frac{\exp\{2t/\kappa + A\} + 1}{\exp\{2t/\kappa + A\} - 1} \right). \quad (6.14)$$

Here we see that, for long enough times, $\theta_{12} \rightarrow \delta + \pi/2$ so depending on the values of δ , we will have anticipated, in-phase and delayed synchronization. These results are in concordance with the numerical simulations shown in figure 31 in which we have chosen $\omega_1 = 3.0 \text{ rad}\cdot\text{s}^{-1}$, $\omega_2 = 2.0 \text{ rad}\cdot\text{s}^{-1}$ and $\kappa = 2.0 \text{ rad}\cdot\text{s}^{-1}$.

Case $1 < c < 2$ In this case, the integral shown in eq. (6.11) takes the form

$$I = - \int \frac{dx}{1 - c - \cos x} \quad (6.15)$$

and, once solving it, we get

$$I = \frac{1}{2c - c^2} \ln \left| \frac{z\sqrt{2-c} + \sqrt{c}}{z\sqrt{2-c} - \sqrt{c}} \right|. \quad (6.16)$$

Introducing this last result in the differential equation, we get that the phase difference is given as follows

$$\theta_{12} = \delta + 2 \arctan \left(\frac{\sqrt{2-c}}{\sqrt{c}} \cdot \frac{\exp\{\sqrt{2c-c^2}(2t/\kappa + A)\} + 1}{\exp\{\sqrt{2c-c^2}(2t/\kappa + A)\} - 1} \right) \quad (6.17)$$

and for long enough times

$$\theta_{12} = \delta + 2 \arctan \left(\frac{\sqrt{2-c}}{\sqrt{c}} \right). \quad (6.18)$$

Again, in this case, depending on the values of c and δ , we can obtain anticipated, in-phase and delayed signals.

Case $c = 2$ Finally, in this last case, the integral shown above takes the following form

$$I = \int \frac{dx}{1 + \cos x} = \tan \left(\frac{\theta_{12} - \delta}{2} \right), \quad (6.19)$$

which substituted in the differential equation leads to the following phase difference

$$\theta_{12} = \delta + 2 \arctan(t/\kappa + A). \quad (6.20)$$

This result, as expected, coincides with the numerical simulations shown in figure 32 where we took $\omega_1 = 3.0 \text{ rad}\cdot\text{s}^{-1}$, $\omega_2 = 2.0 \text{ rad}\cdot\text{s}^{-1}$, $\kappa = 1.0 \text{ rad}\cdot\text{s}^{-1}$ and different values of δ . As we can see there, anticipated and in-phase signals can be obtained, but not delayed.

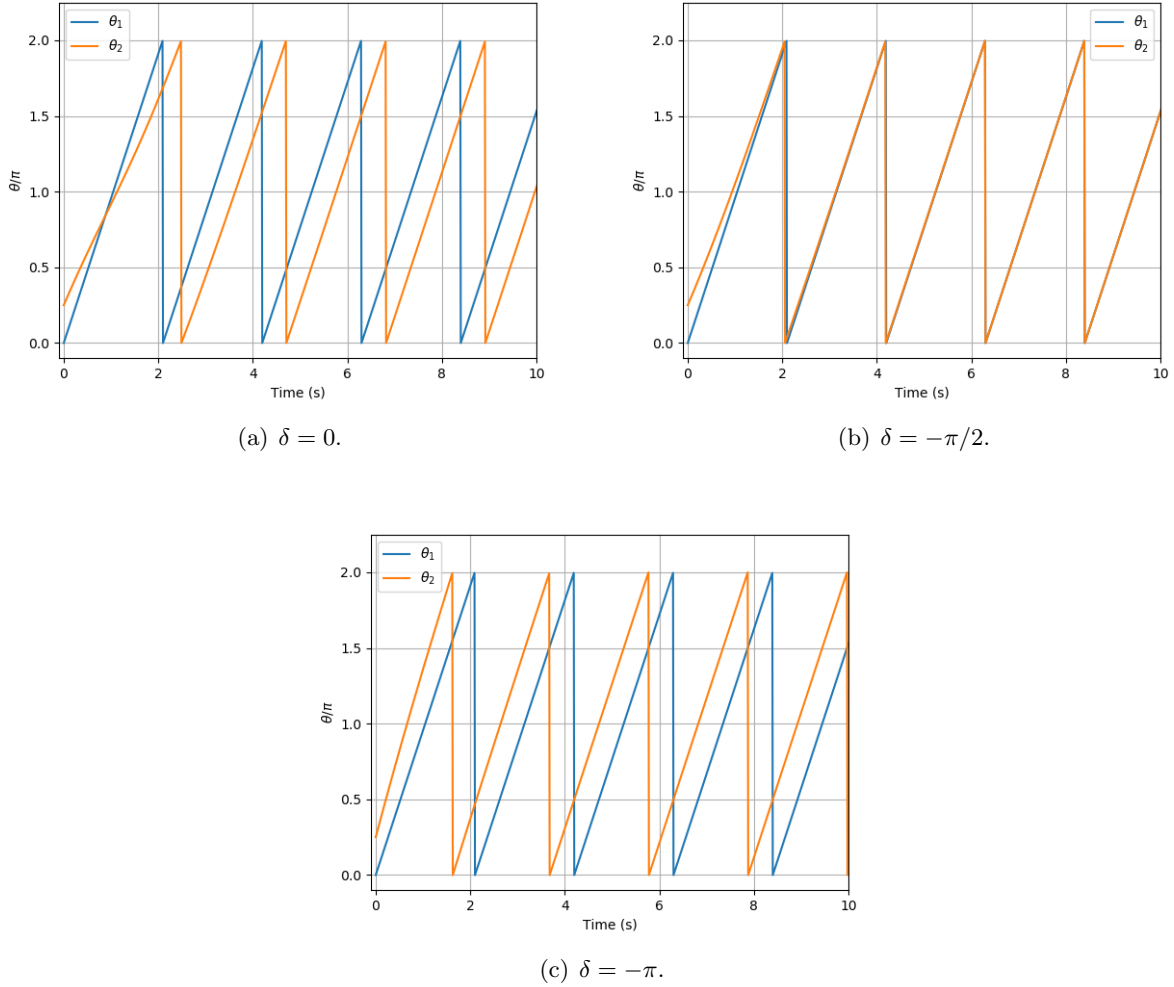


Figure 31: Numerical simulations for different values of δ and $\omega_1 = 3.0 \text{ rad}\cdot\text{s}^{-1}$, $\omega_2 = 2.0 \text{ rad}\cdot\text{s}^{-1}$ and $\kappa = 2.0 \text{ rad}\cdot\text{s}^{-1}$. Anticipated, in-phase and delayed signals are obtained, respectively.

7 Two mutually coupled oscillators with a class 1 coupling

In this section we will implement the new coupling to the mutually coupled oscillators configuration shown in figure 13. Thereby, the system of equations that governs its dynamic is given by

$$\begin{aligned}\dot{\theta}_1 &= \omega_1 + \frac{\kappa'}{2} \left[1 - \cos(\theta_2 - \theta_1 - \delta) \right] \\ \dot{\theta}_2 &= \omega_2 + \frac{\kappa}{2} \left[1 - \cos(\theta_1 - \theta_2 - \delta) \right] .\end{aligned}\quad (7.1)$$

As we did for the master-slave configuration, the same situations studied with the another coupling will be analysed in this case. But before that, let us see something very interesting in this case and is that, if $\delta = 0$ and $\kappa = \kappa'$, then $\dot{\theta}_{12} = \omega_1 - \omega_2$. From here we see that only if $\omega_1 = \omega_2$ we will get a phase locked situation; otherwise, the phase will be continuously changing with time and periodically.

7.1 Excitatory junction with same coupling constants and same natural frequencies

According to what we have commented above, in this subsection we will consider that $\delta \neq 0 + 2n\pi$, $n \in \mathbb{Z}$. Likewise, eq. (7.1) takes the following form

$$\begin{aligned}\dot{\theta}_1 &= \omega + \frac{\kappa}{2} \left[1 - \cos(\theta_{12} + \delta) \right] \\ \dot{\theta}_2 &= \omega + \frac{\kappa}{2} \left[1 - \cos(\theta_{12} - \delta) \right] ,\end{aligned}\quad (7.2)$$

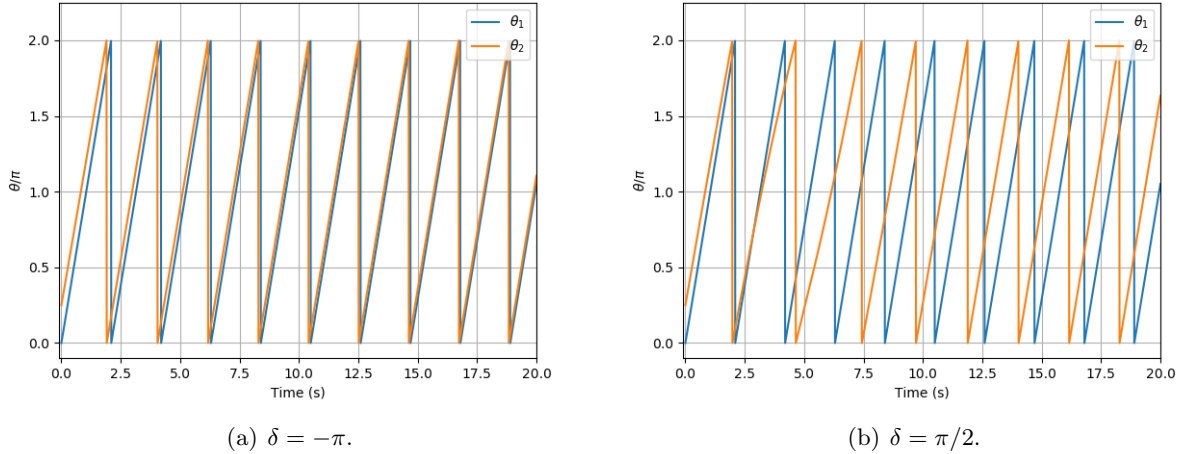


Figure 32: Numerical simulations for different values of $\omega_1 = 3.0 \text{ rad}\cdot\text{s}^{-1}$, $\omega_2 = 2.0 \text{ rad}\cdot\text{s}^{-1}$, $\kappa = 1.0 \text{ rad}\cdot\text{s}^{-1}$. Anticipated and in-phase signals are obtained, respectively.

being the phase difference between both oscillators

$$\dot{\theta}_{12} = \kappa \sin \delta \sin \theta_{12}. \quad (7.3)$$

From here, we can see immediately that the imposition of phase locking to our system leads to $\theta_{12}^* = 0, \pi$. Nevertheless, we are going to solve the differential equation shown above and see how it decays to those values, proving then that those solutions are stable. Concretely, we have

$$\int \frac{d\theta_{12}}{\sin \theta_{12}} = \kappa t \sin \delta + A. \quad (7.4)$$

In fact, the integral that appears in the first term of that differential equation was solved in section 5.1. So, recalling the corresponding result, it can be seen that the phase difference is characterized by

$$\theta_{12} = 2 \arctan(\exp\{\kappa t \sin \delta + A\}), \quad (7.5)$$

so for long enough times, $\theta_{12} \rightarrow \pi$ if $\sin \delta > 0$, something that is true if $\delta \in (0, \pi)$, and $\theta_{12} \rightarrow 0$ if $\sin \delta < 0$, which is valid if $\delta \in (-\pi, 0)$. Such results are in concordance with the numerical analysis shown in figure 33 where we have taken $\omega = \pi \text{ rad}\cdot\text{s}^{-1}$, $\kappa = 1.0 \text{ rad}\cdot\text{s}^{-1}$ and two different values of δ : one positive and the other one negative.

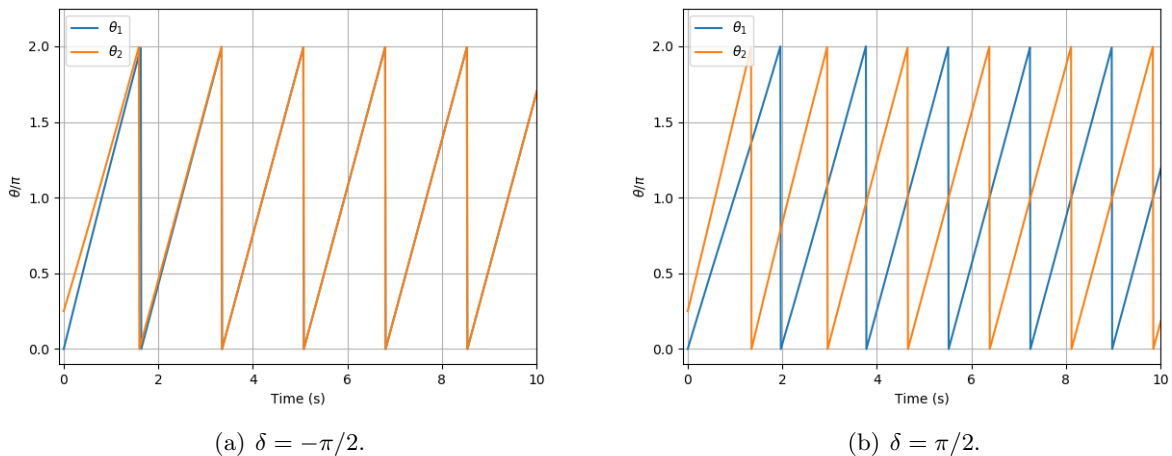


Figure 33: Numerical simulations employing $\omega = \pi \text{ rad}\cdot\text{s}^{-1}$, $\kappa = 1.0 \text{ rad}\cdot\text{s}^{-1}$. In-phase and anti-phase signals are obtained, respectively.

As it happens with the class 2 coupling, the values of δ play an important role in the resultant frequency of the interacting oscillators. Concretely, we obtain for long enough times

$$\dot{\theta}_1 = \dot{\theta}_2 = \omega + \frac{\kappa}{2} [1 \pm \cos \delta] \quad (7.6)$$

where the + solution corresponds to $\theta_{12} = \pi$ and the - one to $\theta_{12} = 0$.

7.2 Inhibitory junction with same coupling constants and same natural frequencies

Again, in this case, we will assume that $\delta \neq 0 + 2n\pi$ with $n \in \mathbb{Z}$. Also, under the circumstances considered, the evolution of each oscillator's phase is characterized by

$$\begin{aligned} \dot{\theta}_1 &= \omega - \frac{\kappa}{2} [1 - \cos(\theta_{12} + \delta)] \\ \dot{\theta}_2 &= \omega - \frac{\kappa}{2} [1 - \cos(\theta_{12} - \delta)] \end{aligned}, \quad (7.7)$$

being the phase difference between them

$$\dot{\theta}_{12} = -\kappa \sin \delta \sin \theta_{12}. \quad (7.8)$$

This relationship we have just obtained is quite similar to the one shown in eq. (7.3), being the main difference in a minus sign. Therefore, proceeding in the same way as we did before, we find that $\theta_{12}(t)$ is given by

$$\theta_{12} = 2 \arctan(\exp\{\kappa t \sin \delta + A\}). \quad (7.9)$$

Unlike the other case shown above, here for long enough times $\theta_{12} \rightarrow \pi$ if $\sin \delta < 0$ and $\theta_{12} \rightarrow 0$ if $\sin \delta > 0$, as it can be seen in the numerical simulations (figure 34) where the same constants are employed.

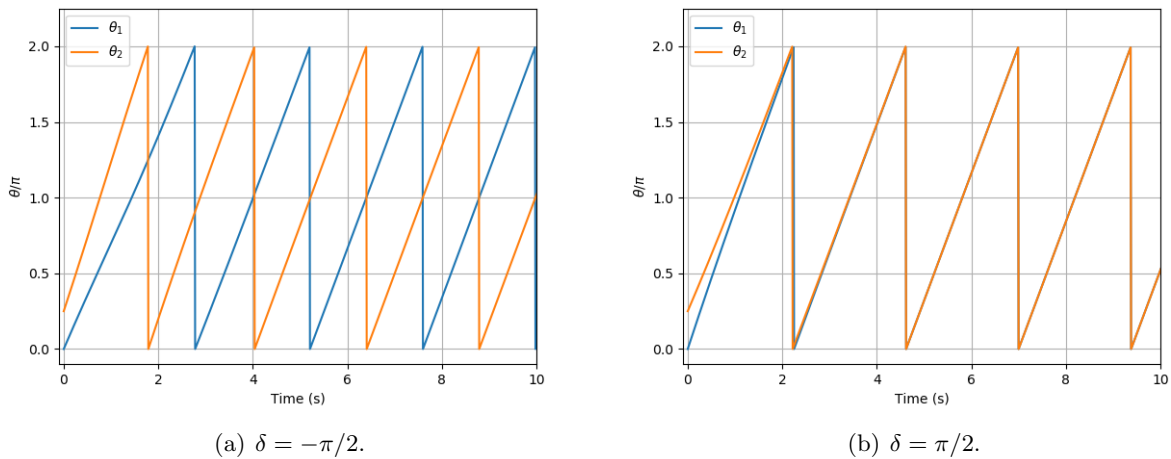


Figure 34: Numerical simulations employing $\omega = \pi \text{ rad}\cdot\text{s}^{-1}$, $\kappa = 1.0 \text{ rad}\cdot\text{s}^{-1}$. Anti-phase and in-phase signals are obtained, respectively.

With respect to the new frequencies of each oscillator, they are equal and described by

$$\dot{\theta}_1 = \dot{\theta}_2 = \omega - \frac{\kappa}{2} [1 \mp \cos \delta] \quad (7.10)$$

where the - solution corresponds to $\theta_{12} = 0$ and the other one to $\theta_{12} = \pi$.

7.3 Excitatory junction with same coupling constants but different natural frequencies

In this case, in principle, there are some values that δ cannot adopt if we want to obtain phase locked solutions, and is $\delta = 0$. Thereby, the equations that govern the evolution with time of the

phases, assuming that $\kappa > 0$, are given by

$$\begin{aligned}\dot{\theta}_1 &= \omega_1 + \frac{\kappa}{2} \left[1 - \cos(\theta_{12} + \delta) \right] \\ \dot{\theta}_2 &= \omega_2 + \frac{\kappa}{2} \left[1 - \cos(\theta_{12} - \delta) \right]\end{aligned}\quad (7.11)$$

Thereby, the time evolution of θ_{12} between oscillators is

$$\dot{\theta}_{12} = \Delta\omega + \kappa \sin \delta \sin \theta_{12}, \quad (7.12)$$

where it can be seen immediately that the phase locking conditions lead us to

$$\theta_{12}^* = \arcsin\left(-\frac{\Delta\omega}{\kappa \sin \delta}\right). \quad (7.13)$$

From this last expression, we see that only values of $c \in [-1, 1]$ are allowed, understanding by c the term $\Delta\omega/\kappa \sin \delta$. Thereby, frequencies higher than the effective coupling constant ($\kappa \sin \delta$) will lead, as we have seen with the other coupling, to a phase difference that change periodically with time. That is the reason why we are going to restrict ourselves to the cases in which $c \geq 1$. However, taking $\Delta\omega < 0$ we have to differ between the cases in which $\sin \delta > 0$ and $\sin \delta < 0$.

7.3.1 Delay contained in $[0, \pi]$

In this case we are under the conditions in which $\Delta\omega < 0$ and $\sin \delta > 0$. Thereby, the differential equation shown in eq. (7.12) is written as follows

$$\int \frac{d\theta_{12}}{c - \sin \theta_{12}} = -\kappa t \sin \delta + A. \quad (7.14)$$

An expression quite similar to this one was analysed in section 5.3.2 so we will restrict ourselves to present the results.

Case $c = 1$ In this case we find that the phase difference is given by

$$\theta_{12} = 2 \arctan\left(1 + \frac{2}{\kappa t \sin \delta + A}\right) \quad (7.15)$$

in such a way that, for long enough times, $\theta_{12} \rightarrow \pi/2$ as it can be seen on figure 35.

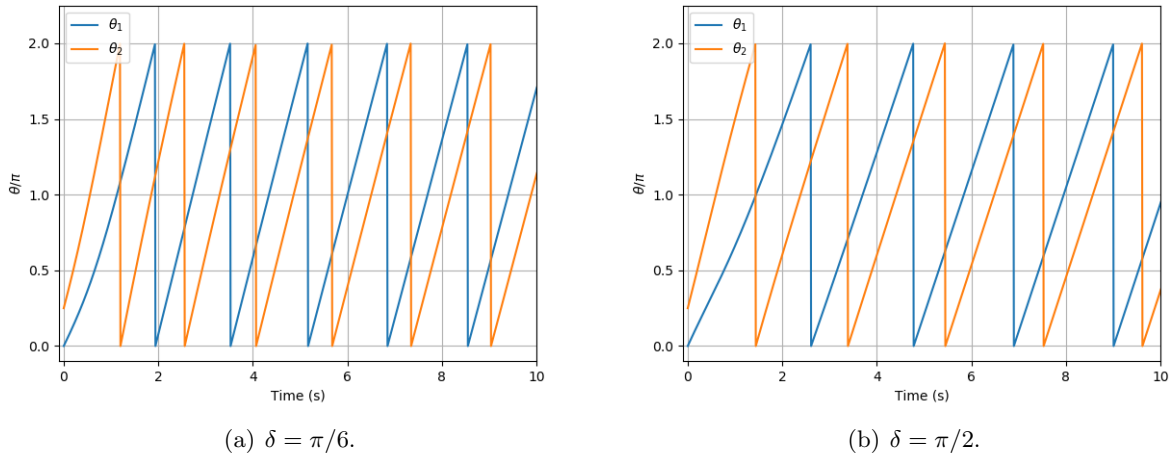


Figure 35: Numerical simulations using different values of δ in such a way that $c = 1$. The main difference between these two graphics lies on the oscillation's frequency.

Another interesting thing is that the possible values of δ have a very important role determining the final frequency of the oscillators. Indeed, when the phase is locked, those frequencies tend to

$$\begin{aligned}\dot{\theta}_1 &= \omega_1 + \frac{\kappa}{2} \left[1 + \sin \delta \right] \\ \dot{\theta}_2 &= \omega_2 + \frac{\kappa}{2} \left[1 - \sin \delta \right]\end{aligned}\quad (7.16)$$

Case $c < 1$ In this case, it can be proved that the phase difference is given by

$$\theta_{12} = 2 \arctan \left(\frac{(1 + \sqrt{1 - c^2}) \exp [\sqrt{1 - c^2}(\kappa t \sin \delta + A)] - 1 + \sqrt{1 - c^2}}{c(\exp [\sqrt{1 - c^2}(\kappa t \sin \delta + A)] - 1)} \right), \quad (7.17)$$

having then for long enough times

$$\theta_{12} = 2 \arctan \left(\frac{1 + \sqrt{1 - c^2}}{c} \right). \quad (7.18)$$

With this result we can see that the phase differences obtained are constant but always positive. Hence, we will not obtain under this circumstances an anticipated signal.

7.3.2 Delay contained in $[-\pi, \pi]$

Here we are under the conditions in which $\Delta\omega < 0$ and $\sin \delta < 0$, so the differential equation that must be solved is

$$- \int \frac{d\theta_{12}}{c + \sin \theta_{12}} = \kappa t \sin \delta + A, \quad (7.19)$$

where we have taken out the negative sign of the $\sin x$ function in such a way that $\sin \delta > 0$. Notice also that this relationship has been analysed in section 5.3.1. Thus, in the following paragraphs, we are going to present the results.

Case $c = 1$ In this case, the differential equation shown above leads to the following phase difference

$$\theta_{12} = 2 \arctan \left(\frac{2}{\kappa t \sin \delta + A} - 1 \right), \quad (7.20)$$

so at very long times $\theta_{12} \rightarrow -\pi/2$, as it can be seen with the numerical simulations shown in figure 36.

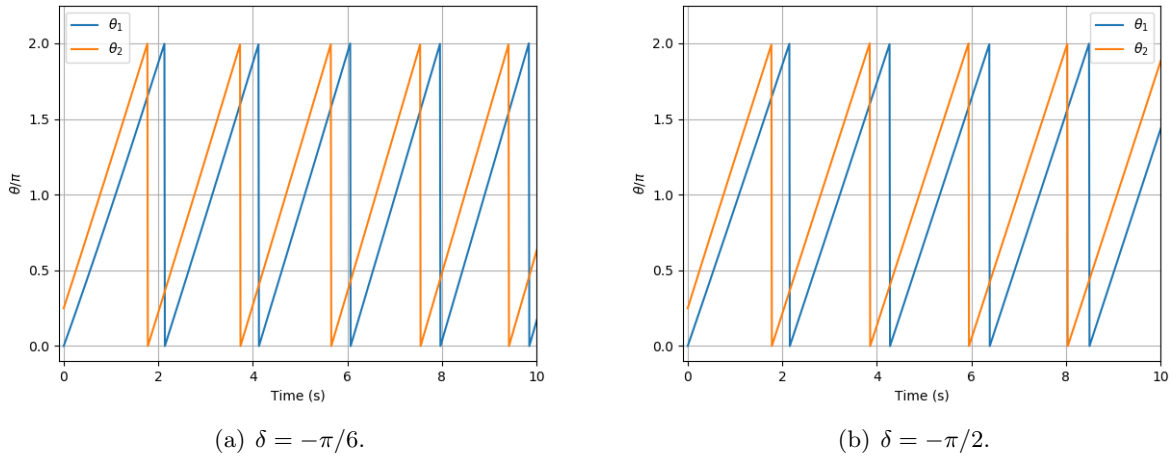


Figure 36: Numerical simulations using different values of δ in such a way that $c = 1$. The main difference between these two graphics lies on the oscillation's frequency (notice that the number of oscillations in the same time interval is different for each oscillator).

As it happened before, the values of δ determine the oscillator's frequency. In fact, the resultant expressions coincide with the ones shown in eq. (7.16).

Case $c < 1$ In this case, we can see that the phase difference is characterized by

$$\theta_{12} = 2 \arctan \left(\frac{(1 - \sqrt{1 - c^2}) \exp [\sqrt{1 - c^2}(\kappa t \cos \delta + A)] - 1 - \sqrt{1 - c^2}}{c(1 - \exp [\sqrt{1 - c^2}(\kappa t \cos \delta + A)])} \right), \quad (7.21)$$

and for long enough times, we get

$$\theta_{12} = -2 \arctan\left(\frac{1 - \sqrt{1 - c^2}}{c}\right) \quad (7.22)$$

Unlike the other case, now the phase differences are always negative so delayed signals will be obtained.

Discussion With the study performed in this subsection, we see that the results are quite similar to the ones obtained with the class 2 coupling. The main difference is that, then, we were dealing with a cosine function and now we have a sine function, being thus the corresponding intervals for δ different.

7.4 Excitatory and inhibitory junctions with the same coupling constants and same natural frequencies

In this subsection we are dealing with a situation in which $\kappa > 0$, $\kappa' < 0$, satisfying both of them that $\kappa = -\kappa'$ and $\omega_1 = \omega_2 = \omega$. Hence, in this case, eq. (7.1) takes the following form

$$\begin{aligned} \dot{\theta}_1 &= \omega - \frac{\kappa}{2} \left[1 - \cos(\theta_{12} + \delta) \right] \\ \dot{\theta}_2 &= \omega + \frac{\kappa}{2} \left[1 - \cos(\theta_{12} - \delta) \right], \end{aligned} \quad (7.23)$$

and from here it can be easily seen that the phase difference between oscillators is given by

$$\dot{\theta}_{12} = -\kappa [1 - \cos \theta_{12} \cos \delta]. \quad (7.24)$$

Considering phase locking conditions in our system, we find

$$\theta_{12}^* = \arccos\left(\frac{1}{\cos \delta}\right), \quad (7.25)$$

something that contrast sharply with the results for class 2 coupling. In that case we saw that all the values of δ were valid, but here only are possible two of them: $\delta = 0$ or π . Otherwise, the system will be unstable.

Instead of seeing how is the time evolution of the oscillators until that phase locked solution is achieved, we shall focus this subsection in analysing the reason why this is obtained when we use a class 1 coupling. For so, let us write more explicitly eq. (7.23)

$$\begin{aligned} \dot{\theta}_1 &= \omega - \frac{\kappa}{2} \left[1 - \cos \theta_{12} \cos \delta + \sin \theta_{12} \sin \delta \right] \\ \dot{\theta}_2 &= \omega + \frac{\kappa}{2} \left[1 - \cos \theta_{12} \cos \delta - \sin \theta_{12} \sin \delta \right] \end{aligned} \quad (7.26)$$

In this last expression we can identify to extreme cases: when $\theta_{12} = 0$ (or π) and when $\theta_{12} = \pi/2$ (or $-\pi/2$). For the former, we get

$$\begin{aligned} \dot{\theta}_1 &= \omega - \frac{\kappa}{2} \left[1 - \cos \theta_{12} \right] \\ \dot{\theta}_2 &= \omega + \frac{\kappa}{2} \left[1 - \cos \theta_{12} \right] \end{aligned} \quad (7.27)$$

and for the latter

$$\begin{aligned} \dot{\theta}_1 &= \omega - \frac{\kappa}{2} \left[1 + \sin \theta_{12} \right] \\ \dot{\theta}_2 &= \omega + \frac{\kappa}{2} \left[1 - \sin \theta_{12} \right] \end{aligned} \quad (7.28)$$

Plotting the coupling terms shown in these expressions, we obtain figure 37 where we can see something very interesting. In picture (a), it is stated that, as the master oscillator's frequency is increasing *clockwise*, the slave's one is also doing it but *anti-clockwise*, that is, the oscillation are equal in magnitude for all values of θ_{12} , but in such a way that they have opposite senses. Therefore, if we apply an inversion operation to one of the oscillators, we get the other one. But indeed, if that symmetry operation is done also to the system structure (see figure 13), it remains unperturbed.

From all what we have just commented, it can be extracted that the problem's symmetry force its possible solutions to be antisymmetric in order to be stable. In fact, this statement contrasts sharply with what we have on picture (b) where the solution has not inversion symmetry and, thereby, those values of δ give unstable results.

However, this situation we have described here is not unique for class 1 couplings, in fact it happens with the other ones but at the moment we described it, we did not analyse it. For instance, if we take there $\delta = 0$ or π , we get a $\sin \theta_{12}$ in eq. (5.26) which leads to a situation very similar to the one exposed in figure 37b.

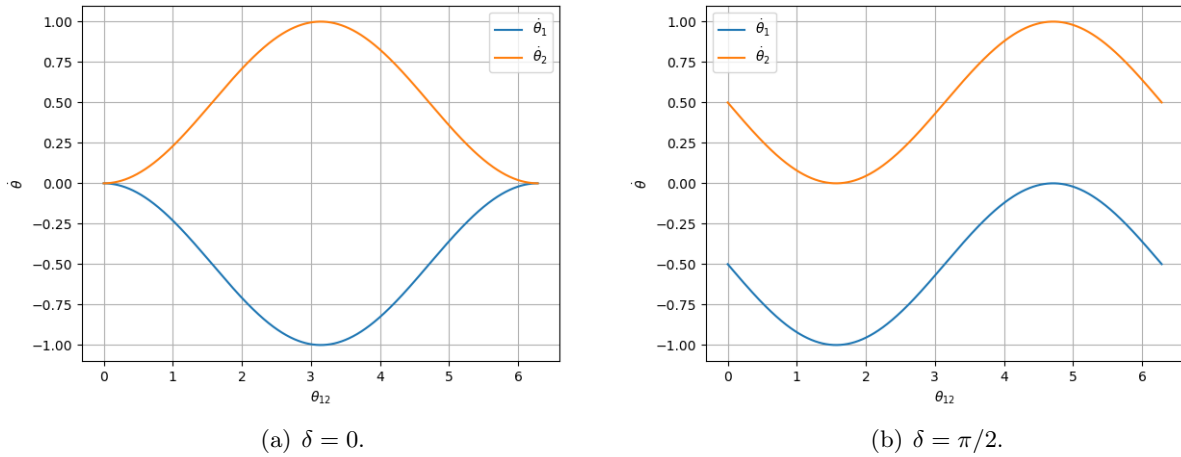


Figure 37: Form of the coupling for each of the cases commented in the text.

7.5 Excitatory and inhibitory junctions with the same coupling constants and different natural frequencies

In this subsection, we will deal with a situation quite similar to the one studied before but with a fundamental change: $\omega_1 \neq \omega_2$. Therefore, in this case, eq. (7.1) is given as follows

$$\begin{aligned} \dot{\theta}_1 &= \omega_1 - \frac{\kappa}{2} [1 - \cos(\theta_{12} + \delta)] \\ \dot{\theta}_2 &= \omega_2 + \frac{\kappa}{2} [1 - \cos(\theta_{12} - \delta)] \end{aligned}, \quad (7.29)$$

being the evolution of the phase difference with time

$$\dot{\theta}_{12} = \Delta\omega - \kappa[1 - \cos \theta_{12} \cos \delta]. \quad (7.30)$$

Assuming that we are under phase locking conditions, then we find that

$$\theta_{12}^* = \arccos\left(\frac{1-c}{\cos \delta}\right). \quad (7.31)$$

This result has very important differences with the situation studied on the previous subsection. Here we see that the condition that must be satisfied in order to obtain phase locked solutions is

$$\left| \frac{1-c}{\cos \delta} \right| \leq 1, \quad (7.32)$$

and taking into account that κ is a positive quantity, this last relationship implies that c cannot be negative, i.e., $\omega_1 \not< \omega_2$, even if $\delta = 0, \pi$. In figure 38, the possible values of $\Delta\omega$ which satisfy eq. (7.32), for each value of δ , are plotted, where we have taken $\kappa = 1.0 \text{ rad}\cdot\text{s}^{-1}$.

We want to understand the reason that allows this system of having $\omega_1 > \omega_2$ and a wide variety of possible values for δ . Comparing the system that we are analysing now with the one studied before, we see that it is not completely antisymmetric as the natural oscillating frequencies for each oscillator are different. However, as they are continuously interacting, depending on the values of $\Delta\omega$ and δ , the stable solutions will be those ones which lead to the most antisymmetric situation.

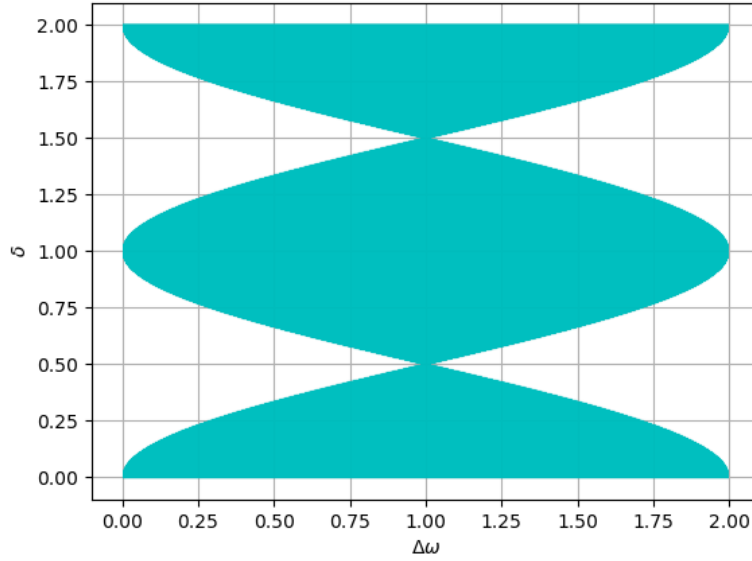


Figure 38: Possible values of $\Delta\omega$ that satisfy eq. (7.32), where we have taken $\kappa = 1.0 \text{ rad}\cdot\text{s}^{-1}$. Because of the plot template, it seems that for $\delta = \pi/2$ and $\delta = 3\pi/2$ there is a stable solution but this is not true.

A prove of this last statement is given by the fact that $\omega_2 > \omega_1$ situations are not found. This does not happens with the class 2 coupling so it is due to the fact that this new coupling always takes positive values and, therefore, recalling eq. (7.29), we see that, under the situation considered, $\dot{\theta}_1$ has as highest value ω_1 while $\dot{\theta}_2$ has $\omega_2 + \kappa/2$, being its lowest $\omega_2 - \kappa/2$. From this results we see that one of the oscillators is moving in a quicker way while the other does it slowly, so, in spite of the fact that the movement takes place out-of-phase, they are not completely antisymmetric (see figure 39).

On the other hand, from figure 38, we see that, studying the situation in which $\omega_2 < \omega_1$, the values of δ which lead to the most antisymmetric situation is $\delta = n\pi$, with $n \in \mathbb{N}$ and as we move towards to $\delta = (2n + 1)\pi/2$, less antisymmetric situations appears. As well, this *antisymmetry* is higher for $\Delta\omega = 1.0 \text{ rad}\cdot\text{s}^{-1}$ (considering $\kappa = 1.0 \text{ rad}\cdot\text{s}^{-1}$) which is something very logical since the highest quantity that can be subtracted to the master oscillator, or well, extracted to the slave one, is 2 (see eq. (7.29)). In the graphics shown in figure 40, we represent some oscillations for different values of δ and $\Delta\omega$, considering in all the cases that $\kappa = 1.0 \text{ rad}\cdot\text{s}^{-1}$.

Discussion With the situations we have studied in this two last subsections, we see that the form of the coupling (excitatory and inhibitory junctions) play a very important role when the coupling (class 1 coupling) takes only positive values. We have been analysing the situation of a completely antisymmetric coupling (an excitatory and inhibitory junction with the same magnitude) and we have seen that, depending on how that coupling is, it affects the oscillations in our system in such a way that, in this case for instance, it obligates the system to adopt an antisymmetric situation in order to have stable solutions in the problem. That is, the *symmetry* of the coupling determines how the oscillations in the system are. For example, in eq. (7.11), we can see that the coupling is only excitatory and, therefore, the oscillations coming from that relationship will tend to be symmetric.

7.6 Excitatory and inhibitory junctions with different coupling constants but same natural frequencies

This situation was not analysed previously but now it seems interesting, according to the results shown above. Previously, we imposed our system's coupling to be completely antisymmetric (same coupling constants where one of them was inhibitory and the other excitatory) with equal and different natural frequencies. In this subsection, we will impose that $\omega_1 = \omega_2 = \omega$ but $\kappa \neq -\kappa'$.

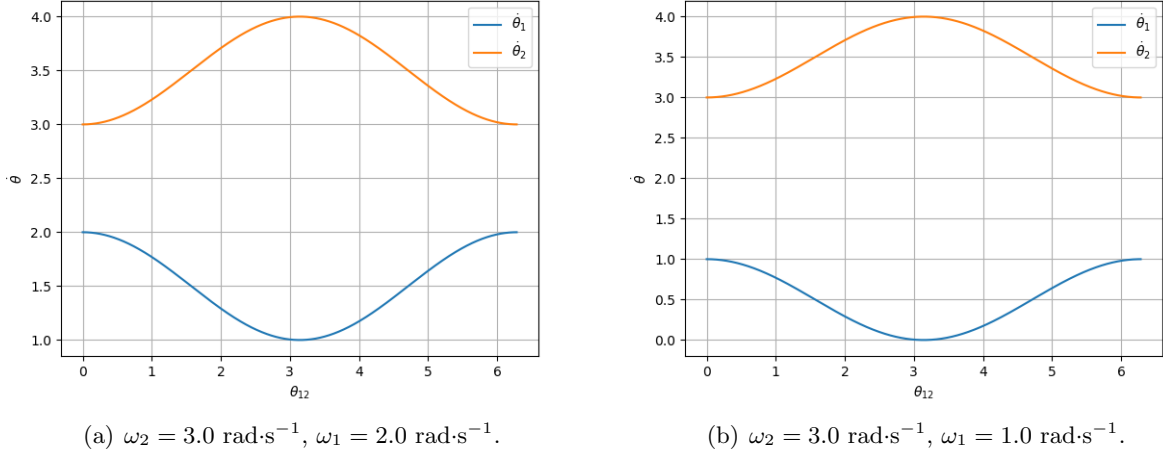


Figure 39: Oscillations for positive values of $\Delta\omega$. In both cases we have taken $\delta = 0$ and $\kappa = 1.0 \text{ rad}\cdot\text{s}^{-1}$.

Therefore, eq. (7.1) adopts the following form

$$\begin{aligned}\dot{\theta}_1 &= \omega - \frac{\kappa'}{2} \left[1 - \cos(\theta_2 - \theta_1 - \delta) \right], \\ \dot{\theta}_2 &= \omega + \frac{\kappa}{2} \left[1 - \cos(\theta_1 - \theta_2 - \delta) \right],\end{aligned}\quad (7.33)$$

so the time evolution for the phase difference is given by

$$\dot{\theta}_{12} = -\frac{\kappa' + \kappa}{2} + \frac{\kappa'}{2} \cos(\theta_{12} + \delta) + \frac{\kappa}{2} \cos(\theta_{12} - \delta), \quad (7.34)$$

and by expanding the trigonometric functions that appear in this last expression under phase locking conditions, we get the following result

$$\frac{\kappa + \kappa'}{2} = \frac{\kappa + \kappa'}{2} \cos \delta \cos \theta_{12}^* + \frac{\kappa - \kappa'}{2} \sin \delta \sin \theta_{12}^*. \quad (7.35)$$

Taking a first look to this last expression, we can see that it is satisfied when $\delta = \theta_{12}^* = 0$ or $\delta = \theta_{12}^* = \pi$. Indeed, this has been proved computationally for different values of the coupling constants, and the numerical results corresponding to that situation are shown in figure 41, where we have taken $\kappa' = -3.0 \text{ rad}\cdot\text{s}^{-1}$ and $\kappa = 1.0 \text{ rad}\cdot\text{s}^{-1}$.

This results are quite similar to the ones shown in section 7.4 and, as we see, making the values of ω_1 and ω_2 equal, lead always to a very restrictive situation. However, in this case is due to the *symmetry* imposed by the oscillations of our system as the constant couplings κ and κ' are different, not being the coupling antisymmetric as it happens with the other cases. Therefore, the stable solutions for our system will be those ones that conserve the *symmetry* imposed by the natural oscillations of the system.

7.7 Excitatory and inhibitory junctions with different coupling constants and natural frequencies

This is the most general case that can be studied and, as we can see, is completely antisymmetric since the coupling constants and the natural frequencies are all different. Unlike the methodology followed in section 5.6, where we showed an example in which that case was reduced as a sum of the previous situations studied, here we will present the general equation and integrals that must be solved. For so, from eq. (7.1) which describes the most general case that can be studied, we find that the phase difference is given by

$$\begin{aligned}\dot{\theta}_{12} &= \Delta\omega - \frac{\kappa + \kappa'}{2} + \frac{\kappa'}{2} \left[\cos \theta_{12} \cos \delta - \sin \theta_{12} \sin \delta \right] + \\ &+ \frac{\kappa}{2} \left[\cos \theta_{12} \cos \delta + \sin \theta_{12} \sin \delta \right],\end{aligned}\quad (7.36)$$

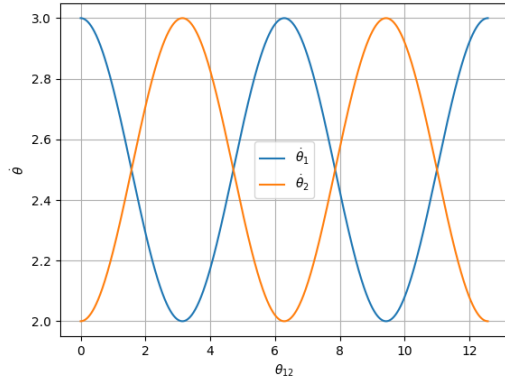
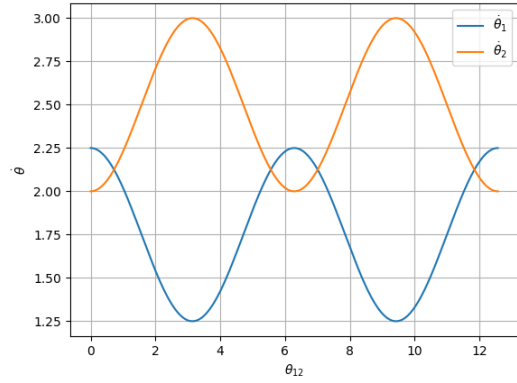
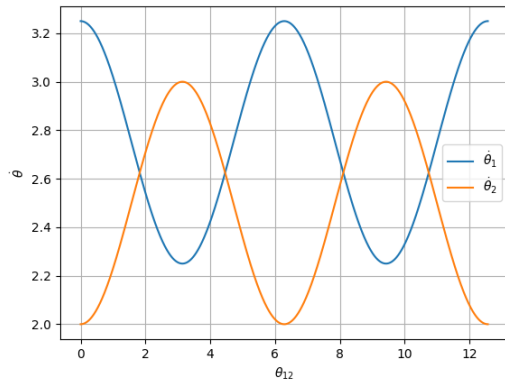
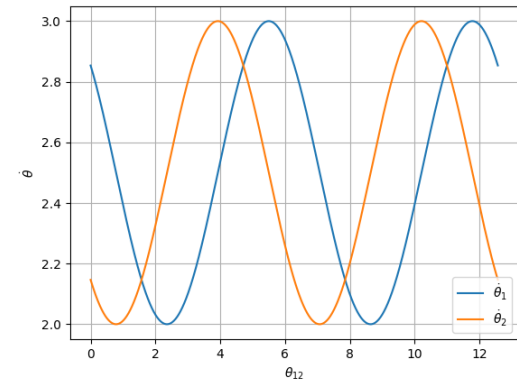
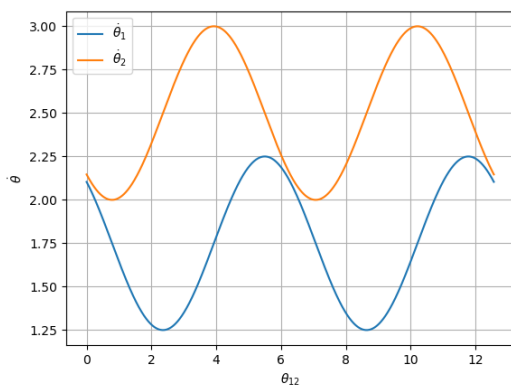
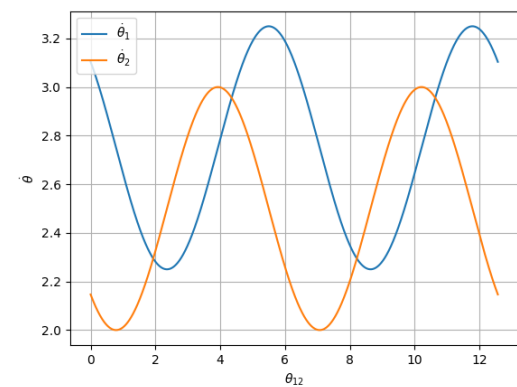

 (a) $\Delta\omega = 1.0 \text{ rad}\cdot\text{s}^{-1}$, $\delta = 0$.

 (b) $\Delta\omega = 0.25 \text{ rad}\cdot\text{s}^{-1}$, $\delta = 0$.

 (c) $\Delta\omega = 1.25 \text{ rad}\cdot\text{s}^{-1}$, $\delta = 0$.

 (d) $\Delta\omega = 1.0 \text{ rad}\cdot\text{s}^{-1}$, $\delta = \pi/4$.

 (e) $\Delta\omega = 0.25 \text{ rad}\cdot\text{s}^{-1}$, $\delta = \pi/4$ (unstable solution).

 (f) $\Delta\omega = 1.25 \text{ rad}\cdot\text{s}^{-1}$, $\delta = \pi/4$.

Figure 40: Oscillations for different values of $\Delta\omega$ and δ . In all the cases we have taken $\kappa = 1.0 \text{ rad}\cdot\text{s}^{-1}$. Notice that one of the situations correspond to an unstable solution.

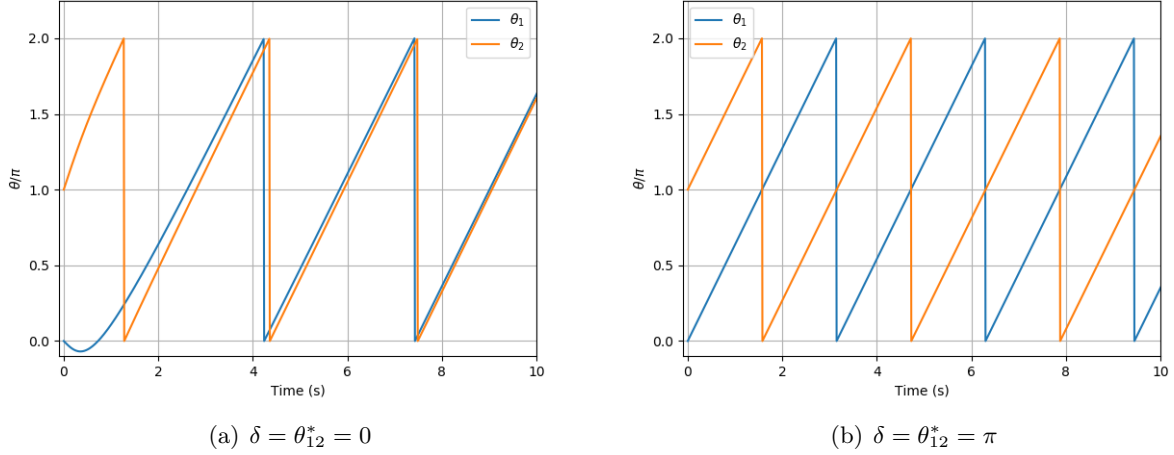


Figure 41: Numerical simulations for the situation analysed. Here, we have taken $\kappa' = -3.0 \text{ rad}\cdot\text{s}^{-1}$ and $\kappa = 1.0 \text{ rad}\cdot\text{s}^{-1}$.

which can be written as

$$\dot{\theta}_{12} = \Delta\omega' + \kappa_1 \sin \theta_{12} + \kappa_2 \cos \theta_{12}, \quad (7.37)$$

where we have defined $\Delta\omega' = \Delta\omega - (\kappa' + \kappa)/2$, $\kappa_1 = [(\kappa' + \kappa) \cos \delta]/2$ and $\kappa_2 = [(\kappa - \kappa') \sin \delta]/2$.

That differential equation can be also written as follows

$$\int \frac{d\theta_{12}}{\Delta\omega + \kappa_1 \sin \theta_{12} + \kappa_2 \cos \theta_{12}} = t + A. \quad (7.38)$$

The integral that appears in the first term of the expression, can be reduced to a rational integral with an order to polynomial by performing the change $z = \tan(\theta_{12}/2)$, having then

$$I = 2 \int \frac{dz}{(\Delta\omega' - \kappa_2)z^2 + 2\kappa_1 z + (\kappa_2 + \Delta\omega)}. \quad (7.39)$$

We have obtained the most general integral for an excitatory and inhibitory junction in a two mutually coupled system and, if we want to study a certain case with given values of the constants introduced before, it shall be done explicitly since here. However, depending on the value for the constants, this integral does not need to be solved explicitly because the results obtained in the previous subsections allow us to predict the oscillator's behaviour, as we did in section 5.6.

8 Sinusoidal modulation in the master-slave configuration

In this section, we will consider once again the master-slave configuration shown in figure 6, but in this case a sinusoidal modulation will be added to the master oscillator. Nevertheless, we are not going to distinguish between a class 1 and a class 2 couplings, in fact we will treat them together because we shall study the limits in which their behaviour approximates to the one they should have if any modulation is applied.

The equations that describe the situation which we are going to analyse, are similar to the ones used in eq. (4.1) as it can be seen in the following expressions

$$\begin{aligned} \dot{\theta}_1 &= \omega_1 + A_m \sin(\omega_e t) \\ \dot{\theta}_2 &= \omega_2 + \kappa f(\theta_1 - \theta_2 - \delta) \end{aligned}, \quad (8.1)$$

where A_m is the amplitude of the sinusoidal oscillation⁴ and ω_e is the correspondent frequency. Instead of obtaining now the phase difference between oscillators as we have been doing along this dissertation, we are going to solve the differential equation corresponding to the master oscillator, having then

$$\theta_1 = \omega_1 t - \frac{A_m}{\omega_e} \cos \omega_e t + A. \quad (8.2)$$

From here we can extract different cases:

⁴Do not get confused with the notation we have being using for the integration constant A .

- If the ratio A/ω_e is small enough, then the solution for this case will tend to the one without oscillation. In fact, this is the behaviour coming from the numerical simulations shown in figure 42, where we have considered a class 2 coupling with $\omega_1 = \omega_2 = \pi \text{ rad}\cdot\text{s}^{-1}$, $\kappa = 1.0 \text{ rad}\cdot\text{s}^{-1}$, $A_m = 0.01 \text{ rad}\cdot\text{s}^{-1}$ and $\omega_e = 10.0 \text{ rad}\cdot\text{s}^{-1}$. Note that the result coincides exactly with the one obtained in section 4.2, as commented.
- If ω_e is a very small quantity, then for short times we can perform the Taylor expansion of eq. (8.2), having then

$$\theta_1 = (\omega_1 + A_m)t. \quad (8.3)$$

From this result it can be seen, for instance, that if $\omega_1 = \omega_2$ and A_m has their order of magnitude, then when t is not long enough we should recover the results corresponding to that case, i.e., a phase-locked situation where the phase difference is characterized by $\theta_{12} = \delta$ and the oscillation frequency is given by $\omega_1 + A_m$. Nevertheless, when t reaches a value whose order of magnitude is similar to ω_e , then we will expect the phase difference to be continuously changing.

The numerical simulations corresponding to this case are shown in figure 43, where we have taken $\omega_1 = \omega_2 = \pi \text{ rad}\cdot\text{s}^{-1}$, $\kappa = 1.0 \text{ rad}\cdot\text{s}^{-1}$, $A_m = \pi \text{ rad}\cdot\text{s}^{-1}$ and $\omega_e = 0.001 \text{ rad}\cdot\text{s}^{-1}$. Notice that for short times, the oscillation's period is 4.0 s and not 2.0 s as it was predicted by eq. (8.3). Nevertheless, for high values of t , this result does not hold because t has the same order magnitude as ω_e in such a way that the Taylor expansion approximation of the cosine function is not valid anymore. Thereby, we reach a situation where the phase difference does not remain constant.

- If A_m has the same order of magnitude than the natural frequencies and ω_e is bigger than those quantities, then the oscillation takes place in a very quicker way, remaining the phase difference unperturbed with respect to the case without oscillation.

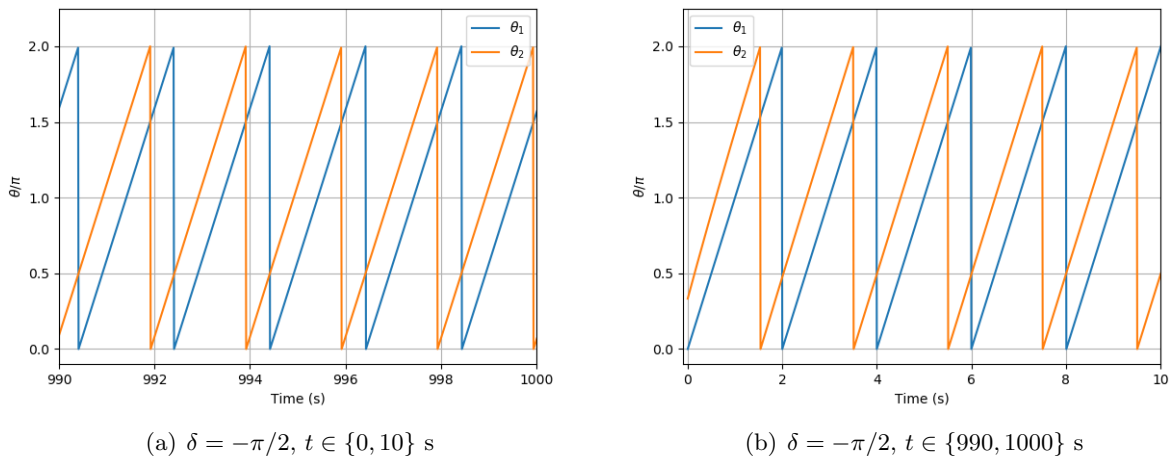


Figure 42: Numerical simulations for the case in which A/ω_e is a very small quantity. In order to obtain these results, we have considered a class 2 coupling with $\omega_1 = \omega_2 = \pi \text{ rad}\cdot\text{s}^{-1}$, $\kappa = 1.0 \text{ rad}\cdot\text{s}^{-1}$, $A_m = 0.01 \text{ rad}\cdot\text{s}^{-1}$ and $\omega_e = 10.0 \text{ rad}\cdot\text{s}^{-1}$.

9 Two mutually coupled oscillators with the same natural frequencies and same constant couplings

In this section, we are going to consider again the situation shown in figure 13 when the natural frequency for both oscillators take the same value like its coupling constants. However, we will treat only the case of a class 2 coupling because the results obtained could be extended to a class 1 coupling. Nevertheless, the most general equations that describe this situation are

$$\begin{aligned} \dot{\theta}_1 &= \omega_1 + \kappa' f(\theta_2 - \theta_1 - \delta) + A_m \sin(\omega_e t) \\ \dot{\theta}_2 &= \omega_2 + \kappa f(\theta_1 - \theta_2 - \delta) \end{aligned}, \quad (9.1)$$

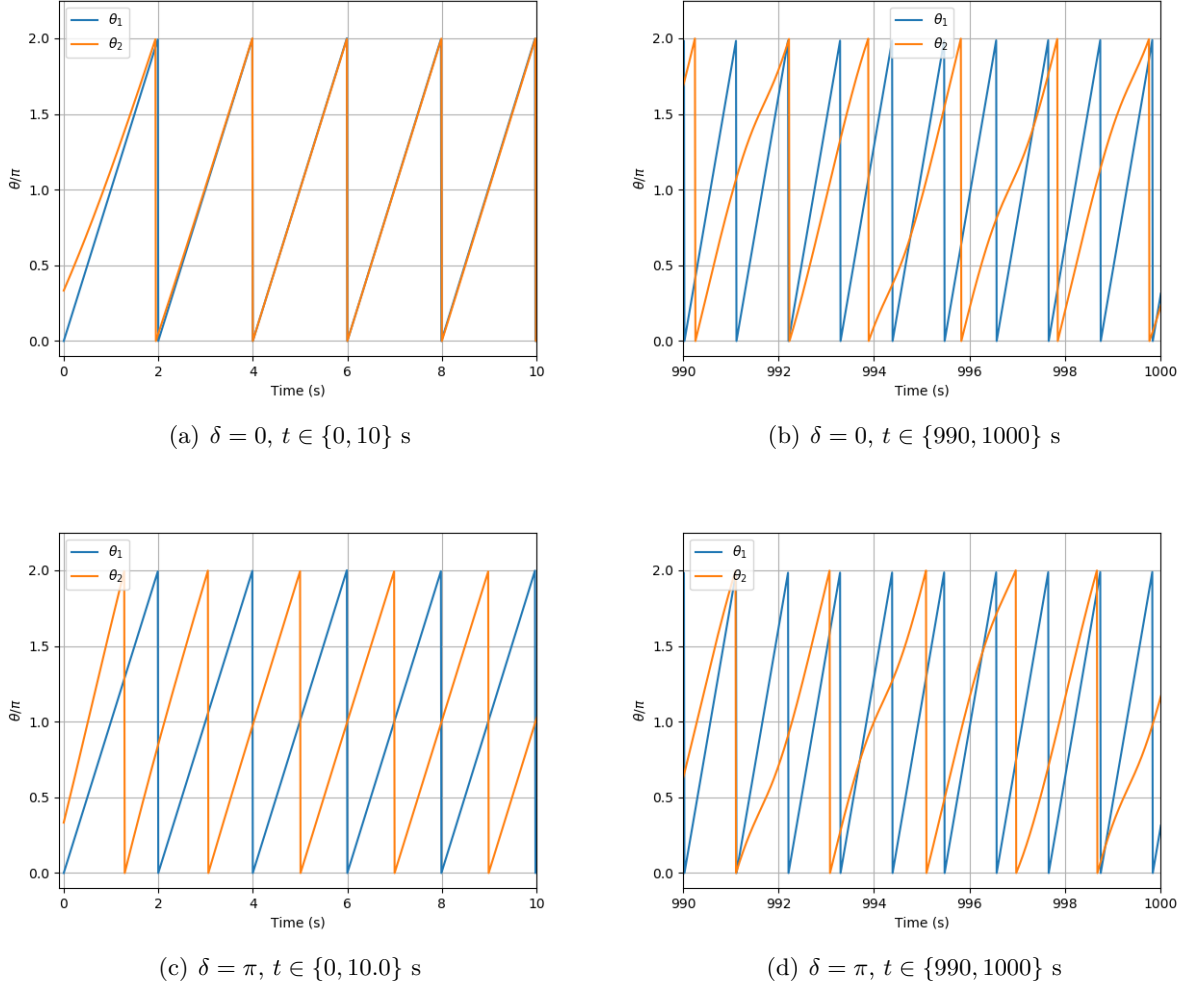


Figure 43: Numerical simulations for the case in which ω_e is a very small quantity. In order to obtain these results, we have considered a class 2 coupling with $\omega_1 = \omega_2 = \pi \text{ rad}\cdot\text{s}^{-1}$, $\kappa = 1.0 \text{ rad}\cdot\text{s}^{-1}$, $A_m = \pi \text{ rad}\cdot\text{s}^{-1}$ and $\omega_e = 0.001 \text{ rad}\cdot\text{s}^{-1}$.

where $f(x)$ is the correspondent function that depends on the coupling's class

Unlike the case analysed in the previous section, now it seems interesting to study the phase difference between oscillators, which is characterized by

$$\dot{\theta}_{12} = A_m \sin(\omega_e t) - 2\kappa \cos \delta \sin \theta_{12}. \quad (9.2)$$

The easiest consideration we can make here is the one corresponding to $\cos \delta = 0$, getting then from eq. (9.2) the following expression for the phase difference

$$\theta_{12} = -\frac{A_m}{\omega} \cos \omega t + A \quad (9.3)$$

and hence, the same cases as the ones presented above appear, having under certain circumstances that the phase difference remains constant, at least during a certain time interval.

Any other situation in which $\cos \delta \neq 0$, will not lead to a phase locked situation. Indeed, assume that we have found a possible value of δ in such a way that $\dot{\theta}_{12} = 0$. Therefore, from eq. (9.2) we get

$$\theta_{12} = \arcsin\left(\frac{A_m \sin(\omega_e t)}{2\kappa \cos \delta}\right), \quad (9.4)$$

but this is not a constant since we have a dependence with the time. Thus, unless we are studying extreme situations for the modulation, i.e., $A_m \rightarrow 0$, a phase locked solution will not be obtained. However, we can ensure that the phase difference will be changing periodically with time as the functions that are involved in eq. (9.2) are all periodic. This last statement has been compared with the numerical simulations which are shown in figure 44, where we can see regions with a bigger *density* of oscillations per unit time for each oscillator.

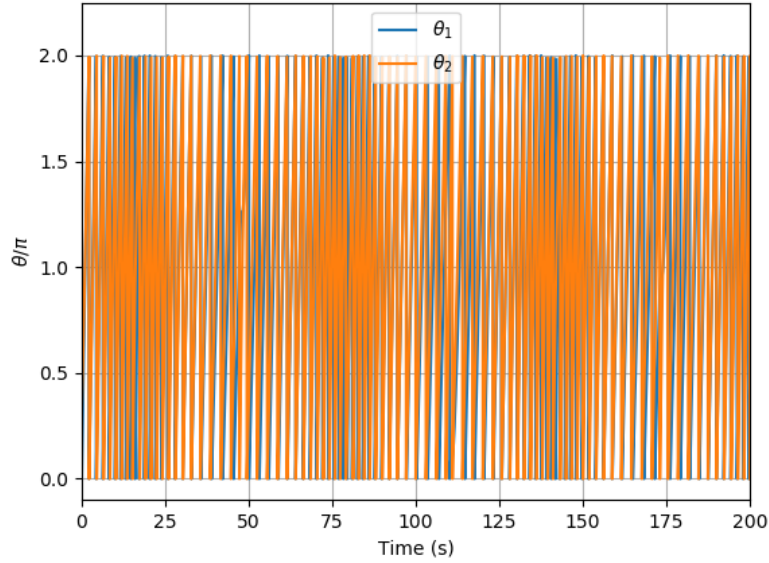


Figure 44: Numerical simulations for the case in which we are applying a sine modulation to our system whose amplitude is $A_m = 2.0 \text{ rad}\cdot\text{s}^{-1}$ and frequency $\omega_e = 0.1 \text{ rad}\cdot\text{s}^{-1}$. We can identify regions where the *density* of oscillations per unit time for each oscillator is higher and which vary periodically.

10 Izhikevich model

Izhikevich model was proposed by Eugene M. Izhikevich in [4] and, as it is said in the abstract, “*it reproduces spiking and bursting behaviour of known types of cortical neurons*”. Mathematically, it is characterized by the following system of ordinary differential equations

$$\begin{aligned} \dot{v} &= 0.04v^2 + 5v + 140 - u + I \\ \dot{u} &= a(bv - u) \end{aligned} \quad , \quad (10.1)$$

satisfying that

$$\text{if } v > 30 \text{ mV, then } \begin{cases} v \leftarrow c \\ u \leftarrow u + d \end{cases} .$$

Here, the variable v represents the membrane potential of the neuron and u the recovery variable which takes into account the activation of K^+ ionic currents and inactivation of Na^+ ionic currents. The other terms that appear in those equations are constants whose meaning is the following, according to [4]

- Parameter a describes the time scale of the recovery variable u .
- Parameter b describes the sensitivity of the recovery variable u to the subthreshold fluctuations of the membrane potential v .
- Parameter c describes the after-spike reset value of the membrane potential v caused by the fast high-threshold conductances K^+ conductances.
- Parameter d describes the after-spike reset of the recovery variable u caused by slow high-threshold Na^+ and K^+ conductances.

Depending on the values of these parameters⁵, different kind of neurons will be described. Along this dissertation, we have been talking about two kind of couplings, class 1 and class 2, so we will concern about those cases. In table 1, we present the values which we have to use in eq. (10.1) if we want to emulate that kind of neurons.

As we see, this model is more realistic as it introduces concepts like the membrane potential and the phenomenons of polarization and depolarization due to the K^+ and Na^+ ionic currents. Then, the reason why we are introducing it is because we want to check some of the results obtained

⁵The dimensions of the parameters are taken in such a way that the membrane potential and the time are given in mV and ms, respectively.

| Type | a | b | c | d | $v(0)$ |
|---------|------|------|-----|-----|--------|
| Class 1 | 0.02 | -0.1 | -55 | 6 | -60 mV |
| Class 2 | 0.2 | 0.26 | -60 | 0 | -64 mV |

Table 1: Values of the constants that appear in eq. (10.1) and initial condition for v .

with the Kuramoto model. Concretely, because of its computational ease, we will study the case of an unidirectional coupling, that is, the master-slave configuration. But for so, we have to seek first the value of the intensity for which the neuron starts to spike. For so, consider that the current in eq. (10.1) is constant, that is, $I(t) = I_0$, depending on the kind of neuron we have, the spiking phenomenon will start at a given certain value and, by increasing it, the period of the pulses decreases, as it can be seen in figure 45.

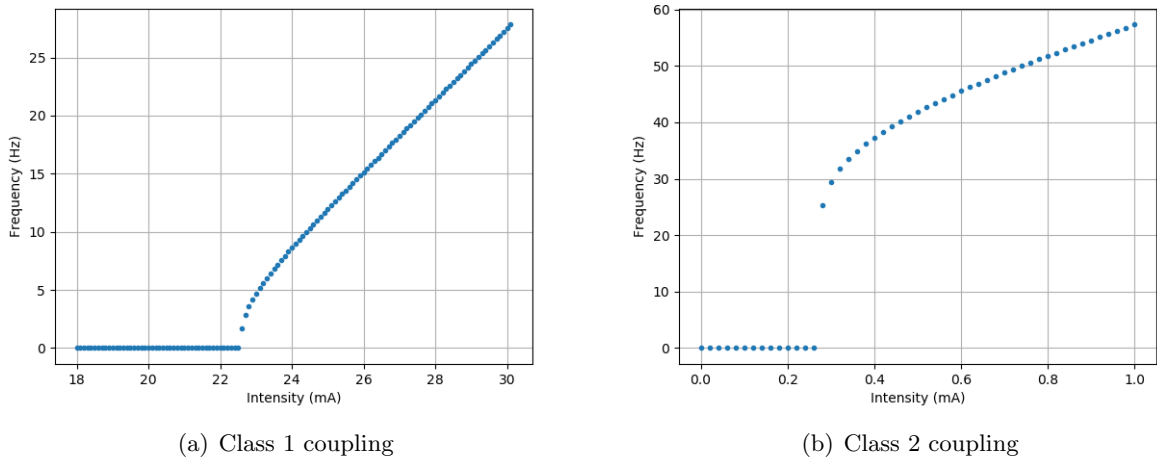


Figure 45: Representation of the pulse's period against the intensity current. As I increases, the frequency between periods also does it.

In that picture, we can distinguish the minimum value of the intensity that we have to apply in order to obtain spiking phenomena on the neuron. Also, another property that can be seen here is that, for a class 1 this phenomenon takes place in a continuous way while in a class 2 coupling we see an abrupt change between $\nu = 0$ Hz and the first value different from zero, as well as the values of the intensity that we have to apply for each of them. In the numerical simulations that we are going to perform for Izhikevich model, we are going to use $I_0 = 25$ mV for class 1 neurons and $I_0 = 0.3$ mV for class 2 neurons.

Due to the lack of time and some difficulties associated to the development of the Python code that solves eq. (10.1), we have analysed only one arrangement: the master-slave configuration. In this case, the master neuron is coupled unidirectionally to the slave, being the main consequence that it perturbs the other oscillator but this one cannot alter the master's spiking. Therefore, the behaviour of that oscillator is given by eq. (10.1) where $I(t) = I_0$, being this intensity the reason why the oscillator spikes.

Because of the junction, the slave neuron is receiving continuously information from the master in form of pulses, which will determine its spiking. Thereby, the intensity current in this other neuron will be given by the sum of I_0 and a certain synapse current I_{syn} in such a way that

$$I_{\text{syn}} = -vg_{\text{AMPA}}(t) - (v + 70)g_{\text{GABA}}(t), \quad (10.2)$$

where g is the synaptic conductance which can be excitatory (g_{AMPA}) or inhibitory (g_{GABA}), so depending on the kind of coupling we are interested in, one of them shall be zero.

Those conductances satisfy the following differential equation, according to [3]

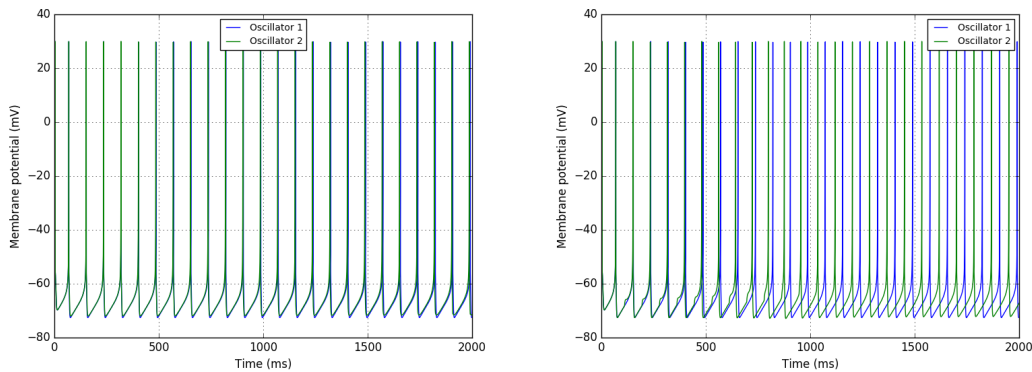
$$\dot{g} = \frac{-g_i + 0.5 \sum_k \delta(t - t_k - \delta)}{\tau_i}, \quad (10.3)$$

where $i = \text{AMPA, GABA}$, t_k is the instant when the spiking takes place and δ represents the time delay associated to the connection. Also, in this expression, the Dirac delta function do not have to

be integrated together with the equation, only takes into account the fact that at times $t = t_\kappa + \delta$, there is a spiking. One thing that we have to take into account is that in [3] a different situation is analysed, so the constant 0.5 that multiplies the Dirac delta function is not big enough if we want to generate a spiking in the second neuron. Thereby, for class 1 neurons we shall employ 100 nS and for class 2 neurons, 10000 nS.

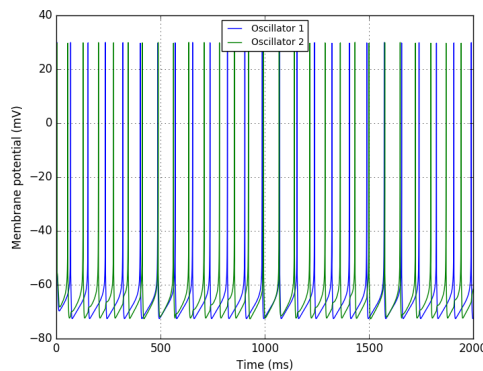
Let us start by talking about class 1 neurons with no associated delay and an excitatory coupling. The results for this case are shown in figure 46, where we can see that the results obtained are the ones predicted by Kuramoto model.

- In picture (a), it do not exist a time delay between the neuron's spiking, having then that both signals are in phase.
- In picture (b), a time delay equal to $T_1/2$ has been added to the numerical simulations, being T_1 the period of the master neuron. According to the Kuramoto model, this time delay corresponds to $\delta = \pi$ obtaining then an out-of-phase synchronization. Notice that in this simulations there is a certain period of time in which the second neuron spiking has to adapt to the period of the first one, something that was also obtained with Kuramoto model.
- Finally, we have considered that both neurons does not have the same spiking frequency, which means that the constant intensity I_0 for both signals are different. However, for small values of that difference, for instance $I_{0,2} - I_{0,1} = 0.5$ mA, where $I_{0,i}$ is the constant intensity for the i th neuron, the same result is obtained: both signals are not synchronized, that is, the solution is not stable. This result correspond to the situation in which $c > 1$ in Kuramoto model and let us conclude that the coupling between both neurons is very weak, i.e., κ is a small quantity. Therefore, Izhikevich model predicts the result for the weak coupling limit coupling between neurons. Nevertheless, this conclusion has to be contrasted with other situations for the same model, for example the case of the bidirectional coupling.



(a) No time delay between signals.

(b) Time delay equal to $T_1/2$, being T_1 the spiking period of the master neuron.



(c) Different constant intensity ($I_{0,2} - I_{0,1} = 0.5$).

Figure 46: Results obtained from the numerical simulations for a class 1 neuron with excitatory coupling under different situations.

The predictions obtained with Kuramoto model are also valid for the case in which we are studying class 1 neurons with inhibitory coupling. Nevertheless, there are some differences that have to be taken into account. As we can see in figure 47, if there is no any additional time delay, we have a phase difference between both neurons which does not correspond with the results predicted by Kuramoto model. However, as it can be seen in eq. (10.2), there is an additional term which introduces the known as *synaptic delay*.

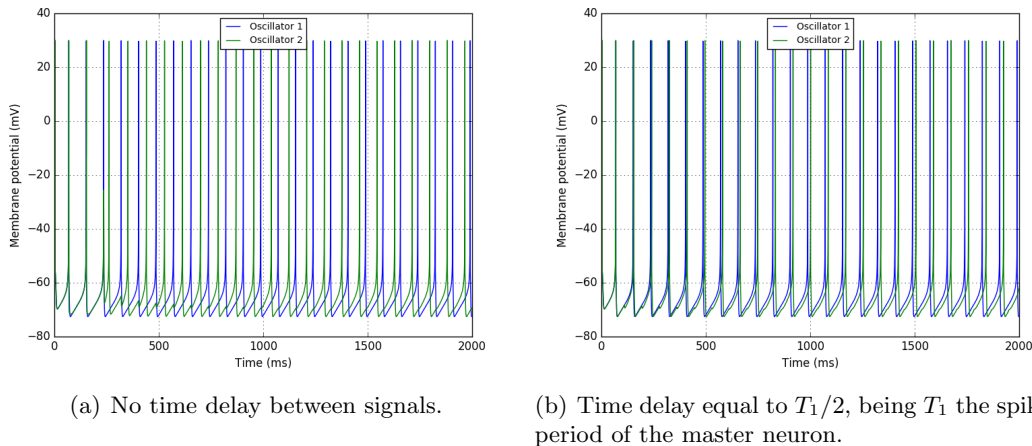


Figure 47: Results obtained from the numerical simulations for a class 1 neuron with inhibitory coupling under different situations.

11 Conclusions

Along this project, we have studied different configurations for a set of two coupled oscillators and we have seen that the time delay δ and the frequency difference between oscillators, play a fundamental role in the obtention of stable synchronized signals having sometimes that the receiver (slave oscillator) anticipates the sender (master oscillator).

Nevertheless, not only the values of those constants are relevant, also the structure of the system determines how the stable solutions are. That is, depending on how the coupling is (excitatory, inhibitory or both at the same time) and the kind of coupling (class 1 or class 2) the symmetry of the problem only allows symmetric solutions to be valid, so there will be circumstances that certain solutions or even certain kinds of synchronization do not take place because of the structure of the system. Another thing is that an external modulation that depends on time does not allow the system to obtain synchronized solutions for long times unless the amplitude of the modulation is small enough.

The results obtained for the unidirectional coupling has been contrasted with another model which introduces variables corresponding to the synaptic phenomenons that take place between the neurons, having that the results coincide very accurately. Thereby, from here we can see that a very simple model of coupled oscillators seems to predict a system of neurons behaviour, but for this to be a *valid* conclusion, it is necessary to compare the results achieved in this project for the Kuramoto model, with other situations of the Izhikevich model and other complex models. Indeed, this can be proposed as another future SURF fellowship and, with this purpose, the code of the program used for the Izhikevich model numerical simulations has been added in appendix C in such a way that it can be useful to model a bidirectional coupling employing the same model.

Acknowledgments

I would like to thank my tutor Claudio R. Mirasso for discussing with me the results obtained in this project and helping me to solve some problems with the numerical simulations.

This work was supported by the SURF@IFISC fellowship.

A Neuron constitution

In this appendix we show which is the structure of a neuron and the function of their elements.

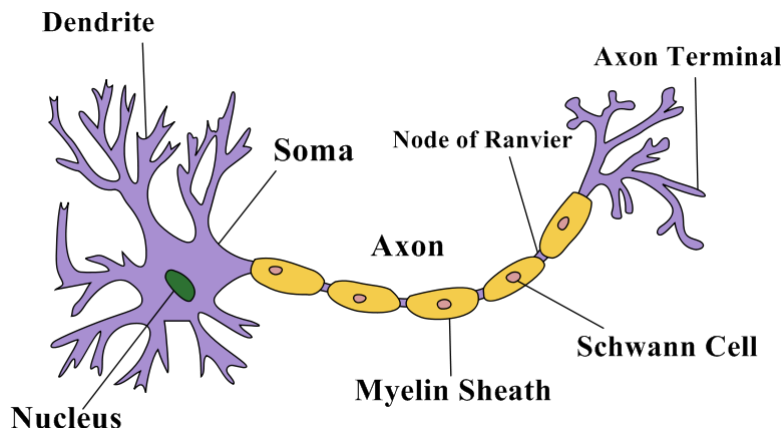


Figure 48: Structure of a neuron. Image extracted from <https://owlcation.com/stem/Structure-of-a-Neuron>.

In figure 48 we distinguish the following elements:

- **Dendrite.** Are the extremes of the neuron from which they receive information from the other ones.
- **Axon.** Is the conductive media from where signals are transported when they receive a stimulus.
- **Axon terminal.** Are connected to the other neuron's dendrites, allowing then the transmission of information.
- **Nucleus.** Contains the basic nutrients for the neuron.
- **Soma.** Is the neuron's head, contains the nucleus, dendrites and the axon's beginning.
- **Myelin Sheath.** Depending on the kind of neuron analysed, they shall appear or not. If they do, the current transmission along the axon takes place in a quicker way as the zones inside them cannot be polarized.
- **Node of Ranvier.** Nodes located between two consecutive myelin sheath. This zone, unlike the other one, can be polarized.
- **Schwann Cell.** They are located inside the myelin sheath and work as an insulator for the *electrical pulse*.

B Phase locking conditions for oscillators with different natural frequencies

In this appendix, we introduce the graphics in which we represent δ against $\Delta\omega$ for oscillators with different natural frequencies, that is, the values of $\Delta\omega$ which satisfy the phase locking condition for every possible value of δ . Also, in all these representations, we will consider that $\kappa = 1.0 \text{ rad}\cdot\text{s}^{-1}$.

B.1 Two mutually coupled oscillators (class 2) with same positive coupling constants

All those values of $\Delta\omega$ contained inside the coloured part, are the ones which are stable for each value of δ . In this representation we only include positive values of $\Delta\omega$, since is symmetric.

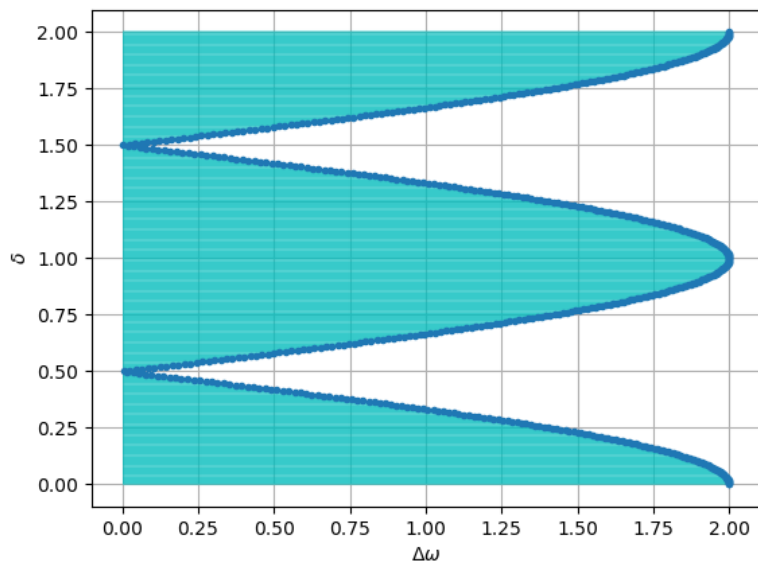


Figure 49: In this representation we have only included positive values of $\Delta\omega$ since the graphic is symmetric.

B.2 Two mutually coupled oscillators (class 2) with same coupling constants with excitatory and inhibitory junctions

All those values of $\Delta\omega$ contained inside the coloured part, are the ones which are stable for each value of δ . In this representation we only include positive values of $\Delta\omega$, since is symmetric.

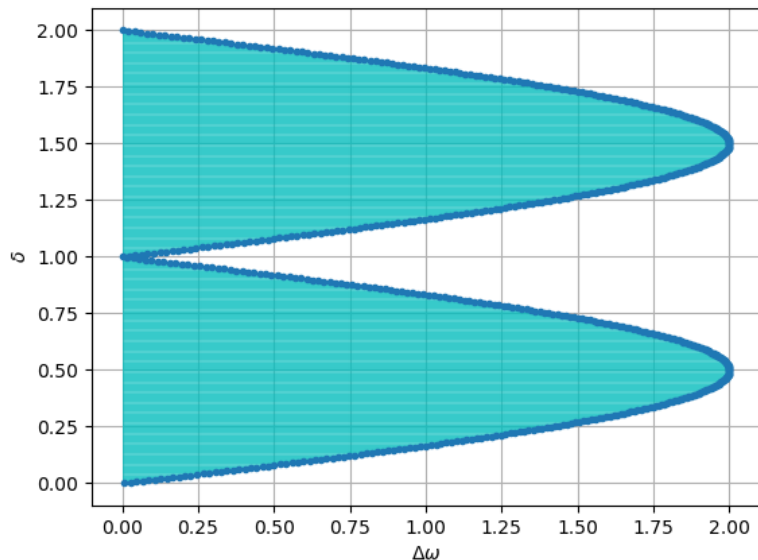


Figure 50: In this representation we have only included positive values of $\Delta\omega$ since the graphic is symmetric.

B.3 Two mutually coupled oscillators (class 1) with same positive coupling constants

All those values of $\Delta\omega$ contained inside the coloured part, are the ones which are stable for each value of δ . In this representation we only include positive values of $\Delta\omega$, since is symmetric.

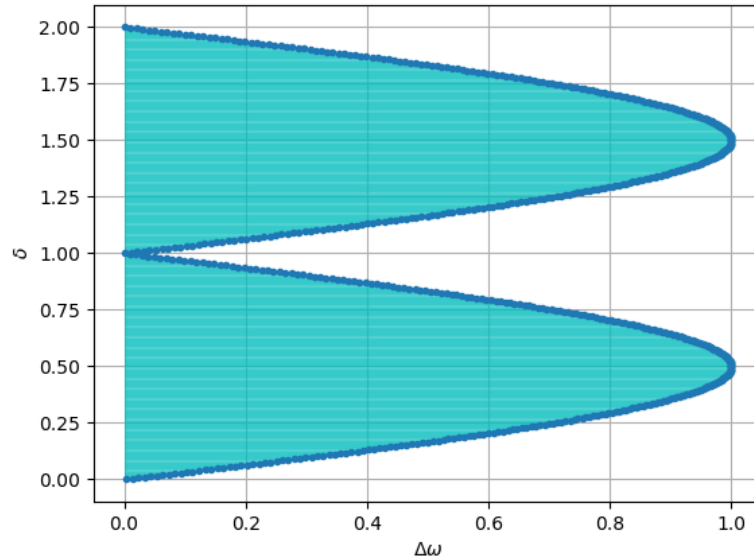


Figure 51: In this representation we have only included positive values of $\Delta\omega$ since the graphic is symmetric.

C Code of the program used to study Izhikevich's model

In this section we present the Python's code of the program used to study Izhikevich's model in. The main goal of introducing it is to help possible future SURF fellowships, assuming that their project concerns this model, and also, if they decide to use it, to improve it whether by correcting the possible mistakes, reducing the computational time and/or introducing more accurate methods than the Euler's one.

```
#We import the necessary packages
from numpy import *
from pylab import *

#We delete any other possible plot
clf()

#We define Euler's method, employed to solve the differential
equations
def euler(f, x_i, y_i, h):
    yeu = y_i + h*f(x_i, y_i)
    return yeu

#Now, we define the equations that govern the first neuron's
movement
class Primer_oscilador:
    def __init__(self, I0=0.4, a = 0.2, b=0.26, c=-60., d=0., yo=
        array([-64, -64*0.26])):
        self.I0 = I0
        self.a = a
        self.b = b
        self.c = c
        self.d = d
        self.yo = yo
    def __call__(self, t, y):
        self.deriv = zeros(2)
        self.deriv[0] = 0.04*y[0]**2+5*y[0] + 140 - y[1] + self.I0
        self.deriv[1] = self.a*(self.b*y[0]-y[1])
    return self.deriv
```

```

#Here, we present the loop that will be employed to solve the
differential equations
Vmax_primer_oscilador = 30.

def resolucion_primer_oscilador(x_ini, x_fin, h):
X = []
Y = []
loc = []
X.append(x_ini)
Y.append(ecdif.yo)
k = x_ini
yi = ecdif.yo
while k < x_fin:
yi = euler(ecdif, k, yi, h)
k = round(k + h, 4)
if yi[0] > Vmax_primer_oscilador:
loc.append(len(X)-2)
yi[0] = ecdif.c
yi[1] = yi[1] + ecdif.d
X.append(k)
Y.append(yi)
return array(X), array(Y), loc

#Now, we proceed to solve the equations
t1, V1, loc_max = resolucion_primer_oscilador(0, 3000.01,
0.001)

#We plot the results corresponding to the first neuron
plot(t1, V1[:, 0])
xlabel("Time_(ms)")
ylabel("Membrane_potential_(mV)")

#We determine when the spiking of that neuron takes place
T_primer_oscilador = t1[loc_max]
T_primer_oscilador = T_primer_oscilador[1:] #The first value is
deleted because it is not a true spiking
T_int = around(T_primer_oscilador*1000, 0)
T = T_primer_oscilador[5] - T_primer_oscilador[4]

#Reached this point, we define the equations for the second
oscillator
class Segundo_oscilador:
def __init__(self, AMPA = 1., GABA = 0., delta = 0., I0=0.4, a
= 0.2, b=0.26, c=-60., d=0., yo= array([-64, -64*0.26, 0,
0])):
#Variables that define the second oscillator
self.I0 = I0
self.a = a
self.b = b
self.c = c
self.d = d
self.yo = yo
#Variables which characterize the coupling
self.AMPA = AMPA
self.GABA = GABA
self.delta = delta
def __call__(self, t, y):
#Equations for the neuron
self.deriv = zeros(4)

```

```

self.deriv[0] = 0.04*y[0]**2+5*y[0] + 140 - y[1] +self.I0 -self
    .AMPA*(y[2]*(y[0])) - self.GABA*(y[3]*(y[0]+70))
self.deriv[1] = self.a*(self.b*y[0]-y[1])
#Equations for the conductivity
self.deriv[2] = (-y[2] + 100*self.delta)/5.26
self.deriv[3] = (-y[3] + 10000*self.delta)/6.
return self.deriv

#As we did before, now we define the method employed to solve
that differential equation
def resolucion_segundo_oscilador(x_ini, x_fin, h):
    ecdif = Segundo_oscilador(delta = 0)
    X = []
    Y = []
    X.append(x_ini)
    exc = []
    Y.append(ecdif.yo)
    k = x_ini
    yi = ecdif.yo
    while k < x_fin:
        tn = where(around(T_int + 1000*round(T/2, 4), 0) == round(1000*k
            , 0))[0] #Here T/2 represents the delay that we are
            introducing
        if len(tn) == 0:
            ecdif = Segundo_oscilador(delta = 0.)
            yi = euler(ecdif, k, yi, h)
            k = round(k + h, 4)
            if yi[0] > 30:
                yi[0] = ecdif.c
                yi[1] = yi[1] + ecdif.d
            else:
                print(k)
                exc.append(k)
                ecdif = Segundo_oscilador(delta = 1.)
                yi = euler(ecdif, k, yi, h)
                k = k + h
            if yi[0] > 30:
                yi[0] = ecdif.c
                yi[1] = yi[1] + ecdif.d
            X.append(k)
            Y.append(yi)
        return array(X), array(Y), exc

#Here, we proceed to solve the equations and plot the results
t2, V2, exc = resolucion_segundo_oscilador(0, 3000.01, 0.001)
plot(t2, V2[:, 0])
xlim(0, 2000)
legend(("Oscillator_1", "Oscillator_2"), loc = "best", fontsize
    = 10)
grid()
show()

```

References

- [1] Chris Bonell. *Kuramoto Oscillators*. http://guava.physics.uiuc.edu/~nigel/courses/569/Essays_Fall2011/Files/bonnell.pdf, December 2011.
- [2] C. Canavier. *Phase response curve*. Scholarpedia, 1(12), 2006.

- [3] Leonardo L. Gollo, Claudio R. Mirasso, Mercedes Atienza, Maite Crespo-García, and Jose L. Cantero. *Theta band zero-lag long-range cortical synchronization via hippocampal dynamical relaying*. PLoS ONE, 6(3):e17756.
- [4] Eugene M. Izhikevich. *Simple Model of Spiking Neurons*. IEE Transactions on Neuronal Networks, 14:1569–1572, November 2003.
- [5] Eugene M. Izhikevich. *Dynamical Systems in Neuroscience: The Geometry of Excitability and Bursting*, chapter 10. Synchronization, pages 435–480. The MIT Press, 2007.
- [6] Eugene M. Izhikevich. *Dynamical Systems in Neuroscience: The Geometry of Excitability and Bursting*, chapter 7. Neuronal Excitability, pages 215–2183. The MIT Press, 2007.
- [7] Beatriz Mato Mora. *Phase response curve of a neuronal circuit*, chapter 2. Phase response curve, pages 7–19. Universitat de les Illes Balears, 2015.